Imperial College London

Multiscale structural, thermal and thermo-structural optimization towards three-dimensional printable structures

by

Imediegwu, Chikwesiri Tolu

Supervisors: Dr. Robert Hewson, Dr. Matthew Santer

Department of Aeronautics,
Imperial College London

Submitted in part fulfilment of the requirements for the degree of
Doctor of Philosophy in the Department of Aeronautics of
Imperial College London,
June 2020

Abstract

This thesis develops a robust framework for the multiscale design of three-dimensional lattices with macroscopically tailored structural and thermal characteristics. The work exploits the high process flexibility and precision of additive manufacturing to the physical realization of complex microstructure of metamaterials by developing and implementing a multiscale approach. Structures derived from such metamaterials exhibit properties which differ from that of the constituent base material. Inspired by the concept of Free Material Optimization (FMO), a periodic microscale model is developed whose geometric parameterization enables smoothly changing properties and for which the connectivity of neighbouring microstructures in the large-scale domain is guaranteed by slowly changing large-scale descriptions of the lattice parameters. The microscale model is evaluated at full-factorial design points to discretely populate material property spaces. A property point is fully defined for a micro-architecture when its elasticity matrix, thermal conductivity matrix and volume fraction is determined. The process of property-space population is facilitated by leveraging the existence of micro-architecture symmetries so that there exists a 95% reduction in the simulations required despite a full-factorial design-of-experiments. The discrete property evaluations are converted to continuous functions by response surface modelling so that the properties exist as continuous functions of the micro-architecture geometry parameters. A lattice-based functional grading of material is derived using the finite element method. The optimization is driven by a chain-rule combination of sensitivities derived by the adjoint method and sensitivities derived from explicit material property expressions. The novelty of the work lies in the use of multiple geometry-based small-scale design parameters for optimization problems in three-dimensional real space. The approach is demonstrated by solving structural, thermal and thermo-structural optimization problems. The results show designs with improved optimality compared to commonly implemented optimization methodologies. The optimal designs obtained are physically realizable by additive manufacturing techniques.

Declaration of Originality

This is to certify that this copy of my thesis, which I have presented for consideration for my PhD degree, embodies the results of my own course of study and research and all else has been appropriately referenced. It has been entirely composed by myself and has been seen by my supervisors before presentation.

Copyright Declaration

The copyright of this thesis rests with the author. Unless otherwise indicated, its contents are licensed under a Creative Commons Attribution-NonCommercial 4.0 International Licence (CC BY-NC).

Under this licence, you may copy and redistribute the material in any medium or format. You may also create and distribute modified versions of the work. This is on the condition that: you credit the author and do not use it, or any derivative works, for a commercial purpose.

When reusing or sharing this work, ensure you make the licence terms clear to others by naming the licence and linking to the licence text. Where a work has been adapted, you should indicate that the work has been changed and describe those changes.

Please seek permission from the copyright holder for uses of this work that are not included in this licence or permitted under UK Copyright Law.

Acknowledgements

I will like to express gratitude to the Federal Government of Nigeria for funding this research program through the Petroleum Technology Development Fund (PTDF). As a recipient of the Presidential Special Scholarship for Innovation and Development, I was given the opportunity of a life-time to make a significant contribution to the field of structural optimization and I will always be eternally grateful.

I will like to express profound gratitude to my supervisors, Dr. Robert Hewson and Dr. Matthew Santer for their delicate and thorough supervision reliant on their wealth of experience and adept knowledge, as they guided me through difficult moments and provided invaluable insight into the subject.

I will like to express gratitude to my friends and colleagues – Dilaksan, Ryan and Morgan for all those many hours in the 'lattice-kids' sessions where we discussed our findings on the subject and demonstrated our passion for the search of optimality. Those many evenings in heated debate targeted towards proving the correctness and relevance of our work will never be forgotten.

I am profoundly grateful to my wife, Chidiuto, for her encouragement and patience with me as I have pursued my passions in research and engineering. I recognize her sacrifices for me and our family and I couldn't have achieved any of this without her unwavering support. My gratitude also go to my parents and siblings.

Finally, I am grateful to God for the opportunity to pursue a life-long dream of cutting-edge research in a world-renowned institution.

Dedication

This thesis is dedicated to the Mechanical Engineering Department of the University of Nigeria, Nsukka, where I obtained my undergraduate degree. I received the inestimable skills that were foundational to the execution of this research and for this I am eternally grateful.

Nomenclature

Latin

$\boldsymbol{E^H}$	Homogenized elasticity matrix
$\boldsymbol{E}$	Elasticity tensor
$\boldsymbol{I}$	Identity matrix
$\boldsymbol{K^H}$	Homogenized thermal conductivity matrix
$\boldsymbol{K}$	Thermal conductivity tensor
$\boldsymbol{n}$	Unit normal vector
$\boldsymbol{r}$	Vector of radii parameters
$\boldsymbol{u}$	Displacement
c_c	Vector of unknown coefficients
D_e	Error functional
dV_e	Volume of element
E_s	Young's Modulus of base material
E_v	Young's Modulus of void
E_y	Young's Modulus

F	Force per unit volume
f_θ	Heat source per unit volume
J	Objective functional
k	Number of elements in polynomial basis vector
K_s	Thermal conductivity of base material
K_v	Thermal conductivity of void
K_y	Thermal conductivity
m_k	Dimension/Number of independent variables
N_e	Macroscale number of elements
n_e	Number of elements along unit cell edge
N_f	Full factorial no. of simulations
n_f	Node fraction
n_k	Polynomial degree
n_L	Number of levels
N_n	Macroscale number of nodes
N_Q	Total number of possible permutations
N_s	Reduced number of simulations
Q	Rotation/Reflection operator
q	Heat flux
r_Q	Number of combined transformation operations
V_D	Design Volume constraint

V_e Volume of unit cell

V_f Macroscale volume fraction

v_f Lattice unit cell volume fraction

z Helmholtz filter radius

n Number of unique transformation operations

V Macroscale domain volume

Greek

$\boldsymbol{\beta}$ Thermo-elasticity tensor

$\boldsymbol{\sigma'}$ Thermally-induced stress tensor

$\boldsymbol{\sigma^T}$ Total cauchy stress tensor

$\boldsymbol{\sigma}$ Cauchy stress tensor

$\boldsymbol{\varepsilon}$ Strain tensor

ϵ Scale separation parameter

η_p Property vector

κ Bulk modulus

λ_e Second Lame's constant

μ Shear modulus

μ_e First Lame's constant

ν Poisson's Ratio

ρ_{max} Upper bound on pseudo-lattice density function

ρ_{min} Lower bound on pseudo-lattice density function

θ Temperature difference

ϱ Mass density

Other Symbols

$\boldsymbol{\mathcal{P}}$ Property polynomial

Abbreviations

AEH Asymptotic Expansion Homogenization

AM Additive Manufacturing

BESO Bi-directional Evolutionary Structural Optimization

CAD Computer-Aided Design

CHS Cylindrical Heat Sink

DoE Design of Experiments

ESO Evolutionary Structural Optimization

FDM Fused Deposition Modeling

FEM Finite Element Method

FMO Free Material Optimization

FRCM Fibre-Reinforced Composite Material

HMM Heterogeneous Multiscale Methods

HPS Hollow-pipe Section

HS Hashin-Shtrikman

LSM Level-Set Method

LUC Lattice Unit Cell

PDE Partial Differential Equation

PDEs Partial Differential Equations

RBF Radial Basis Function

RMSE Root Mean Square Error

RUC Repeating Unit Cell

RSM Response Surface Methodologies

RVE Representative Volume Elements

SIMP Solid Isotropic Material with Penalization

SLA Stereolithography

SLM Selective Laser Melting

SLS Selective Laser Sintering

TLC Top-Loaded Cantilever

TO Topology Optimization

UFL Unified Form Language

Contents

Abstract **1**

Declaration of Originality **3**

Copyright Declaration **4**

Acknowledgements **5**

Dedication **6**

Nomenclature **7**

Abbreviations **11**

1 Introduction **26**

1.1 Context and Motivation 26

1.2 Thesis overview 28

1.3 Aims and Objectives 32

1.4 Contributions 33

1.5 Conference presentations 33

1.6 Publications 34

2 Review of Structural Optimization 35

2.1 Topology Optimization 36

2.1.1 Monoscale (classical) topology optimization 36

2.1.1.1 Solid Isotropic Material with Penalization (SIMP) 37

2.1.1.2 Evolutionary approaches 40

2.1.1.3 Level-Set Methods 40

2.1.2 Multiscale topology optimization 42

2.1.2.1 Concurrent Multiscale Optimization 42

2.1.2.2 Sequential Multiscale Optimization 43

2.2 Free Material Optimization 44

2.3 Optimization of metamaterials 45

2.4 Coupled Sequential Multiscale Optimization 46

2.4.1 Homogenization 49

2.4.2 Response Surface Methodology 51

2.4.2.1 Design of Experiments 52

2.4.2.2 Polynomial Approximation 53

2.4.2.3 Radial Basis Functions Approximation 54

2.4.2.4 Kriging Approximation 55

3 Microscale Model Development 58

3.1 Assumptions 58

3.2 Microscale Parameterization 60

3.3 Element-based material assignment 60

3.4 Asymptotic Expansion Homogenization 62

3.4.1 Strain deformation analyses 63

3.4.2 Thermal Analyses 66

3.4.3 Periodic Boundary Conditions 69

4 Microscale Numerical Implementation 71

4.1 Micro-architecture parameterization 71

4.2 Property Assignment 73

4.3 Asymptotic expansion homogenization 78

4.4 Numerical Verification 83

4.5 Mesh Convergence Studies 86

4.6 Stress Flow Characterization 90

4.7 Heat Flow Characterization 94

5 Material Model Generation 98

5.1 Axis transformation operations 99

5.2 Unit Cell geometry transformation 100

5.3 Material Property Transformation 101

5.4 Property Space Population 103

5.5 Property Space Exploration 105

5.6 Performance against Hashin-Shtrikman Bounds 108

5.7 Response Surface Model Generation 110

6 Macroscale Problem Formulation **114**

6.1 Optimization Phase Overview 114

6.2 Assumptions 115

6.3 Mathematical Formulation 115

6.3.1 Structural Optimization 117

6.3.2 Thermal Optimization 118

6.3.3 Thermo-structural Optimization 119

6.4 Filtering of Control Variables 120

6.5 Sensitivity Analyses 121

6.6 Numerical Implementation 125

6.6.1 Mesh generation 125

6.6.2 Function space generation 126

6.6.3 Domain Initialization 126

6.6.4 Objective functional evaluation 127

6.6.5 Gradient evaluation 127

6.6.6 Constraint evaluation 128

6.6.7 Jacobian evaluation 128

6.6.8 Interior Point Optimizer (`Ipopt`) 128

7 Structural Optimization – Compliance minimization 131

7.1 Case 1: Top-loaded Cantilever Beam 131

7.1.1 Problem Definition 131

7.1.2 Results and Discussion 132

7.2 Case 2: Engine Backet 139

7.2.1 Problem Definition 140

7.2.2 Results and Discussion 140

7.3 Case 3: The Goose-Neck Hinge 145

7.3.1 Problem Definition 146

7.3.2 Results and Discussion 147

8 Structural Optimization – Target Deformation 153

8.1 Case 4: Two-prong gripper 153

8.1.1 Problem Definition 153

8.1.2 Results and Discussion 155

8.2 Case 5: Three-prong gripper 160

8.2.1 Problem Definition 161

8.2.2 Results and Discussion 164

8.3 Structural Optimization: Summary of results 166

9 Thermal and Thermo-structural Optimization 167

9.1 Case 6: Cylindrical Heat Sink 167

9.1.1 Problem Definition 168

9.1.2 Results and Discussion 169

9.1.3 Thermal Optimization: Summary of results 173

9.2 Thermo-structural Optimization 174

9.3 Case 7: Hollow-pipe section 174

9.3.1 Problem Definition 174

9.3.2 Results and Discussion 176

9.3.3 Thermo-structural Optimization: Summary of results 181

10 Conclusion 182

10.1 Summary 182

10.2 Thesis Achievements and Significance 183

10.3 Limitations 185

10.4 Future Research Directions 187

Bibliography 188

List of Tables

4.1 Sample micro-architectures enabled by parameterization 82

5.1 Table of R^2-values and RMSEs for 6th-order polynomial metamodels . . . 111

7.1 Top-loaded Cantilever Beam: Problem Definition 133

7.2 Engine Bracket: Problem Definition 139

7.3 Goose-Neck Hinge: Problem Definition 145

8.1 Two-prong gripper: Problem Definition 154

8.2 Three-prong gripper: Problem Definition 160

9.1 Cylindrical Heat Sink: Problem Definition 168

9.2 Hollow-pipe section: Problem Definition 175

List of Figures

1.1 Process flow chart showing the phases and sub-processes of the developed framework 29

1.2 Hierarchical organization of framework 30

2.1 The effect of the penalization parameter, p on the stiffness-density relationship 38

2.2 Level-Set Method Illustration (Adapted from Van Dijk et al.[1]) 41

2.3 Heterogeneous Multiscale Method 48

2.4 Illustration of homogenization in 2D 49

2.5 The concept of homogenization across scales 50

3.1 2D illustration of element-based material assignment and micro-architecture geometry definition 61

3.2 Unit strain deformation on the LUC (Scale: 0.2:1) 65

3.3 Unit temperature gradient on the LUC 68

3.4 Coordinate system for PBC implementation 69

4.1 Microstructure parameterization 72

4.2 Face member material assignment illustration 74

4.3 Diagonal member material assignment illustration 75

4.4 Geometry periodicity of diagonal members (Assembly of Section C-C) . . . 76

4.5 Example micro-architectures 77

4.6 Element-based material assignment 79

4.7 Displacement field solution given $\bar{\varepsilon}_{ij}$ (Deformation scale = 0.2 : 1) 79

4.8 Temperature field solution given $\nabla\bar{\theta}_i$ 80

4.9 Stress tensor components given $\bar{\varepsilon}_{11}$ (Deformation scale = 0.2 : 1) 81

4.10 Stress tensor components given $\bar{\varepsilon}_{12}$ (Deformation scale = 0.2 : 1) 81

4.11 Heat flux vector components given $\nabla\bar{\theta}_1$ 81

4.12 Material assignment 84

4.13 Effective bulk and shear moduli of composite with spherical void inclusions 85

4.14 Mesh Convergence Studies - All members incremented 86

4.15 Mesh Convergence Studies - Only member 5 incremented 87

4.16 Mesh Convergence Studies - Only member 1 incremented 88

4.17 Mesh Convergence Studies (Thermal conductivity) 89

4.18 Load path through, $\boldsymbol{r} = (0, 0, 0, 0, 0.1, 0.1, 0.1)$ due to $\bar{\varepsilon}_{11}$ 91

4.19 Load path through, $\boldsymbol{r} = (0, 0, 0, 0, 0.1, 0.1, 0.1)$ due to $\bar{\varepsilon}_{12}$ 92

4.20 Load path through, $\boldsymbol{r} = (0.1, 0.1, 0.1, 0.1, 0, 0, 0)$ due to $\bar{\varepsilon}_{11}$ 92

4.21 Load path through, $\boldsymbol{r} = (0.1, 0.1, 0.1, 0.1, 0, 0, 0)$ due to $\bar{\varepsilon}_{12}$ 93

4.22 Load path through, $\boldsymbol{r} = (0.1, 0.1, 0.1, 0.1, 0.1, 0.1, 0.1)$ due to $\bar{\varepsilon}_{11}$ 93

4.23 Load path through, $\boldsymbol{r} = (0.1, 0.1, 0.1, 0.1, 0.1, 0.1, 0.1)$ due to $\bar{\varepsilon}_{12}$ 94

4.24 Thermal load path through, $\boldsymbol{r} = (0, 0, 0, 0, 0.1, 0.1, 0.1)$ due to $\nabla\bar{\theta}_1$ 95

4.25 Thermal load path through, $\boldsymbol{r} = (0.1, 0, 0, 0, 0, 0, 0)$ due to $\nabla\bar{\theta}_1$ 96

4.26 Thermal load path through, $\boldsymbol{r} = (0.1, 0.1, 0.1, 0.1, 0.1, 0.1, 0.1)$ due to $\nabla\bar{\theta}_1$. 96

5.1 Example of symmetry geometries of a parent micro-architecture 104

5.2 Symmetry-driven simulation reduction log-plot (N_f is the full factorial number of simulations and N_s is the reduced number of simulations) 105

5.3 Property space exploration: Projections of micro-architectures on stiffness matrix component-volume fraction planes 106

5.4 Performance of lattice parameterization against Hashin-Shtrikman Bounds 109

5.5 Hyper-planes through typical seven-dimensional K_{xx} metamodels. 112

5.6 Hyper-planes through typical seven-dimensional E_{xx} metamodels. 113

6.1 Macroscale Optimization Loop 129

7.1 Top-loaded Cantilever Beam 132

7.2 Top-loaded Cantilever: Displacement, u (m) at Iteration 1 (Deformation Scale – 32000:1) 134

7.3 Top Loaded Cantilever: Optimal radii distribution for diagonal members 1–4135

7.4 Top Loaded Cantilever: Optimal radii distribution for face members 5–7 . 136

7.5 Top-loaded Cantilever: Minimum and maximum principal stress paths . . . 136

7.6 Post-processed pseudo–lattice–density distribution 137

7.7 Top-loaded Cantilever: Lattice-based material distribution and optimization convergence plot . . . 137

7.8 Top-loaded Cantilever: SIMP material distribution and optimization convergence plot . . . 138

7.9 Top-Loaded Cantilever: Lattice Reconstruction . . . 138

7.10 Engine Backet . . . 139

7.11 Engine Bracket: Non-design region definition . . . 140

7.12 Engine Backet: Displacement, u (m) at Iteriation 1 (Deformation Scale – 25000:1) . . . 140

7.13 Engine Bracket: Maximum principal stress flow path . . . 141

7.14 Engine Bracket: Optimal radii distribution for diagonal members 1–4 . . . 142

7.15 Engine Bracket: Optimal radii distribution for face members 5–7 . . . 142

7.16 Engine Bracket: Lattice-based material distribution and optimization convergence plot . . . 143

7.17 Engine Bracket: SIMP material distribution and optimization convergence plot . . . 143

7.18 Engine Bracket: Lattice Reconstruction . . . 144

7.19 Goose-Neck Hinge (GNH) . . . 145

7.20 GNH: Non-design region definition . . . 146

7.21 GNH: Displacement, u (m) at initial conditions (Deform. Scale, 2000:1) . . . 146

7.22 GNH:Maximum and minimum principal stress paths . . . 147

7.23 GNH: Optimal radii distribution for diagonal members 1–4 . . . 148

7.24 Engine Bracket: Optimal radii distribution for face members 5–7 149

7.25 GNH: Lattice-based material distribution and optimization convergence plot 150

7.26 GNH: SIMP material distribution and optimization convergence plot . . . 150

7.27 GNH: Lattice Reconstruction 151

8.1 Two-prong gripper 154

8.2 Two-prong gripper: Displacement, u (m) at Iteration 1 155

8.3 Two-prong gripper: Optimal radii distribution for diagonal members 1–4 . 156

8.4 Two-prong gripper: Optimal radii distribution for face members 5–7 157

8.5 Two-prong gripper: Displacement Target 157

8.6 Two-prong gripper: Lattice-based material distribution and optimization convergence plot 158

8.7 Two-prong gripper: Lattice Reconstruction 158

8.8 Three-prong gripper 160

8.9 Three-prong gripper: Displacement, u (m) at Iteration 1 161

8.10 Three-prong gripper: Optimal radii distribution for diagonal members 1–4 162

8.11 Three-prong gripper: Optimal radii distribution for face members 5–7 . . . 163

8.12 Three-prong gripper: Displacement Target 164

8.13 Three-prong gripper: Lattice-based material distribution and optimization convergence plot 164

8.14 Local anisotropic micro-architecture 165

8.15 Three-prong gripper: Lattice reconstruction 166

9.1 Cylindrical Heat Sink 167

9.2 Cylindrical Heat Sink: Non-design region definition 169

9.3 Cylindrical Heat Sink: Temperature, θ (K) at Iteration 1 169

9.4 Cylindrical Heat Sink: Optimal radii distribution for diagonal members 1–4 170

9.5 Cylindrical Heat Sink: Optimal radii distribution for face members 5–7 . . 170

9.6 Cylindrical Heat Sink: Lattice-based material distribution and optimization convergence plot 171

9.7 Cylindrical Heat Sink: SIMP material distribution and optimization convergence plot 171

9.8 Cylindrical Heat Sink: Section X-X showing temperature evolution through iterations 172

9.9 Cylindrical Heat Sink: Lattice Reconstruction 173

9.10 Hollow-pipe section 174

9.11 Hollow-pipe section: Non-design region definition 176

9.12 Hollow-pipe section: Temperature, θ (K) on deformed mesh at Iteration 1 . 176

9.13 HPS: Optimal radii distribution for diagonal members 1–4 177

9.14 HPS: Optimal radii distribution for face members 5–7 178

9.15 HPS: Temperature profile (Deformation Scale: 50:1) 178

9.16 HPS: Volume fraction distribution (Deformation Scale: 50:1) 179

9.17 HPS: Lattice-based material distribution and optimization convergence plot 180

9.18 HPS: Lattice Reconstruction 180

Chapter 1

Introduction

1.1 Context and Motivation

The advent of additive manufacturing (AM) and its rapid evolution is increasingly offering tremendous flexibility and precision to the physical realization of metamaterials, potentially expanding the capabilities of some structural optimization techniques [2, 3, 4]. In the past, the realization of optimal structural design was limited to manufacturing techniques such as casting and machining processes which constrained the complexity and precision of realizable designs [5]. Today, the mechanics of metamaterials have defined a class of optimization techniques that allow free variations of the material properties tailored to meet prescribed macroscale objectives. This concept of freely varying material properties in the domain of a structure towards fulfilling functional objectives, with the capacity for physical realization of optimized structures by additive manufacturing techniques provides inspiration for this study.

Additive manufacturing (AM) techniques have broadened the space of admissible structural designs due to their ability to produce complex geometries at very fine scales. Some common AM techniques such as Fused Deposition Modeling (FDM) [6], Selective Laser Sintering (SLS) [7, 8] and Stereolithography (SLA) [9] feature a layer by layer construction

of possibly complex structures. Whether by stratified extrusion of thermoplastic (FDM), sintering of powerdered nylon or metals (SLS) or curing of resin by ultraviolet laser (SLA), these techniques are suitable for rapid prototyping since associated costs are decoupled from the complexity of the structure to be manufactured [10]. Additive manufacturing has enabled the physical realization of optimal structural design that were previously impossible to manufacture or for which precision was compromised to satisfy manufacturing constraints. Topology optimization, concerning the optimal distribution of material within a structure to meet functional objectives, is one such example. The most common approach to topology optimization, parameterizes local material property within a discretized domain of the structure as a weighting of the base material's Young's modulus, requiring a penalization parameter on the weighting function as well as post-processing to yield manufacture-ready optimal solutions. Despite its popularity, the requirement for penalization to derive physical structure leads to sub-optimal real-world design solutions.

A general framework of optimizing directly on a free parameterization of the material tensor, called Free Material Optimization (FMO), is often regarded as the ultimate generalization of the structural optimization problem [11, 12, 13, 14]. The FMO framework employs the components of the constitutive material tensor as design variables which are free to spatially vary throughout the domain of the structure. By definition, FMO yields the optimal structural solution as there exist no restrictions on local properties except that the elastic tensor be symmetric and positive semi-definite – a physical constraint [13]. Though optimization using the unrestricted set of components of the constitutive material tensor as design variables makes no considerations for the physical realization of local structure, mechanics of metamaterials present a means to integrate admissible local structure within an FMO framework.

Structural optimization of metamaterials is a subject of notable interest [15]. These are materials that derive their properties from their underlying micro-architecture rather than their material composition. The design of these metamaterials to match predefined homogeneous material properties is well developed. However, the integration of these ma-

terials into structural optimization strategies to achieve heterogeneous, spatially-varying properties is an active research field [10, 16]. By controlling the geometric parameters of their micro-architectures, metamaterials can be designed to exhibit interesting macroscopic behavior, so that properties of structures built up of these metamaterials can be tailored to satisfy predefined objectives [15]. Equipped with the free parameterization of material property driven by the free design of local architecture, an extension to the FMO framework can be derived that delivers manufacturable optimal designs without sacrificing precision.

This research exploits the process flexibility and precision of additive manufacturing techniques to the physical realization of mechanically and thermally optimized structures using a multiscale approach. The approach is a variant of FMO, with emphasis on delivering a physical optimized solution. A robust optimization framework is derived that executes macroscale structural optimization using geometry parameters of constituting micro-architectures, leading to a design of local architecture as well as material layout. Mapping of compatible and connectable micro-architectures is not required, rather, lattice micro-architectures are derived automatically as optimal values of lattice geometry parameters are computed. The novelty of this research lies in the use of multiple geometry-based small-scale design parameters for optimization problems in three-dimensional real space. The parameterization implemented supports full control over all components of anisotropy with the potential for interesting results. The final outcome is a physically realizable functional grading of the material of structures, mechanically and thermally tailored to satisfy functional objectives.

1.2 Thesis overview

The main goal of this research is to derive a multiscale framework that defines the functional grading of material properties for the purpose of satisfying predefined macroscale objectives, using small-scale lattice geometry micro-parameters as control variables. This

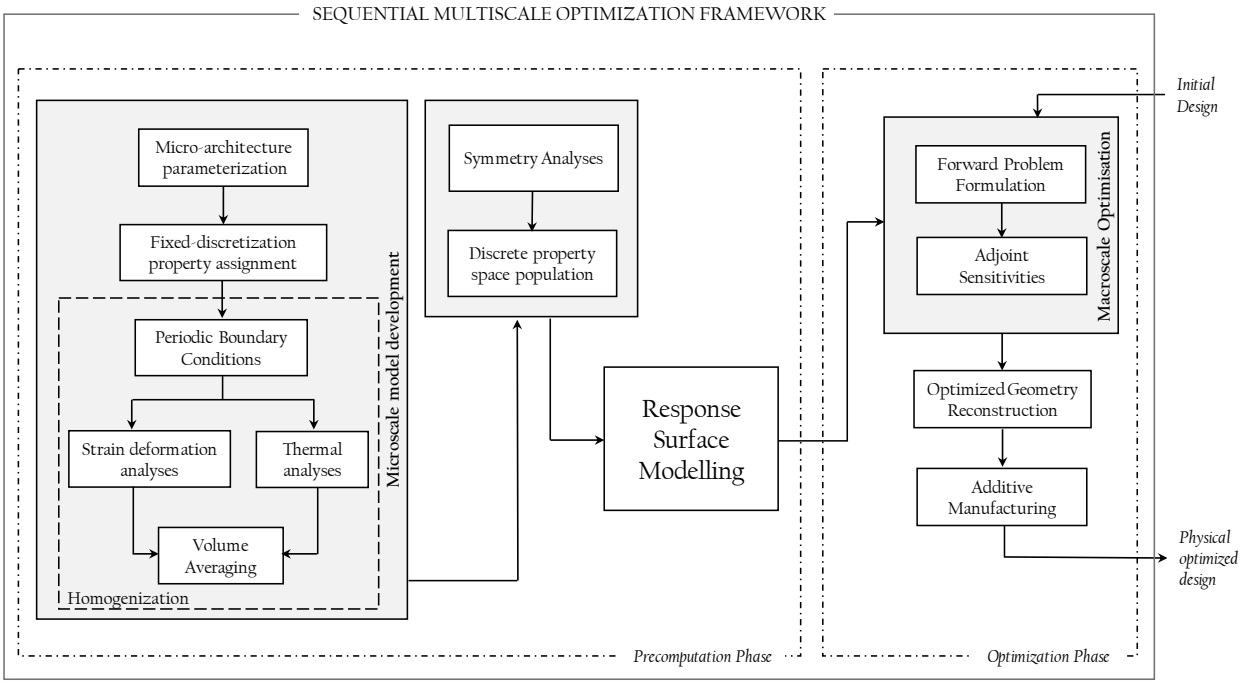


Figure 1.1: Process flow chart showing the phases and sub-processes of the developed framework

sequential multiscale framework is to be deployed over two computational phases. A diagrammatic description of the derived framework is shown in Fig. 1.1.

The first phase comprises an off-line discrete evaluation of effective macroscale properties in the space of microscale lattice geometry parameters. This precomputation involves deriving a parameterization of the small scale that supports a smoothly-changing architecture for smooth pertubations of the geometry parameters. A full factorial design of experiments (DoE) is set up to discretely populate the space of small-scale parameters by perturbing the geometry parameters over several levels and executing numerical homogenization to derive effective material properties of the corresponding micro-architectures. This first phase culminates in the generation of continuous functions of material interpolation derived from the precomputed discrete material property evaluations called response surface models or meta-models. The second phase of the framework constitutes the formulation of structural and thermal optimization at the macroscale using the geometry micro-parameters of the first phase as control variables. Both scales are coupled by the response surface models generated in the first phase. The polynomial approximations,

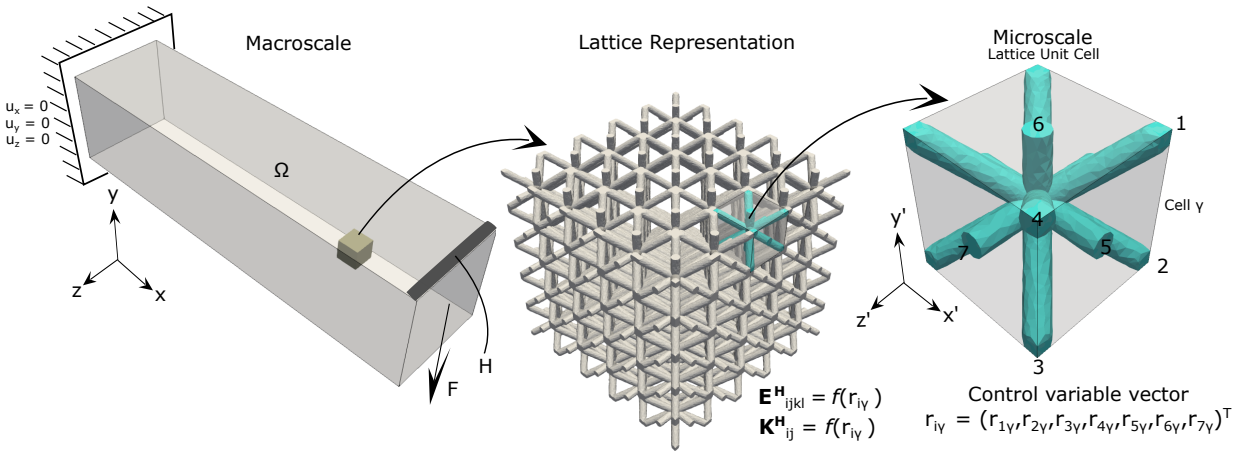


Figure 1.2: Hierarchical organization of framework showing macroscale domain built up of periodic lattice micro-architectures with elastic and thermal properties controlled by lattice micro-parameters

constructed as continuous functions to the discrete evaluations of effective material property, represent functional relationships between the components of the material elastic and conductivity tensors and lattice geometry micro-parameters in the form of explicit expressions, hence enabling significant savings in computational cost. The model form also facilitates explicit derivations of sensitivities as is demonstrated in the macroscale optimization formulation. Though the first phase is associated with significant computational effort, the off-line sampling of the property space needs to be executed only once as the material's Young's modulus and thermal conductivity scales linearly with the elastic and conductivity tensor components respectively [17]. The microscale parameterization implemented supports all components of anisotropy so that optimization formulations in this work have potential to execute multi-objective optimization and to yield interesting results. It is not claimed that the exploration of the property space is exhaustive given the parameterization scheme employed. However, the truss-like parameterization implemented is known to span broad extents of material property [18], providing a broad range of material behaviors, when manufacturing constraints exist. It also ensures connectivity of adjacent micro-architectures and does not support enclosed voids which is suited to the AM techniques intended for this framework. The final result is a functionally graded structure with tailored thermal, structural and thermo-structural macroscale

properties. Figure 1.2 illustrates the hierarchical organization of the framework showing material mechanical and thermal properties of a macroscale problem as functions of lattice geometry parameters. The work described in this thesis is organised as follows:

Chapter 2 presents a survey of the development and evolution of structural optimization methods. It is intended that by guiding the reader through the development of the subject to the state-of-the-art, the reader may appreciate the contribution, context and motivation for this research. In Chapter 3, a description of the microscale model development is initialized by reference to background assumptions. The requirements for a suitable microscale parameterization is presented then the methods for determining the elastic and thermal properties of micro-architecture is described. In Chapter 4, the numerical implementation of the theoretical concepts described in Chapter 3 is presented. A specific microscale model is developed. The effective property evaluations derived by asymptotic expansion homogenization are validated by bench-marking against known analytic expressions for the properties of composites with spherical void inclusions. Mesh convergence studies are performed and the stress and heat flow is characterized for the developed microscale model. In Chapter 5, a material model is generated by discrete evaluations of the microscale model of Chapter 4. These discrete evaluations are then converted to polynomial approximations so that the properties exist as explicit expressions of the micro-architecture geometry parameters. The performance of the material interpolation model is also investigated against the well known Hashin-Shtrikman bounds.

In Chapter 6, the macroscale optimization formulation is presented for structural, thermal and thermo-structural problems of this work. A dedicated section discusses the numerical implementation of the formulations. In Chapters 7, 8 and 9, the multiscale framework is applied to compliance minimization, target deformation, thermal compliance minimization and thermo-structural problems using the property response surface models. Finally, Chapter 10 summarizes and concludes the findings of the study. The achievements of the study are demonstrated by highlighting the contributions of the framework to the state-of-the-art. The limitations of the derived framework are enumerated and sugges-

tions are made for future research directions emanating from the solutions obtained and in a broader context, the derived framework.

1.3 Aims and Objectives

Inspired by the works of Kočvara et al [19, 13, 14] and those of Panetta et al. [10] and Zhu et al. [20] to derive optimized structures built up of manufacturable micro-architectures, this work seeks to exploit the precision and process flexibility of additive manufacturing to the realization of mechanically and thermally optimized structures through a multiscale approach. This thesis aims to:

- develop a microscale model suitable for the multiscale framework to evaluate the effective elastic and conductivity tensor given microscale parameters.
- develop a library of elastic and thermal material properties in the space of microstructure parameters enabled by the discrete evaluation of the microscale model.
- construct response surface models that explicitly express effective mechanical and thermal properties as well as volume fraction of local structure as functions of small-scale geometry parameters to facilitate rapid evaluation of the macroscale solver.
- compute sensitivities by the adjoint method for specified functionals suitable for gradient-based optimization.
- execute macroscale structural, thermal and thermo-structural optimization in the space of small-scale lattice parameters.
- execute lattice reconstruction of the optimized structures given the lattice micro-parameter distributions.
- highlight the capabilities of the derived framework against other conventionally implemented approaches.

1.4 Contributions

The novelty of this research lies in the use of multiple geometry-based small-scale design parameters for multiscale structural, thermal and thermo-structural optimization problems in three-dimensional real space. Key contributions include:

1. the development of a lattice-based parameterization that supports full control over material point anisotropy.
2. the generation of a full-factorial elasticity and thermal conductivity database of lattice micro-architecture properties with their response surface models.
3. the formulation of free material optimization in the space of multiple lattice micro-parameters.

1.5 Conference presentations

Conference presentations arising from the work presented in this thesis are:

1. C. Imediegwu, R. Murphy, R. Hewson, M. Santer, "The design of a lattice-based periodic microstructure model towards 3D printable optimized structures", The 10th European Solid Mechanics Conference, Bologna, Italy (2018).
2. C. Imediegwu, R. Murphy, R. Hewson, M. Santer, "Multiscale structural and thermal optimization towards 3D printable structures", The 9th International Conference on Computational Methods, Rome, Italy (2018).

1.6 Publications

Publications arising from the work presented in this thesis are:

1. C. Imediegwu, R. Murphy, R. Hewson and M. Santer, "Multiscale structural optimization towards three-dimensional printable structures", Structural and Multidisciplinary Optimization, 2019. Multiscale structural optimization towards three-dimensional printable structures
   https://link.springer.com/article/10.1007/s00158-019-02220-y

2. C. Imediegwu, R. Murphy, R. Hewson and M. Santer, "Multiscale thermal and thermo-structural optimization of three-dimensional lattice structures" (Preprint submitted to Computer Methods in Applied Mechanics and Engineering, June, 2020).

Chapter 2

Review of Structural Optimization

The optimal design of continuum structures has the potential to greatly enhance their performance [21]. Structural optimization constitutes a mathematical formulation that enables the choice of the best structural design amongst several design alternatives, while obeying structural mechanics principles. As a consequence, the field of structural optimization combines mechanics, variational calculus and mathematical programming [17] to determine the optimal material distribution of a structural component. Aspects of structural optimization include the sizing, shape and topology of the structure as it is designed to satisfy objectives. The class of structural optimization techniques that constitute the search for optimal topology have garnered significant interest as they emcompass the search for optimal size of entities and optimal shape of the boundaries of the structures. This work focuses on methods that are based on the search for optimal material layout given external loading and boundary conditions and optionally, a limitation on volume of material available to the optimal design. As such, a description of topology optimization presents a natural point of entry into the review of relevant structural optimization literature.

2.1 Topology Optimization

Topology Optimization (TO) is a widely implemented approach to structural optimization. It concerns determining the optimal layout of material within the domain of a structure towards enhancing its performance. The load, boundary conditions and an optional limitation on the availability of material are predefined but the measure of performance chosen by the designer constitutes the predefined functional objective to be satisfied. Common performance metrics for structural design include stiffness maximization (compliance minimization), weight minimization under stress constraints, design for target deformation and compliant mechanisms, deformation minimization, etc. However, the concept of TO extends beyond mechanical problems to several other disciplines such as acoustics [22], electromagnetics [23], aerodynamics [24], fluids [25] and combinations of disciplines thereof.

2.1.1 Monoscale (classical) topology optimization

The development of classical TO finds its origin with the paper presented by Bendsøe et al. [26] which documents the first investigation into the practical implementation of TO. Though a variant of TO based on discrete material/no-material layout within a discretized domain had been proposed earlier by Kohn et al. [27], it was shown to lack the existence of solutions since it resulted in an intractable combinatorial problem and was subject to the properties of the discretization elements [28]. In a later paper, Bendsøe [26] undertook structural optimization in the space of artificial composites in the form of materials with voids and layered materials. The formulation constituted compliance minimization for a given fraction of the initial volume of material, with the goal of attaining the optimal shape of the structure. The properties of each composite microstructure was determined by homogenization. Effective properties of the layered materials could be evaluated analytically but effective properties of the materials with voids had to be determined numerically. Having successfully demonstrated density distribution on

a two-dimensional fixed domain using anisotropic material, Bendsøe [26] proposed the use of an artificial power law as a substitute for the requirement of a homogenization-based functional stiffness-density relationship. The approach offered lower computational expense by circumventing the homogenization process associated with composite micro-architectures and was also capable of achieving a largely binary distribution of density values, enabled by a penalization parameter. This framework constituting the use of a penalized pseudo-density weighting of element-wise solid isotropic material assignment is the variant of topology optimization as implemented today, known as Solid Isotropic Material with Penalization (SIMP) [26, 29].

2.1.1.1 Solid Isotropic Material with Penalization (SIMP)

SIMP belongs to the class of density-based approaches in TO where the geometry of structure is described by material distribution of two or more phases on an element-wise discretization of the structure's domain. It's conceptual simplicity makes it a commonly implemented structural optimization technique. A continuous function, $\rho(x)$ is defined within the design domain, Ω such that $0 \leq \rho(x) \leq 1 \ \forall \ x \in \Omega$. The function is often referred to as an 'artificial' or 'fictitious' density function because it features intermediate densities which have no physical meaning but constitutes the global volume fraction, V evaluated as

$$V = \int_{\Omega} \rho(x) \ d\Omega \tag{2.1}$$

To prevent computational singularities, a lower bound is imposed on the density function so that $\rho_{min} \leq \rho \leq 1$, where typically $\rho_{min} = 10^{-3}$ corresponds to the density of a very weak material. The material model implemented for SIMP is given as

$$E_{ijkl} = \rho(x)^p \ E^0_{ijkl} \tag{2.2}$$

where E^0_{ijkl} represents the stiffness tensor of an isotropic base material (fully defined by the material's Young's modulus, E^0 and Poisson's Ratio, ν) and the penalization parameter

is chosen so that, $p > 1$ to penalize intermediate densities. Penalization of the density function ensures that intermediate densities become expensive and therefore undesirable, offering less stiffness compared to the associated cost (volume fraction) as illustrated in Fig. 2.1.

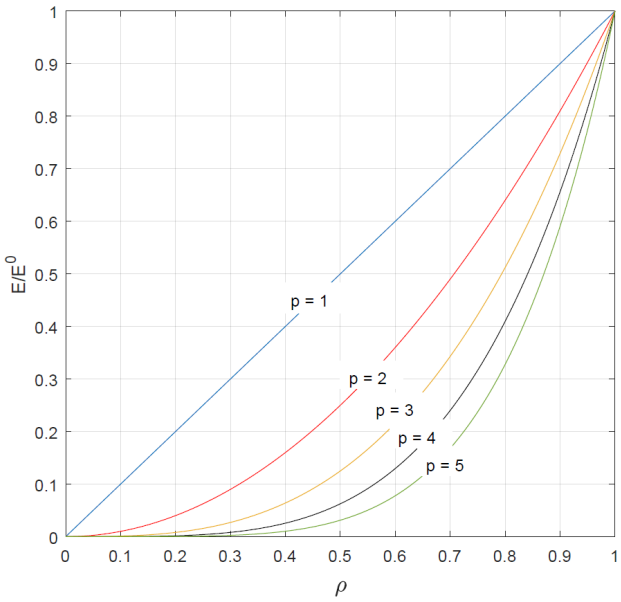


Figure 2.1: The effect of the penalization parameter, p on the stiffness-density relationship

The SIMP approach has been successfully applied to the optimization of mechanical, acoustic, electromagnetic, fluid and thermal properties of structures [21, 2]. By imposing stress and thermal compliance constraints, 2D structures have been optimized to perform better under thermal and mechanical loading [30]. Structures have been designed to minimize heat dissipation [31] with extensions to three-dimensional and multi-material optimization problems [32]. SIMP has also been demonstrated in the optimal design of heat exchangers [33] as well as optimal distribution of conductive material in the interior of biphasic adsorbent beds for the storage of natural gas [34].

Despite its successful application to a broad range of optimization problems across several disciplines, the basic implementation of SIMP has its challenges [17, 2]. The best value of the required penalization parameter is problem dependent with studies suggesting that $p \geq 3$ for a clear description of material or void within optimal solution. The

SIMP algorithm tends to terminate in a local minimum if the penalization parameter p is too high [17]. A basic SIMP implementation also suffers checkerboarding – a density distribution of solid and void in adjacent discretization elements constituting a physically untenable checkerboard-like pattern. Results are also mesh-dependent as mesh refinement results in ever-changing topologies – a consequence rooted in the issue of non-existence of solutions to the continuous problem [35, 2, 17, 36]. Ideally, mesh refinement should result in a clearer description of the same optimal topology and not in a qualitatively different topology with finner scale structures. [36].

Modifications to the SIMP implementation have alleviated some of the numerical issues associated with its basic implementation. Mesh-independent results can be obtained by reducing the space of admissible designs through a local restriction of the variation of the density variable [2] so there exists a limit to the formation of fine-scale structures. It has been demonstrated that stable mesh-independent solutions can be achieved by implementing a filter on the sensitivities or design variable field [37, 38]. This entails prescribing local values of the sensitivity or density variable as averages of neighbourhood values which effectively smooths the variation of the design variable field. Constraints on the perimeter of the structure have been shown to yield mesh-independent convergence [39, 40]. Regularization schemes, which involve imposing a local constraint on the gradient of the material density variable, have been implemented to yield smoother variations of the design variable [35, 41]. Continuation strategies have been implemented to prevent premature termination of the search in local minima, where the penalization parameter is progressively increased with the number of iterations [35, 42, 43]. It has been shown that the implementation of a fixed penalization or choice of continuation scheme applied to the penalization parameter has a significant influence on the optimal topology attained [44]. A variant of continuation strategies feature starting the algorithm with a large density filter radius and gradually decreasing its value to zero with increasing number of iterations [35, 42, 43]. However, most optimal solutions require post-processing due to the presence of meaningless intermediate densities. The SIMP implementation does not perform well

for multi-objective problems and the optimal choice of penalization parameter remains a subject of active investigation [17].

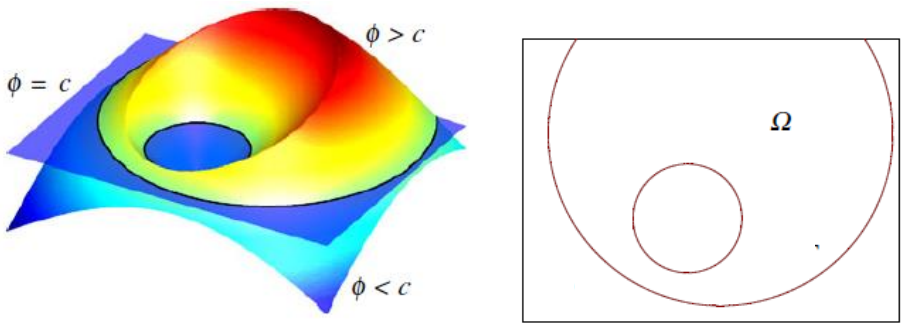
2.1.1.2 Evolutionary approaches

Other density-based TO approaches exist in literature such as Evolutionary Structural Optimization (ESO). Like in the SIMP approach, the parameterization of geometry here is a density-based discrete material layout. However, ESO features discrete density updates based on the removal of elements with the lowest strain-energy density [2]. The approach has been extended to bi-directional ESO (BESO), so that elements can be added or removed as required towards satisfying functional objectives [45]. This discrete update strategy is often driven by adjoint gradients. Unfortunately, ESO/BESO approaches suffer from a lack of algorithmic convergence due to complications associated with discrete density updates [46]. The approaches also suffer from a lack of mathematical generality for the inclusion of multiple non-linear constraints. Today, ESO/BESO are considered as discrete versions of the SIMP implementation [2].

2.1.1.3 Level-Set Methods

Another commonly implemented approach to TO is the Level Set Method (LSM). The advent of LSMs date back to the paper presented by Osher et al. [47] where the modelling of moving boundaries and the evolution of multi-phase flow interphases was presented. In LSMs, the parameterization of geometry uses implicit descriptions of the boundary of the structure. Given a level-set function, $\phi(\boldsymbol{x})$, the material and void regions are demacated by an interphase such that

$$\begin{cases} \phi(\boldsymbol{x}) > c, & \text{for material} \\ \phi(\boldsymbol{x}) = c, & \text{for the interphase} \\ \phi(\boldsymbol{x}) < c, & \text{for void} \end{cases} \tag{2.3}$$



(a) Level-set function, ϕ (b) 2D material domain Ω

Figure 2.2: Level-Set Method Illustration (Adapted from Van Dijk et al.[1])

where $c = 0$. Fig. 2.2 illustrates a level-set function, ϕ and corresponding material domain, Ω. Changing the level-set function alters the boundaries and topology of the structure using shape sensitivity analyses. As a consequence, LSMs are closely related to shape optimization methods [1]. Infact, topological derivative strategies are often incorporated to facilitate the nucleation of new holes in the interior of the material region [48]. Most implementations of LSMs have the level-set function updated via the solution of the Hamilton-Jacobi equation given as

$$\frac{\partial \phi}{\partial t} = -V\boldsymbol{n}.\nabla\phi \tag{2.4}$$

where t is a pseudo-time representing the evolution of the design, V is the velocity field advecting the level-set function and $\boldsymbol{n}$ is the normal to the interphase [1].

A major benefit of LSMs over density-based approaches is that they allow for a clear boundary of the geometry as a consequence of iso-contours of the level-set function. This feature of LSMs can be preserved by implementing conforming discretization at the cost of complications associated with an evolving mesh. Detailed implementation of LSM as applied to structural TO can be found in literature [49]. Density-based level-set methods exist but they suffer from the presence of intermediate densities in the neighbourhood of the interphase, like the SIMP implementation. Unfortunately, the optimal solution of level-set based structural optimization is strongly dependent on domain initialization and hole nucleation strategies. The search is also often trapped in local minima - a problem

common with approaches driven by shape sensitivities [1].

2.1.2 Multiscale topology optimization

In Section 2.1.1.1, it is stated that density-based TO of discretized structures, without implementing a restriction scheme, lacks a solution to the continuous problem. As a consequence, increasing mesh resolution leads to more optimal solutions with finner scale structures. This phenomenon suggests that more optimal structural design may be accessed if the optimization model works at two interconnected levels – a global level which deals with the optimal topology of structure and a local level which deals with optimal design of detailed microstructure representing material point properties.

2.1.2.1 Concurrent Multiscale Optimization

Hierarchical models featuring concurrent topology and material optimization are common in literature [50]. Coelho et al. [51] developed a three-dimensional hierarchical TO model that optimized material layout by the density-based approach without penalization, allowing intermediate densities. The intermediate densities then serve as inputs to the optimal design of local microstructure by the classical SIMP approach. This was further applied to the design of bone apparent density and trabecular structure [52]. Other hierachical formulations exist [53, 54], including those of Lui et al. [55] towards deriving the optimal configuration of material and structure in compliant mechanism with maximum displacement. Xia et al. [56] presented a concurrent TO approach that applied BESO schemes at both scales in the optimal design of structure and material for a compliance minimization problem. Multiscale level-set approaches have been used to design isotropic microstructures for stiffness and thermal conductivity maximization [57]. Many works demonstrate these concurrent multiscale strategies in literature [58, 59]. The major disadvantage of these concurrent multiscale approaches lies with the computational cost of simultaneously designing local material while optimizing structural layout.

2.1.2.2 Sequential Multiscale Optimization

To circumvent the computational issues associated with concurrent design of material and structure, sequential strategies have been developed where inverse homogenization strategies determine optimal configurations for microstructures, which are to be assembled within a global domain to yield an optimal structural layout. Schumacher et al. [16] presented a framework that tiled the interior of structures with micro-architectures that matched defined effective elastic material properties. These micro-architectures were drawn from a precomputed library of indexed microstructure families. A family of microstructures shared similar topologies and had interpolatable properties driven by elasticity parameters. Each family of microstructures differed topologically from other families but potentially yielded similar properties as other families (ie. there existed an overlapping of microstructure elastic behavior in material space). Overlapping of micro-architecture families in material space enabled the synthesis of spatially varying material behaviour. The choice of a specific micro-architecture tile among other suitable candidates was based on the quality of inter-connectivity with adjacent tiles. Zhu et al. [20, 60] also populated a gamut of discrete evaluations of material properties by evolving the geometries of micro-architectures that guaranteed an extension of the boundaries of the material space. This led to the discovery of micro-architectures with extremal properties. By setting up an optimization framework in the space of material parameters of the gamut and discretely mapping the precomputed micro-architectures to the spatially-varying material property description obtained from optimization, a framework for two-scale topology optimization was demonstrated. Similarly, Panetta et al. [10] presented a range of elastic textures (tileable and printable cubic patterns) built of a single material with a broad range of effective material properties that enabled spatial variation of material within a structure towards achieving desired macroscale behavior. These works are sequential approaches featuring discrete mapping of optimized micro-architectures into the interior of macroscale structures.

Though many of the monoscale and multiscale approaches described apriori are widely

implemented commercially, a fundamental limitation exists rooted in their use of only isotropic or orthotropic material point properties. The choice of a free parameterization of the stiffness tensor promises access to full control over anisotropic point properties, with potentially improved structural optimality. In literature, such a method is referred to as Free Material Optimization.

2.2 Free Material Optimization

Free Material Optimization (FMO) is often referred to as the ultimate generalization of structural optimization for elastic problems in continuum mechanics [13, 14]. It is a branch of structural optimization which has garnered significant interest in recent years [14]. FMO was presented by Bendsøe et al. [11] and later developed by Zowe et al. [12] and Ben-Tal et al. [61]. In FMO, the design variables are the unrestricted set of elements of positive semi-definite constitutive tensors so that both the material distribution and material itself can be freely varied. This optimization formulation proffers unconstrained local material properties albeit without prior treatment for realizable physical geometry. The necessary and sufficient condition that the constitutive tensor be symmetric positive semi-definite stipulates that components on the main diagonal of the constitutive tensor, expressed as a 6×6 elasticity matrix in Voigt notation [62] for 3-dimensional problems, remain non-negative [11]. Successful implementations of FMO use invariants of the constitutive tensor as measure of cost, eg. the Trace or Frobenius norm of the elasticity matrix [11, 13]. A concise and detailed description of the FMO formulation is given in Ref. [19]. Kočvara et al. [14, 63] have demonstrated the efficacy of the approach with stress and displacement constraints. The approach has been applied to the conceptual design of aircraft components with potentially tremendous weight savings where post-optimization analyses considered manufacturing technological constraints to yield the final physical product [14].

FMO is considered to yield the ultimate structure by an assumption of unconstrained local

material configuration [13]. To bridge the gap between the results obtained by the FMO framework and the physical realization of local structure, tape-layering technology has been implemented to manufacture fibre-reinforced composite materials (FRCMs), where the fibres are oriented in directions of principal stresses and strains derived from the FMO results [19]. However, there is no record of the loss of precision that may be associated with such a post-processing technique. To evade this possible loss of precision, Hornlein et al. [19] proposed setting up FMO in the space of producible local material. That is, to simulate local structure in the context of the free parameterization of material, the framework must be assembled within the space of material properties associated with a parameterization of physical geometry. The mechanics of a special class of advanced materials called metamaterials could potentially yield a means to match local structure with material design within the FMO framework.

2.3 Optimization of metamaterials

Metamaterials are materials that exhibit properties that differ from those of their base material properties [64]. Their properties are derived from the shape and arrangement of their constituting micro-architectures. The design and programming of metamaterials is an active field of research as their unprecedented properties are often not observable in nature.

The first metamaterials were studied in optics [65], however, their research has spread rapidly to acoustics and mechanics [66, 67]. The relevance of mechanical and thermal metamaterials have garnered significant interest due to their potential towards improving solutions in the field of structural and thermo-structural optimization. Mechanical metamaterials have been designed to exhibit auxetic phenomena [68, 69, 70], negative compressibility (negative bulk modulus) [71], pentamode phenomena (negative shear modulus) [72], etc. Kang et al. [73] demonstrated anisotropic heat transfer through the modular design of thermally tunable unit cells. Lattice materials have been designed to derive

tunable negative thermal expansion with heat management applications [74, 75]. Metamaterials, referred to as left-handed materials, have been designed with negative refractive index or negative bulk moduli [76]. Other metamaterials exhibit energy absorption characteristics and thermo-electric properties all derived from the geometry and arrangement of the microstructures they are built of [77, 60, 78, 79].

With the physical realization of metamaterials facilitated by the precision afforded by additive manufacturing, structural optimization of metamaterials has greatly expanded the possibilities for optimal material layout as well as the design of local material structure [64]. With minimal requirement for post-processing, structures with complex micro-architectures can be generated with higher precision than offered by other manufacturing techniques. They may be built up of periodic assemblies of microstructures to match prescribed homogeneous material properties or may be spatially varied to yield heterogeneous properties [15, 16]. These interesting effective macroscale properties exhibited by metamaterials, if parameterized by microscale geometry parameters of the constituting microstructures, can be tailored to satisfy predefined functional objectives.

2.4 Coupled Sequential Multiscale Optimization

In Section 2.1.2.2, sequential approaches to multiscale optimization were presented as an alternative to computationally expensive concurrent methods. However, such sequential approaches yield strategies that discretely map optimized micro-architectures to macroscale domains. Often, significant computational effort is required to ensure compatibility and connectability of adjacent micro-architectures [16, 20]. Coupled sequential multiscale optimization are approaches that seek to minimize these additional computational efforts by coupling the local and global scales through response surface methodology. A framework for designing such multiscale models is called Heterogeneous Multiscale Methods (HMM) [80, 81].

HMM is a general framework for linking models at different scales. There is usually a significant separation of scales so that the microscale is several orders of magnitude smaller than the macroscale. The word 'heterogeneous' emphasizes that HMM can be applied to multi-physics problems where both scales can be of very different nature [81]. Its relevance lies in the fact that it presents a means to take advantage of relevant information and strategies across both scales so that the derived multiscale model is efficient and accurate. By implementing HMM, a multiscale structural optimization can be derived that enables the free design of local material as well as its structural layout to meet prescribed functional objectives, leveraging the mechanics of metamaterials.

HMM is a methodology with broad application. In a review by Weinan et al. [81], HMM is demonstrated to be applicable across many fields including complex fluids, micro-fluidics, solids, interface problems, stochastic problems and statistically self-similar problems [80]. It is important to note that HMM presents a framework with which several problems are solved across different scales – it is not a specific method. Problem-specific technical tools must be developed to realize the desired multiscale strategy. As a consequence, its implementation can be non-trivial.

HMM follows a top-down strategy [80]. The interaction between the ingredients for HMM implementation as suited to this work are shown in Fig. 2.3. They include:

- A macroscale model: The scale at which the problem is defined which is by itself incomplete, requiring constitutive data from the microscale model. For FEM-based problems, it constitutes the geometry and finite element domain, external loads, boundary conditions and a finite element solver based on a variational formulation of static equilibrium mechanics or steady-state conduction.

- A constrained microscale model: Which exists at sufficient scale separation from the macroscale model, typically at least an order of magnitude smaller as demonstrated by Cheng et al. [4]. For FEM-based problems, computational homogenization provides a means to generate effective properties from localized property

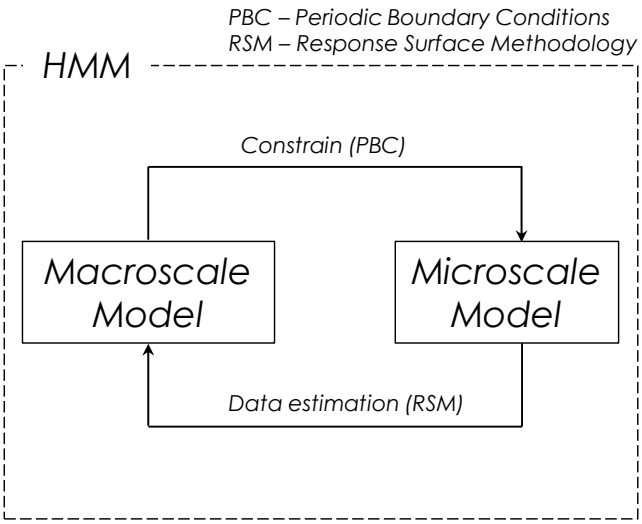


Figure 2.3: Heterogeneous Multiscale Method

evaluations. These effective properties are then passed on to the macroscale model. Constraining the microscale ensures that it is consistent with the local macroscale state [81].

- A means to couple both scales that facilities rapid evaluation of the macroscale model. By coupling both scales, a means is derived to exploit the simplicity and efficiency of the macroscale as well as the accuracy of the microscale constitutive evaluations. The coupling between both scales can be concurrent or sequential. Concurrent coupling methods feature linking of the macroscale and microscale on-the-fly so that constitutive property information is determined only when required by the macroscale model. Sequential coupling methods feature a precomputation of constitutive properties in a series of designed experimental points within a material property space. Facilitated by Response Surface Methodologies (RSM), explicit functions are generated that approximate the discrete small scale evaluations which are readily integrated into the macroscale system.

The challenge of accurate implementation of HMMs lie in the definition of the constrained microscale model such that its evaluations are consistent with its existence within the macroscale model [82, 81]. In the next section, a brief introduction is given of the theory

of homogenization which facilitates the derivation of efficient HMM frameworks.

2.4.1 Homogenization

Homogenization theory enables the evaluation of effective properties of materials built up of micro-architectures. Provided there exists a significant scale separation between the scale of the micro-architectures and the scale of the material they are assembled to form, regular heterogeneities can be identified so that they are approximated as periodic. Several homogenization schemes exist in literature [83, 84, 85, 86, 87], with choice of implementation often based on a trade-off between accuracy and computational cost [87, 88]. The goal of homogenization methods is to derive an equivalent (average or effective) quantity from a fine-scale in-homogeneous quantity, and in so doing, sacrifice some computational precision afforded by the fine scale analyses in exchange for macroscale computational efficiency [89]. Figure 2.4 shows two domains of equivalent material properties in 2-D subjected to the same traction force and displacement boundary condition, enabled by homogenization. For any given material, the effective material properties of structures composed of periodic micro-architectures of a given material can be determined by numerical homogenization, provided the elastic theory remains true for the length scales of the micro-architectures [90]. A method of homogenization called Asymptotic Expansion Homogenization (AEH) relies on the assumption of periodicity and asymptotic expan-

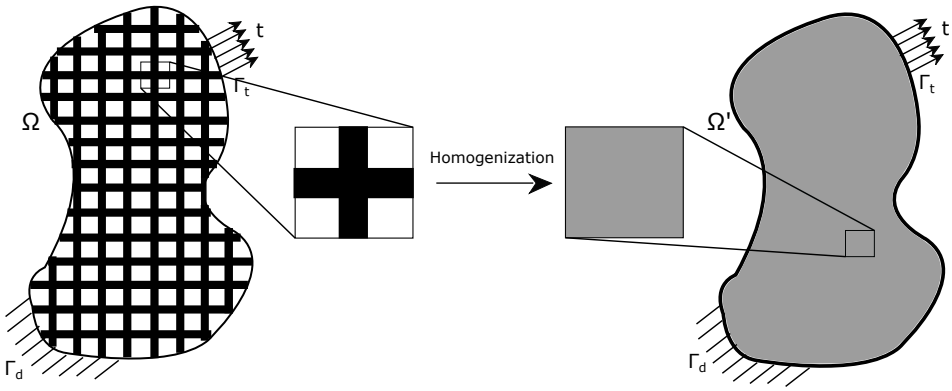


Figure 2.4: Illustration of homogenization in 2D

sion of differential equations which enables the analyses of quantities across distinctively separate scales.

Structures built up of complex micro-architectures such as composites, rebar-reinforced concrete and metamaterials can be efficiently simulated by deriving effective properties of their Representative Volume Elements (RVE) [89]. For structures with periodic micro-architectures, these RVEs consist of a repeating unit cell (RUC), the property of which is fully representative of an infinite assembly of the unit cell in one or more orthonormal directions subjected to periodic boundary conditions. The key assumption being that the micro-architecture length scales are much smaller than the characteristic length over which macroscale loading varies spatially [91].

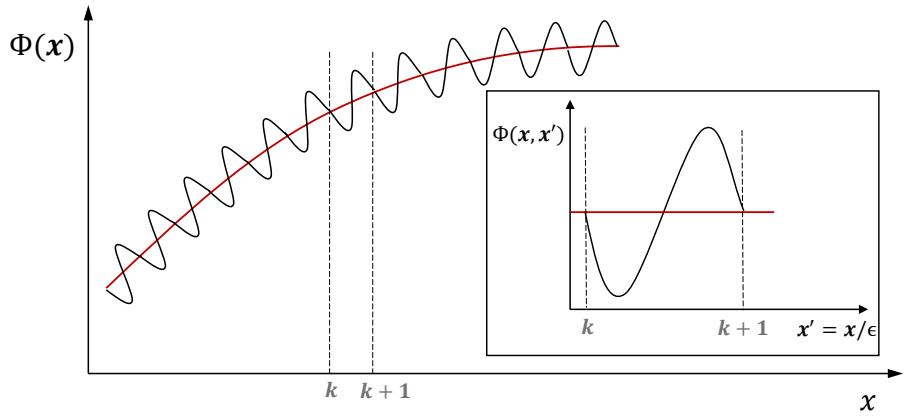


Figure 2.5: The concept of homogenization across scales

Consider the illustration of Fig. 2.5 of the variation of an arbitrary physical quantity, $\Phi(x)$ of a strongly heterogeneous medium in a coordinate system, x. The rapid fluctuations of the quantity within this coordinate system justifies the study of the physical quantity across two scales so that a local coordinate system x' can be defined at the microscale. If these periodic fluctuations occur at a very small scale compared to the scale of the material, then a scale separation parameter can be defined, ϵ of very small value that provides an indication of the proportion between dimensions of the RUC and the material. Also, a magnification factor, $\frac{1}{\epsilon}$ enlarges the dimensions of the RUC to dimensions comparable to those of the material as shown in inset plot of Fig. 2.5. The asymptotic expansion of

a physical quantity of heterogeneous media is therefore expressed as

$$\Phi^{\epsilon}(x) = \Phi^{0}(x, x') + \epsilon\Phi^{1}(x, x') + \epsilon^{2}\Phi^{2}(x, x') + ... \tag{2.5}$$

The first term represents the effective value of the physical quantity, Φ^0 (represented by red line in Fig. 2.5) and the second term represents the rapid oscillations of the quantity at the microscale by virtue of underlying periodic heterogeneities (represented by black wavy lines in Fig. 2.5). Since $\epsilon \to 0$, higher order terms in the asymptotic expansion of the physical quantity are negligible beyond the first order. For this reason, significant scale separation is essential for the correct implementation of the homogenization theory for advanced materials with micro-architectures as the assumption of negligible higher order terms in Eqn. 2.5 degenerates with increasing ϵ. All physical quantities of this work within the multiscale framework associated with the properties of materials with micro-architectures are represented similarly. The theory of homogenization applies to mechanical properties as well as other material properties such as thermal conductivity, thermal expansion, electrical conductivity, etc [90].

2.4.2 Response Surface Methodology

An essential component of HMMs is a means to efficiently evaluate data from the microscale model within the macroscale solver as discussed in Sec. 2.4. A methodology to evade the computational expense associated with 'on-the-fly' microscale evaluations in concurrent methods can be attributed to the implementation of Response Surface Methodologies (RSMs). RSMs refer to mathematical and statistical approaches to the construction of metamodels/surrogate models intended to evaluate the value of a dependent variable (response variable) given a vector of independent variables (predictor variables) at far less computational cost than the models they represent. The generation of response surfaces facilitate rapid evaluation of the macroscale solver and is essential to the derivation of an efficient multiscale framework [81]. The construction of the response surfaces depends

on the generation of data at designed sample points so that the predictive ability of a response surface is dependent on the Design of Experiments (DoE).

2.4.2.1 Design of Experiments

Design of Experiments (DoE) refers to the sample points within the space of predictor variables where the response is evaluated to generate data. Several strategies exist in literature for determining an appropriate DoE and the choice of these points greatly impact the quality of the metamodel. A commonly implemented approach is the full factorial sampling which involves a uniform sampling of the space of predictor variables by sampling on a grid generated by dividing the limits of the variables into a chosen number of levels. As such, sample points are located at all combinations of the different levels. The full factorial sampling however can quickly become expensive to generate since the number of sample points increases exponentially with the dimension of the space of predictor variables, especially, if the microscale model is computationally expensive to execute [92, 93]. Fractional factorial approaches evaluate the response variable at a subset of the full factorial sampling to reduce this computational cost.

Other sampling strategies include the Monte Carlo sampling which generates sample points at random points in the predictor variable space with a drawback of no control over the inclusion of bias to any of the predictors [81, 92, 94]. Latin HyperCube sampling generates sample points on a hyper-grid in such a manner as to have only one sample in each axis-aligned hyper-plane containing the point [95, 96]. Adaptive sampling strategies have been built into macroscale optimization techniques that sample only points required to minimize the objective functional for a given iteration and also improve the approximation of the generated response surface for that iteration. As a consequence, the response surface for any optimization iteration is constructed based on only necessary sample points leading towards the optimal solution [97].

Irrespective of the sampling strategy employed, the goal of efficient DoE is to distribute

sampling points in the space of predictor variables in such a manner as to ensure adequate coverage of the space without bias to any specific predictor variable. It is desired that such a sampling strategy is computationally efficient, particularly if the evaluation of the response is expensive. The response values as well as the predictor variables at the sample points then constitute the data required to develop the response surface model. In following discussions of this section, the data is represented by the response values, $\boldsymbol{y}(\boldsymbol{X})$ for predictor variables, $\boldsymbol{X} = [\boldsymbol{X}_1, \boldsymbol{X}_2, ..., \boldsymbol{X}_m]^\intercal$ for N sample points in an m-dimensional predictor variable space. A brief description of few common approximation methodologies follows.

2.4.2.2 Polynomial Approximation

Polynomial approximations of real functions are a finite sum of terms of a basis vector, $\boldsymbol{b}(\boldsymbol{X})$. In a least square sense, coefficient values are determined by the minimization of the approximation error associated with the polynomial's prediction of the actual data points [98]. These least-square approximations can be ordinary, weighted or moving [98]. In an m-dimensional space, an ordinary least-square approximation is given as

$$\hat{y} = \beta_0 + \sum_{j=1}^{m} \beta_j X_j \tag{2.6}$$

and a quadratic polynomial approximation is given as

$$\hat{y} = \beta_0 + \sum_{j=1}^{m} \beta_j X_j + \sum_{j=1}^{m} \sum_{k=j}^{m} \beta_{jk} X_j X_k \tag{2.7}$$

where β_0, β_j and β_{jk} for j, k = 1, 2, ..., m are components of the error minimizing coefficient vector determined by

$$\boldsymbol{\beta} = \left[\sum_i \boldsymbol{b}(\boldsymbol{X_i}) \boldsymbol{b}(\boldsymbol{X_i})^\intercal \right]^{-1} \sum_i \boldsymbol{b}(\boldsymbol{X_i}) y_i \tag{2.8}$$

for i = 1, 2,..., N.

Ordinary polynomial approximations evaluate rapidly and are easy to implement. They yield readily differentiable expressions that make them attractive as response surfaces within computational models. However, ordinary polynomial approximations are global approximations [98]. A property of global approximations is that they may exhibit regions of poor fit within the space of predictor variables if the response variable varies by over more than an order of magnitude. Other local least-squares approximations that address this issue include Weighted and Moving least-squares approximations [99, 100]. Though more accurate polynomial approximations, these local approximations require more computational effort to be constructed and evaluated.

2.4.2.3 Radial Basis Functions Approximation

Radial Basis Function (RBF) methods were introduced by Rolland Hardy as multiquadric methods because he was not satisfied with the results of polynomial interpolation. They are based on real-valued functions that depend only on the distance of an arbitrary evaluation point from a sampled data point (or any chosen points defined as centres) [101, 102]. An RBF approximation of a data set consists of weighted sums of these radial basis functions defined about the data points. Such an RBF approximation is given as

$$\hat{y} = \sum_{k=1}^{N} a_k \, \mathrm{e}^{-\gamma \|X - X_k\|^2} \tag{2.9}$$

where γ is a positive tuning parameter that adjusts the rate of decay of the basis function and the vector of coefficients $\boldsymbol{a}$ for a solution that approximates exactly on the sample points is given by

$$\boldsymbol{a} = \Psi^{-1} \boldsymbol{y} \tag{2.10}$$

where $\Psi = \mathrm{e}^{-\gamma \|X_j - X_k\|^2}$ and $j, k = 1, 2, \ldots$ N for an $N \times N$ linear system of equations. It is important to note that though the radial basis function utilized in Eqn. 2.9 is a Gaussian function, other RBFs such as multiquadric, inverse quadratic and inverse multiquadric functions can be implemented [103, 104].

2.4.2.4 Kriging Approximation

Kriging methods originated from the field of geostatistics [105, 106, 107]. Ordinary kriging approximations of $N-$sample point data, $(\boldsymbol{X}, \boldsymbol{y})$ is given as

$$\hat{y} = \beta + r^{\intercal}(\boldsymbol{X})\boldsymbol{R}^{-1}(\boldsymbol{y} - \mathbf{1}\beta) \tag{2.11}$$

where $\mathbf{1}$ denotes a vector of ones of length N, $\boldsymbol{R}$ is the symmetric square $N \times N$ correlation matrix of any two sampled data points X_j and X_k. Typically, a Gaussian correlation function is specified to assemble $\boldsymbol{R}$ such that

$$R(X_j, X_k) = \mathrm{e}^{-\theta\|X_j - X_k\|^2} \tag{2.12}$$

and $r^{\intercal}$ is the correlation vector of length N between an arbitrary point X and the sampled points $\boldsymbol{X}$ given as

$$r^{\intercal}(\boldsymbol{X}) = [R(X, X_1), R(X, X_2), ..., R(X, X_N)]^{\intercal} \tag{2.13}$$

The vector of coefficients β of Eqn. 2.11 is estimated by

$$\boldsymbol{\beta} = (\mathbf{1}^{\intercal}\boldsymbol{R}^{-1}\mathbf{1})^{-1}\mathbf{1}^{\intercal}\boldsymbol{R}^{-1}\boldsymbol{y} \tag{2.14}$$

Approaches to determine suitable values for the correlation parameters θ are discussed in detail in literature [108, 92]. Kriging approximations are often regarded as the best linear unbiased estimators hence perform excellently as response surface models. However, the computational cost associated with their construction does not scale well with the number of sample points due to the the size of the $N \times N$ correlation matrix [92]. Other response surface methods exist in literature including Artificial Neural Networks (ANN) [109, 110, 111], Gradient-Enhanced Kriging (GEK) [112, 113], Support Vector Machines (SVM) [114, 115], etc, all targeted towards approximation or prediction of response quantities in the

space of predictor variables. In this work, methods that scale well with the dimension of sample points and present explicitly differentiable expressions are of particular interest.

In the context of coupled sequential strategies, the effective material property evaluation (response) is to be evaluated given micro-architecture parameters (predictors). The generation of response surface models here enables rapid local material property evaluation given micro-architecture parameters. Several works in literature feature the implementation of coupled multiscale optimization strategies. Xia et al. [116] constructed an approximate constitutive model for strain energy density evaluated on a material microstructure so that homogenized strain energy and stress-strain relations could be expressed explicitly, thereby reducing the computational cost associated with a concurrent multiscale framework developed earlier [56]. Cheng et al. [4] developed a framework for functional grading of lattice by determining effective elastic properties by asymptotic expansion homogenization and created explicit expressions in the form of a fourth-order polynomial for these properties as functions of a single density design variable. Colabella et. al [117] developed an ordinary least-squares response model that expressed components of the elastic tensor as a function of geometric micro-parameters that defined biomimetic cancellous bone cellular micro-architectures.

Recently, Wu et al. [3] presented a multiscale optimization of structures built up of orthotropic lattice micro-architectures subjected to thermo-mechanical loads. The framework was demonstrated by the optimal design of an injection-mould. Material interpolation was executed as a function of lattice microstructure relative density. Though a means was derived for the physical realization of micro-architecture of intermediate properties, the parameterization of the micro-architecture offered no means of modelling anisotropic material behavior since the parameterization implemented allowed only isotropic or orthotropic micro-architectures.

The review of structural optimization strategies and their development suggests that computational efficiency as well as full control of material point properties are main drivers towards improved optimization strategies. FMO is regarded as the ultimate general-

ization of structural optimization. Unfortunately, such a free parameterization of the stiffness tensor makes no consideration for deriving local structure within the optimization framework. On the other hand, the sequential multiscale approaches demonstrated by Schumacher et al. [16] and Zhu et al. [20] are not capable of full material point design as they do not support anisotropic material properties. They also require additional computational effort to verify connectability and compatibility requirements of the discrete micro-architecture assembly. These multiscale approaches with discrete assemblies of optimized micro-architectures represent recent significant advancements in structural optimization techniques.

This work seeks to formulate an optimization framework using metamaterials such that the parameterization of local physical geometry supports the free variation of local material properties towards meeting macroscale functional objectives. As a consequence, it is a variant of FMO that supports Hornlein's proposal [19] for setting up FMO in the space of producible local material. Such an optimization framework demands a computationally efficient multiscale methodology that enables the derivation of effective properties of micro-architecture by homogenization. Polynomial approximations are used to represent the effective properties as functions of lattice micro-parameters due to their ease of construction. They are also easily differentiable and hence support gradient-driven searches for optimality in a computationally efficient manner. A consequence of such a coupled sequential multiscale formulation is that connectability and compatibility of adjacent micro-architectures are inherently satisfied. The result is the derivation of a novel coupled sequential multiscale structural and thermal optimization framework for three-dimensional problems.

In the next chapter, the derivation of the framework is commenced by presenting the methods for microscale model development.

Chapter 3

Microscale Model Development

In this Chapter, a description of the microscale model development is presented. Fundamental assumptions are stated. Subsequent sections then describe the theoritical methods applied to determine the effective properties of micro-architectures.

3.1 Assumptions

Considerations for pure structural formulations of this work have been limited to three-dimensional (3D) linear elastic problems across both scales so that the general relationship between the Cauchy stress tensor, $\boldsymbol{\sigma}_{ij}$ and the strain tensor, $\boldsymbol{\varepsilon}_{kl}$ at every material point in the design domain is linear, given by Hooke's Law

$$\boldsymbol{\sigma}_{ij} = \boldsymbol{E}_{ijkl}\ \boldsymbol{\varepsilon}_{kl} \tag{3.1}$$

where

$$\boldsymbol{E}_{ijkl} = \boldsymbol{E}_{klij} = \boldsymbol{E}_{jikl} = \boldsymbol{E}_{ijlk} \tag{3.2}$$

is the 4th-rank elasticity tensor with 81 components for i, j, k, l = 1, 2, or 3. For the purpose of the formulations of this work, the symmetries associated with the elasticity

tensor as shown in Eqn. 3.2, allows the tensor to be presented in Voigt notation with 21 unique components in its most general case of anisotropy. The minimum length-scale of structure set by manufacturing constraints satisfies Eqn. 3.1 and only small deformations are assumed. Strain-displacement relations are given by

$$\boldsymbol{\varepsilon}_{ij} = \frac{1}{2}\left(\boldsymbol{u}_{i,j} + \boldsymbol{u}_{j,i}\right) \tag{3.3}$$

Equations 3.1 - 3.3 constitute the theory of linear elasticity for continuum mechanics as implemented here. Static equilibrium mechanics is assumed so that

$$\boldsymbol{\sigma}_{ij,j} + \boldsymbol{F}_i = 0 \tag{3.4}$$

where $\boldsymbol{F}_i$ is the sum of all external forces per unit volume of the design domain, Ω. Inertial forces due to impact or dynamic loading are neglected.

The thermal formulations of the microscale are governed by steady-state pure conduction given by the steady-state heat equation

$$\boldsymbol{q}_{i,i} + \boldsymbol{f}_{\boldsymbol{\theta}} = 0 \tag{3.5}$$

and Fourier's law

$$\boldsymbol{q}_i = -\boldsymbol{K}_{ij}\, \boldsymbol{\theta}_{,j} \tag{3.6}$$

where $\boldsymbol{q}_i$ is the heat flux vector, $\boldsymbol{f}_{\boldsymbol{\theta}}$ is heat source per unit volume of the design domain, Ω, $\boldsymbol{K}_{ij}$ is the symmetric thermal conductivity tensor, $\boldsymbol{\theta}$ is temperature difference and $\boldsymbol{\theta}_{,j}$ is the temperature gradient in the direction j for $j = 1$, 2 and 3. It is also assumed that material thermal conductivity tensor remains unchanged and insensitive to temperature changes.

3.2 Microscale Parameterization

The objective of the microscale model development is to derive a parameterization of the small scale geometry that facilitates an efficient population of material property space. The choice of parameterization defines the extent of material property explored. Ideally, the parameterization should enable the largest possible property space to be considered. However, manufacturing constraints limit the space of admissible properties. Acceptable parameterization schemes must satisfy the conditions on the physical realization of corresponding micro-architecture unit cells. The parameterization must support:

1. *a micro-architecture geometry that evolves smoothly as the micro-parameters are smoothly varied to ensure connectivity between neighbour unit cells.*

2. *a micro-architecture geometry that is periodic so that the elastic and thermal behavior of the micro-architecture is representative of an infinite assembly of the micro-architecture.*

3. *a micro-architecture geometry that does not generate enclosed voids or suspended solids so as to be suited to applicable additive manufacturing techniques.*

Any parameterization of micro-architecture geometry that satisfies the conditions above is suited to the framework. For subsequent sections of this work, such a parameterization is defined such that the effective properties of any given unit cell are controlled by a vector of geometry-defining microparameters, denoted as $\boldsymbol{r_m}$ of dimension m.

3.3 Element-based material assignment

Given a suitable parameterization of micro-architecture geometry, local material assignment is executed based on a fixed discretization of the unit cell domain. This structured

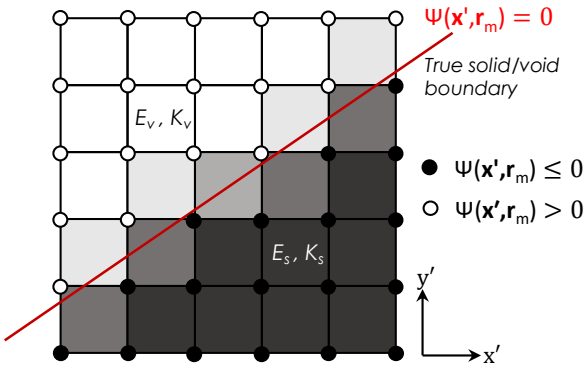


Figure 3.1: 2D illustration of element-based material assignment and micro-architecture geometry definition

discretization supports the implementation of periodic boundary conditions but also eliminates complications associated with unstructured mesh reconstruction for complex micro-architecture geometries. Consider the material assignment illustration on the 2-D unit cell domain of Fig. 3.1. A function, $\Psi(\boldsymbol{x'}, \boldsymbol{r}_m)$ is defined within the discretized unit cell domain that takes the coordinates of all nodes and maps to a binary space that defines if the node lies within material structure or void according to the parameterization implemented. The discretized elements are then assigned material properties (E_e, K_e) based on each element's node fraction, n_f given as

$$n_f = \frac{N_m}{N} \tag{3.7}$$

where N_m is the number of the element's nodes within material structure and $N = 4$ is the total number of nodes for each element. Node fraction values vary between 0 and 1. Local elastic modulus is determined by

$$E_e = n_f E_s + (1 - n_f) E_v \tag{3.8}$$

where E_s and E_v represent the Young's moduli of the base material and void respectively. Similarly, local thermal conductivity is determined by

$$K_e = n_f K_s + (1 - n_f) K_v \tag{3.9}$$

where K_s and K_v represent the thermal conductivity of the base material and void respectively. Within the unit cell, void is modeled as a weak elastic material with very low thermal conductivity to prevent singularities during numerical simulation. Elements in the viscinity of the true solid/void boundary defined by the line $\Psi(\boldsymbol{x'}, \boldsymbol{r}_m) = 0$ exhibit intermediate Young's modulus and thermal conductivity values as a consequence of intermediate node fraction values. The material assignment scheme and consequent geometry definition can be generalized to 3-dimensional micro-architecture unit cells or voxels where $\Psi(\boldsymbol{x'}, \boldsymbol{r}_m) = 0$ constitutes a surface boundary between solid and void regions and $N = 8$ for structured hexahedral elements. Section 4.2 presents a numerical implementation of the material assignment described here within 3-D voxels for a parameterization scheme that satisfies the conditions given in Sec. 3.2

3.4 Asymptotic Expansion Homogenization

In this section, the numerical approach to obtaining the homogenized elasticity tensor, $\boldsymbol{E}^H$ and thermal conductivity tensor, $\boldsymbol{K}^H$ of a lattice-based micro-architecture is summarized. The homogenization process follows the principles of asymptotic expansion homogenization which is suited to periodic micro-architectures as described in [118, 119, 120, 87, 90]. The objective of the homogenization process is to substitute the inherent heterogeneities of the lattice microstructure with an equivalent homogeneous media with the benefit of a massive reduction in the degrees of freedom associated with modelling materials composed of architectures. The theory of homogenization as applied to linear elastic structures with periodic micro-architectures is well developed. The fundamental assumption associated with the correct implementation of homogenization is that the macroscale media is built up of periodic representative volume elements (RVEs) at a distinctly separate length scale from the scale of the structure. Mathematically,

$$\boldsymbol{x'} = \frac{\boldsymbol{x}}{\epsilon} \tag{3.10}$$

where $\boldsymbol{x'}$ and $\boldsymbol{x}$ are the coordinate systems of the microscale and macroscale respectively. The value of the scale-separation parameter, ϵ is often chosen as $\epsilon << 1$ so that local microscale field variables vary $1/\epsilon$ times more rapidly than corresponding macroscale field variables. All relevant field variables are therefore approximated by an asymptotic expansion that captures their macroscopic uniform distribution as well as their periodically-fluctuating distribution on the microscale.

3.4.1 Strain deformation analyses

The exact displacement field of periodic elastic structures of this work is given as

$$u_i^\epsilon(x_i, x_i') = \epsilon^0 u_i^0(x_i, x_i') + \epsilon^1 u_i^1(x_i, x_i') + \epsilon^2 u_i^2(x_i, x_i') + ... \tag{3.11}$$

where the u_i^0 is the macroscopic uniform displacement and u_i^1, u_i^2, etc., represent the microscale periodic oscillations in the field variable as a consequence of the underlying heterogeneities of the microscale. A first order approximation of the displacement field, u_i^ϵ is often adequate since $\epsilon << 1$. As a consequence, the higher order terms of Eqn. 3.11 are neglected so that it is sufficient to state that

$$u_i^\epsilon(x_i, x_i') = u_i^0(x_i, x_i') + \epsilon^1 u_i^1(x_i, x_i') \tag{3.12}$$

Derivatives of any of the variables in the multiscale framework follow the chain rule of function differentiation given as

$$\frac{\partial(\ )^\epsilon}{\partial x_i} = \frac{\partial(\ )}{\partial x_i} + \frac{1}{\epsilon}\frac{\partial(\ )}{\partial x_i'} \tag{3.13}$$

so that the strain-displacement relation is

$$\varepsilon_{ij}(\boldsymbol{u}) = \frac{1}{2}\left(\frac{\partial u_i^\epsilon}{\partial x_j} + \frac{\partial u_j^\epsilon}{\partial x_i}\right) = \frac{1}{2}\left[\left(\frac{\partial u_i^0}{\partial x_j} + \frac{\partial u_j^0}{\partial x_i}\right) + \left(\frac{\partial u_i^1}{\partial x_j'} + \frac{\partial u_j^1}{\partial x_i'}\right) + \epsilon\left(\frac{\partial u_i^1}{\partial x_j} + \frac{\partial u_j^1}{\partial x_i}\right) + ...\right] \tag{3.14}$$

Neglecting terms $\mathcal{O}(\epsilon)$ and higher, Eqn. 3.14 becomes

$$\varepsilon_{ij} = \bar{\varepsilon}_{ij} + \varepsilon^*_{ij} \tag{3.15}$$

where

$$\begin{aligned} \bar{\varepsilon}_{ij} &= \frac{1}{2}\left(\frac{\partial u^0_i}{\partial x_j} + \frac{\partial u^0_j}{\partial x_i}\right) \\ \varepsilon^*_{ij} &= \frac{1}{2}\left(\frac{\partial u^1_i}{\partial x'_j} + \frac{\partial u^1_j}{\partial x'_i}\right) \end{aligned} \tag{3.16}$$

The microstructural strain tensor, ε_{ij} given by Eqn. 3.15 therefore comprises the macroscopic strain tensor, $\bar{\varepsilon}_{ij}$ and the periodically-fluctuating strain tensor, ε^*_{ij} which exists as a consequence of microscale heterogeneities. Substituting the microstructural strain tensor into the variational form of the linear elastic equation gives

$$\int_{\Omega^\epsilon} \boldsymbol{E}_{ijkl}\ \left(\varepsilon^0_{ij}(v) + \varepsilon^1_{ij}(v)\right)\ \left(\bar{\varepsilon}_{ij}(u) + \varepsilon^*_{ij}(u)\right)\ d\Omega^\epsilon = \int_{\Gamma_t} t_i\ v_i\ d\Gamma \tag{3.17}$$

where $\varepsilon^0_{ij}(v)$ and $\varepsilon^1_{ij}(v)$ are the virtual macroscopic and microscopic strains respectively, with t_i as the traction at the traction boundary, Γ_t. If the virtual displacement is chosen such that it varies periodically on the microscale but remains constant on the macroscale, Eqn. 3.17 becomes

$$\int_{\Omega^\epsilon} \boldsymbol{E}_{ijkl}\ \varepsilon^1_{ij}(v)\ \left(\bar{\varepsilon}_{ij}(u) + \varepsilon^*_{ij}(u)\right)\ d\Omega^\epsilon = 0 \tag{3.18}$$

Taking an integral over the representative volume element, Eqn. 3.18 can be expressed as

$$\int_V \boldsymbol{E}_{ijkl}\ \varepsilon^1_{ij}(v)\ \varepsilon^*_{ij}(u)\ dV = -\int_V \boldsymbol{E}_{ijkl}\ \varepsilon^1_{ij}(v)\ \bar{\varepsilon}_{ij}(u)\ dV \tag{3.19}$$

where V and dV are the volumes of the unit cell and finite element discretization respectively. Provided periodic boundary conditions are imposed on the boundaries of the RVE, Equation 3.19 presents the variational form with which the periodically-fluctuating strain

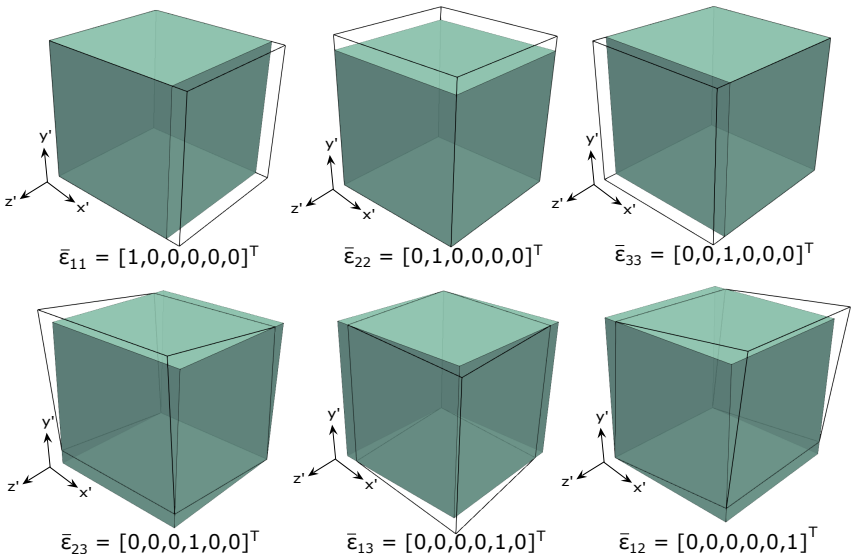


Figure 3.2: Unit strain deformation on the LUC (Scale: 0.2:1)

tensor, ε^*_{ij} of a representative unit volume of any periodic structure can be derived, given an arbitrary macroscopic strain, $\bar{\varepsilon}_{ij}$. Details of the procedure for periodic boundary condition implementation on a discretization of the volume element are presented in Sec. 3.4.3. The formulation of Eqn. 3.19 lends itself to finite element analysis in its discretized form. Six independent macroscale unit strain deformation analyses are sequentially substituted into Eqn. 3.19. The unit macroscale unit strains are shown in Fig. 3.2. The solution to each strain deformation analysis is the microscale periodic displacement, from which the periodically-fluctuating strain tensor is determined. By applying Eqn. 3.15, the microscale strain tensor is derived. Finally, the microscale stress tensor at each element of the unit cell is given by

$$\sigma_{ij} = 2\mu_e(\varepsilon^*_{ij} + \bar{\varepsilon}_{ij}) + \lambda_e tr(\varepsilon^*_{ij} + \bar{\varepsilon}_{ij})I \tag{3.20}$$

where I is the identity matrix and

$$\mu_e = \frac{E_e}{2(1+\nu)}$$
$$\lambda_e = \frac{E_e\ \nu}{(1+\nu)(1-2\nu)} \tag{3.21}$$

are the element-wise Lamé constants defined given the element-wise Young's modulus, E_e of the element-based property assignment of Sec. 3.3. The macroscopic stress tensor is derived from a volume-averaging of element-wise stress tensors of Eqn. 3.20 so that

$$\bar{\sigma}_{ij} = \frac{1}{V} \int_v \sigma_{ij} \, dV \tag{3.22}$$

Having obtained $\bar{\sigma}_{ij}$ for each unit macroscopic strain, $\bar{\varepsilon}_{ij}$, all 36 terms of the homogenized stiffness matrix is obtained from

$$\bar{\sigma}_i = \boldsymbol{E}^H_{ij} \, \bar{\varepsilon}_j \tag{3.23}$$

where $\bar{\sigma}_i$ and $\bar{\varepsilon}_j$ are the macroscopic stress and strain tensors expressed in the Voigt notation for i and $j = 1, 2, ...6$. Inherent properties of symmetry and positive semi-definiteness must be satisfied by $\boldsymbol{E}^H_{ij}$ expressed as a tensor to satisfy Eqn. 3.2.

3.4.2 Thermal Analyses

Extending asymptotic expansion homogenization theory to the determination of effective thermal properties of periodic structures is analogous to the process described in Sec. 3.4.1 for mechanical properties. For completeness, the theory is briefly summarized as follows. The exact temperature field of periodic structures of this work are given as

$$\theta^\epsilon(x_i, x'_i) = \epsilon^0\theta^0(x_i, x'_i) + \epsilon\theta^1(x_i, x'_i) + \epsilon^2\theta^2(x_i, x'_i) + ... \tag{3.24}$$

where θ^0 is the macroscopic uniform temperature field and θ^1, θ^2, etc., represent the microscale oscillations in the field variable as a consequence of underlying heterogeneities of the microscale. A major difference is that where displacement is a vector field in elastic theory, temperature is a scalar field as indicated in Eqn. 3.24. Again, since $\epsilon << 1$, it suffices to represent the field by a first order approximation. As a consequence, Eqn. 3.24 can be expressed as

$$\theta^\epsilon(x_i, x'_i) = \theta^0(x_i, x'_i) + \epsilon\theta^1(x_i, x'_i) \tag{3.25}$$

By Eqn. 3.13 and neglecting terms $\mathcal{O}(\epsilon)$ and higher, temperature gradient based on the multiscale framework is expressed as

$$\frac{\partial \theta^{\epsilon}}{\partial x_i} = \frac{\partial \theta^0}{\partial x_i} + \frac{\partial \theta^1}{\partial x_i'} \tag{3.26}$$

where

$$\begin{aligned} \nabla \bar{\theta}_i &= \frac{\partial \theta^0}{\partial x_i} \\ \nabla \theta_i^* &= \frac{\partial \theta^1}{\partial x_i'} \end{aligned} \tag{3.27}$$

are the macroscale average temperature gradient and microscale periodically-fluctuating temperature gradient respectively. As a consequence, Eqn. 3.26 gives the microstructural temperature gradient and can be expressed as

$$\nabla \theta_i = \nabla \bar{\theta}_i + \nabla \theta_i^* \tag{3.28}$$

Substituting the microstructural temperature gradient into the variational form of the Poisson equation for heat conduction gives

$$\int_{\Omega^{\epsilon}} \boldsymbol{K}_{ij} \, (\nabla w_i^0 + \nabla w_i^1) \, (\nabla \bar{\theta}_i + \nabla \theta_i^*) \, d\Omega^{\epsilon} = f \, w \, d\Gamma_f \tag{3.29}$$

where ∇w_i^0 and ∇w_i^1 are the virtual macroscopic and microscopic temperature gradients respectively, with f as the heat source on the part of the boundary it acts on, Γ_f. If the virtual temperature is chosen such that it varies periodically on the microscale but remains constant on the macroscale, Eqn. 3.29 becomes

$$\int_{\Omega^{\epsilon}} \boldsymbol{K}_{ij} \, \nabla w_i^1 \, (\nabla \bar{\theta}_i + \nabla \theta_i^*) \, d\Omega^{\epsilon} = 0 \tag{3.30}$$

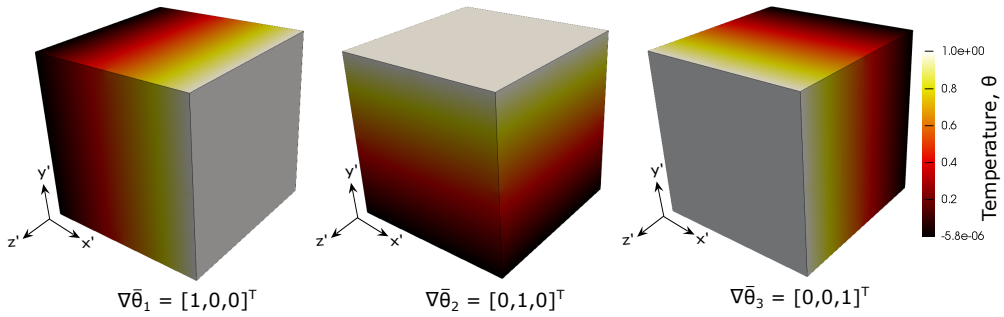


Figure 3.3: Unit temperature gradient on the LUC

Taking an integral over the representative volume element, Eqn. 3.30 can be expressed as

$$\int_V \boldsymbol{K}_{ij}\ \nabla w_i^1\ \nabla\theta_i^*\ dV = -\int_V \boldsymbol{K}_{ij}\ \nabla w_i^1\ \nabla\bar{\theta}_i\ dV \tag{3.31}$$

Again, provided periodic boundary conditions are imposed on the boundaries of the RVE, Eqn. 3.31 presents the variational form with which the periodically-fluctuating temperature gradient, $\nabla\theta_i^*$ of a representative unit volume of any periodic structure can be derived, given an arbitrary macroscopic temperature gradient, $\nabla\bar{\theta}_i$. The formulation of Eqn. 3.31 can be solved by finite element analysis in its discretized form. Three independent macroscale unit temperature gradients are shown in Fig. 3.3. The solution to each thermal analysis is the microscale periodic temperature distribution, from which the periodically-fluctuating temperature gradient vector is determined. By applying Eqn. 3.28, the microscale temperature gradient vector is derived. Finally, the microscale heat flux vector at each element of the discretized unit cell is given by

$$q_i = K_e\ (\nabla\theta_i^* + \nabla\bar{\theta}_i) \tag{3.32}$$

where K_e is the element-wise constant thermal conductivity coefficient defined by the element-based property assignment described and illustrated in Sec. 3.3. The macroscopic heat flux vector is derived from a volume-averaging of the element-wise heat flux vector of Eqn. 3.32 so that

$$\bar{q}_i = \frac{1}{V}\int_v q_i\ dV \tag{3.33}$$

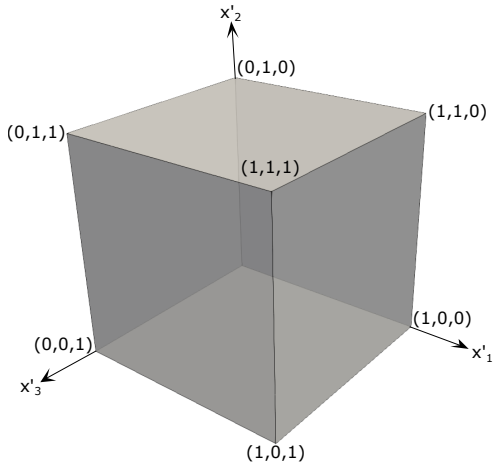


Figure 3.4: Coordinate system for PBC implementation

Having obtained $\bar{q}_i$ for each unit macroscopic temperature gradient, $\nabla\bar{\theta}_i$, all 9 terms of the homogenized conductivity tensor is obtained from

$$\bar{q}_i = \boldsymbol{K}_{ij}^H \, \nabla\bar{\theta}_j \tag{3.34}$$

for i and $j = 1$, 2, and 3. Inherent properties of symmetry must be satisfied by $\boldsymbol{K}_{ij}^H$.

3.4.3 Periodic Boundary Conditions

One of the conditions for ensuring suitability of parameterization is geometric periodicity as presented in Sec. 3.2. Geometric periodicity ensures that there is member continuity across neighbouring micro-architectures. For homogenization theory as applied to multiscale frameworks, where field variables change at distinctly separate scales, ensuring geometry periodicity is not sufficient for the correct evaluation of effective properties. The representative unit cell must be constrained by an association of degrees of freedom on opposite external surface boundaries. Such constraints are called Periodic Boundary Conditions (PBC). These constraints ensure that the response (structural and thermal) of the unit cell is representative of material point properties so that the behavior of the unit cell approximates the behavior of the periodic material they form. Imposing PBC ensures that the microstructure boundaries deform identically so that neighbouring micro-

architectures are compatible. For a hexahedral unit cell in $x_1' \in [0,\ 1]$, $x_2' \in [0,\ 1]$ and $x_3' \in [0,\ 1]$ (see Fig. 3.4), PBC implementation for structural problems of this work are displacement constraint equations applied to solve the discretized form of Eqn. 3.19

$$\begin{aligned} u_i^{jk}(0,\ x_2',\ x_3') &= u_i^{jk}(1,\ x_2',\ x_3') \\ u_i^{jk}(x_1',\ 0,\ x_3') &= u_i^{jk}(x_1',\ 1,\ x_3') \\ u_i^{jk}(x_1',\ x_2',\ 0) &= u_i^{jk}(x_1',\ x_2',\ 1) \end{aligned} \tag{3.35}$$

where the constraint is applied on the i-th component of the displacement vector due to macroscopic strain, $\bar{\varepsilon}_{jk}$ for i, j, $k = 1$, 2 and 3. PBC implementation for thermal problems of this work are temperature constraint equations applied to solve the discretized form of Eqn. 3.31

$$\begin{aligned} \theta^i(0,\ x_2',\ x_3') &= \theta^i(1,\ x_2',\ x_3') \\ \theta^i(x_1',\ 0,\ x_3') &= \theta^i(x_1',\ 1,\ x_3') \\ \theta^i(x_1',\ x_2',\ 0) &= \theta^i(x_1',\ x_2',\ 1) \end{aligned} \tag{3.36}$$

due to macroscopic temperature gradient, $\nabla\bar{\theta}_i$ in the i-th direction for $i = 1$, 2 and 3.

In the next chapter, a numerical implementation of the methods for the microscale model development is presented.

Chapter 4

Microscale Numerical Implementation

4.1 Micro-architecture parameterization

Researchers have demonstrated that parameterization with beam-like structures have the potential to cover large extents of the material property space [18, 10], particularly where manufacturing constraints exits [121]. Physically-realizable topology optimization solutions also suggest strut-like structures as optimal configurations for compliance minimization problems as the constituent members are oriented along the directions of principal stresses to resist strains. According to the suitability conditions of Sec. 3.2, it is intended that the parameterization employed easily captures periodicity so as to lend itself to homogenization theory as do lattice-based unit cells. Periodic micro-architectures can be analysed by considering the repeating configuration they are composed of such that the mechanical and thermal properties of a representative volume is equivalent to that of an infinite assembly of the repeating micro-architecture.

To demonstrate the derived framework, Lattice Unit Cells (LUC) are employed for microscale parameterization. The parameterization provides smoothly-changing geometry for slowly-changing micro-parameters. Sufficient scale separation is an assumption of heterogeneous multiscale methods [81] that validates the homogenization theory as imple-

mented. The scale separation ensures that the micro-architecture length scales are much smaller than the characteristic length over which macroscale field variables change [91] so that material property variations are efficiently captured by the smooth variation of microstructure parameters. The parameterization is also suited to the intended additive manufacturing techniques presenting no enclosed volumes or suspended solids within the unit cell. Each LUC is characterised by four strut-like members connecting opposite

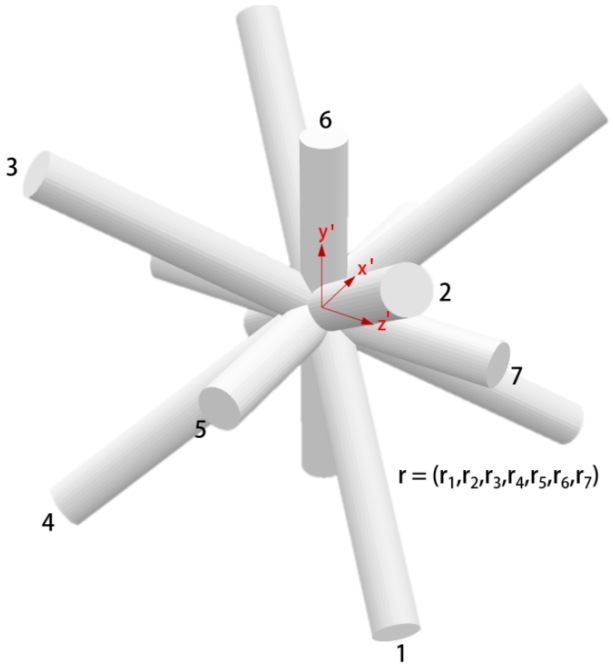


Figure 4.1: Microstructure parameterization: The properties of the micro-architecture are controlled by the components of its vector of normalized radii parameters. Each member has a fixed orientation and the coordinate axes of the microscale are consistent with the macroscale so that the orientations of each member remains unchanged for large-scale optimization.

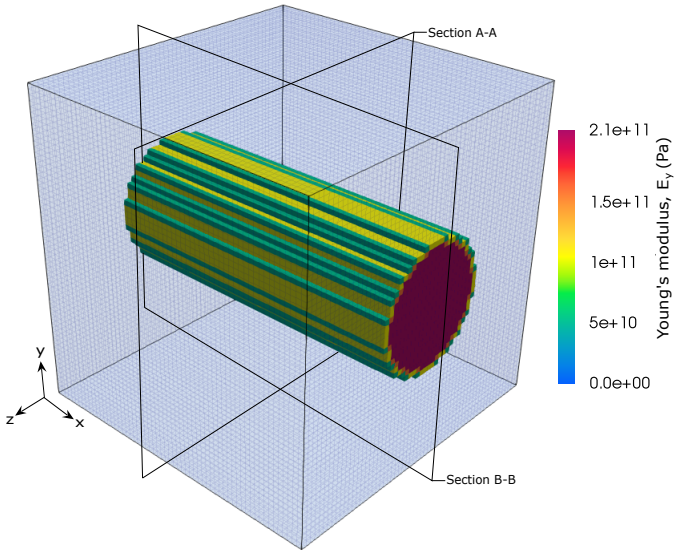
corners (termed diagonal members) and three similar members connecting opposite face centers (termed face members). The lattice configuration is comprised of members of circular cross-section as shown in Fig. 4.1. By varying the radii of each of these lattice members, the material property of the unit cell is altered, hence leading to a parameterization scheme. Each of the seven radii is normalized by the unit cell length. Section 5.6 investigates the performance of the parameterization employed against material property bounds for composites comprised of mechanical mixtures of two material phases [122, 123]. However, other parameterization schemes are suited to the developed framework provided

they satisfy the suitability conditions of Sec. 3.2. Figure 4.1 illustrates a typical micro-structure with its vector of normalized radii parameters, $\boldsymbol{r}$ as well as its orientation in three-dimensional space. This orientation is preserved for subsequent macroscale analyses.

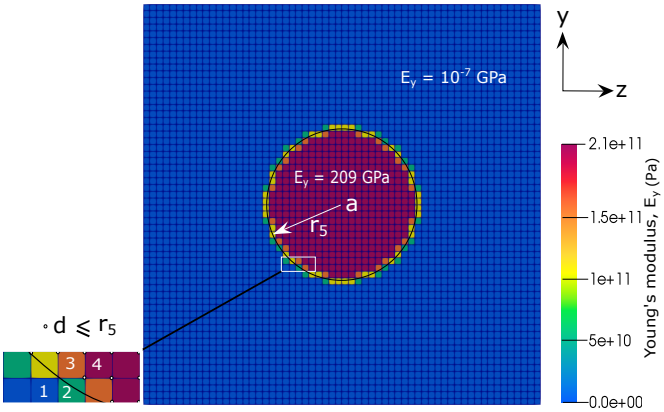
4.2 Property Assignment

Local material assignment within the LUC is initialized by discretization of the unit cell domain. Structured 8-noded linear hexahedral elements are used and kept fixed for all micro-architecture analyses. Mesh convergence studies presented in Section 4.5 yielded a mesh refinement of 70^3 finite elements within the LUC as converged for the structural and thermal property evaluations of the small-scale analyses of this work. This structured discretization supports the implementation of periodic boundary conditions but also eliminates complications associated with unstructured mesh re-construction for complex geometries. All micro-architectures achievable by the parameterization scheme are generated by an element-based material assignment. The position vectors of the 8 nodes of each element determine the material property for the given element.

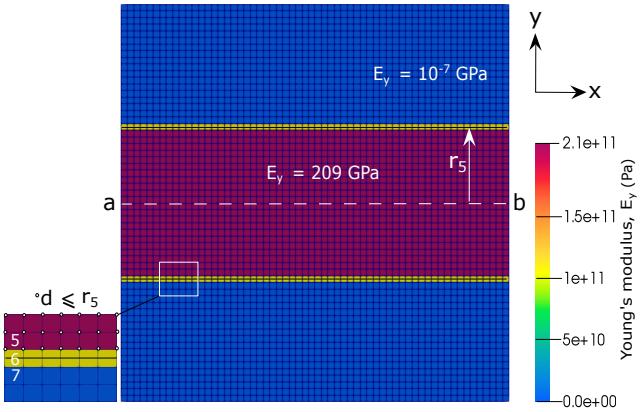
Consider the material assignment for the micro-architecture whose vector of radii parameters is given as $\boldsymbol{r} = (0, 0, 0, 0, 0.19, 0, 0)$ shown in Fig. 4.2a. As indicated by $\boldsymbol{r}$, member 5 has a non-dimensionalized radius of 0.19. Each element in the discretization is assigned a Young's modulus of E_e given by Eqn. 3.8 where $E_s = 209$ GPa and $E_v = 10^{-7}$ GPa represent the Young's moduli of the base material and void respectively. Void is modelled as a very weak material since zero stiffness constitutes a singularity during numerical implementation. Similarly, each element is also assigned a thermal conductivity coefficient of K_e given by Eqn. 3.9 where $K_s = 40$ $\mathrm{Wm^{-1}K^{-1}}$ and $K_v = 0.024$ $\mathrm{Wm^{-1}K^{-1}}$ represent the conductivity of the base material and void respectively. The node fraction for each element, n_f is the proportion of its eight nodes that exist within the subdomain of a member. The subdomain of a member is defined as the region enclosed by the radial distance about the centroidal axis of the member. The through-sections shown in Figs 4.2b



(a) Lattice Unit Cell, $\boldsymbol{r} = (0, 0, 0, 0, 0.19, 0, 0)$



(b) Through-section A-A, $\boldsymbol{r} = (0, 0, 0, 0, 0.19, 0, 0)$



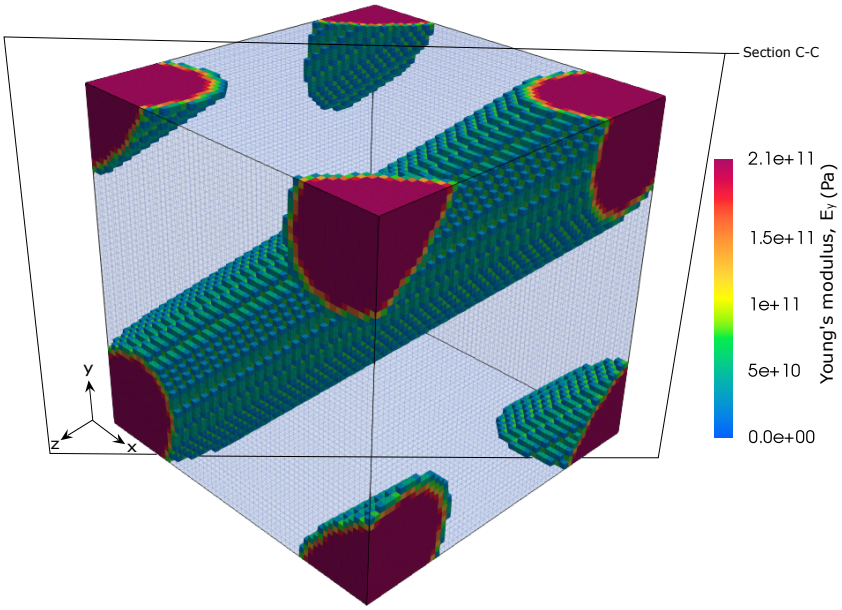
(c) Through-section B-B, $\boldsymbol{r} = (0, 0, 0, 0, 0.19, 0, 0)$

Figure 4.2: Face member material assignment illustration

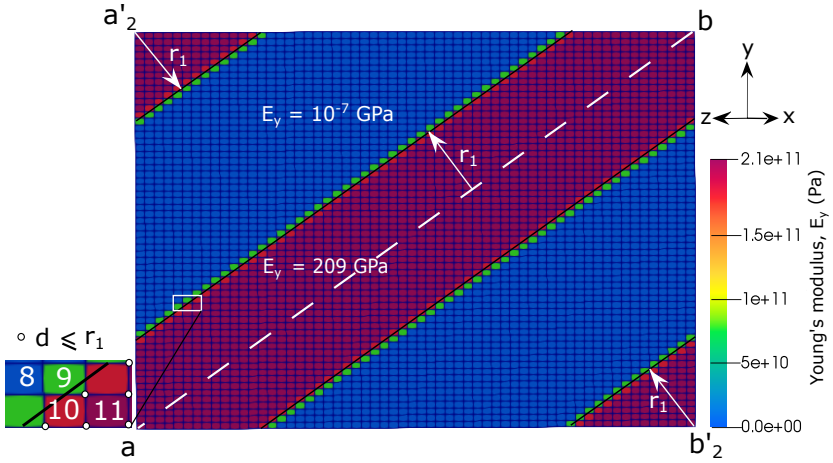
and 4.2c represent the subdomain for Member 5 of the LUC, $\boldsymbol{r} = (0, 0, 0, 0, 0.19, 0, 0)$. The true solid/void boundary within the unit cell is given as

$$\Psi(\boldsymbol{x'}, \boldsymbol{r}_m) = \frac{|(\mathbf{b}(\boldsymbol{x'}) - \mathbf{a}(\boldsymbol{x'})) \times (\mathbf{a}(\boldsymbol{x'}) - \mathbf{c}(\boldsymbol{x'}))|}{|\mathbf{b}(\boldsymbol{x'}) - \mathbf{a}(\boldsymbol{x'})|} - \boldsymbol{r}_m = 0 \qquad m = 1,\ 2,\ \ldots,\ 7 \tag{4.1}$$

where $\mathbf{a}$ and $\mathbf{b}$ are the position vectors of the nodes within the microscale coordinate system, $\boldsymbol{x'}$, at both end vertices of the centroidal axis of the given member. Position vector, $\mathbf{c}$ corresponds to any given node. The first term on the r.h.s of Eqn. 4.1 is the distance of a point from a line in three-dimensional real space. If the position of a given



(a) Lattice Unit Cell, $\boldsymbol{r} = (0.19, 0, 0, 0, 0, 0, 0)$



(b) Through-section C-C, $\boldsymbol{r} = (0.19, 0, 0, 0, 0, 0, 0)$

Figure 4.3: Diagonal member material assignment illustration

node relative to a member's centroidal axis satisfies the relation

$$\frac{|(\mathbf{b}(\boldsymbol{x'}) - \mathbf{a}(\boldsymbol{x'})) \times (\mathbf{a}(\boldsymbol{x'}) - \mathbf{c}(\boldsymbol{x'}))|}{|\mathbf{b}(\boldsymbol{x'}) - \mathbf{a}(\boldsymbol{x'})|} - \boldsymbol{r}_m \leq 0 \qquad m = 1,\ 2,\ \ldots,\ 7 \tag{4.2}$$

for which $\boldsymbol{r}_m$ is the normalized radius of the m-th member, then that node belongs to the subdomain defining the m-th member. Equation 3.8 is then evaluated to determine the Young's modulus of each 8-noded element in the LUC domain. The LUC of Fig. 4.2 has position vectors of $\mathbf{a} = (0, 0.5, 0.5)$ and $\mathbf{b} = (1, 0.5, 0.5)$ for member 5 with $r_5 = 0.19$. Figure 4.2 shows that elements of intermediate Young's modulus exist in the neighbourhood

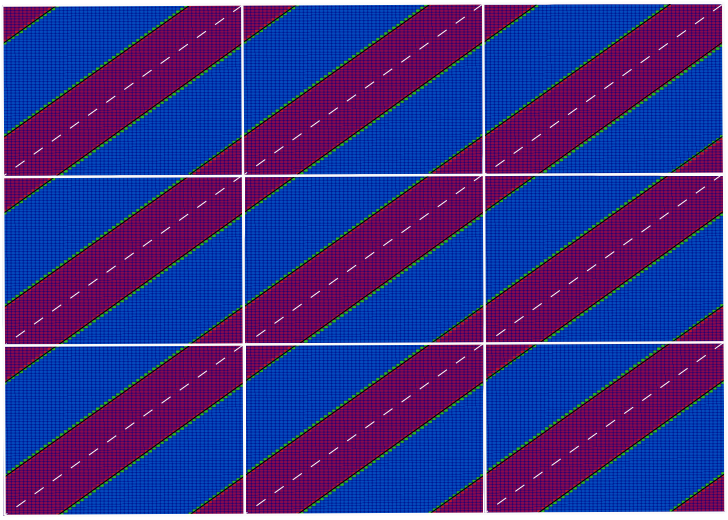


Figure 4.4: Geometry periodicity of diagonal members (Assembly of Section C-C)

of $r_5 = 0.19$. From Fig. 4.2b, all nodes of Element 1 do not satisfy Eqn. 4.2 so that $n_f = 0$ and $E_e = E_v$. On the other hand, Element 4 has $n_f = 1$ so that $E_e = E_s$. Elements 2 and 3 have $n_f = 0.25$ and 0.75 with $E_e = 0.25E_s$ GPa and $0.75E_s$ GPa respectively. Figure 4.2c shows Element 6 with $n_f = 0.5$ and $E_e = 0.5E_s$ GPa. Similar considerations apply to the local assignment of the thermal conductivity coefficient.

The material assignment for diagonal members is similar to the element-based material assignment governed by distance of nodal positions from member subdomains but with adaptations to satisfy the geometry periodicity requirements. Consider the LUC with $\boldsymbol{r} = (0.19, 0, 0, 0, 0, 0, 0)$ shown in Fig. 4.3. Member 1 has centroidal axis with $\mathbf{a} = (0, 0, 1)$, $\mathbf{b} = (1, 1, 0)$ with $r_1 = 0.19$. The through-section C-C shown in Fig. 4.3b is orientated so that its plane lies along the centroidal axis of Member 1 and not in any of the 3 orthonormal axes. Like the face member illustrated in Fig. 4.2, elements with intermediate Young's modulus lie in the neighbourhood of $r_1 = 0.19$ so that element 9 and 10 have $E_e = 0.375E_s$ and $E_e = 0.875E_s$ respectively. However, to ensure periodicity of the microstructure, trucated regions at the corners must be recaptured within the LUC. This is achieved by material assignment based on translated centroidal axes for each of the diagonal Members 1 – 4 along each of the three orthonormal axes. The new position vectors of the end vertices of the translated centroidal axes in the i-th orthonormal

direction, $\mathbf{a}'_i$ and $\mathbf{b}'_i$ are given as

$$\begin{aligned}
\mathbf{a}'_1 &= (a_x \pm L_x,\, a_y,\, a_z) \\
\mathbf{a}'_2 &= (a_x,\, a_y \pm L_y,\, a_z) \\
\mathbf{a}'_3 &= (a_x,\, a_y,\, a_z \pm L_z) \\
\mathbf{b}'_1 &= (b_x \pm L_x,\, b_y,\, b_z) \\
\mathbf{b}'_2 &= (b_x,\, b_y \pm L_y,\, b_z) \\
\mathbf{b}'_3 &= (b_x,\, b_y,\, b_z \pm L_z)
\end{aligned} \tag{4.3}$$

where $L_x = L_y = L_z = 1$ for the LUC. In Fig. 4.3b, the through-section C-C captures the effect of this consideration achieved by material assignment for the translated centroidal axis of Member 1 along the positive and negative y-axis such that $\mathbf{a}'_2 = (a_x, a_y + 1, a_z)$ and $\mathbf{b}'_2 = (b_x, b_y - 1, b_z)$. Applying Eqn. 4.3 yields the periodic configuration of Fig. 4.3a with corner material assignment within the LUC for $\boldsymbol{r} = (0.19, 0, 0, 0, 0, 0, 0)$. These considerations yield a periodic micro-architecture as demonstrated by an assembly of multiple LUCs (see Fig. 4.4) and have been applied to the material assignment for diagonal Members 1–4 for all micro-architectures of this work. This consideration for diagonal

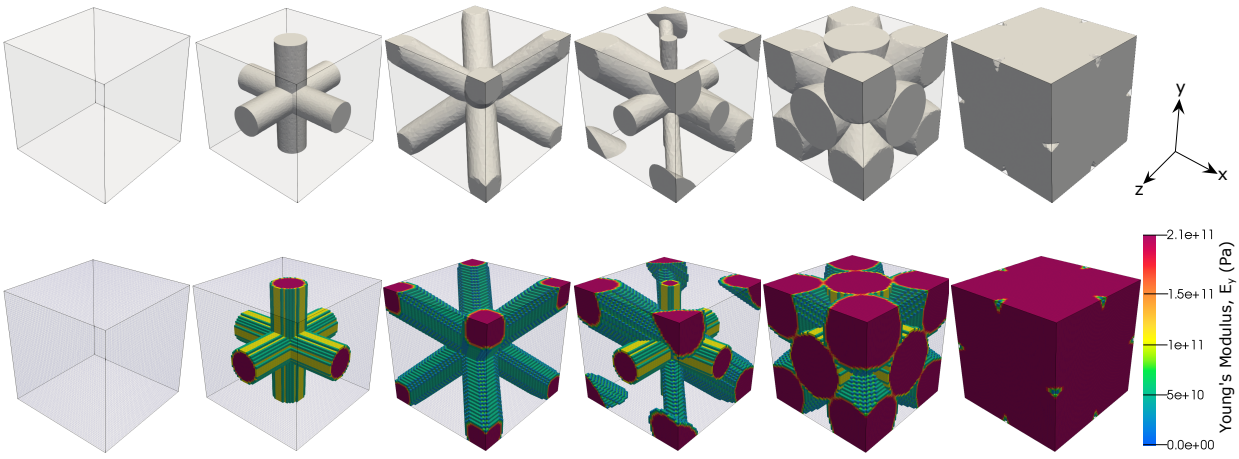


Figure 4.5: Example micro-architectures with vector of radii parameters, $\boldsymbol{r} = (0, 0, 0, 0, 0, 0, 0)$, $(0, 0, 0, 0, 0.13, 0.13, 0.13)$, $(0.13, 0.13, 0.13, 0.13, 0, 0, 0)$, $(0, 0.19, 0.06, 0, 0.13, 0.06, 0.13)$, $(0.25, 0.25, 0.25, 0.25, 0.25, 0.25, 0.25)$, and $(0.38, 0.38, 0.38, 0.38, 0.38, 0.38, 0.38)$ (left-to-right).

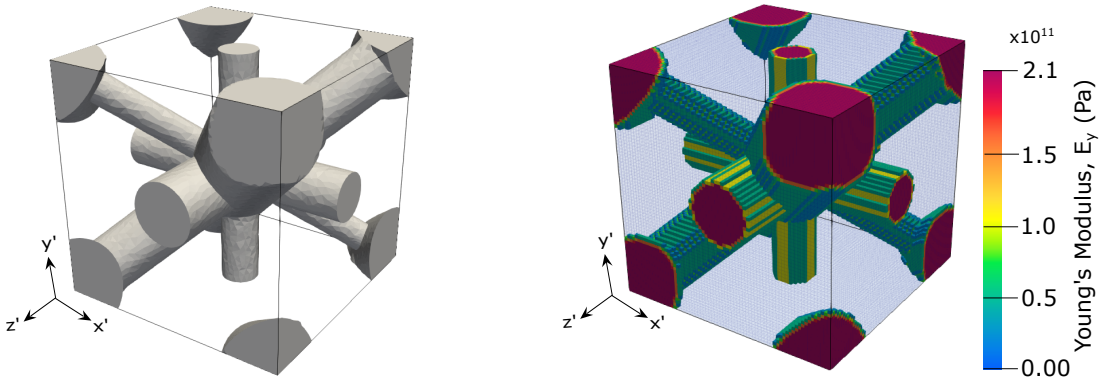
members does not apply to Members 5–7 since these face members are already periodic with member subdomains fully contained within the LUC.

Figure 4.5 shows examples of micro-architectures that can be derived from the parameterisation described above, along with their fixed-discretization representation. The fixed-discretization representations have been thresholded for visualization at $E_e = 0.01E_s$. Having derived an efficient parameterization, the microscale model is completed by evaluating the effective mechanical and thermal properties of all micro-architectures achievable by the parameterization implemented.

4.3 Asymptotic expansion homogenization

To demonstrate the determination of effective mechanical and thermal properties of the LUCs of this work using the homogenization theory described in Sec. 3.4, an account of the numerical procedures for an arbitrary LUC is documented as follows:

An LUC with vector of parameters, $\boldsymbol{r} = (0.12, 0.06, 0, 0.2, 0.1, 0.08, 0.13)$ is considered to demonstrate the capability for full control over anisotropy afforded by the parameterization scheme developed in Sec. 4.1. First, a unit cube is defined and its domain is discretized into n_e^3 8-noded hexahedral elements. Mesh convergence studies of Sec. 4.5 have determined the choice of $n_e = 70$. According to Sec. 4.2, material assignment is executed given $\boldsymbol{r}$. Base material properties are consistent with that used in Sec. 4.2 and remains the same throughout this work. As a consequence, element-wise Young's Modulus and thermal conductivity are assigned based on Eqns. 3.8 and 3.9. Considerations are made to ensure geometric periodicity as described for diagonal lattice members. To prevent rigid body translation, a Dirichlet boundary condition is imposed at $\boldsymbol{x'} = (0, 0, 0)$ on the unit cell so that $u_i = 0$ for $i = 1$, 2 and 3. Figures 4.6a and 4.6b illustrate the material assignment on a fixed structured mesh. Periodic boundary conditions are imposed across opposite external boundaries of the unit cell. This is achieved by enforcing associations



(a) $\boldsymbol{r}$ = (0.12,0.06,0,0.2,0.1,0.08,0.13) (b) Fixed-discretization representation

Figure 4.6: Element-based material assignment

of degrees of freedom on the LUC boundary nodes as defined by Eqns. 3.35 and 3.36. More precisely, the external boundary nodes are classified as master or slave nodes. By convention, master nodes reside on entities connected to the origin, $\boldsymbol{x'} = (0, 0, 0)$. An entity is a corner, edge or face of the LUC. The degrees of freedom of slave nodes are

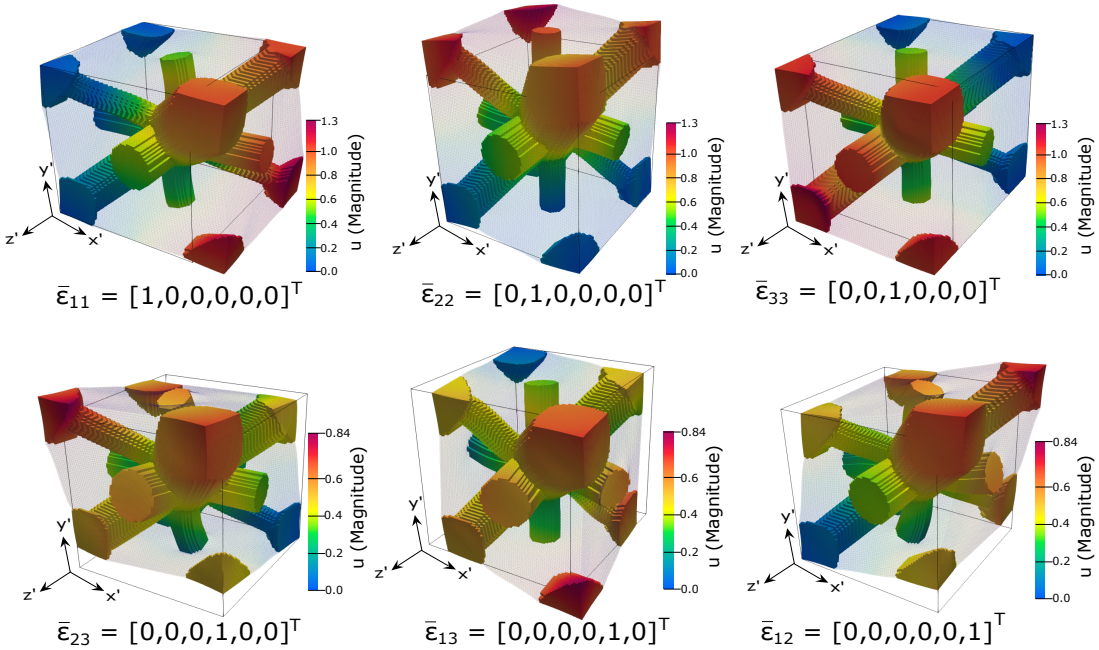


Figure 4.7: Displacement field solution given $\bar{\varepsilon}_{ij}$ (Deformation scale = 0.2 : 1)

linked to corresponding master nodes through constraint equations so that they respond structurally and thermally in an identical manner as the master nodes, the constraints here being the periodic boundary conditions of Eqns. 3.35 and 3.36. The structured dis-

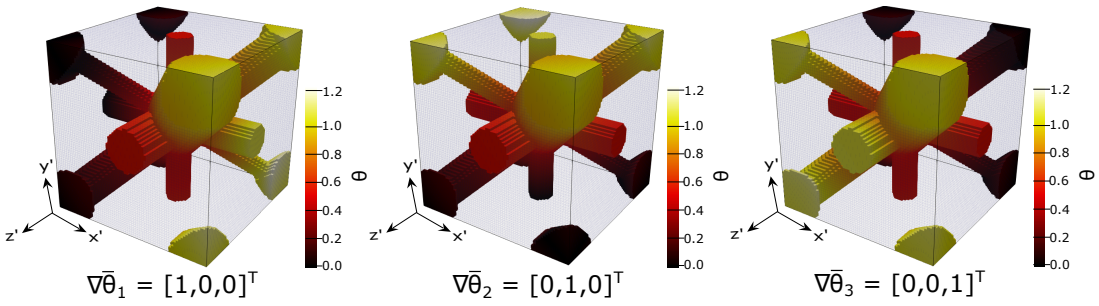


Figure 4.8: Temperature field solution given $\nabla\bar{\theta}_i$

cretization implemented ensures that there are always corresponding nodes on opposite external boundaries so that the constraint equations are precisely implemented. Nodes residing on edge or corner entities belong to two or three separate degree-of-freedom associations respectively. Nodes residing on face entities only belong to a single association, with the corresponding node on the opposite face.

Having ensured geometric periodicity and periodic boundary condition implementation on the fixed discretization representation of the microstructure, Eqns. 3.19 and 3.31 are implemented to numerically solve for the periodically-fluctuating displacement field and temperature distribution for each of the six unit strains of Fig. 3.2 and three unit temperature gradient across the LUC of Fig. 3.3 respectively. Figure 4.7 shows the displacement field obtained for each unit strain. Figure 4.8 shows the temperature field obtained for each temperature gradient imposed on the LUC. The solutions, u and θ give ε^*_{ij} and $\nabla\theta^*_i$ which are substituted into Eqns. 3.20 and 3.32 to obtain the microscale stress tensor, σ_{ij} and heat flux vector, q_i respectively. Figures 4.9 and 4.10 show the stress tensor component fields for macroscale direct strain, $\bar{\varepsilon}_{11}$ and macroscale shear strain, $\bar{\varepsilon}_{12}$. Figure 4.11 shows the microscale heat flux vector components, q_i, for macroscale temperature gradient in the x-direction, $\nabla\bar{\theta}_1$.

The macroscale stress tensor and heat flux vector components were derived by Eqns. 3.22 and 3.33 respectively. Finally, the mechanical and thermal properties of the micro-

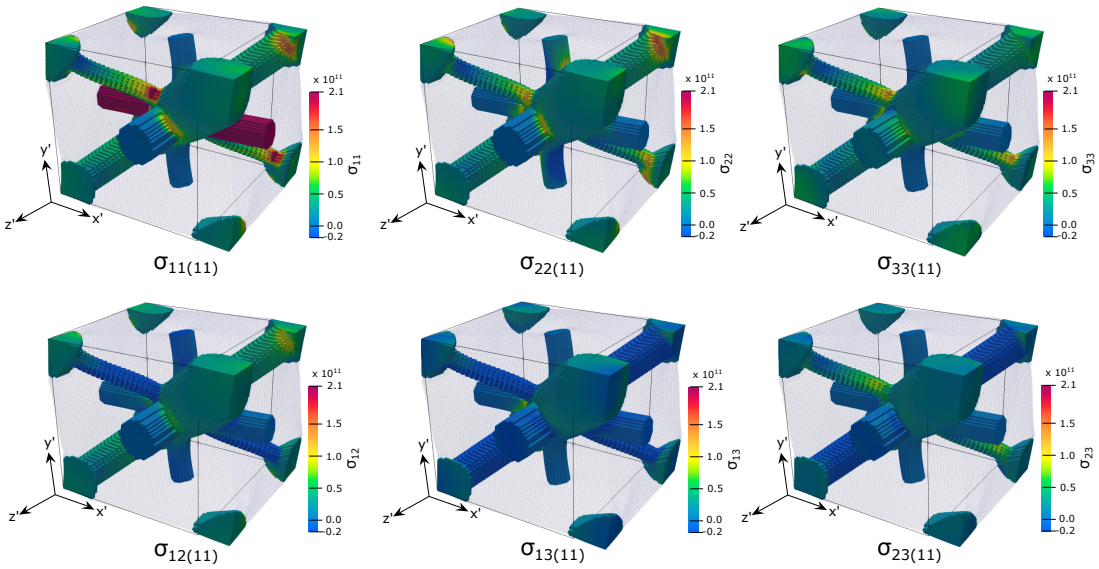


Figure 4.9: Stress tensor components given $\bar{\varepsilon}_{11}$ (Deformation scale = 0.2 : 1)

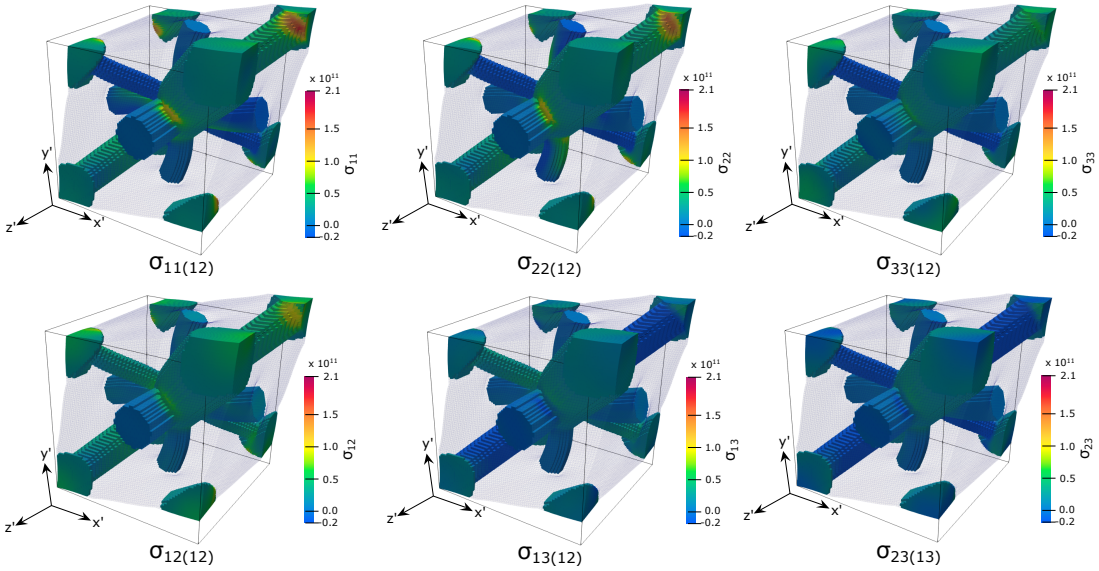


Figure 4.10: Stress tensor components given $\bar{\varepsilon}_{12}$ (Deformation scale = 0.2 : 1)

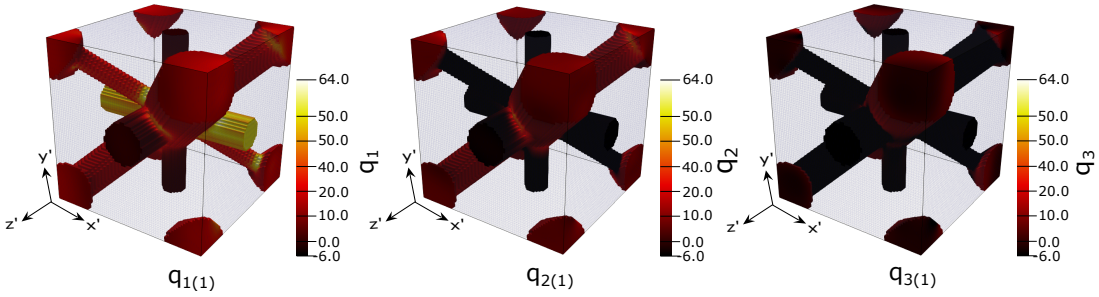


Figure 4.11: Heat flux vector components given $\nabla\bar{\theta}_1$

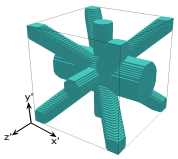
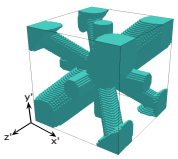
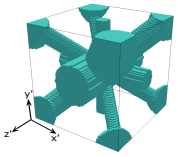
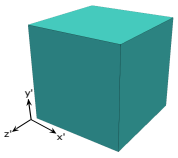
architecture were determined by Eqns. 3.23 and 3.34 respectively to give:

$$\boldsymbol{E}_{ij}^{H} = \begin{bmatrix} E_{11} & E_{12} & E_{13} & E_{14} & E_{15} & E_{16} \\ & E_{22} & E_{23} & E_{24} & E_{25} & E_{26} \\ & & E_{33} & E_{34} & E_{35} & E_{36} \\ & & & E_{44} & E_{45} & E_{46} \\ & sym & & & E_{55} & E_{56} \\ & & & & & E_{66} \end{bmatrix} = \begin{bmatrix} 19.29 & 9.80 & 8.75 & 3.57 & 1.53 & 7.78 \\ & 16.17 & 8.62 & 3.59 & 1.98 & 7.72 \\ & & 27.78 & 3.72 & 1.63 & 6.35 \\ & & & 8.77 & 6.53 & 2.20 \\ & sym & & & 8.91 & 3.53 \\ & & & & & 9.78 \end{bmatrix} \text{GPa} \tag{4.4}$$

and

$$\boldsymbol{K}_{ij}^{H} = \begin{bmatrix} K_{11} & K_{12} & K_{13} \\ & K_{22} & K_{23} \\ sym & & K_{33} \end{bmatrix} = \begin{bmatrix} 6.30 & 3.34 & 0.82 \\ & 5.67 & 1.62 \\ sym & & 7.62 \end{bmatrix} \text{Wm}^{-1}\text{K}^{-1} \tag{4.5}$$

The fully populated stiffness and conductivity matrices of Eqns. 4.4 and 4.5 demonstrate

Type/ Parameters	**Geometry** -	**Elasticity Matrix** (GPa)	**Conductivity Matrix** ($\text{Wm}^{-1}\text{K}^{-1}$)
Orthotropic (0.1,0.1,0.1,0.1,0.2,0.1,0.1)		$\begin{bmatrix} 35.1 & 7.29 & 7.29 & 0 & 0 & 0 \\ & 17.8 & 7.64 & 0 & 0 & 0 \\ & & 17.8 & 0 & 0 & 0 \\ & & & 7.21 & 0 & 0 \\ & sym & & & 7.05 & 0 \\ & & & & & 7.05 \end{bmatrix}$	$\begin{bmatrix} 7.68 & 0 & 0 \\ & 5.45 & 0 \\ sym & & 5.45 \end{bmatrix}$
Monoclinic (0.2,0.1,0.1,0.2,0.1,0.1,0.1)		$\begin{bmatrix} 33.1 & 18.0 & 15.5 & 0 & 0 & 9.54 \\ & 33.1 & 15.4 & 0 & 0 & 9.54 \\ & & 42.1 & 0 & 0 & 6.42 \\ & & & 15.6 & 6.75 & 0 \\ & sym & & & 15.6 & 0 \\ & & & & & 17.4 \end{bmatrix}$	$\begin{bmatrix} 9.87 & 3.32 & 0 \\ & 9.87 & 0 \\ sym & & 11.2 \end{bmatrix}$
Anisotropic (0.12,0.08,0.06,0.2,0.1,0.07,0.2)		$\begin{bmatrix} 23.1 & 12.1 & 10.4 & 3.09 & 1.77 & 7.68 \\ & 18.2 & 9.85 & 3.18 & 2.31 & 7.54 \\ & & 44.0 & 3.58 & 2.24 & 5.40 \\ & & & 10.3 & 5.91 & 2.36 \\ & sym & & & 10.7 & 3.08 \\ & & & & & 11.7 \end{bmatrix}$	$\begin{bmatrix} 7.52 & 3.23 & 0.78 \\ & 6.70 & 1.29 \\ sym & & 10.01 \end{bmatrix}$
Isotropic (0.38,0.38,0.38,0.38,0.38,0.38,0.38)		$\begin{bmatrix} 281 & 120 & 120 & 0 & 0 & 0 \\ & 281 & 120 & 0 & 0 & 0 \\ & & 281 & 0 & 0 & 0 \\ & & & 80.4 & 0 & 0 \\ & sym & & & 80.4 & 0 \\ & & & & & 80.4 \end{bmatrix}$	$\begin{bmatrix} 39.9 & 0 & 0 \\ & 39.9 & 0 \\ sym & & 39.9 \end{bmatrix}$

The base material properties for these micro-architectures are consistent with those of Sec. 4.2 and for all micro-architectures of this work. However, the components of the elasticity and conductivity matrices scale linearly with those of the base material so that the database of material properties is suited to all other base materials, provided the Poisson's Ratio remains unchanged.

Table 4.1: Sample micro-architectures enabled by parameterization

the capacity for anisotropy control afforded by the chosen parameterization. Orthotropic and monoclinic micro-architectures are also derivable. Table 4.1 illustrates sample micro-architectures enabled by the parameterization scheme employed. The mechanical and thermal properties of all simulated micro-architectures of this work have been determined by the homogenization process described above.

4.4 Numerical Verification

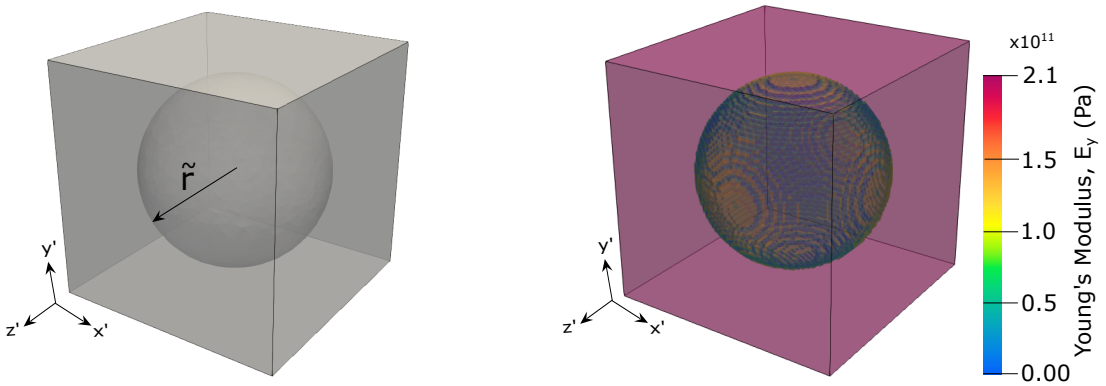
To validate the homogenization implementation of this work, the method is compared with analytical expressions derived by Hashin et al. [122] for determining the effective moduli of perforated composites (ie. composites of a certain base material with a periodic distribution of spherical void inclusions). These expressions are generalized as the elastic limits for a mechanical mixture of isotropic materials and are explored further in relation to the composite micro-architecture of this work in Sec. 5.6. Here, the Hashin-Shtrikman upper bound is used to validate this work's implementation of the asymptotic expansion homogenization. Hashin demonstrated that the elastic upper bound for a two-phase composite was achieved by one comprised of a matrix of a stronger phase material with spherical inclusions of a weaker phase material. Mathematically, the bulk and shear moduli are presented as

$$\kappa_u^* = \kappa_2 + \frac{v_{f_1}}{\frac{1}{\kappa_1 - \kappa_2} + \frac{3v_{f_2}}{3\kappa_2 + 4\mu_2}} \tag{4.6}$$

and

$$\mu_u^* = \mu_2 + \frac{v_{f_1}}{\frac{1}{\mu_1 - \mu_2} + \frac{6(\kappa_2 + 2\mu_2)v_{f_2}}{5\mu_2(3\kappa_2 + 4\mu_2)}} \tag{4.7}$$

respectively where κ_2, μ_2 and v_{f_2} are the bulk moduli, shear moduli and volume fraction of the stronger phase material and κ_1, μ_1 and v_{f_1} are those of the weaker phase material respectively. In this section, it is demonstrated that the implementation of asymptotic



(a) $\boldsymbol{r} = \tilde{r}$ (b) Fixed-discretization representation

Figure 4.12: Material assignment

expansion homogenization in this work remains valid regardless of the microscale parameterization implemented. It also verifies that perforated composites yield limit properties as stated by Hashin [122].

Consider the unit cell parameterization shown in Fig. 4.12 which models composites with spherical void inclusions. An infinite assembly of the unit cell yields a perforated composite of the base material of this work. The spherical voids are represented with properties of a very weak material. The unit cell is parameterized by the normalized radius of the spherical void, $0 \leq \tilde{r} \leq 0.5$ with its center coinciding with that of the unit cell. By varying $\tilde{r}$ within the unit cell, perforated composites of varying material properties are derived. The homogenization technique described in Sec. 4.3 is then implemented to derive the elastic properties of the unit cell. Hill [123] presented relations to derive the bulk and shear moduli of a material given its elasticity matrix components. They are

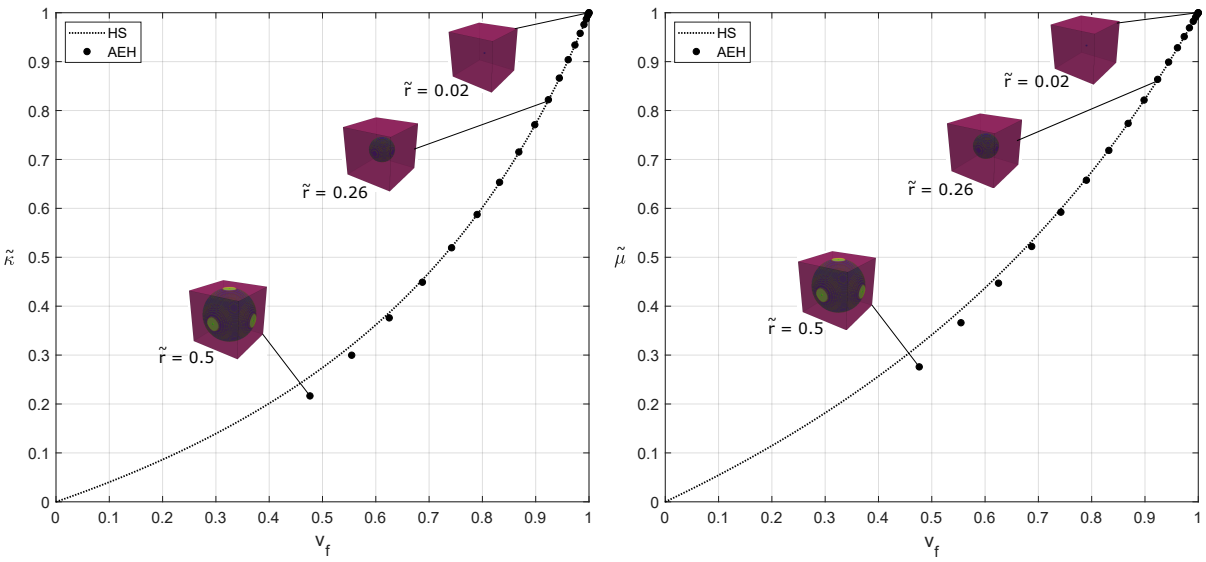
$$9\kappa^* = (E_{11} + E_{22} + E_{33}) + 2(E_{23} + E_{13} + E_{12}) \tag{4.8}$$

and

$$15\mu^* = (E_{11} + E_{22} + E_{33}) - (E_{23} + E_{13} + E_{12}) + 3(E_{44} + E_{55} + E_{66}) \tag{4.9}$$

respectively.

The normalized radius parameter was varied over 20 equal increments across the range



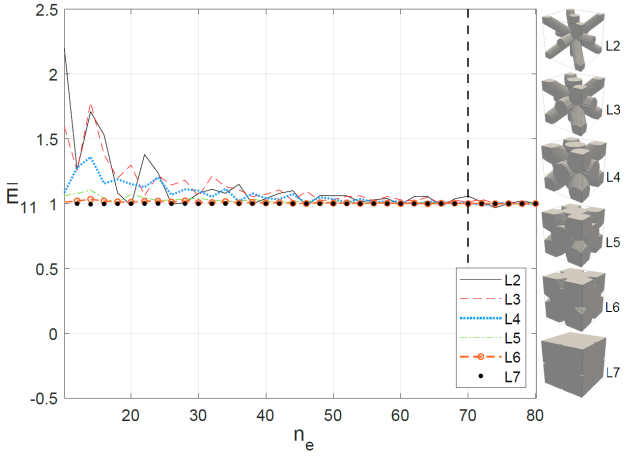
(a) Normalized κ vs v_f (b) Normalized μ vs v_f

Figure 4.13: Effective bulk and shear moduli of composite with spherical void inclusions

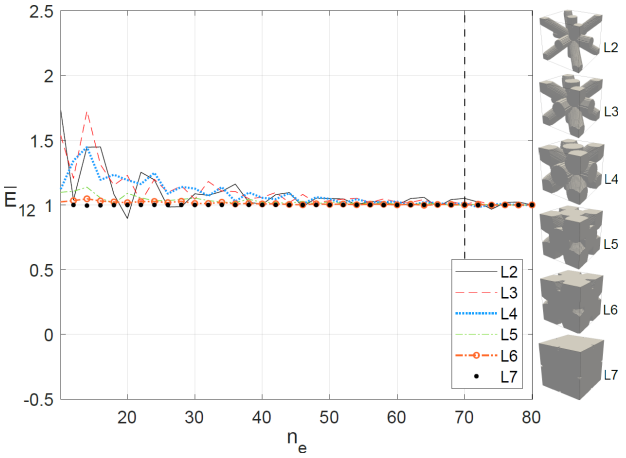
of possible values ie. $0 \leq \tilde{r} \leq 0.5$. For each value of the normalized radius, the volume fraction, v_f, bulk modulus, $\tilde{\kappa}$ and shear modulus, $\tilde{\mu}$ were determined. Figure 4.13 shows the variation of effective bulk and shear moduli with varying volume fraction for a composite of the base material with spherical void inclusions. The dashed-line is the Hashin-Shtrikman (HS) upper limit which is presented as the exact value for the moduli of perforated composites. The solid dots show the moduli computations based on the elastic matrix components derived by asymptotic expansion homogenization (AEH) as implemented in this work. The implementation of homogenization in this work is validated by Figures 4.13a and 4.13b as the moduli computations for the perforated composite coincides with the HS-upper bounds. This is in agreement with Hashin's demonstration that perforated composites yield limit moduli properties. Micro-architectures of these perforated composites with high void radii ($v_f < 0.6$) feature deviations from the HS line which may be attributed to the interaction of void regions across adjacent micro-architectures as the extent of the void regions begin to intersect. It is worthy of note to state that perforated composites used for the validation of the implemented homogenization technique demonstrate limit properties but feature an unsuitable parameterization since they support enclosed volumes.

4.5 Mesh Convergence Studies

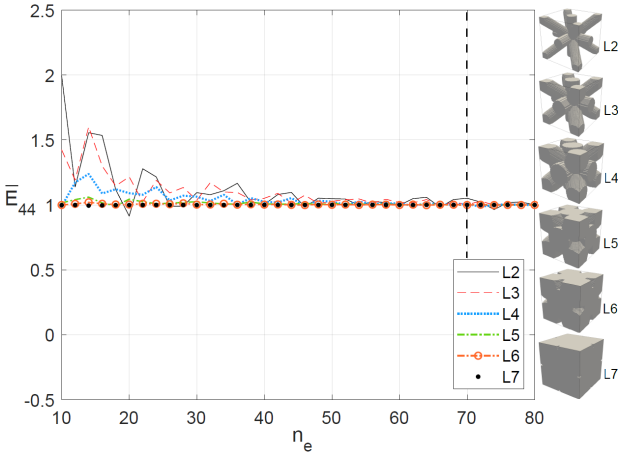
All microscale simulations have been executed by implementing finite element analyses as illustrated in the previous sections. Finite element analyses involves the discretization of infinite-dimensional systems to form approximate finite representations of the systems. Increasing the number of discretization elements improves the accuracy of the approximation but also increases the computational cost of solving the system. Mesh convergence studies were carried out to ensure that an efficient discretization density was implemented to yield converged homogenized properties of the micro-architectures with minimal computational cost. The results of the study are presented in Figs. 4.14–4.17. Each of



(a) Normalized E_{11} vs n_e

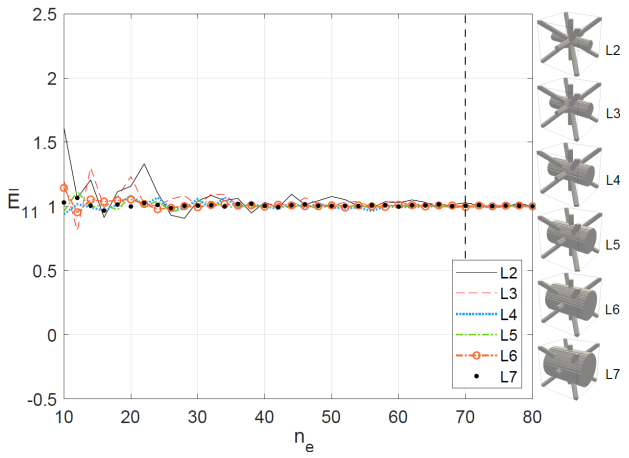


(b) Normalized E_{12} vs n_e

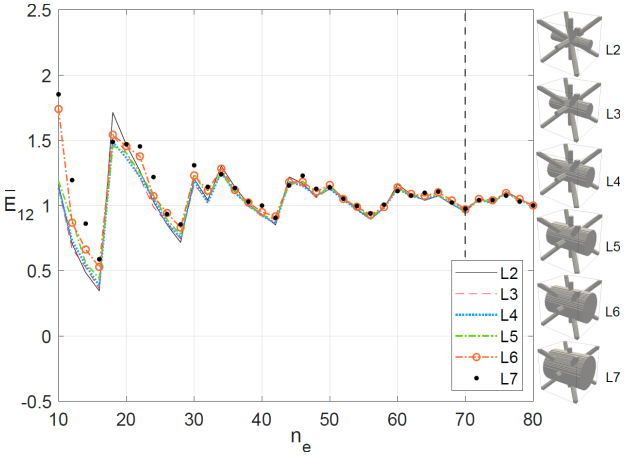


(c) Normalized E_{44} vs n_e

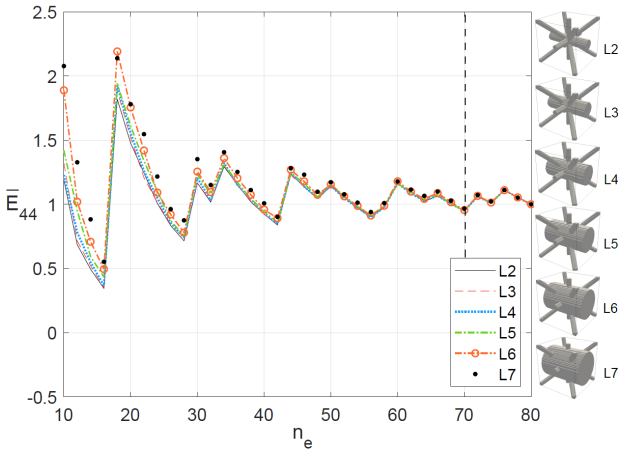
Figure 4.14: Mesh Convergence Studies - All members incremented



(a) Normalized E_{11} vs n_e



(b) Normalized E_{12} vs n_e



(c) Normalized E_{44} vs n_e

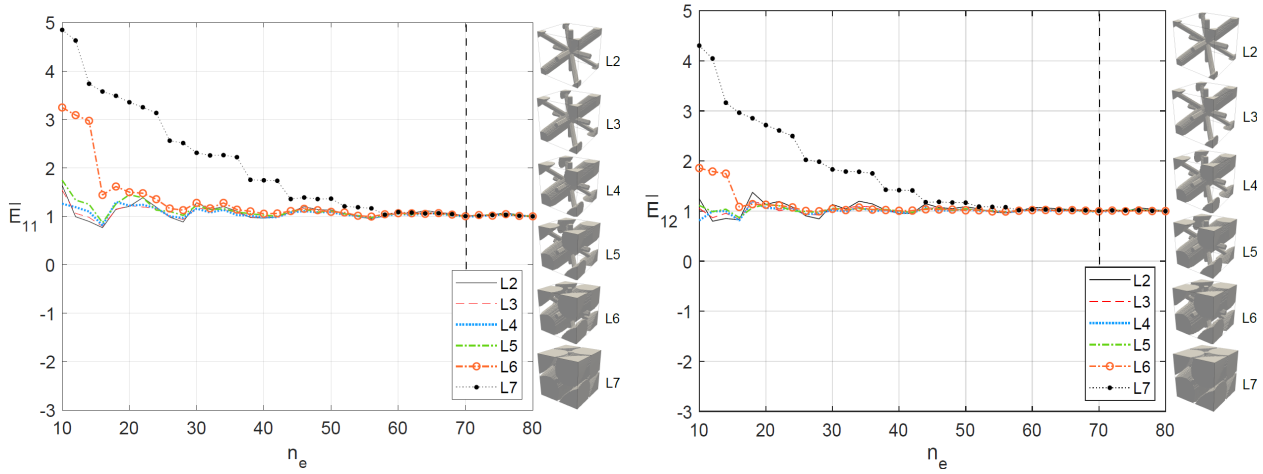
Figure 4.15: Mesh Convergence Studies - Only member 5 incremented

the plots demonstrates the variation of the normalized value of a stiffness or conductivity matrix component against an increasing level of discretization. The discretization level, represented by the number of elements along the edge of the unit cell, is varied such that

$$10 \leq n_e \leq 80 \qquad \text{in even increments} \tag{4.10}$$

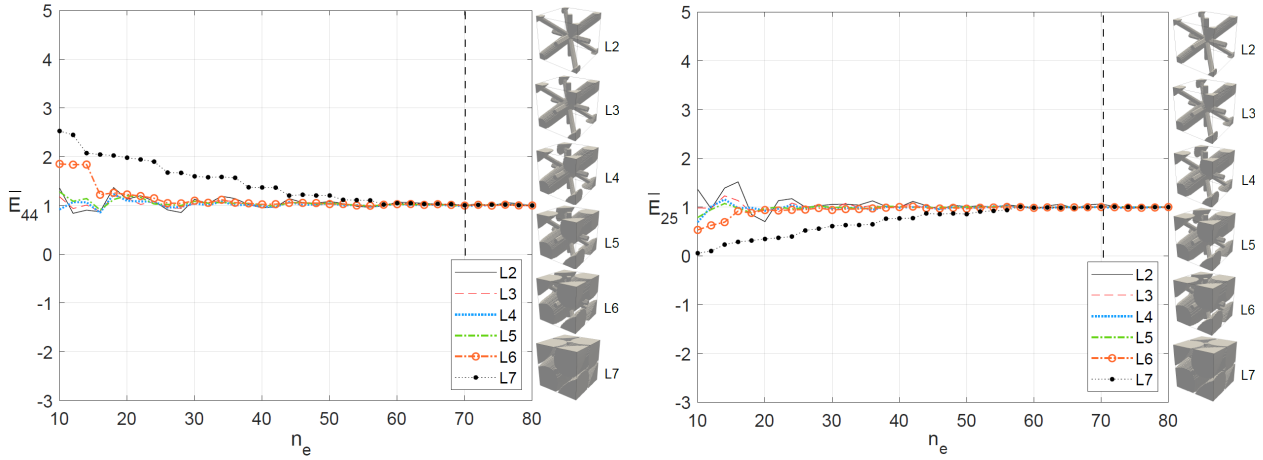
The effect of increasing micro-architecture volume fraction by changing member sizes over 6 levels was also investigated. The nature of member variation over the 6 levels is shown on the right of each plot. Figure 4.14a shows mesh convergence when all members are incremented. No shear-extension elasticity matrix components studies have been conducted since the derived micro-architecture always remains orthotropic or isotropic

(as is the case when the unit cell becomes fully dense). Micro-architectures of higher volume fraction (higher member levels) are shown to attain mesh convergence at lower mesh resolutions than those of lower volume fraction. Figure 4.15 features convergence



(a) Normalized E_{11} vs n_e

(b) Normalized E_{12} vs n_e



(c) Normalized E_{44} vs n_e

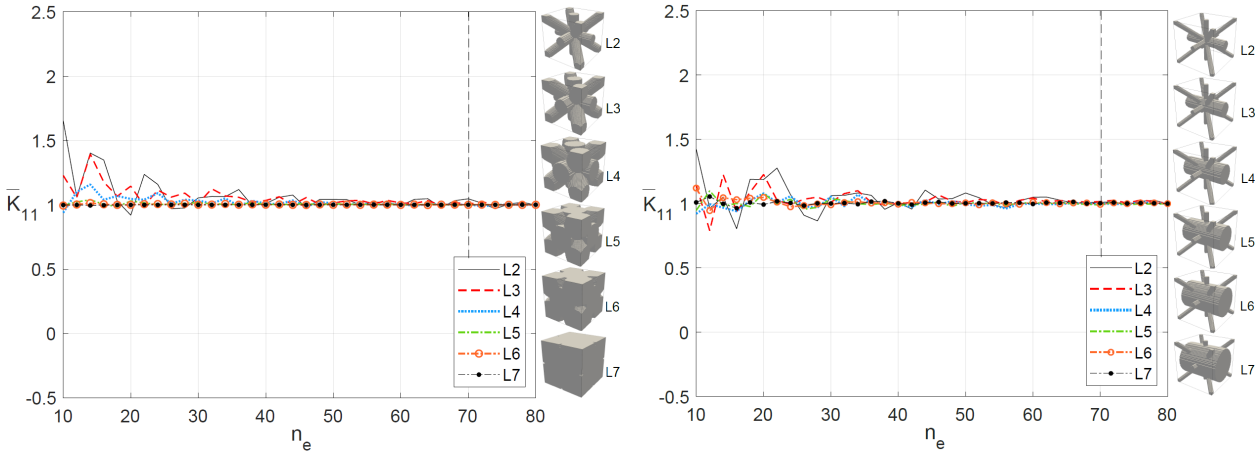
(d) Normalized E_{25} vs n_e

Figure 4.16: Mesh Convergence Studies - Only member 1 incremented

plots when a single face member is incremented. Again, shear-extension components are not shown since the member variation features only orthotropic micro-architectures across the variation. However, it was observed that increasing the face member did not noticeably improve convergence results for extension-normal extension and shear-shear elasticity matrix components. Increasing mesh density improved the normalized values of these matrix components to within 5% of the converged solution at $n_e = 70$. Direct-direct extension components were fully converged at this mesh density for all variations of the

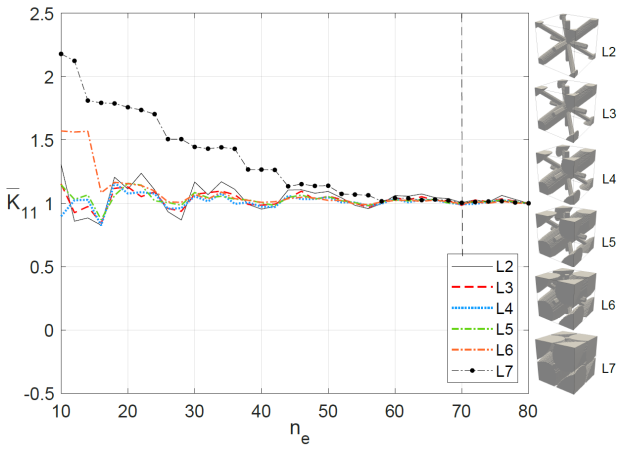
face member as shown in Fig 4.15a.

Figure 4.16 features convergence plots when a single diagonal member is incremented. Mesh convergence was attained at $n_e = 70$ for all elasticity components across all variations of the single diagonal member radius. It was observed that micro-architectures with lower levels of the diagonal member attained convergence sooner than those with higher levels of the diagonal member radius. This is due to the material assignment at the corners of the unit cell due to geometry periodicity considerations as discussed in Sec. 4.2, resulting in a highly anisotropic micro-architecture. Figure 4.17 features convergence plots for

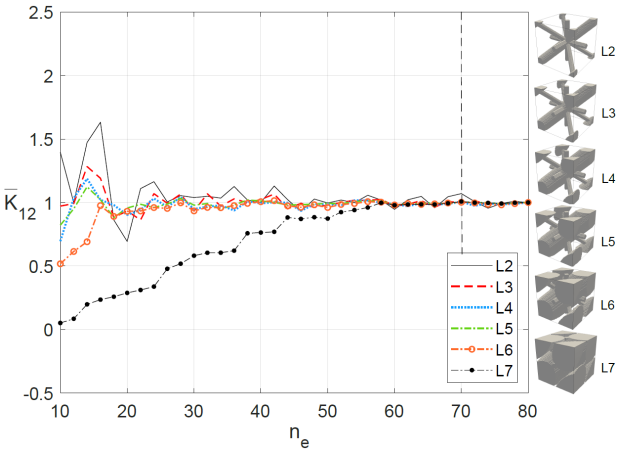


(a) Normalized K_{11} vs n_e

(b) Normalized K_{11} vs n_e



(c) Normalized K_{11} vs n_e



(d) Normalized K_{12} vs n_e

Figure 4.17: Mesh Convergence Studies - All members incremented(Figs. 4.17a), Member 5 incremented(Fig. 4.17b) and Member 1 incremented (Fig. 4.17c and 4.17d) incremented

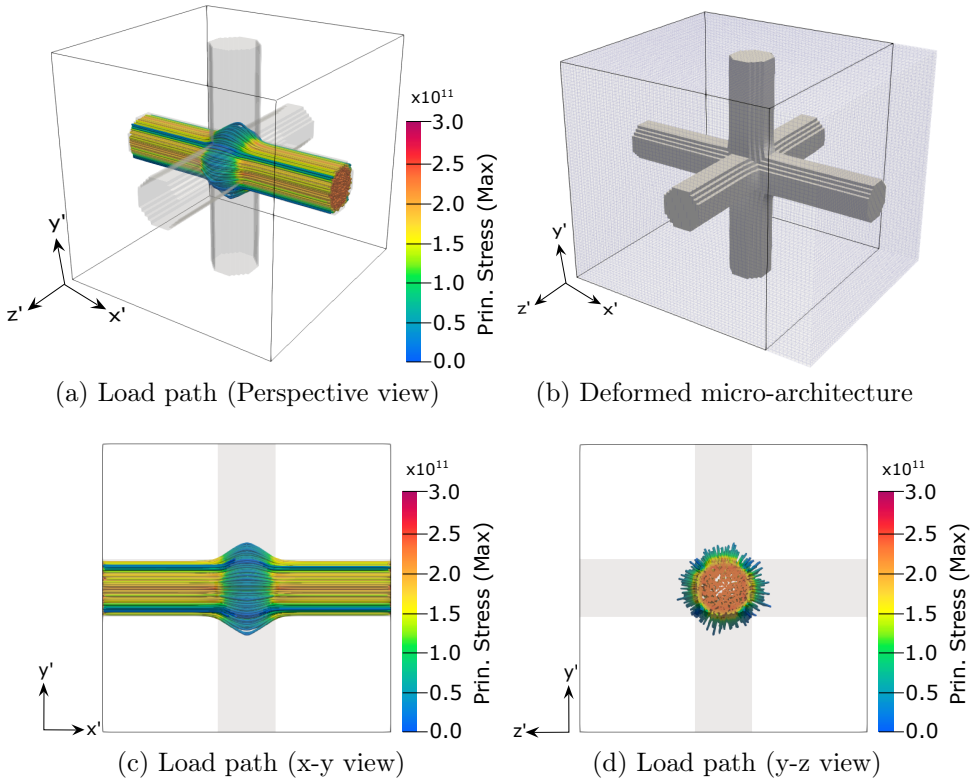
the thermal conductivity matrix components. The effect of increasing micro-architecture

volume fraction by changing member sizes over 6 levels on the convergence plots was also investigated. All components investigated yielded converged solutions at $n_e = 70$ for all micro-architectures.

4.6 Stress Flow Characterization

The suitability of the microscale parameterization was investigated by evaluating mechanical load paths through typical micro-architectures when subjected to direct and shear strains of Fig. 3.2. For brevity, considerations were limited to load paths due to direct strain, $\bar{\varepsilon}_{11}$ and shear strain, $\bar{\varepsilon}_{12}$. Recall that the orientation of the LUCs are aligned to the macroscale domain coordinate system. Principal stress magnitudes and directions were determined by evaluating the eigenvalues and eigenvectors of the local stress tensor at each element within the LUC. Load paths are defined as tangential everywhere to the principal stress directions. Figures 4.18 - 4.23 show the maximum principal stress magnitudes and directions through micro-architectures of only face members, only diagonal members as well as both diagonal and face members. The radii of the members in the figures are kept uniform for emphasis on the orientation of the members rather than member sizes. Figure 4.18 shows a periodic micro-architecture with only face members 5, 6 and 7 subjected to direct strain, $\bar{\varepsilon}_{11}$.

High magnitude stress flow through Member 5 suggests that resistance to direct strain, $\bar{\varepsilon}_{11}$ is most sensitive to member 5 by virtue of its orientation relative to the strain applied. As a consequence, the stiffness of the micro-architecture can be increased most effectively by increasing r_5. It is demonstrated that face members are suited to resist direct strain in any of the orthonormal axes since their centroidal axes are aligned to these axes. The same micro-architecture is however not suited to shear strains as shown in Fig. 4.19. Here, stress flow with much lower magnitudes through face members 5 and 6 result in bending of the members due to shear strain, $\bar{\varepsilon}_{12}$. By virtue of their orientation, face members are demonstrated to offer less resistance to shear strain as beams are much less stiff in bending



(a) Load path (Perspective view)

(b) Deformed micro-architecture

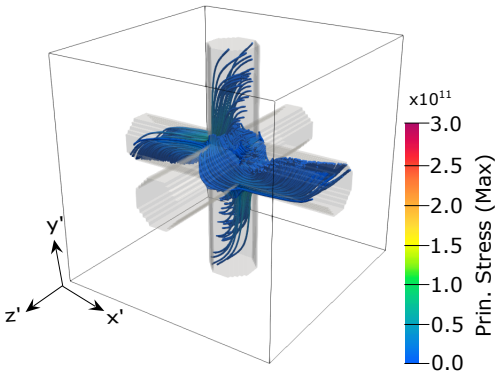
(c) Load path (x-y view)

(d) Load path (y-z view)

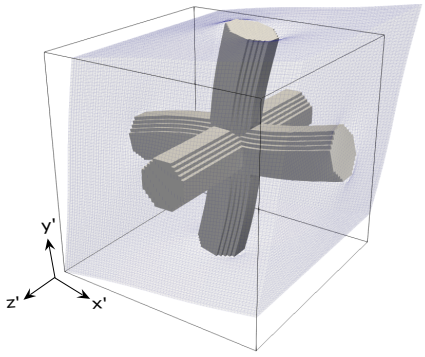
Figure 4.18: Load path through, $\boldsymbol{r} = (0, 0, 0, 0, 0.1, 0.1, 0.1)$ due to $\bar{\varepsilon}_{11}$

than in tension or compression. Consider the micro-architecture with diagonal members of Fig. 4.21 subject to the same shear strain, $\bar{\varepsilon}_{12}$. The stress flow through members 1 and 4 are along the centroidal axes of the members so that they are in tension as a consequence of their orientation in the LUC. Stress flow through members 2 and 3 are compressive and can be visualized by plotting minimum principal stress directions. It is demonstrated that the diagonal members 1, 2, 3 and 4 are suited to resist any of the shear strains, $\bar{\varepsilon}_{ij}$ by virtue of their orientation. The diagonal members are also capable of resisting direct strains as shown by Fig. 4.20, however, the orientation of the diagonal members suggests that they are not as efficient as the face members, since they offer normal resistance to direct strain only in pairs.

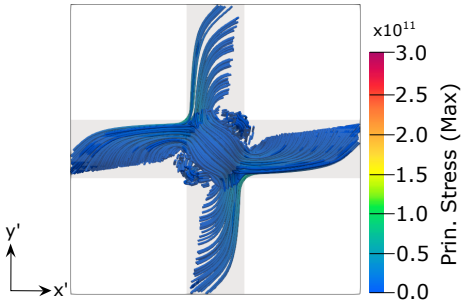
The parameterization scheme of this work seeks to take advantage of the benefits of both face and diagonal members. Figures 4.22 and 4.23 demonstrate that the face members are suited to efficient resistance to direct strain while the diagonal members are better suited



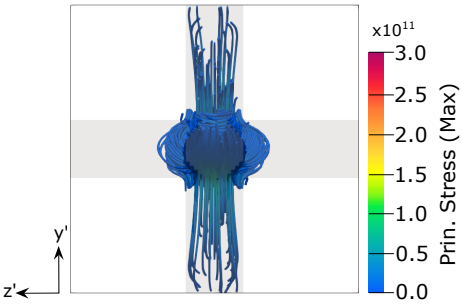
(a) Load path (Perspective view)



(b) Deformed micro-architecture

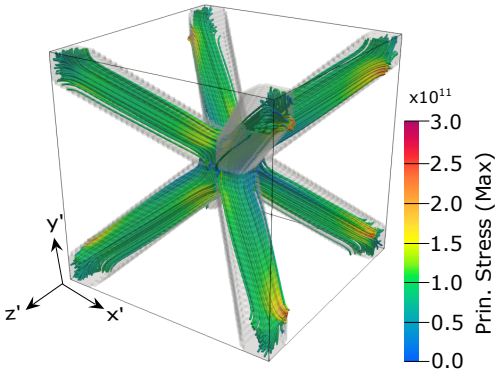


(c) Load path (x-y view)

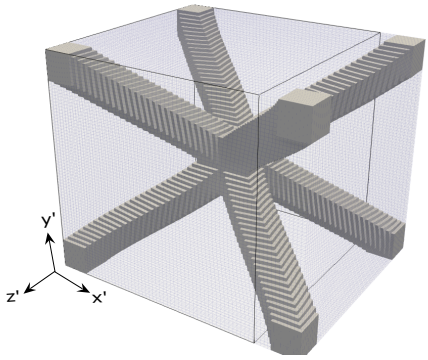


(d) Load path (y-z view)

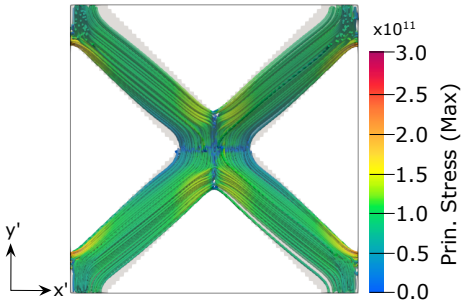
Figure 4.19: Load path through, $\boldsymbol{r} = (0, 0, 0, 0, 0.1, 0.1, 0.1)$ due to $\bar{\varepsilon}_{12}$



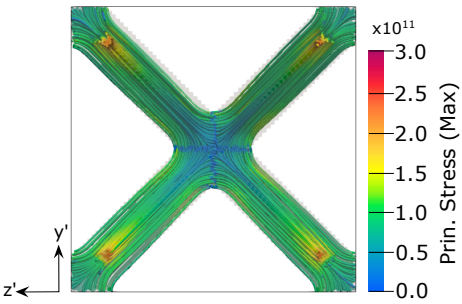
(a) Load path (Perspective view)



(b) Deformed micro-architecture

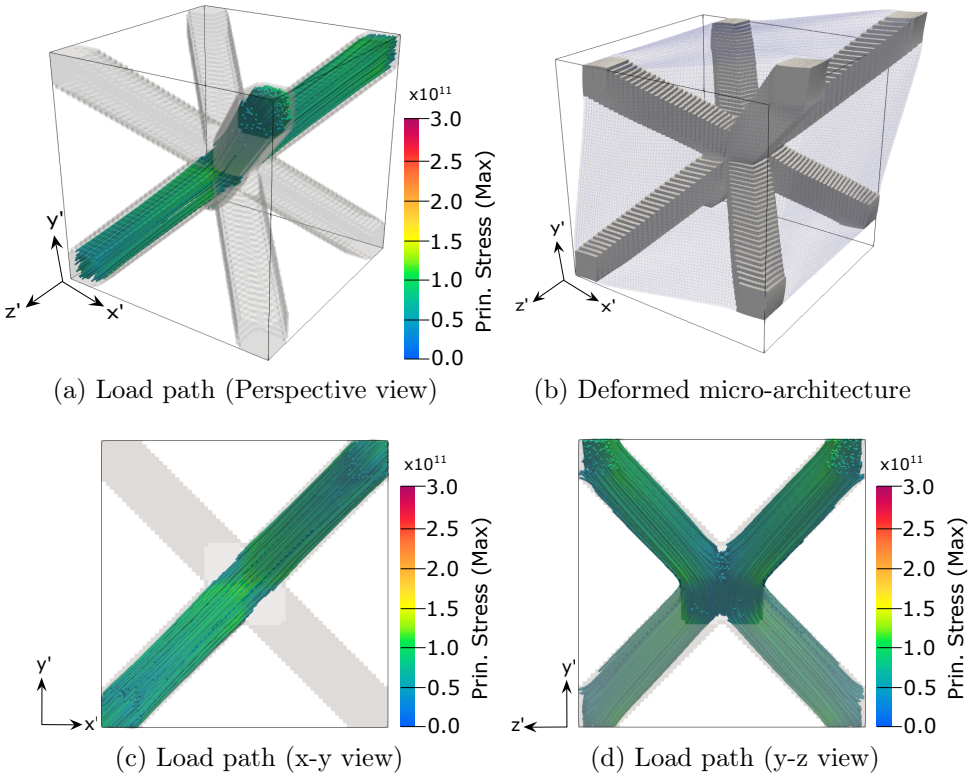


(c) Load path (x-y view)



(d) Load path (y-z view)

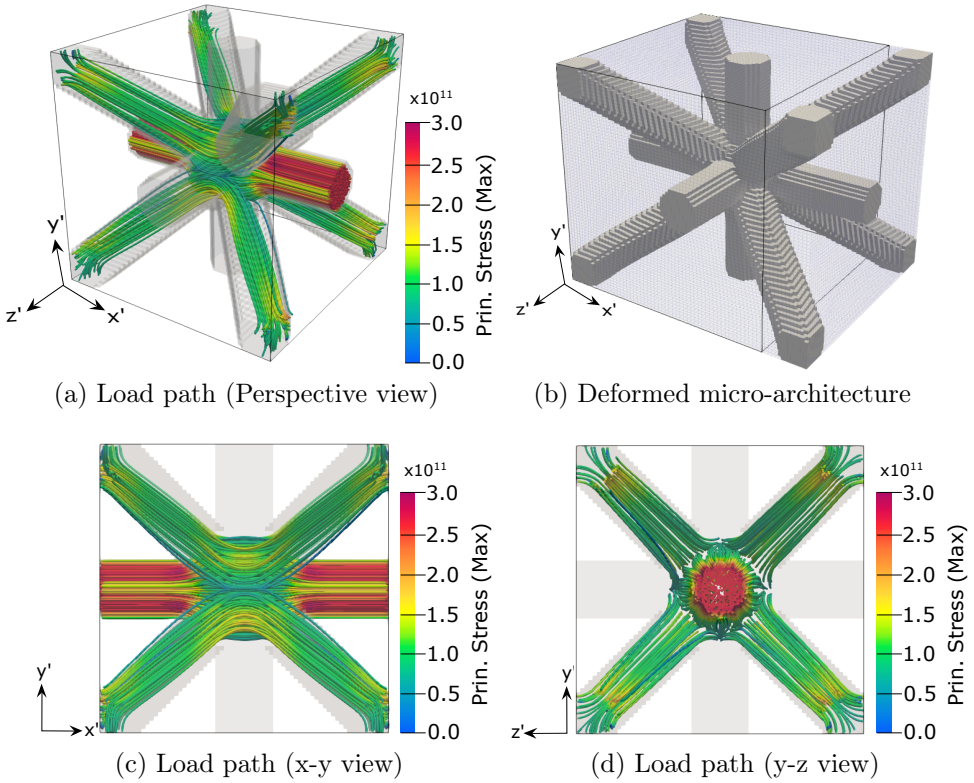
Figure 4.20: Load path through, $\boldsymbol{r} = (0.1, 0.1, 0.1, 0.1, 0, 0, 0)$ due to $\bar{\varepsilon}_{11}$



(a) Load path (Perspective view) (b) Deformed micro-architecture

(c) Load path (x-y view) (d) Load path (y-z view)

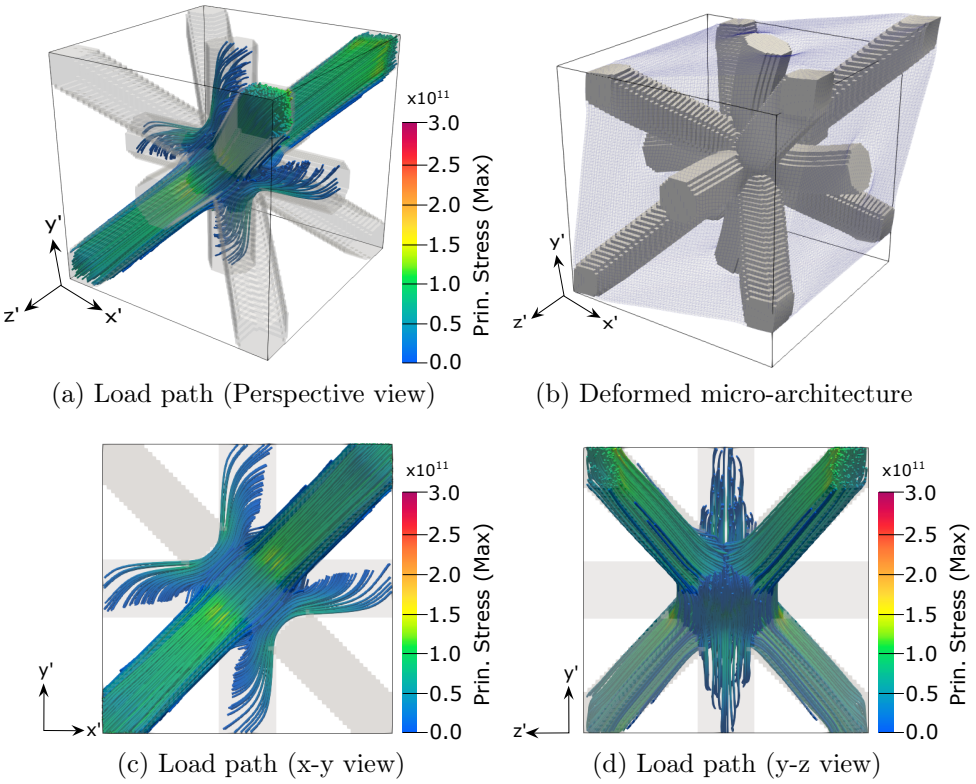
Figure 4.21: Load path through, $\boldsymbol{r} = (0.1, 0.1, 0.1, 0.1, 0, 0, 0)$ due to $\bar{\varepsilon}_{12}$



(a) Load path (Perspective view) (b) Deformed micro-architecture

(c) Load path (x-y view) (d) Load path (y-z view)

Figure 4.22: Load path through, $\boldsymbol{r} = (0.1, 0.1, 0.1, 0.1, 0.1, 0.1, 0.1)$ due to $\bar{\varepsilon}_{11}$



(a) Load path (Perspective view)

(b) Deformed micro-architecture

(c) Load path (x-y view)

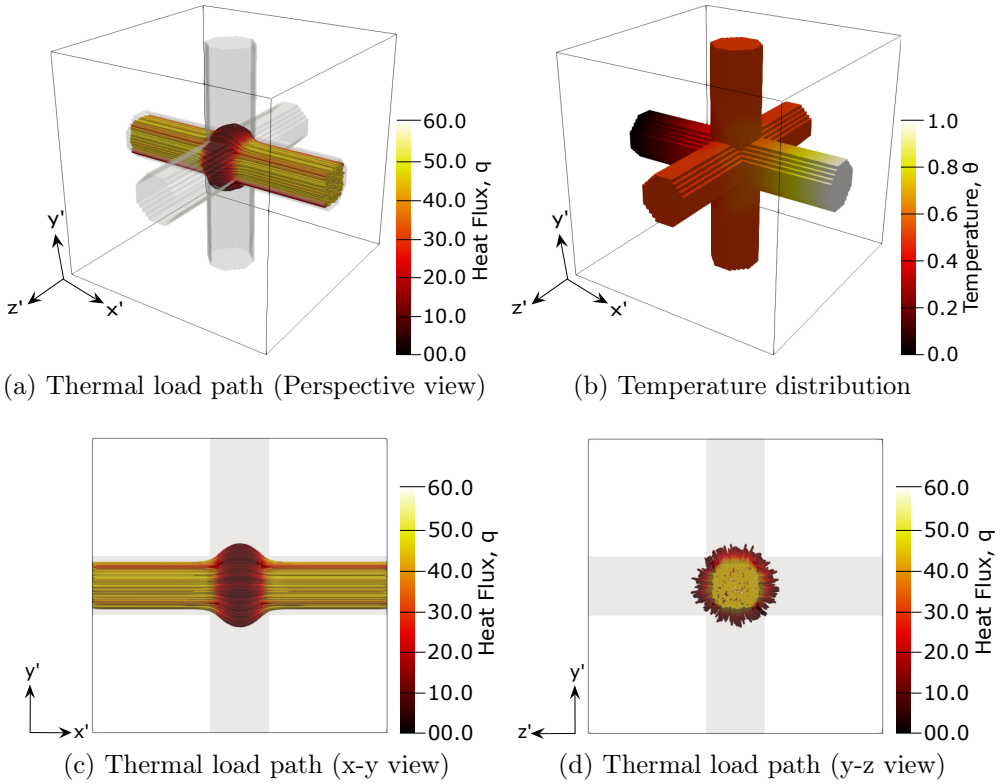
(d) Load path (y-z view)

Figure 4.23: Load path through, $\boldsymbol{r} = (0.1, 0.1, 0.1, 0.1, 0.1, 0.1, 0.1)$ due to $\bar{\varepsilon}_{12}$

to resisting shear strains. It is worth noting that in practice, each micro-architecture encounters combinations of these direct and shear strains. The parameterization employed allows the variations of the radii of the lattice members to yield efficient micro-architectures with the desired mechanical properties.

4.7 Heat Flow Characterization

The suitability of the microscale parameterization implemented was also investigated by evaluating thermal load paths through typical micro-architectures when subjected to temperature gradients. For brevity, considerations were limited to heat flow due to temperature gradient in the x-direction $\nabla\bar{\theta}_1$. Recall that the heat flux vector was determined at every element within the LUC by evaluating Fourier's conduction law as in Eqn. 3.32, from which the magnitude and directions of the heat flow is derived. Figures 4.24 - 4.26 show the magnitude and direction of heat flux through micro-architectures of only face mem-



(a) Thermal load path (Perspective view)

(b) Temperature distribution

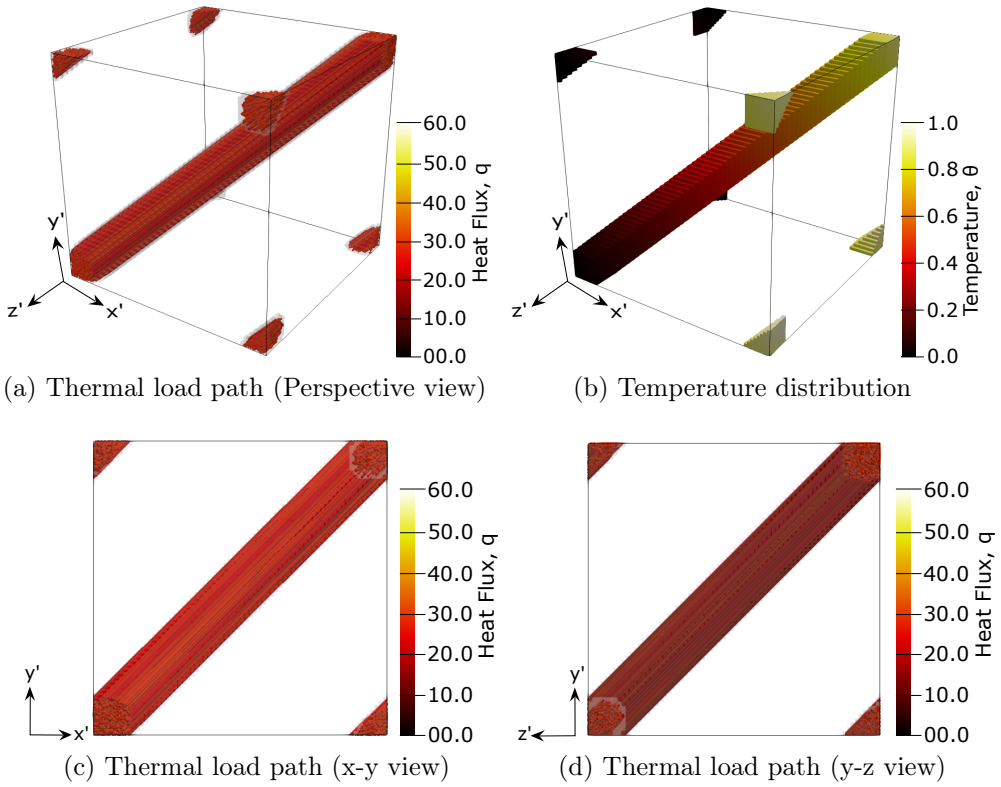
(c) Thermal load path (x-y view)

(d) Thermal load path (y-z view)

Figure 4.24: Thermal load path through, $\boldsymbol{r} = (0, 0, 0, 0, 0.1, 0.1, 0.1)$ due to $\nabla\bar{\theta}_1$

bers, a single diagonal member as well as both diagonal and face members. As in Sec. 4.6, the radii of the members in the figures are kept uniform for emphasis on the orientation of the members rather than member sizes. Figure 4.24 shows a periodic micro-architecture with only face members 5, 6, and 7 subjected to a temperature gradient, $\nabla\bar{\theta}_1$. High magnitude heat flow through Member 5 suggests that it best conducts the heat across the temperature gradient by virtue of its orientation relative to the imposed temperature gradient. As a consequence, the most effective way to make the micro-architecture more conductive is by increasing r_5. Indeed, the face members are best suited to conduct heat in any of the orthonormal directions since their centroidal axes are aligned along these axes.

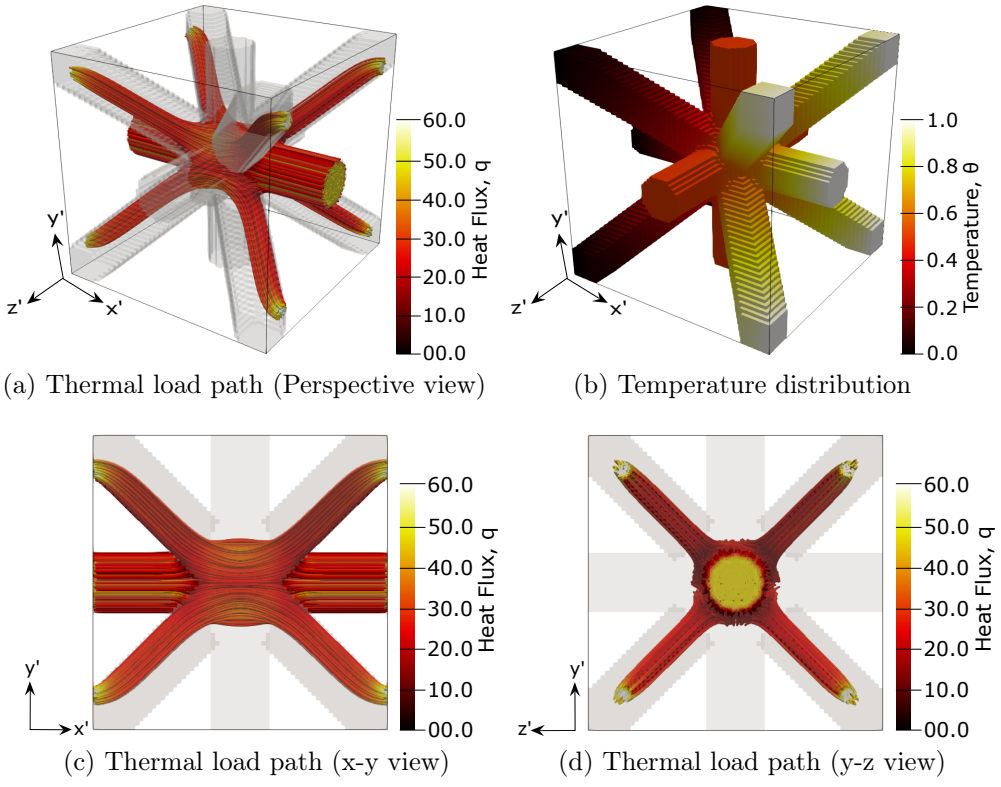
Figure 4.25 shows a periodic micro-architecture with a single diagonal member. It illustrates the conduction of heat across the temperature gradient, though the heat flux magnitude is less than for a face member by virtue of its orientation. However, this



(a) Thermal load path (Perspective view) (b) Temperature distribution

(c) Thermal load path (x-y view) (d) Thermal load path (y-z view)

Figure 4.25: Thermal load path through, $\boldsymbol{r} = (0.1, 0, 0, 0, 0, 0, 0)$ due to $\nabla\bar{\theta}_1$



(a) Thermal load path (Perspective view) (b) Temperature distribution

(c) Thermal load path (x-y view) (d) Thermal load path (y-z view)

Figure 4.26: Thermal load path through, $\boldsymbol{r} = (0.1, 0.1, 0.1, 0.1, 0.1, 0.1, 0.1)$ due to $\nabla\bar{\theta}_1$

orientation of the diagonal member demonstrates that heat conduction in orthonormal directions, different from that along which a temperature gradient is imposed, is possible. The consequence of this is that the conductivity matrix of Eqn. 3.34 has off-diagonal terms. This feature of the microscale parameterization promises interesting capability in macroscale optimization. Finally, the periodic micro-architecture of Figure 4.26 demonstrates that the benefits of face members and diagonal members can be combined to yield micro-architectures with interesting thermal properties. Again, each micro-architecture encounters combinations of these temperature gradients in practice, so that variations of the radii of the lattice members enables the design of efficient micro-architectures with the required thermal properties.

Chapter 5

Material Model Generation

Having developed an efficient parameterization of the small-scale and a means to determine converged structural and thermal properties of the derivable micro-architectures given their vector of radii parameters, a description of the discrete material property space population follows, culminating in the construction of response surface models for the components of the property matrices.

It was identified that the micro-architecture parameterization implemented yielded geometries with recognizable rotation and reflection symmetries. As a consequence, a full factorial design of experiments could be implemented with potentially significant computational savings derived from leveraging the existence of the symmetries. The total number of evaluation points in the space of material properties associated with a full factorial DoE, N_f is given as

$$N_f = n_L^{m_k} \tag{5.1}$$

where n_L is the number of levels of pertubation of the small scale parameters and m_k is the number of degrees of freedom associated with the parameterization (corresponding to the number of components in the vector of radii parameters). In this work, $m_k = 7$ and $n_L = 7$ so that $N_f = 823,543$. Without leveraging the existence of symmetries, the number of required property evaluation points associated with a full factorial DOE will

lead to high computational expense. To take advantage of existing symmetries, recourse was taken to axis and material tensor transformation operations to develop an index of micro-architecture geometries along with their mechanical and thermal properties. This involved the generation of a parent-child micro-architecture classification grid. A 'parent' micro-architecture in this work is defined as a micro-architecture whose unique properties cannot be derived from the properties of apriori simulated micro-architectures but from which other micro-architectures can derive their own properties by rotation or reflection symmetry analyses. These micro-architectures whose material properties do not need to be simulated but are derived from the parent micro-architecture are called 'children'. Details of the construction of the parent-children microstructure grid follow. First, for the sake of completeness, the well-known axis transformation operations are enumerated. Material property tensor transformation operations are then generated from the axis transformation operations. A detailed description of the creation of the micro-structure library is given. The outcome is the generation of 823,543 micro-architecture geometries with their mechanical and thermal property tensors as well as volume fraction at a much lower computational cost compared to that required for a full factorial evaluation.

5.1 Axis transformation operations

Rotation transformation operators about the x, y and z-axes are given as

$$Q_{R_x} = \begin{bmatrix} 1 & 0 & 0 \\ 0 & c & -s \\ 0 & s & c \end{bmatrix}, \quad Q_{R_y} = \begin{bmatrix} c & 0 & s \\ 0 & 1 & 0 \\ -s & 0 & c \end{bmatrix} \text{ and } Q_{R_z} = \begin{bmatrix} c & -s & 0 \\ s & c & 0 \\ 0 & 0 & 1 \end{bmatrix} \tag{5.2}$$

respectively where $c = \cos\theta$ and $s = \sin\theta$. All rotations considered in this work are such that $\theta = 90°$. Reflection transformation operators of the yz, xz and xy planes along the

x, y and z-axes are given as

$$Q_{R_{yz}} = \begin{bmatrix} -1 & 0 & 0 \\ 0 & 1 & 0 \\ 0 & 0 & 1 \end{bmatrix}, \; Q_{R_{xz}} = \begin{bmatrix} 1 & 0 & 0 \\ 0 & -1 & 0 \\ 0 & 0 & 1 \end{bmatrix} \text{ and } Q_{R_{xy}} = \begin{bmatrix} 1 & 0 & 0 \\ 0 & 1 & 0 \\ 0 & 0 & -1 \end{bmatrix} \tag{5.3}$$

5.2 Unit Cell geometry transformation

To derive all possible geometry transformations of the unit cell, the base orientation of Fig. 3.4 is defined for the unit cell and translated such that its center coincides with the origin of the coordinate system, $\mathcal{O}(0, 0, 0)$. A 3×8 matrix of the unit cell vertex coordinates, M_v is defined for the base geometry (See Fig. 5.1). By applying the transformation operators of Eqns. 5.2 and 5.3 in every possible order of execution without repetition to the matrix of vertex coordinates, all achievable unit cell orientations are derived. Mathematically,

$$M_v' = \boldsymbol{Q} \; M_v \tag{5.4}$$

where M_v' is the matrix of vertex coordinates for the transformed geometry and $\boldsymbol{Q}$ is the operator derived from sequentially combined operators. It is important to note that the rotation transformation operations are not commutative. However, reflection transformation operations are commutative. The total number of possible permutations of the transformation operators is determined by

$$N_Q = \sum_{r_Q=1}^{r_Q=n} \frac{n!}{(n - r_Q)!} \tag{5.5}$$

where $n = 6$ is the number of unique transformation operations and r_Q is the number of transformation operations combined ie. executed sequentially on the matrix of vertex coordinates to derive a new geometry transformation. For clarity, when a single operation is executed, $r_Q = 1$, and when two operators are combined, $r_Q = 2$. Forty seven (47) unique geometry transformations of the base orientation are derived. As a consequence,

there are 48 possible geometry transformations associated with a unit cell for $\theta = 90°$, regardless of the enclosed micro-architecture. These 47 unique transformation operations are then applied to the material property tensors of the base orientation of each parent microstructure to determine the unique material transformations associated with a given parent micro-architecture.

5.3 Material Property Transformation

The general 6×6 rotation transformation matrix for the elasticity tensor is given as

$$R_R = \begin{pmatrix} A & B \\ C & D \end{pmatrix} \tag{5.6}$$

where

$$A = \begin{pmatrix} l_1^2 & m_1^2 & n_1^2 \\ l_2^2 & m_2^2 & n_2^2 \\ l_3^2 & m_3^2 & n_3^2 \end{pmatrix} \tag{5.7}$$

,

$$B = \begin{pmatrix} 2m_1n_1 & 2n_1l_1 & 2l_1m_1 \\ 2m_2n_2 & 2n_2l_2 & 2l_2m_2 \\ 2m_3n_3 & 2n_3l_3 & 2l_3m_3 \end{pmatrix} \tag{5.8}$$

,

$$C = \begin{pmatrix} l_2l_3 & m_2m_3 & n_2n_3 \\ l_1l_3 & m_1m_3 & n_1n_3 \\ l_1l_2 & m_1m_2 & n_1n_2 \end{pmatrix} \tag{5.9}$$

and

$$D = \begin{pmatrix} m_2n_3 + m_3n_2 & n_2l_3 + n_3l_2 & m_2l_3 + m_3l_2 \\ m_1n_3 + m_3n_1 & n_1l_3 + n_3l_1 & m_1l_3 + m_3l_1 \\ m_1n_2 + m_2n_1 & n_1l_2 + n_2l_1 & m_1l_2 + m_2l_1 \end{pmatrix} \tag{5.10}$$

for

$$Q_R = \begin{bmatrix} l_1 & m_1 & n_1 \\ l_2 & m_2 & n_2 \\ l_3 & m_3 & n_3 \end{bmatrix} \tag{5.11}$$

where $Q_R = Q_{R_x}$, $Q_R = Q_{R_y}$ and $Q_R = Q_{R_z}$ for rotations about the x, y and z-axes respectively. Rotationally transformed elasticity tensors expressed as stiffness matrices are derived by

$$\boldsymbol{E}'_{ij} = [R_R]\ \boldsymbol{E}_{ij}\ [R_R]^T \tag{5.12}$$

for i, $j = 1, 2, \ldots 6$.

The general reflection transformation matrix for fourth rank tensors such as the elasticity tensor is given as

$$\boldsymbol{E'}_{ijkl} = Q_{im}\ Q_{jn}\ Q_{ko}\ Q_{lp}\ \boldsymbol{E}_{mnop} \tag{5.13}$$

where $Q = Q_{R_{yz}}$, $Q = Q_{R_{xz}}$ and $Q = Q_{R_{xy}}$ for reflections of the yz, xz and xy planes along the x, y and z-axes respectively. Also, i, j, k, l, m, n, o and $p = 1, 2$ and 3 are the indices locating the components of the reflection transformation matrix Q as well as the components of the elasticity tensor, $\boldsymbol{E}$.

The rotation and reflection transformation matrix for the thermal conductivity matrices are given as

$$\boldsymbol{K'}_{ij} = [Q]\ \boldsymbol{K}_{ij}\ [Q]^T \tag{5.14}$$

where $Q = Q_{R_x}$, $Q = Q_{R_y}$ and $Q = Q_{R_z}$ for rotations about the x, y and z-axes respectively and $Q = Q_{R_{yz}}$, $Q = Q_{R_{xz}}$ and $Q = Q_{R_{xy}}$ for reflections of the yz, xz and xy planes along the x, y and z-axes respectively. The derivations of the axis transformation equations are detailed in [124, 125, 126, 127, 128].

By applying the 47 unique axis transformation operations derived in Sec. 5.2 on parent micro-architectures, all possible material transformations were attained. In the most

general case of anisotropy, where the vector of radii parameters of a micro-architecture had 7 unique components, 23 material transformations were derived from the base orientation. Consequently, there are 24 material transformations associated with a fully anisotropic micro-architecture - half the number of unique geometry transformations. There exists an invariance in material behaviour associated with each member within a unit cell when its end vertices' coordinates are interchanged. Hence, the reduction in the total number of material transformations relative to the geometry transformations. The parent micro-architectures of this work yielded varying symmetry properties and hence varying numbers of children micro-architectures, ranging from no children (isotropic micro-architectures) to 23 children (fully anisotropic micro-architectures).

5.4 Property Space Population

To populate the space of material properties, a full-factorial list of micro-architectures was developed by a sequential array of their vector of radii parameters. Each micro-architecture within this array shared the base orientation of Fig. 3.4 and were potential parent micro-architectures, which had to be simulated. In a sequential manner, the elasticity tensor, thermal conductivity matrix and volume fraction, collectively called the property vector, η_p was evaluated as described in Secs. 4.2 and 3.4. Mathematically, each micro-architecture simulation yielded

$$\eta_p = (\boldsymbol{E}, \boldsymbol{K}, v_f)_p \tag{5.15}$$

where $p = 1, 2, ..., N_f$. Next, the 47 unique transformation operators were applied to the unit cell of the simulated parent micro-architecture and the corresponding material transformation operations were applied to the derived elasticity tensor and thermal conductivity matrix. The volume fraction, v_f is invariant to the transformation operations so that all children micro-architectures share the volume fraction of the parent micro-architecture. Finally, the children micro-architectures were eliminated from the full factorial array of

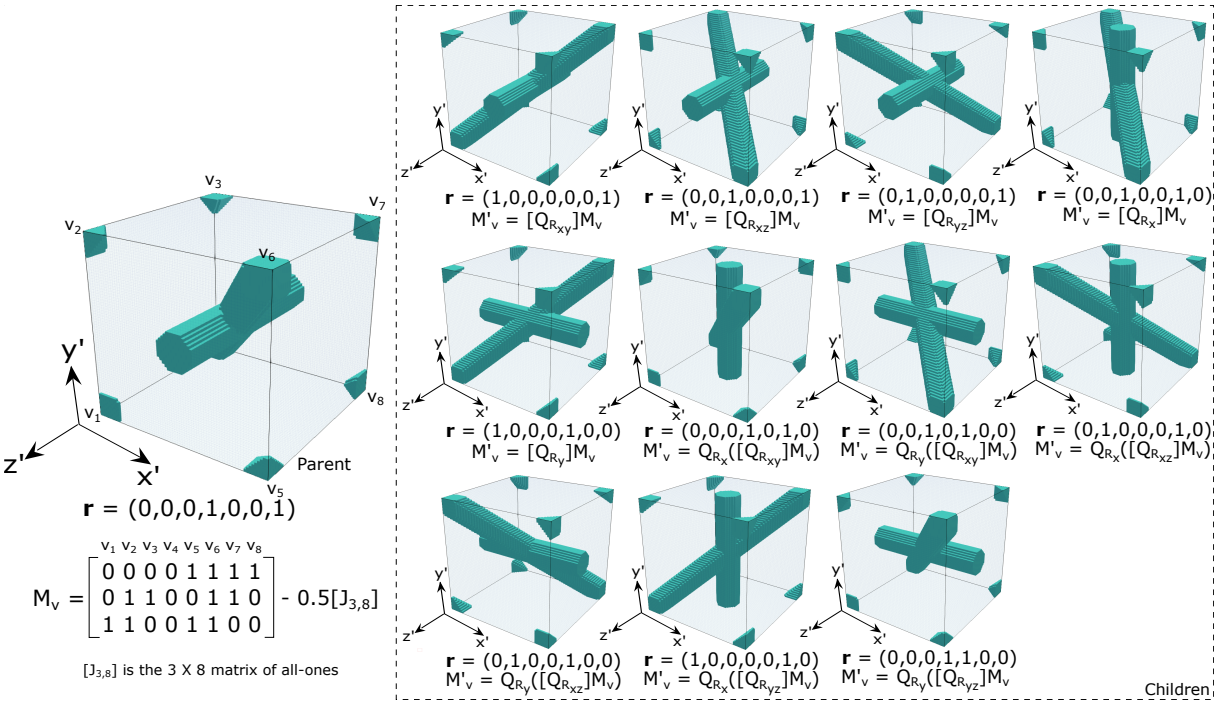


Figure 5.1: Example of symmetry geometries of a parent micro-architecture

micro-architectures to prevent redundant re-simulations. The parent micro-architecture index, p was then incremented until the next unsimulated parent micro-architecture was encountered in the array. Figure 5.1 shows a parent micro-architecture with all of its children. For ease of visualization, a micro-architecture with a single diagonal member and face member has been used for the illustration. Only a single simulation to the determine the property vector of the parent is required for this family of micro-architectures. The population of the material space described above yielded only 40,817 simulations/parents, yet delivering a full factorial micro-architecture property evaluation of 823,543. This constitutes a 95% reduction in required simulations. Figure 5.2 presents the significant reduction in required simulations associated with symmetry considerations when the number of levels by which each component of the vector of radii parameters is perturbed varies from unity to n_L. Properties derived from symmetry considerations were verified by property simulations on a random selection of children micro-architectures.

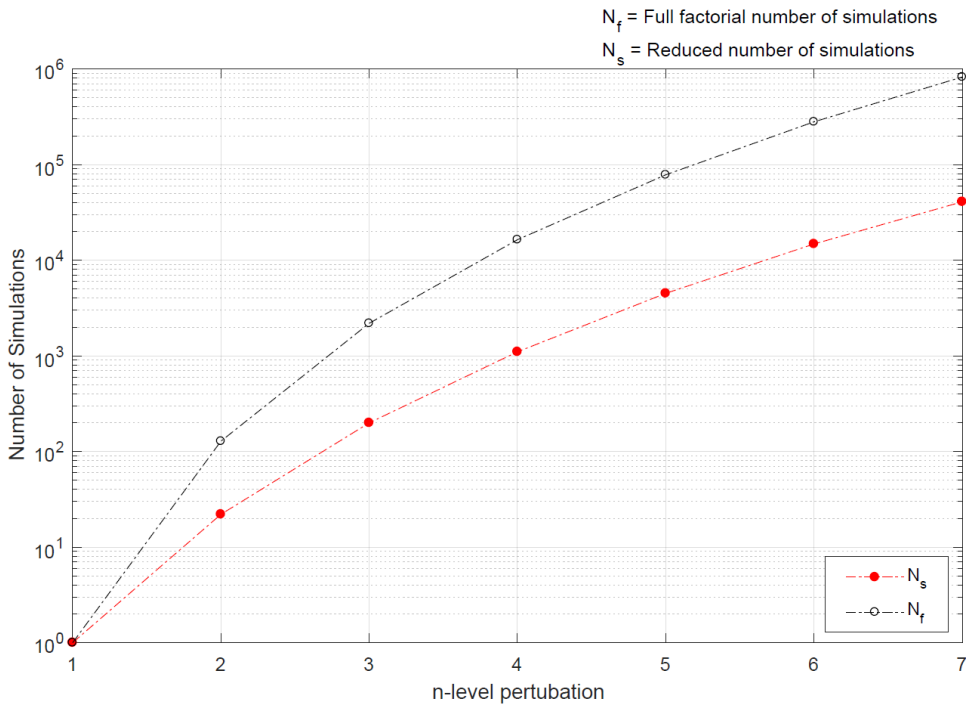
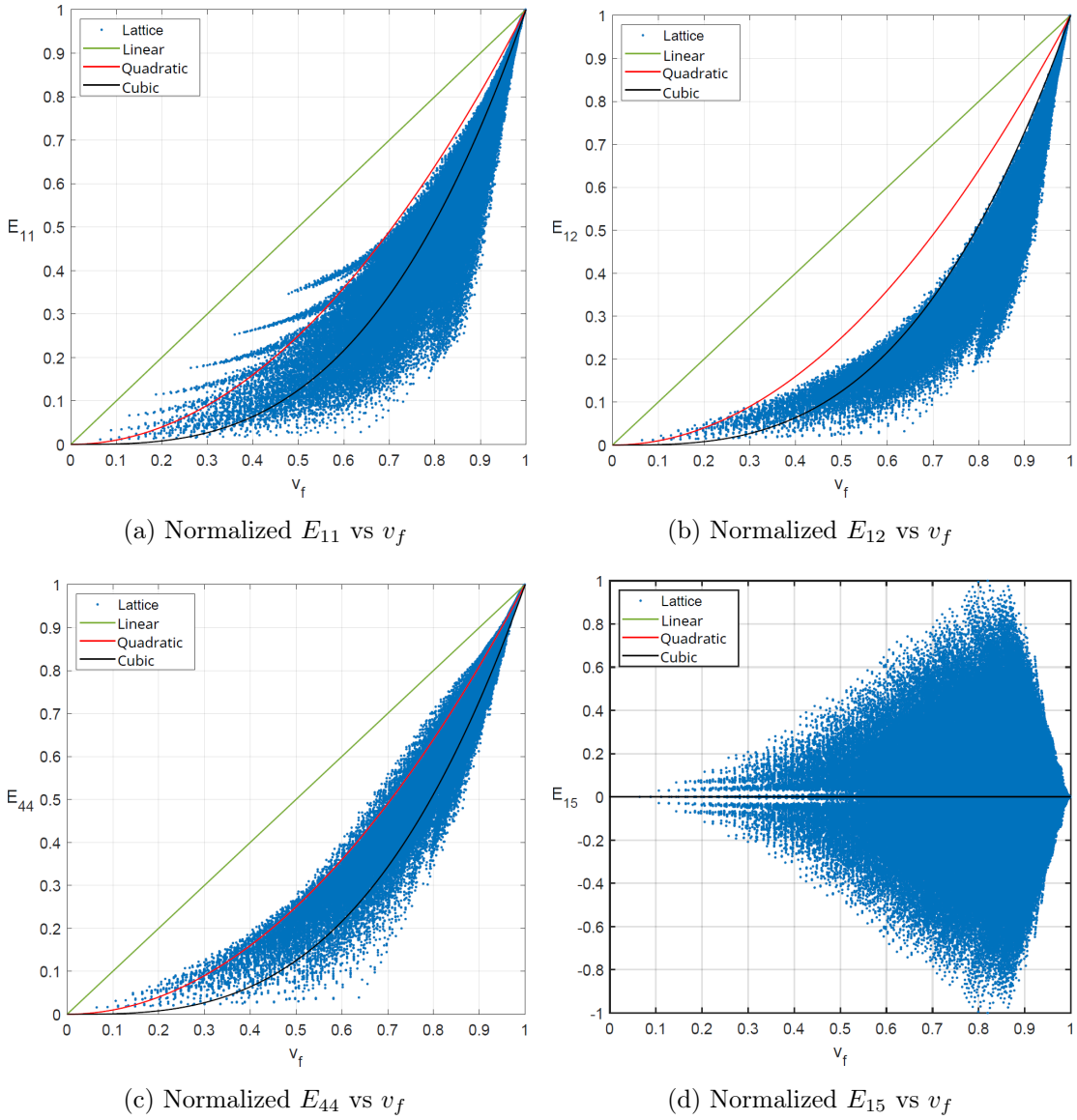


Figure 5.2: Symmetry-driven simulation reduction log-plot (N_f is the full factorial number of simulations and N_s is the reduced number of simulations)

5.5 Property Space Exploration

The property space population of Sec. 5.4 involved the determination of the property vector, η_p, associated with each micro-architecture derived in the full factorial design of experiments. This constitutes discrete property evaluations within a 7-dimensional space – an evaluation of the components of the stiffness and conductivity matrices as well as volume fraction in the space of the vector of radii parameters. It is impossible to visualize the evaluation points within the 7-dimensional space. However, to highlight interesting features of the micro-architecture parameterization implemented, Fig. 5.3 presents projections of the evaluation points for each of the 823,543 micro-architectures on a component-volume fraction plane for stiffness matrix components E_{11}, E_{12}, E_{44} and E_{15}. There are 21 such discrete material property space populations and 6 thermal property space populations corresponding to each of the components of the stiffness and thermal conductivity matrices respectively. To highlight certain features of the property data, each of the plots features superimposed linear, quadratic and cubic stiffness - volume fraction interpolation lines.



(a) Normalized E_{11} vs v_f

(b) Normalized E_{12} vs v_f

(c) Normalized E_{44} vs v_f

(d) Normalized E_{15} vs v_f

Figure 5.3: Property space exploration: Projections of micro-architectures on stiffness matrix component-volume fraction planes

Observe that the lattice micro-architectures feature an inherent penalization of intermediate densities. More precisely, this inherent penalization of the micro-architectures with the highest stiffness to volume fraction ratios offer less penalization but remain physically realizable. For example, micro-architectures located within the finger-like projections of Fig. 5.3a feature high stiffness to volume fraction ratio in the x-direction with a dominant face member 5. These are advantageous for compliance minimization problems. Similar benefits in material interpolation are observed for E_{22} and E_{33} corresponding to dominant members 6 and 7 respectively in the finger-like projections (not shown for brevity). Fig-

ure 5.3b demonstrates that there exists an inherent cubic penalization for $v_f > 0.7$ but a less than cubic for $v_f < 0.7$ for E_{12}. Similar properties were observed for all direct-normal extension coupling terms of the stiffness matrix, E_{13} and E_{23} (not shown for brevity). For shear-shear coupling terms of the stiffness matrix as shown in Fig. 5.3c, the inherent penalization of micro-architectures with the highest stiffness to volume fraction ratios are less than quadratic for all v_f. Finally, the extension-shear coupling terms of the stiffness matrix as shown in Fig. 5.3d exhibit shear capabilities that are not possible with the SIMP material interpolation law since isotropic materials exhibit zero shear-extension capabilities. In general, several micro-architectures exist for any given volume fraction, offering a range of stiffness properties in different directions. The SIMP material interpolation with similar penalization as inherently provided by the lattice parameterization of this work would constitute large regions of meaningless intermediate densities in large-scale optimization. The SIMP material interpolation also features only a single stiffness value for a given volume fraction.

Provided a means is derived to represent the discrete material property evaluations as continuous property interpolation functions, these features could yield important and interesting benefits in gradient-based large-scale optimization. The shear capabilities of the lattice parameterization will also be exploited in large-scale optimization sections of this work.

5.6 Performance against Hashin-Shtrikman Bounds

Hashin et al. [122] presented the bounds for the effective elastic moduli of multiphase materials where the materials may be considered to be composed of a mechanical mixture of isotropic and homogeneous elastic phases. The lower and upper bounds for effective bulk moduli of two phase materials are given as

$$\kappa_l^* = \kappa_1 + \frac{v_{f_2}}{\frac{1}{\kappa_2 - \kappa_1} + \frac{3v_{f_1}}{3\kappa_1 + 4\mu_1}} \tag{5.16}$$

and

$$\kappa_u^* = \kappa_2 + \frac{v_{f_1}}{\frac{1}{\kappa_1 - \kappa_2} + \frac{3v_{f_2}}{3\kappa_2 + 4\mu_2}} \tag{5.17}$$

respectively for $\kappa_2 > \kappa_1$ and $\mu_2 > \mu_1$. The lower and upper bounds for effective shear moduli of two phase materials are given as

$$\mu_l^* = \mu_1 + \frac{v_{f_2}}{\frac{1}{\mu_2 - \mu_1} + \frac{6(\kappa_1 + 2\mu_1)v_{f_1}}{5\mu_1(3\kappa_1 + 4\mu_1)}} \tag{5.18}$$

and

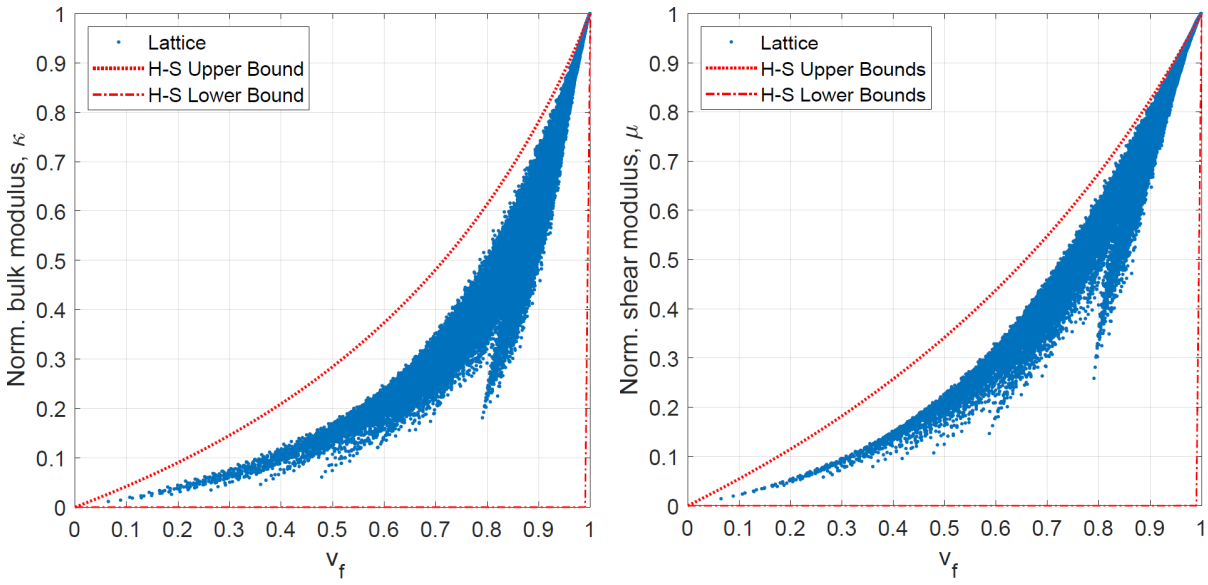
$$\mu_u^* = \mu_2 + \frac{v_{f_1}}{\frac{1}{\mu_1 - \mu_2} + \frac{6(\kappa_2 + 2\mu_2)v_{f_2}}{5\mu_2(3\kappa_2 + 4\mu_2)}} \tag{5.19}$$

respectively for $\kappa_2 > \kappa_1$ and $\mu_2 > \mu_1$. For the LUCs of this work, κ_2 and μ_2 are the bulk and shear moduli of the base material while κ_1 and μ_1 are those for void (reresented as a very weak material). The base material volume fraction, v_{f_2} satisfies the relation

$$v_{f_2} = 1 - v_{f_1} \tag{5.20}$$

where $v_f = v_{f_2}$ is the volume fraction of the LUC. The derivations of Eqns. 5.16 – 5.19 are detailed in [122].

The bulk and shear moduli of a given material given its elasticity matrix components as



(a) Normalized κ vs v_f (b) Normalized μ vs v_f

Figure 5.4: Performance of lattice parameterization against Hashin-Shtrikman Bounds

presented by Hill [123] is given by Eqns. 4.8 and 4.9 used in Sec. 4.4. Figures 5.4a and 5.4b show the bulk and shear moduli Hashin-Shtrikman bounds for the multiphase materials of this work along with the bulk and shear moduli of all 823,543 micro-architectures derived by the parameterization implemented. It was observed that the micro-architecture bulk and shear moduli evaluations satisfied the bound constraints. Hashin et al. [122] demonstrated that these bounds correspond exactly to the bulk and shear moduli of composites comprised of matrix of phase one with spherical inclusions of phase two and vice versa. By virtue of the parameterization implemented, the micro-architectures of intermediate densities of this work are short of attaining the theoritical upper bound of bulk and shear moduli. However, the micro-architectures are fully realizable by additive manufacturing where matrix-inclusion composites (such as perforated composites) are not. This suggests that manufacturing constraints could possibly lower the upper bounds for three-dimensional additively manufacturable structures [121].

5.7 Response Surface Model Generation

The purpose for the development of a small scale parameterization and its evaluation at discrete points to populate the space of material properties is for gradient-driven large scale optimization in the space of the microscale parameters. The material properties must be evaluated by continuous and differentiable functions since sensitivities of the properties must be evaluated with respect to the design variables. In this subsection, the development of response surface models (also called metamodels) is presented. These metamodels are continuous functions of the vector of radii parameters and their development consists of local approximations of the discrete evaluation points of the DoE in a least squares sense by a function, through the minimization of the error functional,

$$D_e = \sum_i \left| \mathcal{P}(\boldsymbol{r_i}) - \boldsymbol{\mathcal{P}_i} \right|^2 \tag{5.21}$$

where $\mathcal{P}(\boldsymbol{r_i})$ belongs to the space of polynomials of a chosen degree and dimension, m_k and $\boldsymbol{\mathcal{P}_i}$ is the material property response at evaluation point i, for $i \in [1...N_f]$. Details of the ordinary least square polynomial formulation is well documented in literature [98]. For completeness, the derived polynomial function, $\mathcal{P}(\boldsymbol{r_i})$, whose coefficients minimize the error of Eqn. 5.21 can be expressed as

$$\mathcal{P}(\boldsymbol{r}) = \boldsymbol{b}(\boldsymbol{r})^\intercal \ \boldsymbol{c}_c \tag{5.22}$$

where $\boldsymbol{b}(\boldsymbol{r})$ is the polynomial basis vector of choice and $\boldsymbol{c}_c$ is the vector of unknown coefficients which is given as

$$\boldsymbol{c}_c = \left[\sum_i \boldsymbol{b}(\boldsymbol{r_i}) \boldsymbol{b}(\boldsymbol{r_i})^\intercal \right]^{-1} \sum_i \boldsymbol{b}(\boldsymbol{r_i}) \boldsymbol{\mathcal{P}_i} \tag{5.23}$$

The number of terms in the polynomial basis vector is given as

$$k = \frac{(n_k + m_k)!}{n_k!\ m_k!} \tag{5.24}$$

where n_k is the degree of the polynomial and m_k is the number of independent variables or degrees of freedom. The general form of the response surface models of this work is given as

$$\mathcal{P}(\boldsymbol{r}) = \sum_{\eta=1}^{k} c_\eta \prod_{\beta=1}^{m_k} r_\beta{}^{\alpha_\beta} \tag{5.25}$$

where c_η is the corresponding coefficient to the η-th term of the polynomial function determined by Eqn. 5.23 and α_β permutates through non-negative integers such that

$$\begin{aligned} &\alpha_\beta \in [0, ..., n_k] \qquad \text{and} \\ &\sum_{\beta=1}^{m} \alpha_\beta \leq n_k \end{aligned} \tag{5.26}$$

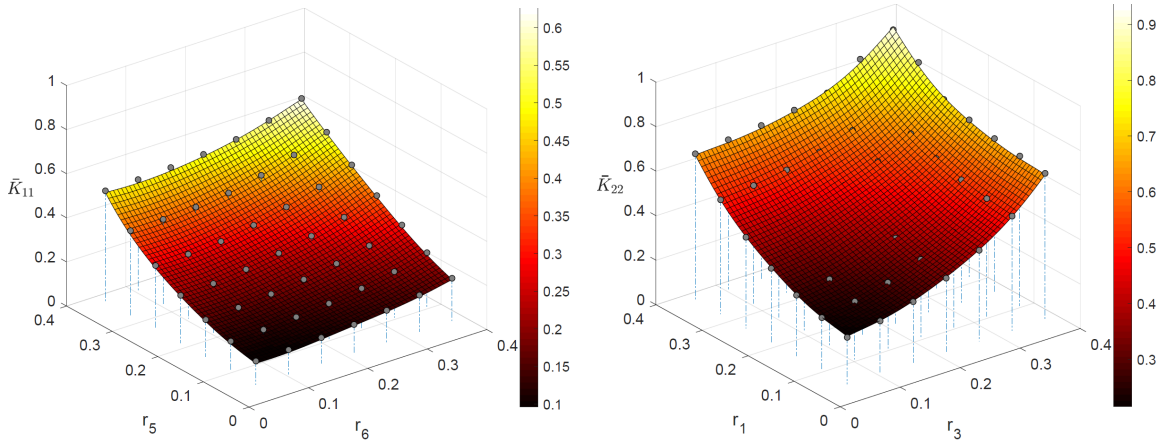
Polynomial metamodels of this work are such that $n_k = 6$ and $m_k = 7$ as polynomial functions of $n_k > 6$ suffered overfitting so that they performed poorly in approximating intermediate points in the parameter space. Figures 5.5 and 5.6 show hyper-planes through typical seven-dimensional metamodels of this work. The stemmed points represent the material point evaluation for the given conductivity/elasticity matrix component. The mesh plots demonstrate the approximation and interpolation capability of the corresponding metamodel constructed as a least square fitting function to the scatter stemmed points. A metamodel was also created for each micro-architecture volume fraction, v_f. These metamodels are differentiable and continuous functions which facilitate the rapid

Property	**Type**	R^2	$RMSE$
K_{11}, K_{22}, K_{33}	–	0.9986	0.0071
K_{12}, K_{13}, K_{23}	–	0.9928	0.0140
E_{11}, E_{22}, E_{33}	Direct/Direct Extension	0.9975	0.0118
E_{12}, E_{13}, E_{23}	Direct/Normal Extension	0.9969	0.0136
E_{15}, E_{16}, E_{24}	Shear/Extension	0.9923	0.0185
E_{26}, E_{34}, E_{35}	Shear/Extension	0.9923	0.0185
E_{14}, E_{25}, E_{36}	Shear/Extension	0.9934	0.0172
E_{44}, E_{55}, E_{66}	Shear/Shear	0.9987	0.0080
E_{45}, E_{46}, E_{56}	Shear/Shear	0.9938	0.0128
V_f	–	0.9991	0.0021

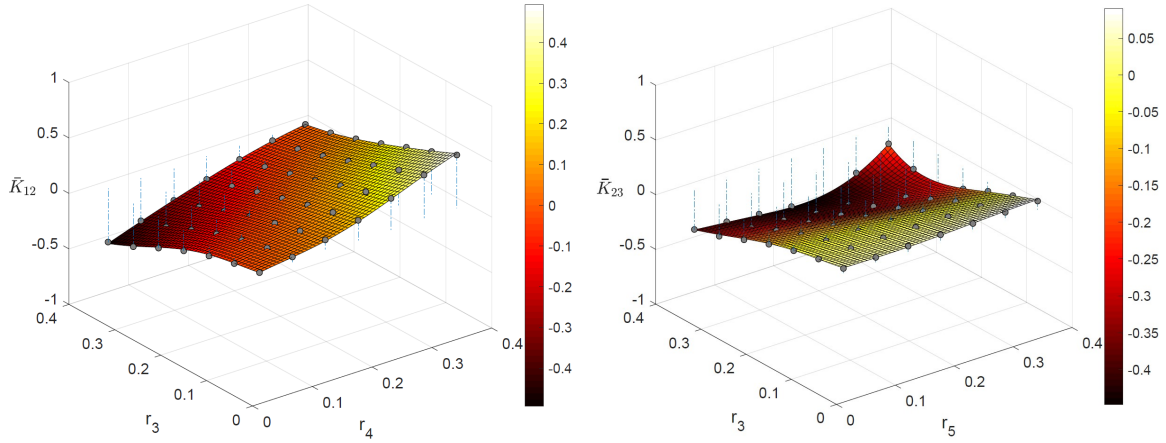
Table 5.1: Table of R^2-values and RMSEs for 6th-order polynomial metamodels

evaluation of local material properties and volume fraction given the vector of radii parameters. They are therefore suited to gradient-based optimization.

Table 5.1 shows the coefficients of determination (R^2 values) and Root Mean Square Errors (RMSEs) associated with the constructed metamodels.

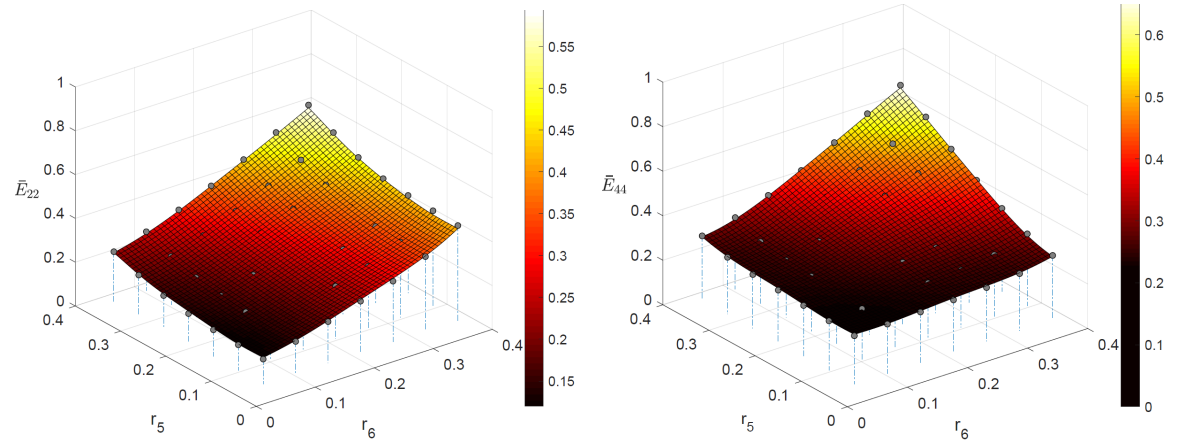


(a) $\bar{K}_{11}$ vs (r_5, r_6), $r_1 = r_2 = r_3 = r_4 = r_7 = 0.105$ (b) $\bar{K}_{22}$ vs (r_1, r_3), $r_1 = r_2 = r_3 = r_4 = r_7 = 0.105$

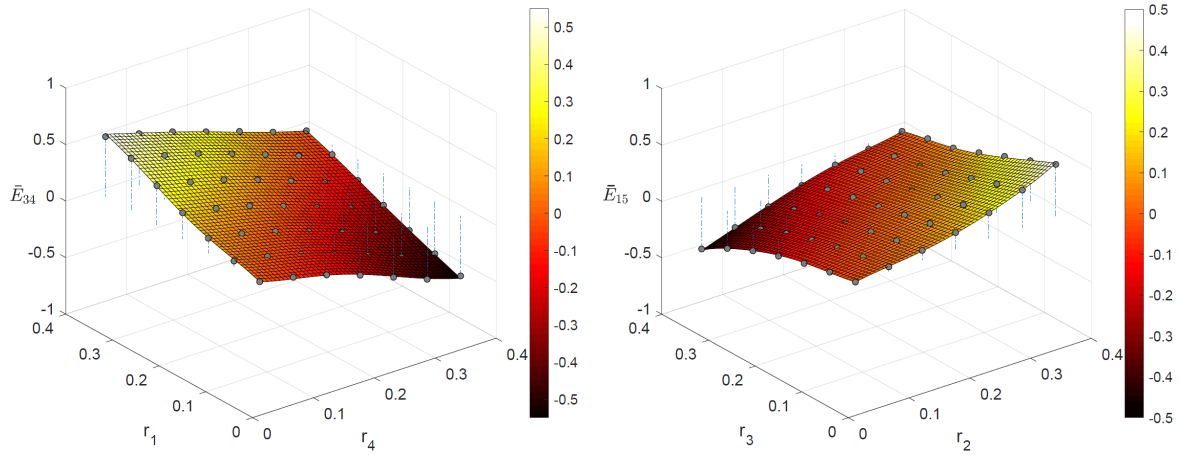


(c) $\bar{K}_{12}$ vs (r_3, r_4), $r_1 = r_2 = r_5 = r_6 = r_7 = 0.105$ (d) $\bar{K}_{23}$ vs (r_3, r_5), $r_1 = r_2 = r_4 = r_6 = r_7 = 0.105$

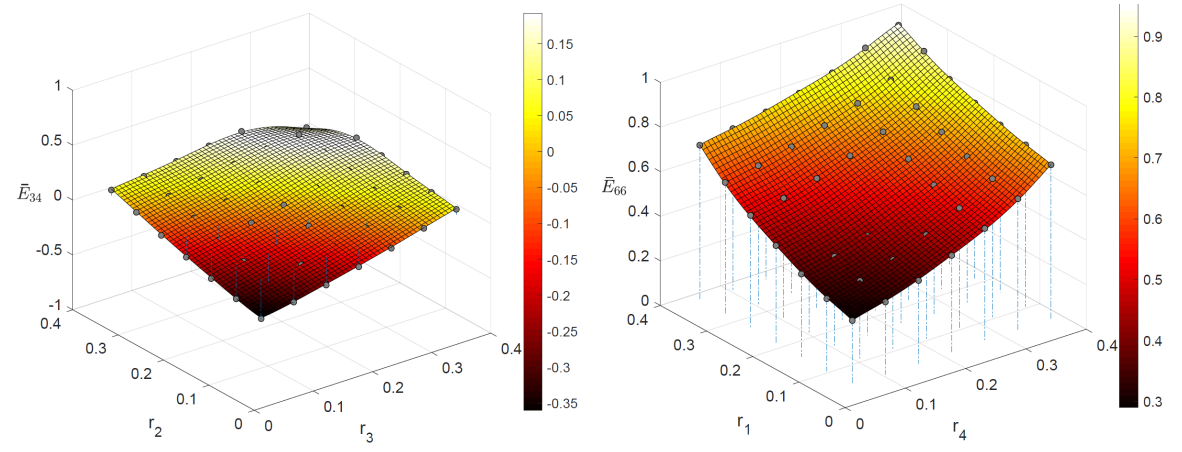
Figure 5.5: Hyper-planes through typical seven-dimensional K_{xx} metamodels.



(a) $\bar{E}_{22}$ vs (r_5, r_6), $r_1 = r_2 = r_3 = r_4 = r_7 = 0.105$ (b) $\bar{E}_{44}$ vs (r_5, r_6), $r_1 = r_2 = r_3 = r_4 = r_7 = 0.16$



(c) $\bar{E}_{34}$ vs (r_1, r_4), $r_2 = r_3 = r_5 = r_6 = r_7 = 0.105$ (d) $\bar{E}_{15}$ vs (r_3, r_2), $r_1 = r_4 = r_5 = r_6 = r_7 = 0.105$



(e) $\bar{E}_{34}$ vs (r_2, r_3), $r_1 = r_4 = r_5 = r_6 = r_7 = 0.105$ (f) $\bar{E}_{66}$ vs (r_1, r_4), $r_2 = r_3 = r_5 = r_6 = r_7 = 0.16$

Figure 5.6: Hyper-planes through typical seven-dimensional E_{xx} metamodels.

Chapter 6

Macroscale Problem Formulation

In this chapter, the mathematical formulations for macroscale optimization is presented. Key theoretical assumptions are stated and the response surface models of Chapter 5 are integrated into variational formulations for the classes of problems treated in this work. It concludes with a description of the numerical implementation of the macroscale optimization algorithm.

6.1 Optimization Phase Overview

The optimization phase consists of macroscale optimization formulation in the space of the microscale parameters enabled by the meta-models generated in the preceding sections. This is the core optimization framework, converting an initial structural layout to its optimized design. Equipped with explicit expressions of large-scale (homogenized) properties as functions of the small-scale lattice parameters, functional grading of the material of structures is formulated in the space of the precomputed material properties. The design domain is defined and discretized into finite elements. In contrast to the SIMP approach, where each cell of the discretized domain is assigned an artificial density function as a measure of local stiffness to derive the optimal distribution of material, this

framework leverages the continuous functions of material property evaluation derived in the pre-computation phase. As a consequence, local properties are controlled at the scale of the lattice micro-architectures by controlling the value of the components of the vector of lattice parameters, $\boldsymbol{r}$ within each cell.

6.2 Assumptions

The pure structural and pure thermal assumptions of Sec. 3.1 also apply to the macroscale analyses. In addition, for thermo-elastic formulations, Eqn. 3.1 becomes

$$\boldsymbol{\sigma^T}_{ij} = \boldsymbol{E}_{ijkl}\ \boldsymbol{\varepsilon}_{kl} + \boldsymbol{\beta}_{ij}\ \boldsymbol{\theta} \tag{6.1}$$

so that the total Cauchy stress tensor, $\boldsymbol{\sigma^T}_{ij}$ comprises a linear combination of mechanical strain-induced and thermal strain-induced stresses. The symmetric thermo-elasticity tensor, $\boldsymbol{\beta}_{ij}$, for thermally-induced stresses across a temperature difference, $\boldsymbol{\theta}$ is given as

$$\boldsymbol{\sigma'}_{ij} = \boldsymbol{\beta}_{ij}\ \boldsymbol{\theta} \tag{6.2}$$

6.3 Mathematical Formulation

Consider the domain of an externally loaded and constrained initial structure discretized into N_e elements and with N_n nodes. The scale of this structural component defines the macroscale. Recall that an assumption upon which the theoretical concepts of homogenization rely is that there is sufficient separation between the macroscale and the scale of the micro-architectures (Eqn. 3.10). The class of optimization problems which the derived optimization framework solves refer to those constrained by physical phenomena represented by Partial Differential Equations (PDEs). As a consequence, the general formulation

of the optimization problems is given as

$$\begin{aligned} \text{minimize:} \quad & J\big(\boldsymbol{u}(\boldsymbol{r}_\gamma), \boldsymbol{r}_\gamma\big) \\ \text{subject to:} \quad & F(\boldsymbol{u}(\boldsymbol{r}_\gamma), \boldsymbol{r}_\gamma) = 0 \\ & \int_\Omega V(\boldsymbol{r}_\gamma)\ d\Omega \leq V_D \\ & r_{min} \leq r_{i\gamma} \leq r_{max} \\ & \rho_{min} \leq \rho_\gamma \leq \rho_{max} \end{aligned} \tag{6.3}$$

for $\gamma = 1,\ 2,\ ...N_n$ and $i = 1,\ 2,\ ...m$ where

$$\boldsymbol{r}_\gamma = [r_{1\gamma}, r_{2\gamma}, r_{3\gamma}, r_{4\gamma}, r_{5\gamma}, r_{6\gamma}, r_{7\gamma}, \rho_\gamma]^\intercal \tag{6.4}$$

is the stacked vector of control variables with length $8N_n$. The real-valued objective functional, J depends on the solution, $\boldsymbol{u}$, of a PDE that defines the physics of the problem. It also depends on the stacked vector of control variables, $\boldsymbol{r}_\gamma$. The solution to the PDE must also satisfy a prescribed equilibrium constraint, $F = 0$. There is an optional cost constraint that controls the overall volume fraction of the optimized structure as shown in Eqn. 6.3 for which the volume fraction meta-model is evaluated at each node as

$$V(\boldsymbol{r}_\gamma) = \rho_\gamma V(r_{1\gamma}, r_{2\gamma}, r_{3\gamma}, r_{4\gamma}, r_{5\gamma}, r_{6\gamma}, r_{7\gamma}) \tag{6.5}$$

A pseudo-lattice-density variable, ρ_γ is introduced in the formulation as shown in Eqns. 6.3 – 6.5. Penalizing this variable in a SIMP-like manner discourages intermediate values of the variable so that it defines a layout of lattice or no-lattice regions in the optimal solution. Finally, there exist bound constraints on the components of the stacked vector of control variables as shown in Eqn. 6.3. The lower bound is set based on a limiting computational ability to determine true material behaviour with decreasing member radii at the chosen mesh discretization. The lower bound must also satisfy manufacturing constraints as there are limitations to the smallest permissible thickness associated with every base

material. Below a specific length scale for a given homogeneous base material, the material properties deviate from documented structural behaviour [129, 130]. The upper bound is set by the highest level of perturbation of the lattice parameters for the micro-architecture to attain the properties of a fully dense block. The bounds of the pseudo-lattice-density variable $\rho_{min} = 0$ and $\rho_{max} = 1$ define the regions of no lattice micro-architecture and lattice-micro-architecture respectively since the variable is penalized to discourage intermediate values. The optimization framework as defined was applied to pure structural problems, pure thermal problems and thermo-structural problems. For each problem-type, the robustness of the derived framework is demonstrated by solving common optimization problems of structural and thermal compliance minimization subject to limited material availability, as well as target deformation inspired by mechanical loads. The numerical implementation of the derived framework to these classes of optimization problems are described below.

6.3.1 Structural Optimization

Static equilibrium mechanics of Sec. 3.1 as shown in Eqn. 3.4 can be expressed in its variational form as

$$\int_{\Omega} \boldsymbol{\sigma}(\boldsymbol{u}, \boldsymbol{r}_{\gamma}) : \boldsymbol{\varepsilon}(v)\ d\Omega - \int_{\Omega} \boldsymbol{f} \cdot v\ d\Omega - \int_{\Gamma} \boldsymbol{T} \cdot v\ d\Gamma = 0 \quad \forall v \in \mathcal{V} \tag{6.6}$$

where the stress tensor is given as

$$\boldsymbol{\sigma}(\boldsymbol{u}, \boldsymbol{r}_{\gamma}) = \boldsymbol{E}(\boldsymbol{r}_{\gamma}) \cdot \boldsymbol{\varepsilon}(\boldsymbol{u}) \tag{6.7}$$

for which $\boldsymbol{E}(\boldsymbol{r}_{\gamma}) = \rho_{\gamma}^{p} \boldsymbol{K}(r_{1\gamma}, r_{2\gamma}, r_{3\gamma}, r_{4\gamma}, r_{5\gamma}, r_{6\gamma}, r_{7\gamma})$ is constructed from the meta-models generated in Sec. 5.7 with a penalization parameter, p on the pseudo-lattice-density variable that defines the macroscale lattice density distribution. A test function, v is defined

that belongs to the space of all admissible displacement functions $\mathcal{V}$, $\boldsymbol{f}$ represents the sum of all internal forces acting within the domain of the structure, Ω such as body weight, $\boldsymbol{T}$ represents the sum of all external traction forces acting on the boundary of the domain, Γ and $\boldsymbol{u}$ is the solution to the PDE satisfying the static equilibrium constraint.
For compliance minimization problems, the objective functional for structural problems is given as

$$J_{uc}\big(\boldsymbol{u}(\boldsymbol{r}_\gamma), \boldsymbol{r}_\gamma\big) = \int_\Omega \boldsymbol{f} \cdot \boldsymbol{u} \; d\Omega + \int_\Gamma \boldsymbol{T} \cdot \boldsymbol{u} \; d\Gamma \tag{6.8}$$

For target deformation problems, the objective functional is given as

$$J_{ud}\big(\boldsymbol{u}(\boldsymbol{r}_\gamma), \boldsymbol{r}_\gamma\big) = \int_\Gamma ||\boldsymbol{u} - \boldsymbol{u_D}||^2 \; d\Gamma \tag{6.9}$$

where $\boldsymbol{u_D}$ is a prescribed target displacement function.

6.3.2 Thermal Optimization

According to the steady state pure conduction assumptions stated in Sec. 3.1, the heat equation can be expressed in its variational form as

$$\int_\Omega \boldsymbol{q}(\theta, \boldsymbol{r}_\gamma) : \nabla w \; d\Omega - \int_\Omega \boldsymbol{f_\theta} \cdot w \; d\Omega - \int_\Gamma \boldsymbol{T_\theta} \cdot w \; d\Gamma = 0 \quad \forall w \in \mathcal{W} \tag{6.10}$$

where the heat flux is given as

$$\boldsymbol{q}(\theta, \boldsymbol{r}_\gamma) = -\boldsymbol{K}(\boldsymbol{r}_\gamma) \cdot \nabla\theta \tag{6.11}$$

for which $\boldsymbol{K}(\boldsymbol{r}_\gamma) = \rho_\gamma^p \boldsymbol{K}(r_{1\gamma}, r_{2\gamma}, r_{3\gamma}, r_{4\gamma}, r_{5\gamma}, r_{6\gamma}, r_{7\gamma})$ is constructed from the meta-models generated in Sec. 5.7 with a penalization parameter, p on the pseudo-lattice-density variable that defines the macroscale lattice density distribution. A test function, w is defined that belongs to the space of all admissible temperature functions $\mathcal{W}$, $\boldsymbol{f_\theta}$ represents the sum of all internal heat sources per unit volume of the domain of the structure, Ω, $\boldsymbol{T_\theta}$ rep-

resents the sum of all external heat sources per unit area of the boundary of the domain, Γ and θ is the solution to the PDE satisfying the steady state constraint. For thermal compliance (average temperature) minimization problems, the objective functional for pure thermal conduction problems of this work is given as

$$J_{\theta c}\big(\theta(\boldsymbol{r}_\gamma), \boldsymbol{r}_\gamma\big) = \int_\Omega \boldsymbol{f_\theta} \cdot \theta \; d\Omega + \int_\Gamma \boldsymbol{T_\theta} \cdot \theta \; d\Gamma \tag{6.12}$$

6.3.3 Thermo-structural Optimization

Based on the assumptions of linear elastic static equilibrium and steady state pure conduction as presented in Sec. 3.1, the variational form of a weakly coupled thermo-structural strong form equation for this work is given as

$$\begin{aligned} &\int_\Omega \boldsymbol{\sigma}^{\boldsymbol{T}}(\boldsymbol{u}, \theta, \boldsymbol{r}_\gamma) : \boldsymbol{\varepsilon}(v) \; d\Omega + \int_\Omega \boldsymbol{q}(\theta, \boldsymbol{r}_\gamma) : \nabla w \; d\Omega \\ -\int_\Omega \boldsymbol{f} \cdot v \; d\Omega - \int_\Gamma \boldsymbol{T} \cdot v \; d\Gamma - \int_\Omega \boldsymbol{f_\theta} \cdot w \; d\Omega - \int_\Gamma \boldsymbol{T_\theta} \cdot w \; d\Gamma &= 0 \\ &\forall v \in \mathcal{V}, \; \forall w \in \mathcal{W} \end{aligned} \tag{6.13}$$

where $\boldsymbol{\sigma_T}$ is the total stress induced by mechanical and thermal strains as in Eqn. 6.1 and with all other symbols remaining as denoted in Secs. 6.3.1 and 6.3.2. The formulation is referred to as weakly coupled because the temperature field is decoupled from the displacement field, however, the mechanical response depends on the temperature field due to the presence of thermal strains in the thermo-elastic constitutive relation as shown in Eqn. 6.1. The objective functional for thermo-structural problems of this work is given as

$$J_{\boldsymbol{u}\theta d}\big(\boldsymbol{u}(\theta(\boldsymbol{r}_\gamma)), \boldsymbol{r}_\gamma\big) = \int_\Gamma ||\boldsymbol{u} - \boldsymbol{u_D}||^2 \; d\Gamma \tag{6.14}$$

6.4 Filtering of Control Variables

The direct implementation of the derived framework using low-order finite element discretization is subject to checker-boarding. It also yields mesh-dependent optimal solutions. Checker-boarding can be minimized by regularization or the use of higher-order finite elements with concomitant increase in computational cost. To eliminate checker-boarded solutions and to ensure mesh-independent optimal results, this work features the filtering of the stacked vector of radii parameters using a Helmholtz-type filter as described by Lazarov et. al [36]. The aim of this filtering technique is to define the control variables at a particular node as a function of the variable field within a support neighbourhood defined by a filter radius. The filter is defined implicitly as a solution to the Helmholtz PDE in its strong form as

$$-z^2\nabla^2\tilde{\boldsymbol{r}}_\gamma + \tilde{\boldsymbol{r}}_\gamma = \boldsymbol{r}_\gamma \tag{6.15}$$

where $\boldsymbol{r}_\gamma$ is the unfiltered stacked vector of radii parameters, $\tilde{\boldsymbol{r}}_\gamma$ is the filtered stacked vector of radii parameters and z is the filter radius. Homogeneous Neumann boundary conditions are applied to the boundary of the domain of the structure so that

$$\frac{\partial\tilde{\boldsymbol{r}}}{\partial\boldsymbol{n}} = 0 \tag{6.16}$$

where $\boldsymbol{n}$ is the unit normal vector. The weak form of Eqn. 6.15 is given as

$$\int_\Omega z^2\nabla\tilde{\boldsymbol{r}}_\gamma\cdot\nabla s\ d\Omega + \int_\Omega \tilde{\boldsymbol{r}}_\gamma\cdot s\ d\Omega - \int_\Omega \boldsymbol{r}_\gamma\cdot s\ d\Omega = 0 \quad \forall s\in\mathcal{S} \tag{6.17}$$

where $\mathcal{S}$ is the space of all admissible control test functions, s. It should be noted that considerations must be made for design variable filtering in order to maintain the correct evaluations of the volume constraint given by Eqn. 6.3 where

$$V = V(\tilde{\boldsymbol{r}}) \tag{6.18}$$

gives the local volume fraction of filtered variables. The sensitivity of the volume fraction to the stacked vector of radii parameters as well as the sensitivity of the objective functionals of this work make considerations for the implementation of variable filtering as will be clearly demonstrated in Sec. 6.5.

6.5 Sensitivity Analyses

The computational cost of evaluating the PDEs of this work motivated the implementation of a gradient-based optimization approach. It followed that the sensitivities of the objective functional to the stacked vector of control parameters, $\frac{dJ}{d\boldsymbol{r}_{\boldsymbol{\gamma}}}$ had to be determined in addition to the value of the objective functional, J so that gradient information could be implemented in the search direction computations. In presenting the details of the derivations of the relevant sensitivities, it is assumed that all derivatives exist and are sufficiently smooth.

Consider the objective functional of the general problem formulation of Eqn. 6.3. Let M denote the dimension of the solution space and $L = 8N_n$ denote the dimension of the parameter space. The objective functional can be written as

$$J\big(\boldsymbol{u}(\mathcal{P}(\tilde{\boldsymbol{r}}_\gamma)), \mathcal{P}(\tilde{\boldsymbol{r}}_\gamma)\big) \tag{6.19}$$

since the solution of the PDE is dependent on the material properties controlled by the stacked vector of control parameters. Recall that the meta-models generated in Sec. 5.7 are explicit expressions of material property (structural and thermal) as functions of the stacked vector of control variables so that

$$\mathcal{P}(\tilde{\boldsymbol{r}}_\gamma) = \begin{cases} E_{ij}(\tilde{\boldsymbol{r}}_\gamma), & \text{if elasticity matrix component} \\ K_{pq}(\tilde{\boldsymbol{r}}_\gamma), & \text{if conductivity matrix component} \end{cases} \tag{6.20}$$

where i, j =1, 2, ...6 and p, q =1, 2 and 3. The sensitivities of J are given as

$$\frac{dJ}{d\boldsymbol{r}_\gamma} = \frac{dJ}{d\mathcal{P}} \frac{d\mathcal{P}}{d\tilde{\boldsymbol{r}}_\gamma} \frac{d\tilde{\boldsymbol{r}}_{\boldsymbol{\gamma}}}{d\boldsymbol{r}_\gamma} \tag{6.21}$$

Expanding $\dfrac{dJ}{d\mathcal{P}}$ gives

$$\underbrace{\frac{dJ}{d\boldsymbol{r}_\gamma}}_{1\times L} = \left(\underbrace{\frac{\partial J}{\partial \boldsymbol{u}}}_{1\times M} \underbrace{\frac{d\boldsymbol{u}}{d\mathcal{P}}}_{M\times M} + \underbrace{\frac{\partial J}{\partial \mathcal{P}}}_{1\times M} \right) \underbrace{\frac{d\mathcal{P}}{d\tilde{\boldsymbol{r}}_\gamma}}_{M\times L} \underbrace{\frac{d\tilde{\boldsymbol{r}}_\gamma}{d\boldsymbol{r}_\gamma}}_{L\times L} \tag{6.22}$$

The derivative, $\dfrac{du}{d\mathcal{P}}$ is difficult to attain since the PDE solution is an implicit function of the material property. It would require solving an $M \times M$ linear system for each component of $\boldsymbol{r}_\gamma$. To circumvent the exorbitant computational cost associated with the sensitivity computation of Eqn 6.22, the discrete adjoint method is employed. From Eqn. 6.3, the equilibrium constraint is written as

$$F(\boldsymbol{u}(\mathcal{P}), \mathcal{P}) = 0 \tag{6.23}$$

so that

$$\underbrace{\frac{dF}{d\mathcal{P}}}_{M\times M} = \underbrace{\frac{\partial F}{\partial \boldsymbol{u}}}_{M\times M} \underbrace{\frac{d\boldsymbol{u}}{d\mathcal{P}}}_{M\times M} + \underbrace{\frac{\partial F}{\partial \mathcal{P}}}_{M\times M} = 0 \tag{6.24}$$

to give

$$\frac{d\boldsymbol{u}}{d\mathcal{P}} = -\frac{\partial F}{\partial \mathcal{P}} \left(\frac{\partial F}{\partial \boldsymbol{u}} \right)^{-1} \tag{6.25}$$

Substituting Eqn. 6.25 into Eqn. 6.22 yields

$$\frac{dJ}{d\boldsymbol{r}_\gamma} = \left(- \frac{\partial J}{\partial \boldsymbol{u}} \frac{\partial F}{\partial \mathcal{P}} \left(\frac{\partial F}{\partial \boldsymbol{u}} \right)^{-1} + \frac{\partial J}{\partial \mathcal{P}} \right) \frac{d\mathcal{P}}{d\tilde{\boldsymbol{r}}_\gamma} \frac{d\tilde{\boldsymbol{r}}_\gamma}{d\boldsymbol{r}_\gamma} \tag{6.26}$$

Re-ordering the derivatives and taking the transpose of both sides yields

$$\underbrace{\frac{dJ}{d\boldsymbol{r}_\gamma}^{\intercal}}_{L\times 1} = \underbrace{\frac{d\tilde{\boldsymbol{r}}_\gamma}{d\boldsymbol{r}_\gamma}^{\intercal}}_{L\times L}\underbrace{\frac{d\mathcal{P}}{d\tilde{\boldsymbol{r}}_\gamma}^{\intercal}}_{L\times M}\left(-\underbrace{\frac{\partial F}{\partial \mathcal{P}}^{\intercal}}_{M\times M}\overbrace{\underbrace{\left(\frac{\partial F}{\partial \boldsymbol{u}}\right)^{-\intercal}}_{M\times M}}^{\lambda}\underbrace{\frac{\partial J}{\partial \boldsymbol{u}}^{\intercal}}_{M\times 1} + \underbrace{\frac{\partial J}{\partial \mathcal{P}}^{\intercal}}_{M\times 1}\right) \tag{6.27}$$

where

$$\left(\frac{\partial F}{\partial \boldsymbol{u}}\right)^{\intercal}\lambda = \frac{\partial J}{\partial \boldsymbol{u}}^{\intercal} \tag{6.28}$$

is the adjoint system associated with the PDE $F(\boldsymbol{u}(\mathcal{P}), \mathcal{P}) = 0$. The adjoint variable, λ is associated with the solution, $\boldsymbol{u}$ and has the same dimension as the solution so that each component of $\boldsymbol{u}$ has a corresponding adjoint variable. By solving the adjoint problem, the derivative of the objective functional with respect to the stacked vector of control parameters is solved at a computational cost comparable to solving the governing PDE for the solution $\boldsymbol{u}$ once. As a consequence, the adjoint method is suited to determining the sensitivities of functionals with respect to control parameters of large dimension and is used in this work.

The first term of Eqn. 6.27, $\dfrac{d\tilde{\boldsymbol{r}}_\gamma}{d\boldsymbol{r}_\gamma}$ is the sensitivity of the filtered stacked vector of control parameters to the stacked vector of control parameters, a consequence of variable filtering. The second term, $\dfrac{d\mathcal{P}}{d\tilde{\boldsymbol{r}}_\gamma}$ is the sensitivity of material property matrices, $(\boldsymbol{E_{ij}}, \boldsymbol{K_{pq}})$ to the filtered stacked vector of control parameters. Following from Eqn. 6.21, the numerical implementation for deriving the sensitivity of the objective functional to the stacked

vector of control parameters for structural and thermal problems of this work are

$$\left.\frac{dJ}{d\boldsymbol{r}_\gamma}\right)_{\boldsymbol{u}} = \frac{d\tilde{\boldsymbol{r}}_\gamma}{d\boldsymbol{r}_\gamma} \begin{bmatrix} \sum_{i=1}^{6}\sum_{j=i}^{6} \frac{dJ}{dE_{ij}} \frac{dE_{ij}}{d\tilde{r}_{1\gamma}} \\ \sum_{i=1}^{6}\sum_{j=i}^{6} \frac{dJ}{dE_{ij}} \frac{dE_{ij}}{d\tilde{r}_{2\gamma}} \\ \vdots \\ \sum_{i=1}^{6}\sum_{j=i}^{6} \frac{dJ}{dE_{ij}} \frac{dE_{ij}}{d\tilde{r}_{7\gamma}} \\ \sum_{i=1}^{6}\sum_{j=i}^{6} \frac{dJ}{dE_{ij}} \frac{dE_{ij}}{d\tilde{\rho}_{\gamma}} \end{bmatrix} \tag{6.29}$$

and

$$\left.\frac{dJ}{d\boldsymbol{r}_\gamma}\right)_{\theta} = \frac{d\tilde{\boldsymbol{r}}_\gamma}{d\boldsymbol{r}_\gamma} \begin{bmatrix} \sum_{p=1}^{3}\sum_{q=p}^{3} \frac{dJ}{dK_{pq}} \frac{dK_{pq}}{d\tilde{r}_{1\gamma}} \\ \sum_{p=1}^{3}\sum_{q=p}^{3} \frac{dJ}{dK_{pq}} \frac{dK_{pq}}{d\tilde{r}_{2\gamma}} \\ \vdots \\ \sum_{p=1}^{3}\sum_{q=p}^{3} \frac{dJ}{dK_{pq}} \frac{dK_{pq}}{d\tilde{r}_{7\gamma}} \\ \sum_{p=1}^{3}\sum_{q=p}^{3} \frac{dJ}{dK_{pq}} \frac{dK_{pq}}{d\tilde{\rho}_{\gamma}} \end{bmatrix} \tag{6.30}$$

respectively. The jacobian matrix (the matrix of constraint sensitivities to the unfiltered stacked vector of control parameters) is required for problems with a constraint on the availability of material. This is given as

$$\frac{dV}{d\boldsymbol{r}_\gamma} = \frac{d\tilde{\boldsymbol{r}}_\gamma}{d\boldsymbol{r}_\gamma} \frac{dV}{d\tilde{\boldsymbol{r}}_\gamma} \tag{6.31}$$

All sensitivities are rigorously verified by finite differencing so that the derivative of the objective functional with respect to the i-th component of the stacked vector of control variables is given as

$$\frac{dJ}{dr_i} = \lim_{h\to 0} \frac{J(\boldsymbol{r}_\gamma + h\xi_i) - J(\boldsymbol{r}_\gamma)}{h} \tag{6.32}$$

where the perturbation is $h = 0.0001$ and ξ_i is the vector of zeros of the same length as

$\boldsymbol{r}_\gamma$ with 1 in the i-th entry.

6.6 Numerical Implementation

With the ability to evaluate objective functionals constrained by partial differential equations as well as capability for an efficient evaluation of objective functional sensitivities, large-scale optimization is executed in the space of the small scale design variables. `FEniCS` [131] is the open source finite element solver implemented for the large-scale optimization algorithms of this work. A general description of the numerical implementation of the optimization formulation in `FEniCS` follows:

6.6.1 Mesh generation

`FEniCS` is equipped with a basic in-built mesh generator for simple 2D and 3D geometries. For more complex geometries, `Gmsh` – an open source three-dimensional finite element mesh generator is used. Complex geometries are developed with commercial CAD software and imported into `Gmsh` as `.stp` files. In addition to mesh generation, `Gmsh` supports the creation of elementary entities and physical groups to enable the generation of domain and boundary indicators. The `.msh` file format from `Gmsh` is then converted to `.xml` file format and imported into `FEniCS`. Where domain/boundary indicators have been defined within `Gmsh`, the conversion also yields `.xml` files for physical and facet regions used for marking sub-domains and sub-boundaries respectively within the `FEniCS` formulation. The marking of sub-domains and sub-boundaries facilitate the implementation of mechanical and thermal loads as well as dirichlet boundary conditions.

6.6.2 Function space generation

Finite element function spaces are defined over the imported mesh for field variables. Vector function spaces are defined over the mesh for displacement in pure elastic formulations and scalar function spaces are defined over the mesh for temperature in pure thermal problems. A scalar function space is also defined over the mesh for the control variables. For thermo-structural formulations, mixed function spaces are defined. In all cases, linear Continuous Garlekin (Lagrange) elements are implemented so that solution space evaluations are executed on the mesh nodes.

6.6.3 Domain Initialization

The domain is initialized by assigning dof values corresponding to the radii distribution of the inital design. This is achieved by assigning a stacked vector of radii parameters as the control variable vector for the optimization algorithm. Non-design regions are assigned radii values corresponding to fully dense unit cells. For this work, the initial radii distribution within the design region corresponds globally to the design volume constraint value for each problem. The initial radii distribution constitutes the 'start point' within the space of parameters. This stacked vector of control variables is then mapped to the mesh vertices within the domain function space. For problems with restricted design regions, the vector of control variables is mapped only to vertices within the designable region function space. To prevent checkerboarding due to the use of linear Lagrange elements (low-order elements) and to impose a restriction scheme for mesh-independence, the Helmholtz filter of Sec. 6.4 is applied so that the value of control variable is a function of the variable field within a support neighbourhood defined by a filter radius.

6.6.4 Objective functional evaluation

FEniCS features many sparse direct solvers used to solve the underlying linear systems implied by the variational forms of Sec. 6.3. It also offers full control over many solver parameters and preconditioners. Material properties for the constitutive relations in the formulations are given by the explicit response surface models generated in precomputation phase. The language used to express these variational forms called Unified Form Language (UFL), facilitates ease of expressing complicated terms in partial differential equations. The solution yielded by the direct solvers (displacement or temperature distributions) are visualized by exporting `.vtu` file representations of the FEniCS field variables to Paraview – an open-source data analysis and visualization application. The objective functional is then evaluated according to Eqns. 6.8, 6.9, 6.12 and 6.14.

6.6.5 Gradient evaluation

The formulation of the macroscale optimization as a gradient-based algorithm is necessitated by the high computational cost of solving the large linear systems derived by the discretization of the variational formulations of this work. As a consequence, for each iteration, the optimization searches for a better design than that of the previous iteration by leveraging sensitivity information. In FEniCS, adjoint sensitivities are derived through dolfin-adjoint [131]. Dolfin-adjoint is a Python library within FEniCS [132, 133] which solves the adjoint system of Eqn. 6.28 at a computational cost comparable with solving the PDE once. Explicit sensitivity expressions are combined with these adjoint sensitivities to derive the gradients that drive the optimization algorithm as shown in Eqns. 6.29 and 6.30. The outcome is a stacked vector of sensitivities whose dimension corresponds to the dimension of the stacked vector of control parameters. Sensitivities are rigorously verified by finite differencing of Eqn. 6.32.

6.6.6 Constraint evaluation

In this work, the constraint evaluation corresponds to computing the integral of the volume fraction response surface, $V(\tilde{\boldsymbol{r}}_\gamma)$ and ensuring that it satisfies the restriction on availability of material, V_D. This information is only required for problems defined with volume constraints.

6.6.7 Jacobian evaluation

The jacobian is the stacked vector of constraint sensitivities. These sensitivities are available as explicit expressions derived from differentiating the volume constraint response surface model. The jacobian is only required for problems defined with volume constraints. It is also rigorously verified by finite differencing.

6.6.8 Interior Point Optimizer (`Ipopt`)

In its discretized form, Eqn. 6.3 is solved with a robust gradient-based numerical optimizer based on an interior point algorithm, `Ipopt` [134]. `Ipopt` is an open source software package for large-scale nonlinear optimization. To implement `Ipopt` within `FEniCS`, a python connector, `PyIpopt` is used. `PyIpopt` uses the definition of the optimization start point from the domain initialization, objective functional evaluation, gradient evaluation, constraint evaluation (if required) and jacobian evaluation (if required) to derive the next design iteration (See Fig. 6.1). It is important to note that derivatives of the objective and constraint are with respect to the unfiltered stack of control variables as shown by Eqns. 6.29, 6.30 and 6.31. However, the forward solve and global volume fraction are evaluated with the filtered stacked vector of control variables. The large-scale optimization is terminated when an iterate satisfies the conditions of a first-order Karush-Kuhn-Tucker (KKT) point, indicating that the solution at the current point is a strict local minimizer of the constrained optimization problem or by a limit on the maximum number of

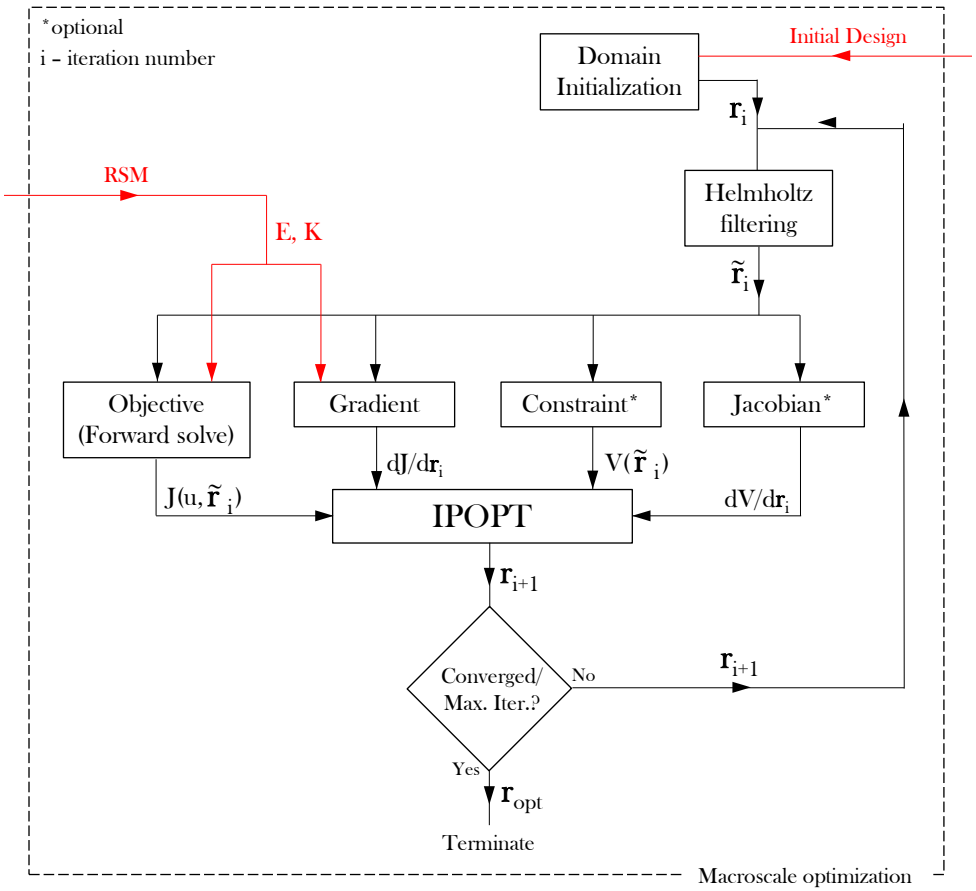


Figure 6.1: Macroscale optimization loop showing how next design iteration is derived towards attaining optimal design

optimization iterations.

In the following three chapters, the robustness of the derived optimization framework is investigated by its application to seven test cases of large-scale structural, thermal and thermo-structural optimization problem-types followed by a discussion of the results obtained. For each test case, a description of the initial domain dimensions with thermal or structural loading and boundary conditions is given. All other settings associated with the implementation of `Ipopt` are specified along with specific problem definition of each test case. Reference is made to the appropriate mathematical formulation from Sec. 6.3. The results for each case comprises figures showing the volume fraction distribution within the design domain, the optimal radii distribution for each component of the vector of radii parameters within the design domain, and a convergence plot of the objective functional during the optimization iterations. Each test case features a lattice reconstruction of

the optimal solution towards the realization of the physical optimal solution by additive manufacturing. For target deformation problems, the prescribed target deformation as well as the deformed displacement field solution is presented. Where relevant, the solution obtained is compared against bench-mark approaches in literature. The coordinate system of the large-scale optimization domain coincides with that of the micro-architecture of Fig. 4.1. Finally, a discussion of the results is made, with emphasis on the main advantages of the derived framework over more conventionally employed approaches.

Chapter 7

Structural Optimization – Compliance minimization

In this chapter, three test cases demonstrate the suitability of the derived framework to the compliance minimization problem where the stiffest structural layout is determined given a constraint on the availability of material. It begins with the cantilever test case presented by Imediegwu et al. [135] with the inclusion of an additional pseudo-lattice-density variable that defines the macroscale lattice density distribution. Two more problems are then presented to demonstrate the capacity of the derived framework for real-world applications.

7.1 Case 1: Top-loaded Cantilever Beam

7.1.1 Problem Definition

Consider the cantilever beam with geometrical dimensions $L \times W \times W$, with material properties and loading conditions as specified in the problem definition of Fig. 7.1 and Table 7.1. The goal of the optimization formulation is to minimize the compliance/strain

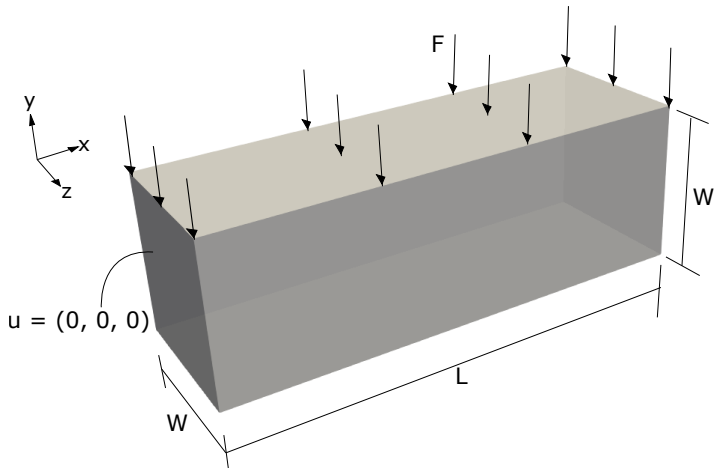


Figure 7.1: Top-loaded Cantilever Beam

energy of the cantilever beam subject to a constraint on the availability of base material such that the volume fraction of the optimized design, $V_D = 0.3$. The cantilever beam is also constrained to satisfy static equilibrium mechanics presented in the weak formulation of Eqn. 6.6.

7.1.2 Results and Discussion

In response to the uniformly distributed external load on the cantilever beam, the displacement of the cantilever is shown for the material properties specified at the beginning of the optimization search in Fig. 7.2. The bound constraints on the components of the stacked vector of control variables confine the material space of possible designs to the precomputed property space. The optimal distribution of radii parameters at termination of the search are displayed in Figs. 7.3 and 7.4 for the diagonal and face members respectively.

The solid regions in the solutions depict $r_{i\gamma} \geq 0.30$. The pale blue regions depict regions where $r_{min} < r_{i\gamma} < 0.30$. All other regions represent $r_{i\gamma} = r_{min}$. This representation of the results facilitate the visualization of spatially varying radii distributions of this work.

The macroscale lattice density distribution forms an I-beam-like section. I-beam sections possess high second moment of area due to an increased off-set of the sectional area from

Domain	
Design Region	Full
L, W	3, 1 m
Force, F	1000 N/m^2
Base material, E_s, ν	209 GPa, 0.3
Mesh discretization	
Element type	Structured hexahedral
No. of elements, N_e	24000
No. of design nodes, N_n	26901 of 26901
No. of variables	$8 \times N_n$
Optimization settings	
Starting point, $r_{i\gamma}$, ρ_γ	0.113, 1
Bound constraints, r_{min}, r_{max}	0.07, 0.38
Bound constraints, ρ_{min}, ρ_{max}	0, 1
Filter radius, z	0.03
Step-size update strategy	Adaptive
Pseudo–lattice–density function penalization	$p = 3$
Volume constraint, V_D	$0.3 \times V$
Max. Iter.	250
Obj. Tol.	1×10^{-5}

Table 7.1: Top-loaded Cantilever Beam: Problem Definition

the neutral axis in comparison to uniform sections, hence offering higher resistance to bending. The orientations of Members 1 and 4 (Figs. 7.3a and 7.3d) are suited to convey the compressive principal stresses from the external top-load to the Dirichlet boundary condition at the lower part of the fixed end. Members 2 and 3 (Figs. 7.3b and 7.3c) have orientations that are suited to convey tensile principal stresses from the top part of the fixed end towards the bottom face of the cantilever.

Figure 7.5 shows the minimum and maximum principal stress paths for the top-loaded cantilever of this work. Observe that the maximum radii distributions coincide with the regions of highest tensile or compressive principal stresses – at the fixed end of the cantilever and near the top and bottom surfaces respectively. The symmetries in the radii distributions of Members 1 and 4 as well as Members 2 and 3 demonstrate that the orientations of the members determine to their regions of dominance.

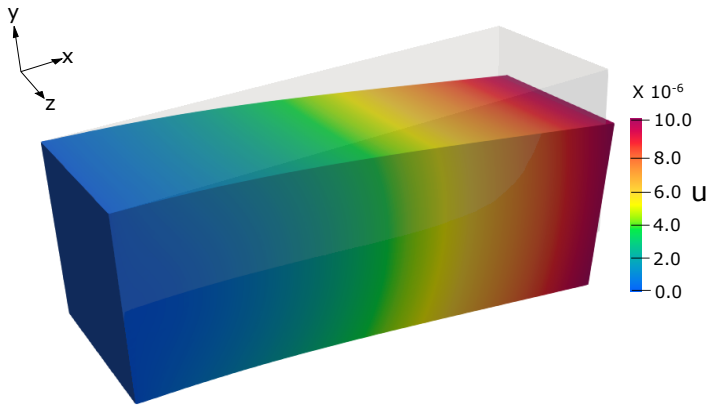
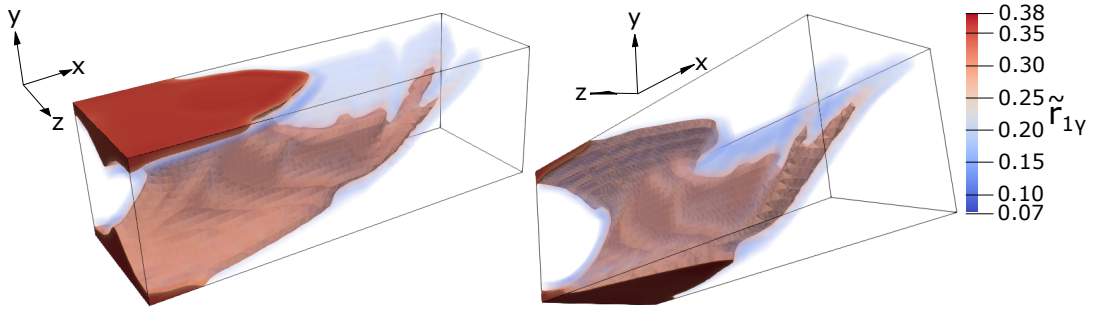


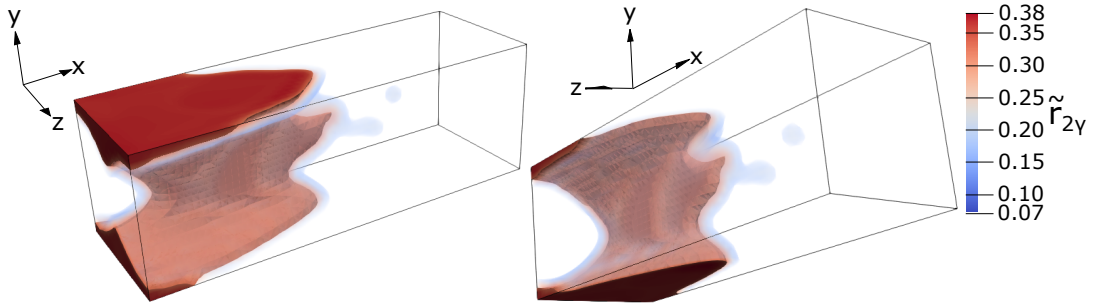
Figure 7.2: Top-loaded Cantilever: Displacement, u (m) at Iteration 1 (Deformation Scale – 32000:1)

Towards the free end of the cantilever, where principal stress magnitudes are lower, it becomes more efficient for face member 5 to provide the resistance to bending while member 6 supports the top-load, providing resistance to shear stresses. Member 7 (Fig. 7.4c) does not contribute significantly to maximizing the stiffness of the beam as a consequence of its orientation and hence is least dominant within the design domain. The pseudo-lattice-density function (Fig. 7.6) defines the macroscale lattice density distribution in a similar manner to the pseudo–density function of the SIMP method. The penalization of the pseudo–lattice–density function discourages intermediate weighting values so that it approximates the regions of lattice or no-lattice.

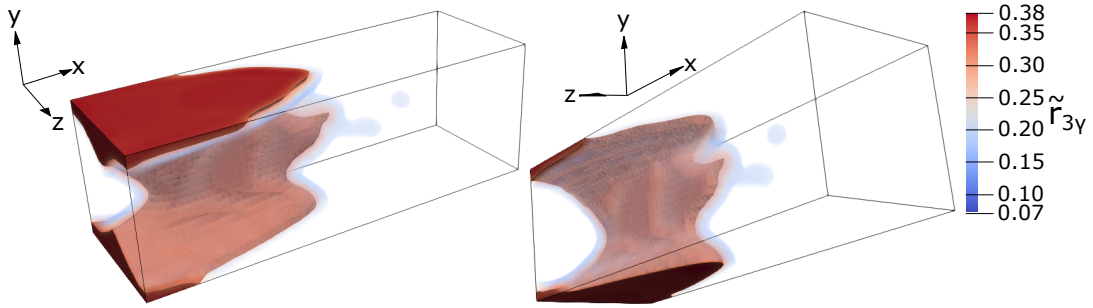
Figure 7.7a shows the optimal local volume fraction distribution based on the optimal cantilever radii distributions of Figs. 7.3 and 7.4. It demonstrates that optimal geometry is an I–beam–like with greatest material distribution in regions close to the fixed end where maximum stresses exist. However, the sensitivities of each degree of freedom to the compliance differs as a consequence of the orientations of the members so that the most efficient member is used locally to offer stiffness in relevant directions. The optimization convergence plot is shown in Fig. 7.7b and shows a minimum strain energy value, $J_{uc} = 0.00186$ J. Figure 7.8 presents the density distribution and optimization convergence plot for a SIMP solution of the same cantilever problem. The SIMP solution converges to



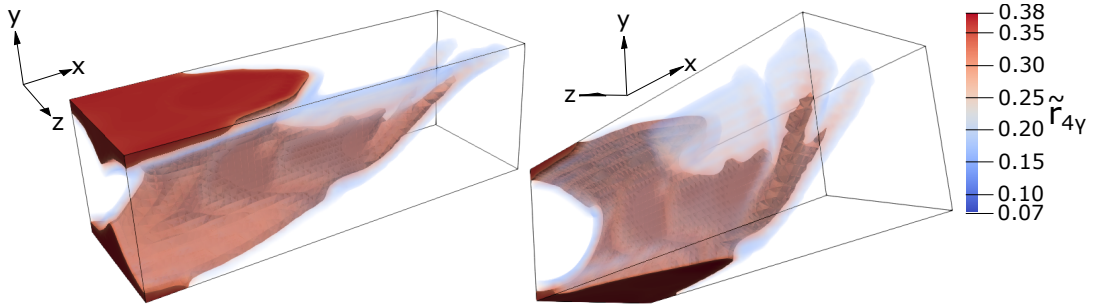
(a) Member 1



(b) Member 2

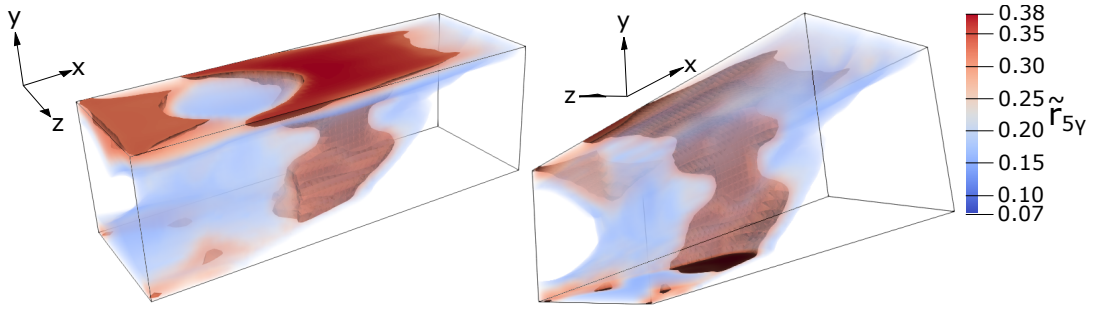


(c) Member 3

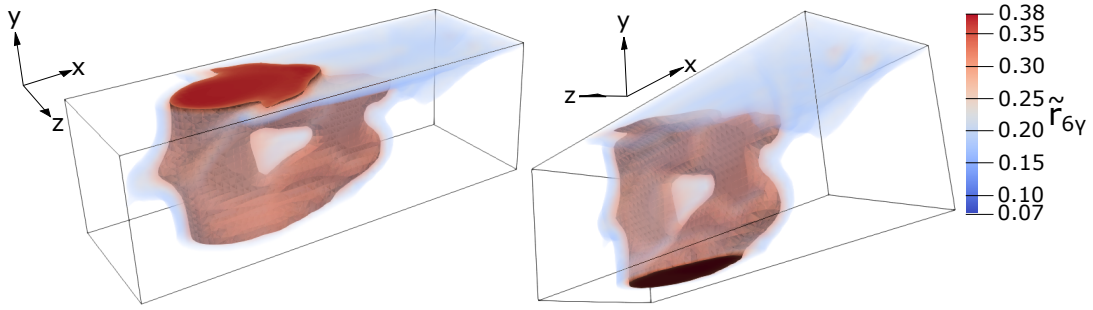


(d) Member 4

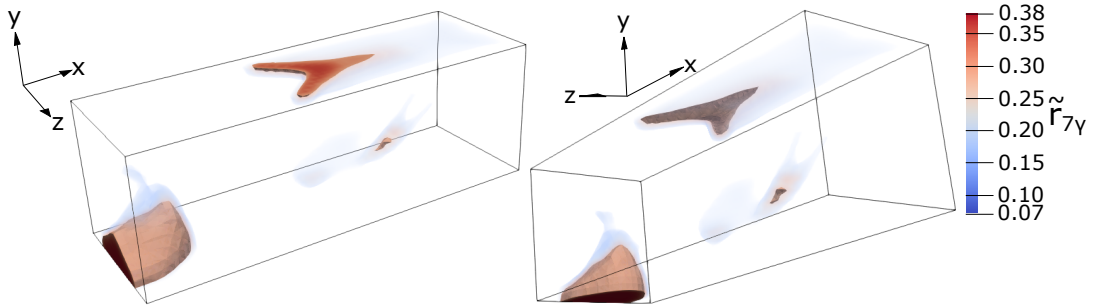
Figure 7.3: Top Loaded Cantilever: Optimal radii distribution for diagonal members 1–4



(a) Member 5



(b) Member 6



(c) Member 7

Figure 7.4: Top Loaded Cantilever: Optimal radii distribution for face members 5–7

a worse objective functional value, $J_{uc} = 0.00221$ J compared to the lattice-based solution, hence highlighting a major merit to the derived lattice-based framework. The difference

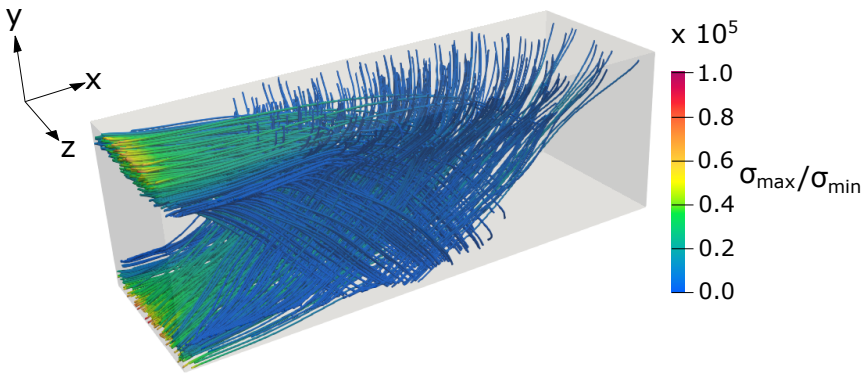


Figure 7.5: Top-loaded Cantilever: Minimum and maximum principal stress paths

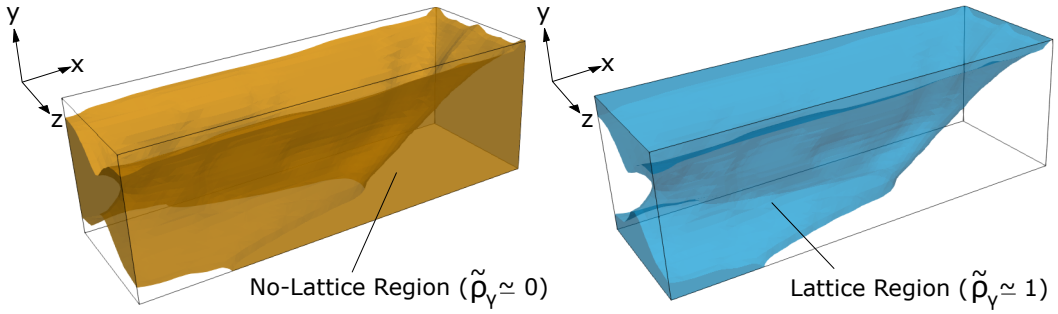
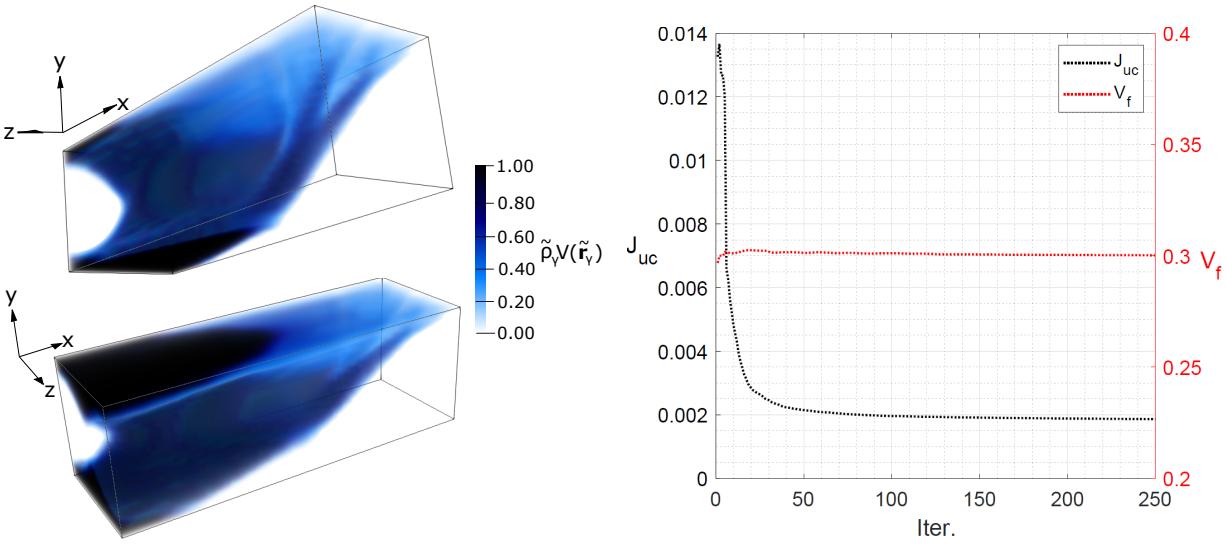


Figure 7.6: Post-processed pseudo–lattice–density distribution



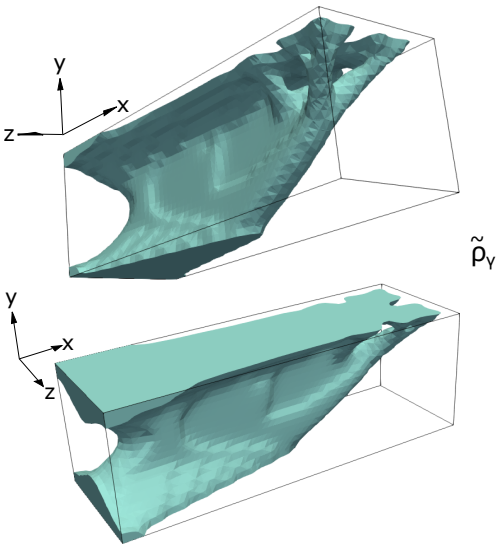
(a) Volume fraction distribution

(b) Lattice-based optimization convergence plot

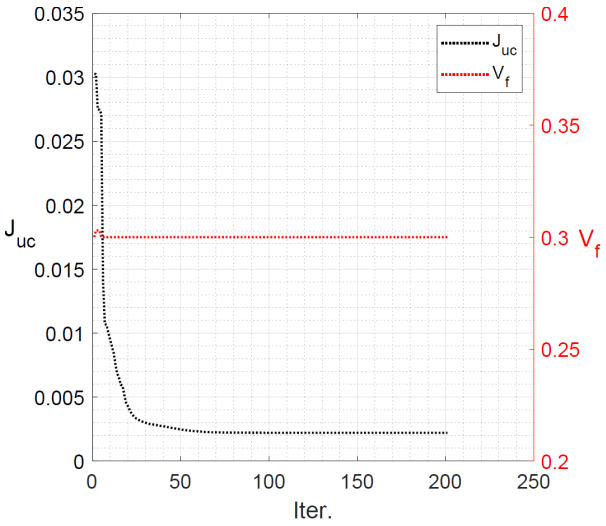
Figure 7.7: Top-loaded Cantilever: Lattice-based material distribution and optimization convergence plot

in objective functional value corresponds to a 15.8% further reduction in minimum strain energy for the lattice-based solution, for the same available material (volume constraint). Figure 7.9 shows the lattice reconstruction derived given radii distributions. The reconstruction is based on a marching cubes algorithm that converts volume data generated from radii distribution data to lattice surface mesh [136, 137].

Two test cases are now considered to demonstrate the application of the framework to compliance minimization of real-world components. Both problems feature a restricted design domain with unstructured domain discretization.



(a) Density distribution, $\rho_{viz} = 0.8$



(b) SIMP-based optimization convergence plot

Figure 7.8: Top-loaded Cantilever: SIMP material distribution and optimization convergence plot

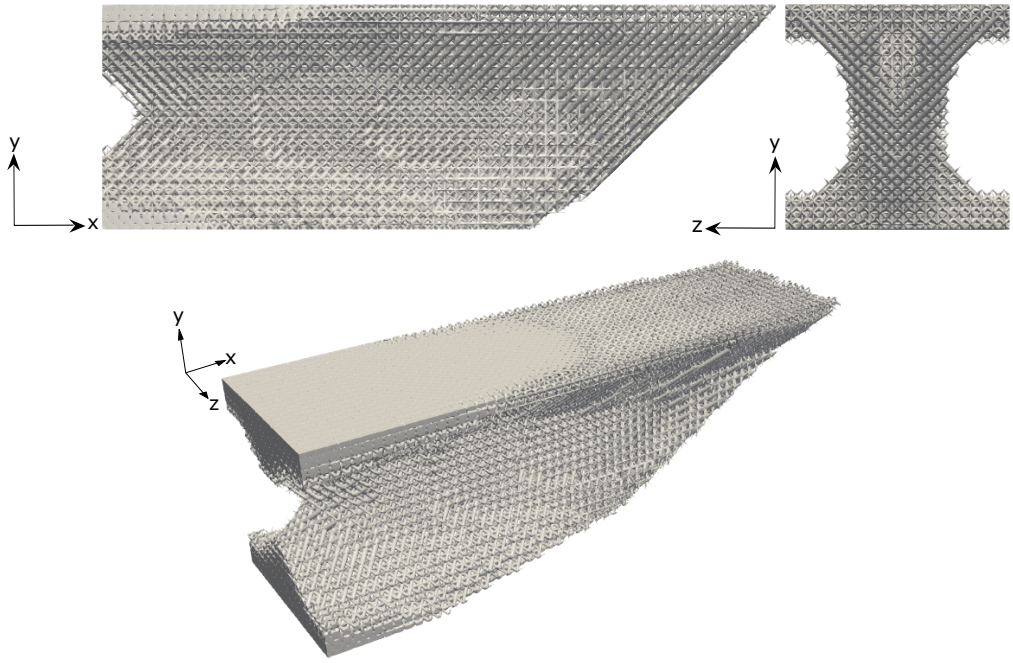


Figure 7.9: Top-Loaded Cantilever: Lattice Reconstruction

7.2 Case 2: Engine Backet

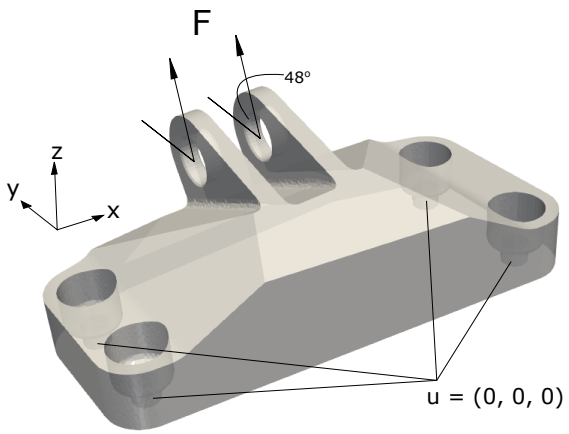


Figure 7.10: Engine Backet

Domain	
Design region	Restricted
Geometry	Ref. [138]
Design space volume, V	4.63×10^{-4} m^3
Force, F	42258 N/m^2
Base material, E_s, ν	209 GPa, 0.3
Mesh discretization	
Element type	Unstructured tetrahedral
No. of elements, N_e	357678
No. of design nodes, N_n	68158 of 69816
No. of variables	$8 \times N_n$
Optimization settings	
Starting point, $r_{i\gamma}$, ρ_γ	0.113, 1
Bound constraints, r_{min}, r_{max}	0.07, 0.38
Bound constraints, ρ_{min}, ρ_{max}	0, 1
Filter radius, z	0.001
Step-size update strategy	Adaptive
Pseudo–lattice–density function penalization	$p = 5$
Volume constraint, V_D	$0.32 \times V$
Max. Iter.	200
Obj. Tol.	1×10^{-5}

Table 7.2: Engine Bracket: Problem Definition

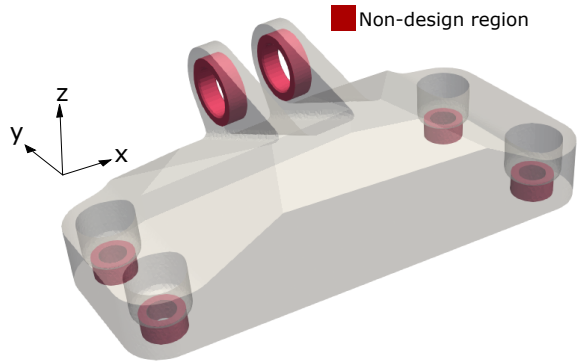


Figure 7.11: Engine Bracket: Non-design region definition

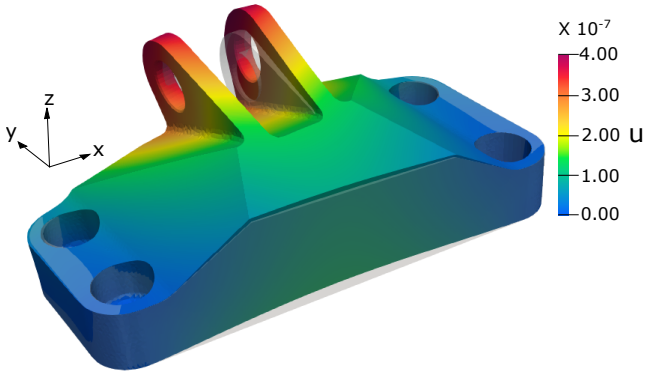


Figure 7.12: Engine Backet: Displacement, u (m) at Iteriation 1 (Deformation Scale – 25000:1)

7.2.1 Problem Definition

Consider the engine bracket with geometrical dimensions given within the General Electric bracket challenge description [138], with material properites and loading conditions as specified in the problem definition of Figs. 7.10 and Table 7.2. As in Sec. 7.1, the goal of the optimization formulation is to minimize the compliance of the bracket subject to a constraint on the availability of material such that $V_D = 0.32$. However, in this case, a design sub-domain exists so that regions around all holes are non-design space as shown in Fig. 7.11.

7.2.2 Results and Discussion

In response to the external loads on the bracket, the displacement of the bracket is shown for the material properties specified at the beginning of the optimization search

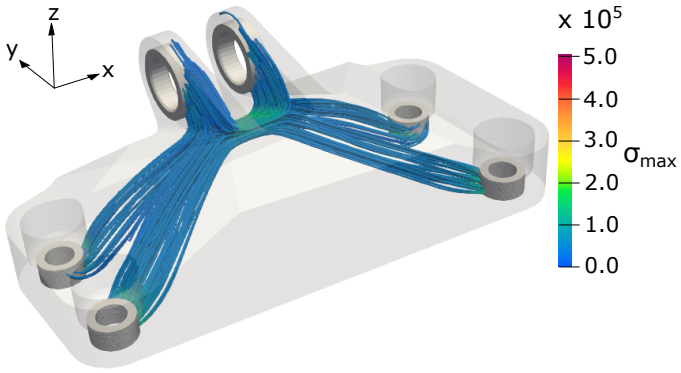
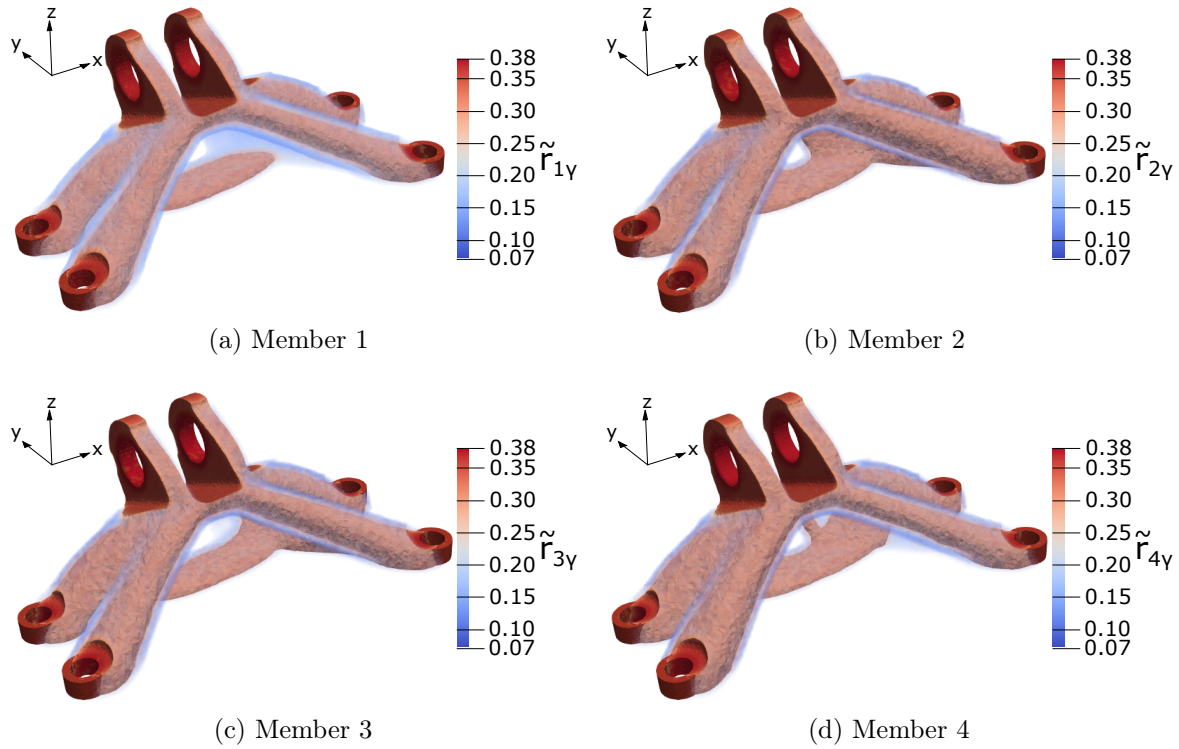


Figure 7.13: Engine Bracket: Maximum principal stress flow path

in Fig. 7.12. Bound constraints are imposed on the components of the stacked vector of control variables so that the optimization search is confined to the precomputed material property space. The bracket is also constrained to satisfy static equilibrium mechanics presented in the weak formulation of Eqn. 6.6. The optimal distribution of radii parameters at termination of the search are displayed in Figs. 7.14 and 7.15 for the diagonal and face members respectively. The solid regions in the solutions depict $r_{i\gamma} \geq 0.30$. The pale blue regions depict regions where $r_{min} < r_{i\gamma} < 0.30$. All other regions represent $r_{i\gamma} = r_{min}$. The diagonal members of Fig. 7.14 are best suited to resist stresses induced in the bracket due to the external loads. This is a consequence of their orientation relative to the principal stress directions between the applied load and the Dirichlet boundary conditions. The face members of Fig. 7.15 have orientations that are not suited to efficiently resist the principal stress flow hence, their much lower normalized radii distributions (see Fig. 7.13).

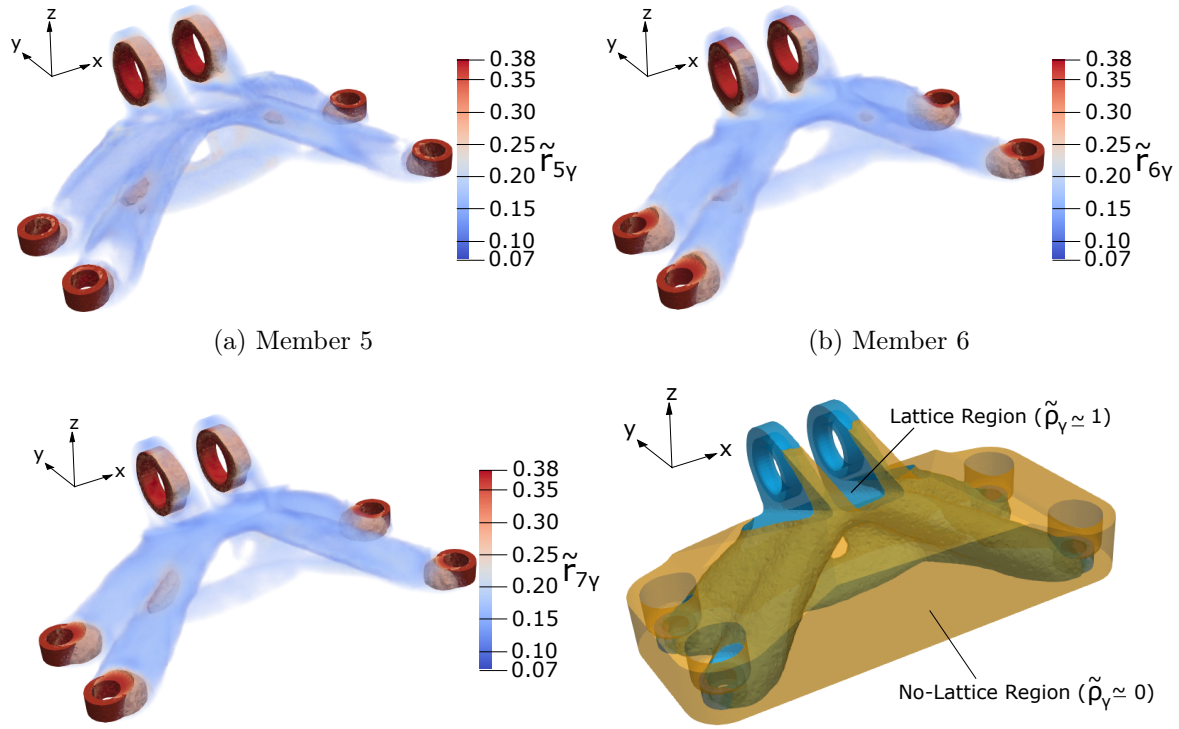
The benefits of the lattice-based optimization are highlighted by this preference of diagonal members for compliance minimization for this problem as their orientations make the compliance objective more sensitive to their changes. Macroscopically, the optimal geometry also differs from that obtained by the implementation of SIMP as shown in Figs. 7.16a and 7.17a. The penalized pseudo–lattice–density function (Fig. 7.15d) defines the macroscale lattice density distribution in a similar manner to the penalized pseudo–density function of the SIMP methodology.



(a) Member 1 (b) Member 2

(c) Member 3 (d) Member 4

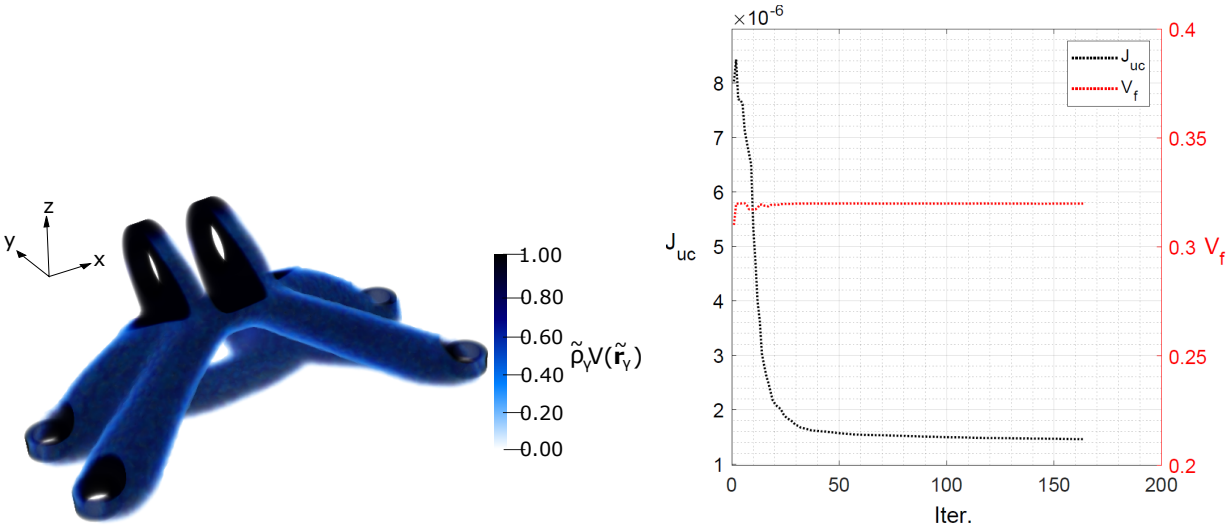
Figure 7.14: Engine Bracket: Optimal radii distribution for diagonal members 1–4



(a) Member 5 (b) Member 6

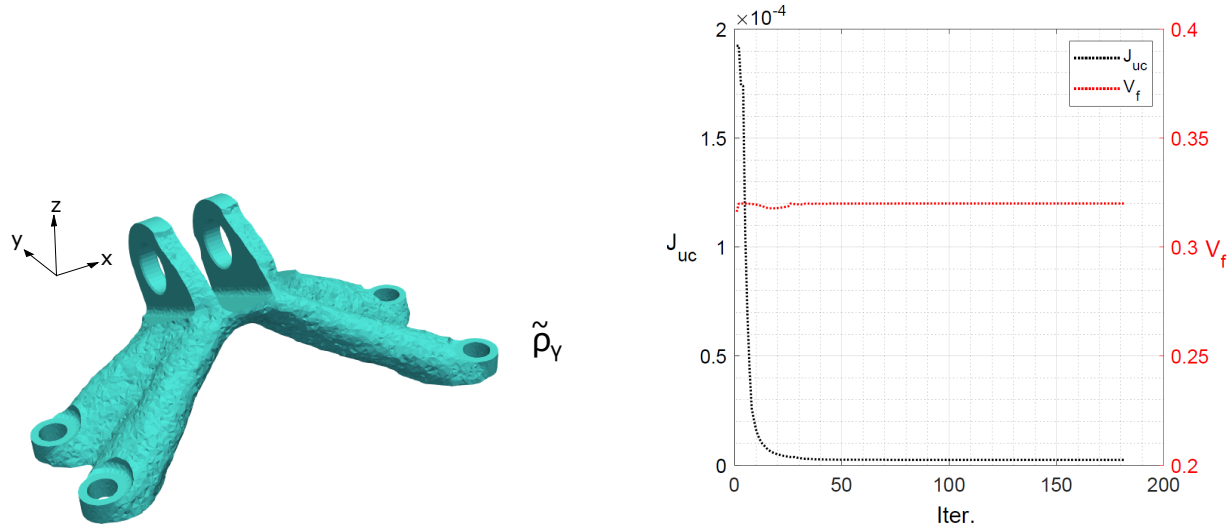
(c) Member 7 (d) Post-processed pseudo–lattice–density distribution

Figure 7.15: Engine Bracket: Optimal radii distribution for face members 5–7



(a) Volume fraction distribution (b) Lattice-based optimization convergence plot

Figure 7.16: Engine Bracket: Lattice-based material distribution and optimization convergence plot



(a) Density distribution, $\rho_{viz} = 0.8$ (b) SIMP-based optimization convergence plot

Figure 7.17: Engine Bracket: SIMP material distribution and optimization convergence plot

Figure 7.16a shows the optimal local volume fraction distribution based on the optimal bracket radii distributions of Figs. 7.14 and 7.15. The optimization convergence plot is shown in Fig. 7.16b with a minimum strain energy value of, $J_{uc} = 1.458 \times 10^{-6}$ J. In comparison, the convergence plot of the SIMP methodology attains only a minimum strain energy of, $J_{uc} = 2.391 \times 10^{-6}$ J – a worse final objective. The objective function value of the lattice-based solution corresponds to a 39% reduction in strain energy for

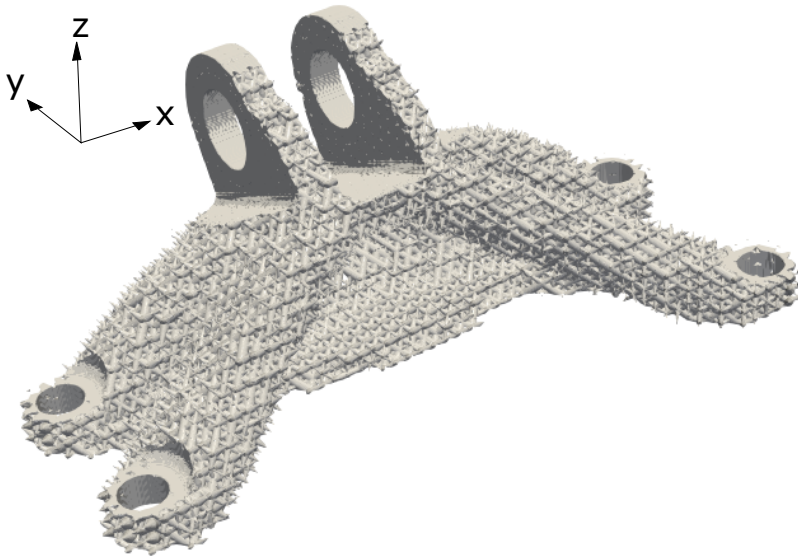


Figure 7.18: Engine Bracket: Lattice Reconstruction

the same available material compared to the SIMP solution. It is of note to highlight the fact that the SIMP methodology as applied has a starting point objective of much higher value than the corresponding lattice-based methodology for an equivalent starting volume fraction distribution. This is due to the penalization parameter assigned to the pseudo–density function to discourage intermediate densities. Continuation methods are often applied to prevent this effect in SIMP algorithms. The derived lattice-based methodology does not require continuation methods since the penalization parameter is assigned to the pseudo–lattice–density function and not the radii parameters. The penalized pseudo–lattice–density function can be commenced with a value of unity while for compliance minimization problems, the radii parameters can be commenced at values corresponding to the desired design volume fraction, V_D. For an equivalent starting volume fraction, the lattice-based framework will always commence the search of the design space from a better starting point than a SIMP formulation of the same problem. Figure 7.18 shows the lattice reconstruction derived given radii distributions.

7.3 Case 3: The Goose-Neck Hinge

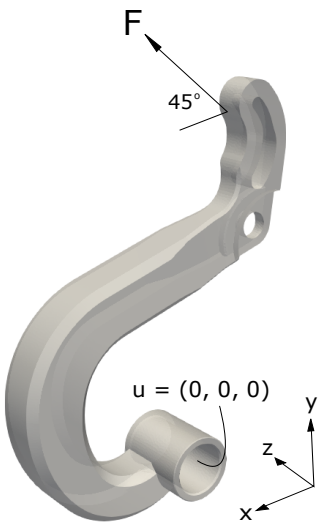


Figure 7.19: Goose-Neck Hinge (GNH)

Domain	
Design region	Restricted
Design space volume, V	3.57×10^{-4} m^3
Force, F	5656.85 N/m^2
Base material, E_s, ν	209 GPa, 0.3
Mesh discretization	
Element type	Unstructured tetrahedral
No. of design nodes, N_n	37538 of 55548
No. of variables	$8 \times N_n$
Optimization settings	
Starting point, $r_{i\gamma}$, ρ_γ	0.113, 1
Bound constraints, r_{min}, r_{max}	0.07, 0.38
Bound constraints, ρ_{min}, ρ_{max}	0, 1
Filter radius, z	2
Step-size update strategy	Adaptive
Pseudo–lattice–density function penalization	$p = 5$
Volume constraint, V_D	$0.45 \times V$
Max. Iter.	200
Obj. Tol.	1×10^{-5}

Table 7.3: Goose-Neck Hinge: Problem Definition

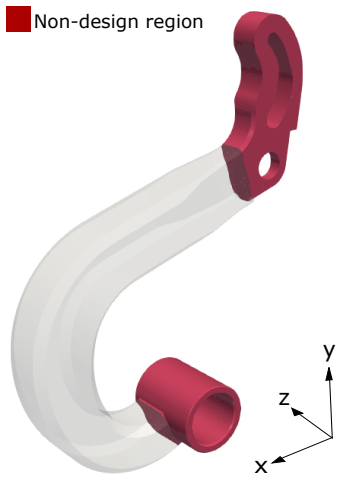


Figure 7.20: GNH: Non-design region definition

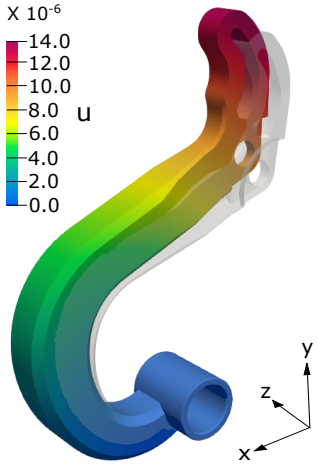


Figure 7.21: GNH: Displacement, u (m) at initial conditions (Deform. Scale, 2000:1)

7.3.1 Problem Definition

Consider the Goose-Neck Hinge (GNH) with material and loading conditions specified in the problem definition of Figs. 7.19 and Table 7.3. The goal of the optimization formulation is to minimize the compliance of the hinge subject to a constraint on the availability of material such that $V_D = 0.45$. A non-design sub-domain exists as shown in Fig. 7.20 and bound constraints are imposed on the stacked vector of control variables so that the search is confined to the precomputed material space.

7.3.2 Results and Discussion

In response to the external load on the GNH, the displacement of the hinge is shown for the material properties specified at the beginning of the optimization search in Fig. 7.21. Like the previous two cases, this problem belongs to the class of PDE-constrained problems where static equilibrium laws must be satisfied. The optimal distribution of radii parameters are shown in Figs. 7.23 and 7.24 for the diagonal and face members respectively. To facilitate visualization, a threshold has been set so that $r_{viz} = 0.20$. Therefore, the solid regions in the solutions depict $r_{i\gamma} \geq 0.2$. The design region is enclosed by transparent boundaries to facilitate the visualization of the radii distributions within the design region defined by the curved profile of the GNH. The external load applied to the GNH as shown in Fig. 7.19 subjects the hinge to bending. Macroscopically, the radii distribution result in higher material distribution in regions close to the inner and outer curved surfaces of the GNH relative to the x-y plane to resist bending as shown in Fig. 7.25a. These regions are the regions with the highest magnitudes of tensile and compressive principal stresses as shown in Fig. 7.22.

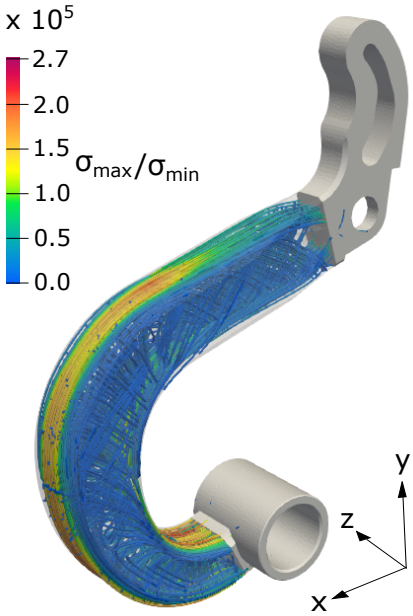
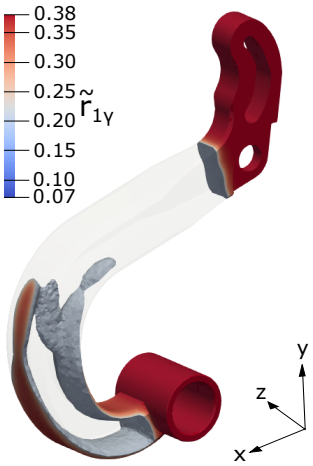
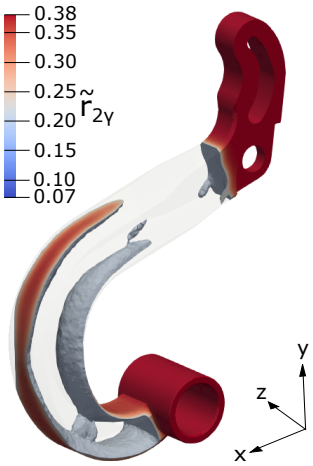


Figure 7.22: GNH:Maximum and minimum principal stress paths

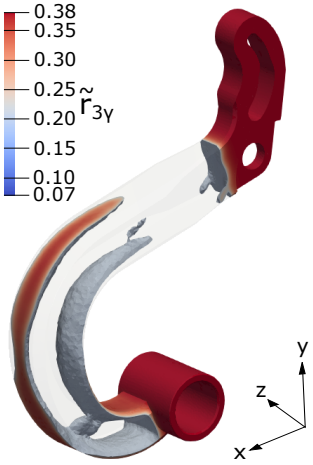
The pseudo–lattice–density function describes the macroscale lattice density distribution which demonstrates the requirement for an I–beam–like structure to withstand the bend-



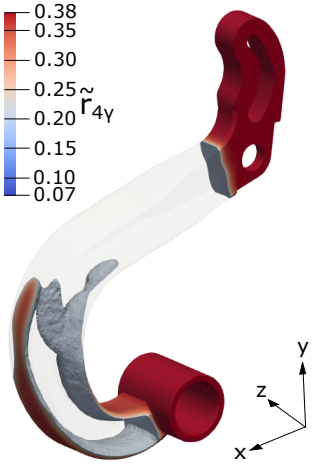
(a) Member 1, $r_{viz} = 0.20$



(b) Member 2, $r_{viz} = 0.20$

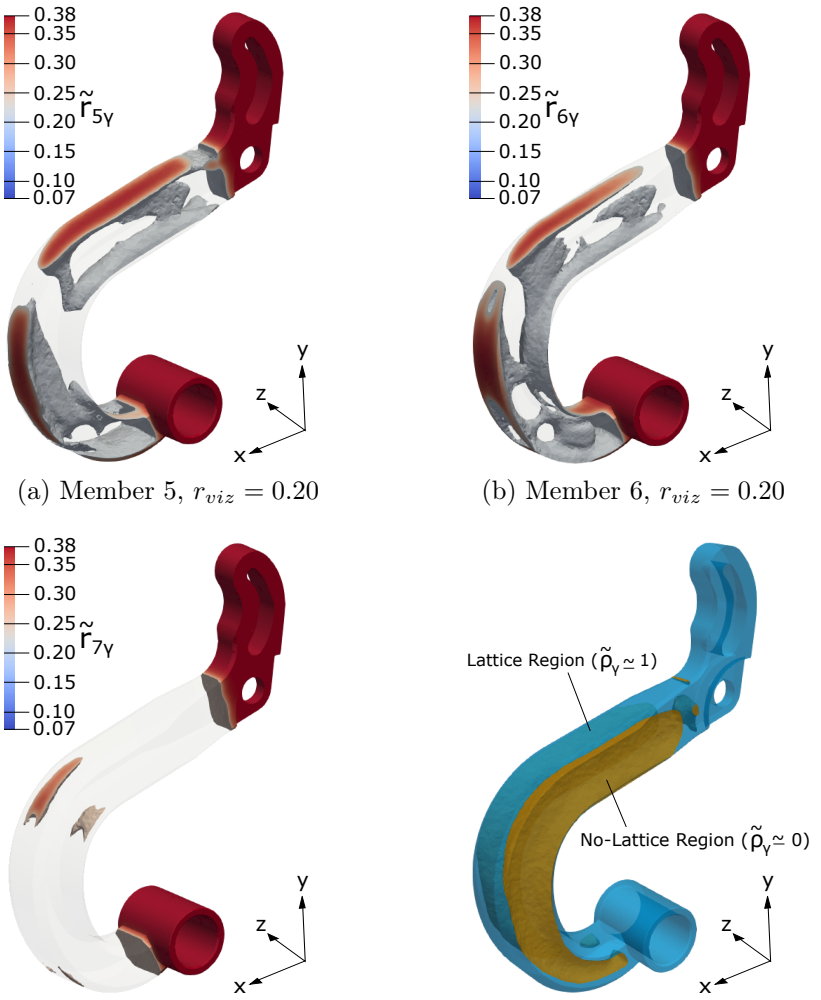


(c) Member 3, $r_{viz} = 0.20$



(d) Member 4, $r_{viz} = 0.20$

Figure 7.23: GNH: Optimal radii distribution for diagonal members 1–4



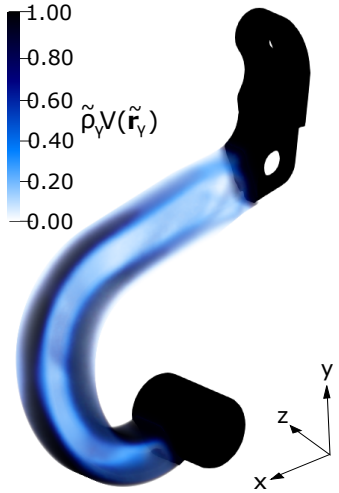
(a) Member 5, $r_{viz} = 0.20$

(b) Member 6, $r_{viz} = 0.20$

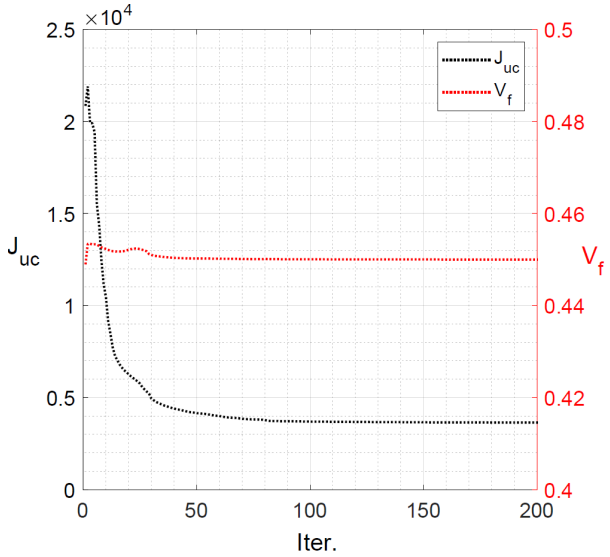
(c) Member 7, $r_{viz} = 0.20$

(d) Post-processed pseudo–lattice–density distribution

Figure 7.24: Engine Bracket: Optimal radii distribution for face members 5–7

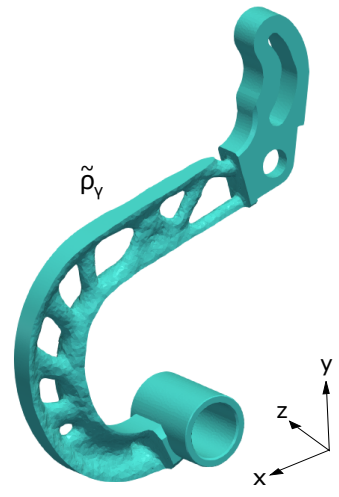


(a) Volume fraction distribution

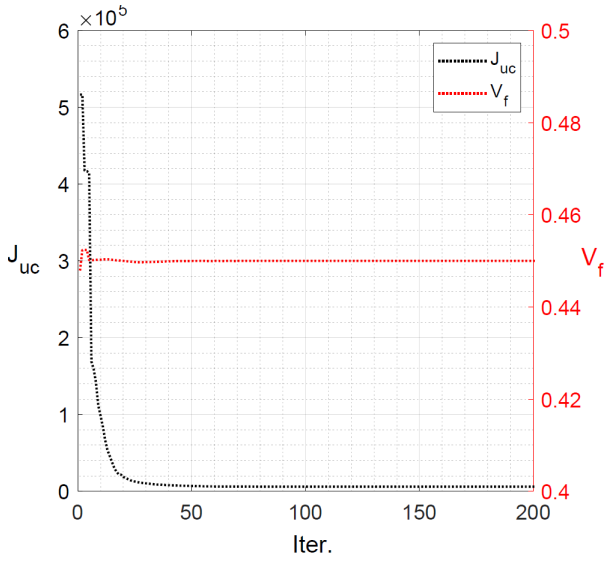


(b) Lattice-based optimization convergence plot

Figure 7.25: GNH: Lattice-based material distribution and optimization convergence plot



(a) Density distribution, $r_{viz} = 0.7$



(b) SIMP-based optimization convergence plot

Figure 7.26: GNH: SIMP material distribution and optimization convergence plot

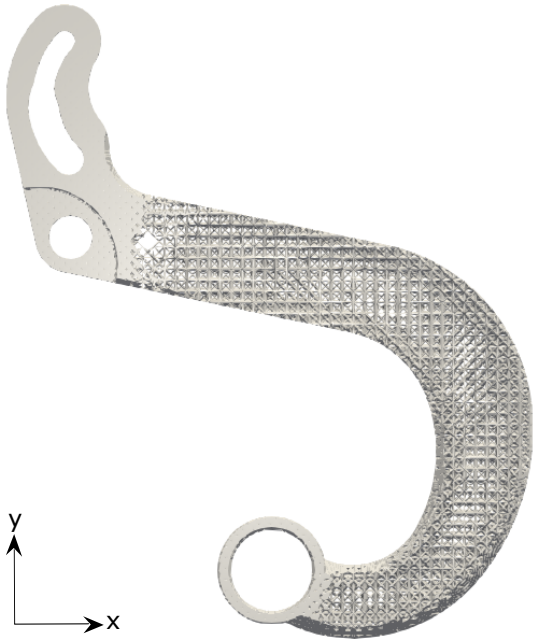


Figure 7.27: GNH: Lattice Reconstruction

ing stresses (Figure 7.24d. This is consistent with the topography of the top-loaded cantilever subjected to bending in case 1. Microscopically, the diagonal members are dominant in the regions with greater curvature close to the pivot hinge with a distinctive similarity between the distributions of member 1 and 4 as well as between member 2 and 3 – a consequence of their relative orientations. Members 5 and 6 (Figs. 7.24a and 7.24b are dominant in the part of the design region close to where the external load is applied. The compliance of the GNH is least sensitive to changes in member 7 as a consequence of its orientation and is therefore essentially absent as shown in Fig. 7.24c. The optimization convergence plot is shown in Fig. 7.25b so that $J_{uc} = 3.63 \times 10^5$ Nmm. In comparison, the convergence plot the SIMP methodology attains only a minimum strain energy of, $J_{uc} = 6.03 \times 10^5$ Nmm. The minimum strain energy by the lattice-based solution corresponds to a 39.8% reduction compared to the SIMP-based solution. Figure 7.27 shows the lattice reconstruction derived given radii distributions.

The three test cases presented demonstrate that the framework consistently delivers improved structurally optimal solutions for single-objective problems in comparison to the SIMP methodology. However, the parameterization scheme implemented in this work fea-

tures the capacity to model orthotropic and anisotropic material point properties. In the next chapter, the derived framework is applied to multi-objective structural optimization problems towards attaining prescribed target deformations.

Chapter 8

Structural Optimization – Target Deformation

In this chapter, the capability of the derived framework is demonstrated in solving multi-objective optimization problems. Multi-objective functionals consists of weighted sums of separate objective functionals. Two test cases are presented - one to benchmark the derived framework against existing methology as presented by Zhu et al. [20], and the other to demonstrate this frameworks extended capacity for controlling anisotropic material point properties to meet macroscale objectives.

8.1 Case 4: Two-prong gripper

8.1.1 Problem Definition

Taking inspiration from the works of Zhu et al. [20], the performance of the derived lattice-based framework is investigated against a benchmark target deformation problem. Consider the two-prong gripper with material properties and Dirichlet boundary conditions specified in the problem definition of Fig. 8.1 and Table 8.1. The displacement profile

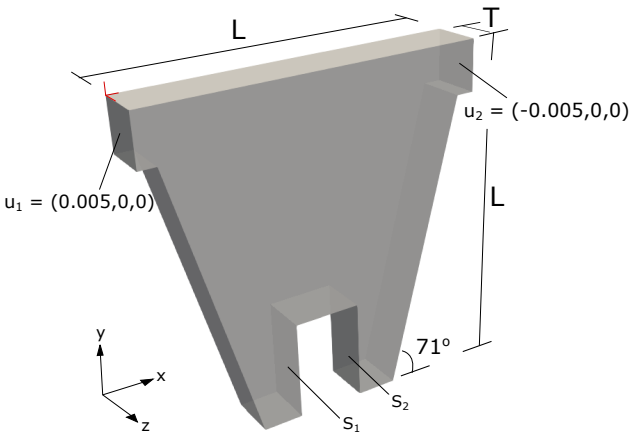


Figure 8.1: Two-prong gripper

Domain	
Design region	Full
L, T	0.1, 0.015 m
Design space volume, V	9.86×10^{-5} m^3
Base material, E_s, ν	209 GPa, 0.3
Mesh discretization	
Element type	Unstructured tetrahedral
No. of design nodes, N_n	25774 of 25774
No. of variables	$8 \times N_n$
Optimization settings	
Starting point, $r_{i\gamma}$, ρ_γ	0.113, 1
Bound constraints, r_{min}, r_{max}	0.07, 0.38
Bound constraints, ρ_{min}, ρ_{max}	0, 1
Filter radius, z	0.001
Step-size update strategy	Adaptive
Pseudo–lattice–density function penalization	$p = 3$
Volume constraint, V_D	–
Max. Iter.	300
Obj. Tol.	1×10^{-5}

Table 8.1: Two-prong gripper: Problem Definition

attributed to the imposed conditions at the beginning of the optimization search is shown in Fig. 8.2. The goal of the optimization is to minimize the error functional between this displacement profile, u and predefined target displacements on specified target surfaces using the radii parameters as design variables. For this problem, two target displacements

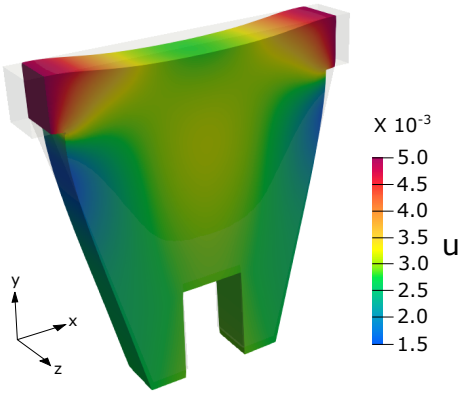


Figure 8.2: Two-prong gripper: Displacement, u (m) at Iteration 1

are defined, u_{D1} and u_{D2}, defined mathematically within the design domain as

$$u_{D1}(x,y,z) = \begin{cases} (-0.17y - 0.0117, 0, 0) & \text{if } x < 0.05 \text{ and } y < -0.07 \\ (0,0,0) & \text{everywhere else} \end{cases} \tag{8.1}$$

and

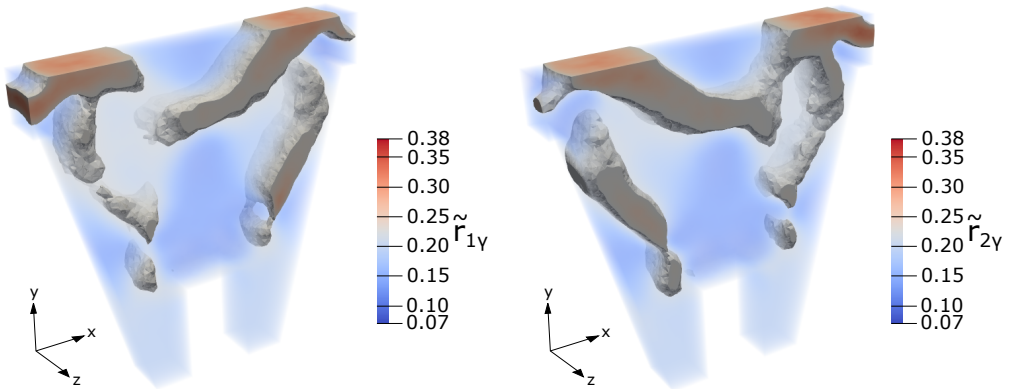
$$u_{D2}(x,y,z) = \begin{cases} (0.17y + 0.0117, 0, 0) & \text{if } x > 0.05 \text{ and } y < -0.07 \\ (0,0,0) & \text{everywhere else} \end{cases} \tag{8.2}$$

Two target surfaces, S_1 and S_2 can be identified in Fig. 8.1. The target displacement distributions of Eqns. 8.1 and 8.2 are shown in Fig. 8.5a.

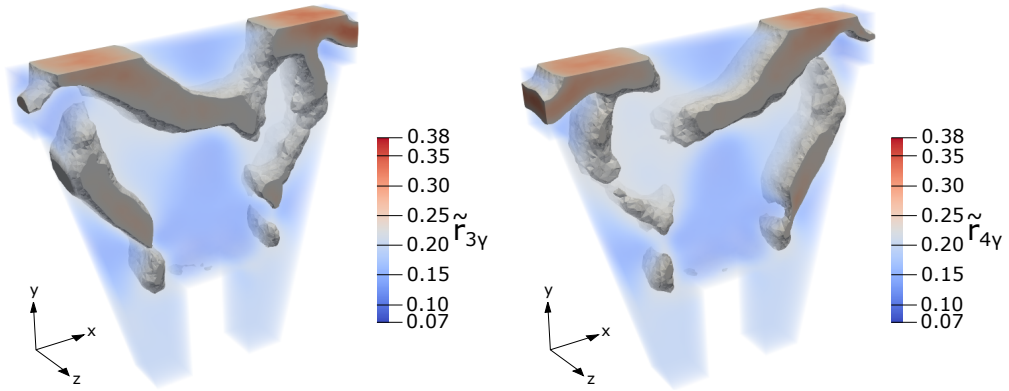
The error functional is evaluated as a weighted sum of the squared differences between the displacement of the target surfaces and their corresponding prescribed target displacements. Bound constraints have been imposed on the stacked vector of control variables so that the search is confined to the precomputed material space. Static equilibrium mechanics govern the linear elastic response. There is no prescribed design volume constraint.

8.1.2 Results and Discussion

The optimal distribution of radii parameters at termination of the search are displayed in Figs. 8.3 and 8.4 for the diagonal and face members respectively. To facilitate visual-



(a) Member 1, $r_{viz} = 0.22$ (b) Member 2, $r_{viz} = 0.22$



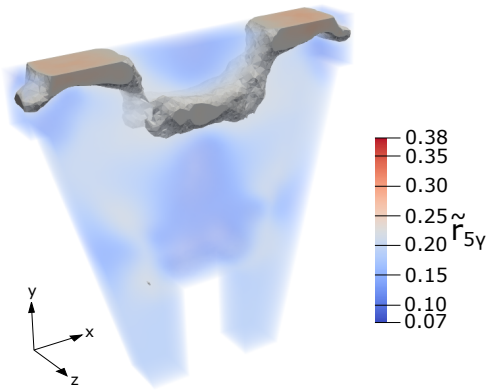
(c) Member 3, $r_{viz} = 0.22$ (d) Member 4, $r_{viz} = 0.22$

Figure 8.3: Two-prong gripper: Optimal radii distribution for diagonal members 1–4

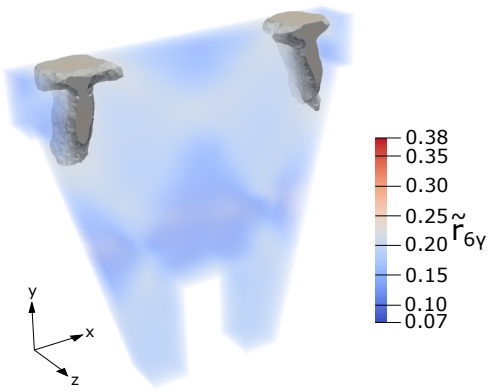
ization, a threshold has been set so that $r_{viz} = 0.22$. The solid regions in the solutions depict $r_{i\gamma} \geq 0.22$. The pale blue regions depict regions where $r_{min} \leq r_{i\gamma} < 0.22$.

Macroscopically, the radii distributions yield a volume fraction distribution that forms a compliant mechanism that allows the target deformations to be attained as shown by Fig.8.6a. To facilitate a description of the mechanism, the region connecting the two Dirichlet boundary conditions will be referred to as the actuation shaft.

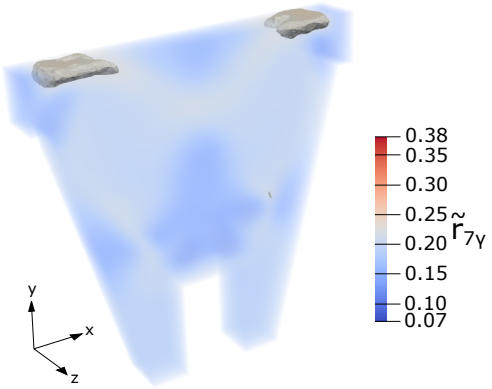
As in the cases above, the diagonal members demonstrate symmetry similarities in radii distribution by virtue of their orientation. Members 1 and 4 (Figs. 8.3a and 8.3d) feature dominant-radii region on the far side of the gripper which actuates the gripper jaws associated with target surface S_2. Members 2 and 3 (Figs. 8.3b and 8.3c) feature a similar region on the left which actuates the gripper jaw associated with target surface, S_1. Member 5, oriented collinearly with the direction of the external displacements, features a radii dis-



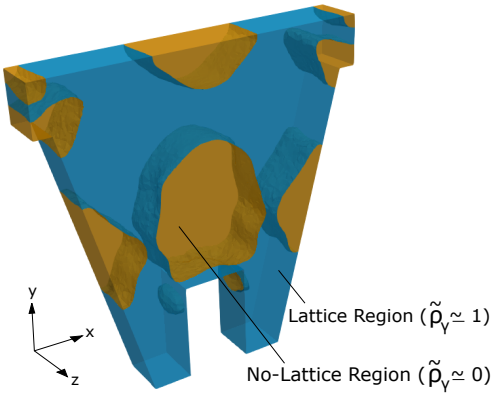
(a) Member 5, $r_{viz} = 0.22$



(b) Member 6, $r_{viz} = 0.22$

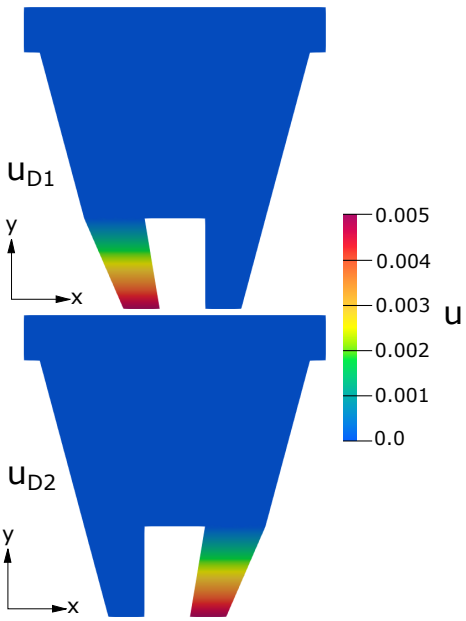


(c) Member 7, $r_{viz} = 0.22$

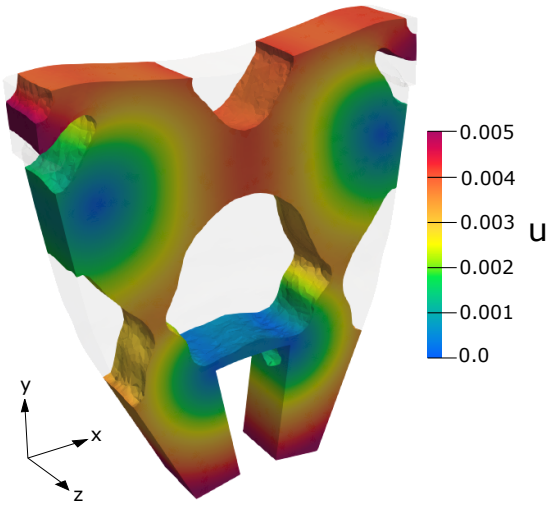


(d) Post-processed pseudo–lattice–density distribution

Figure 8.4: Two-prong gripper: Optimal radii distribution for face members 5–7

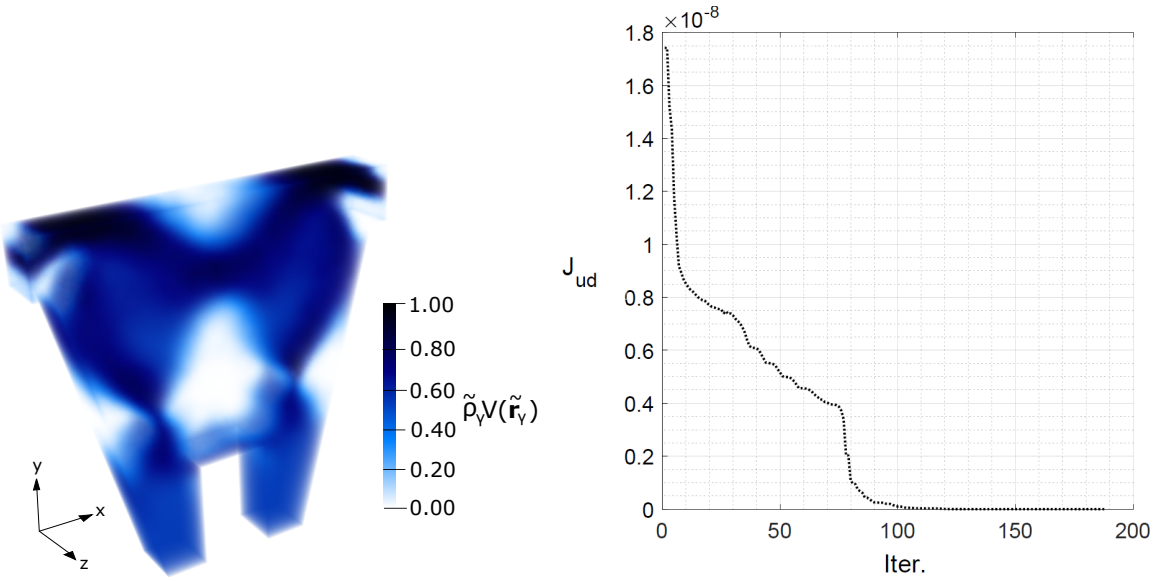


(a) Prescribed Target deformations



(b) Deformed Two-prong gripper

Figure 8.5: Two-prong gripper: Displacement Target



(a) Volume fraction distribution (b) Lattice-based optimization convergence plot

Figure 8.6: Two-prong gripper: Lattice-based material distribution and optimization convergence plot

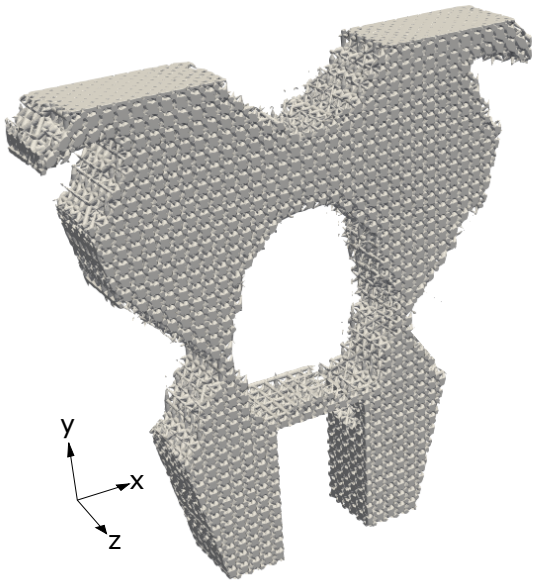


Figure 8.7: Two-prong gripper: Lattice Reconstruction

tribution that offers less resistance to the applied displacements along the actuation shaft. The radii distribution of Member 6 connects the dominant regions of the diagonals to the actuation shaft. Finally, Member 7 does not contribute significantly to attaining the target displacements by virtue of its orientation hence features no regions of dominance. The pseudo–lattice–density function defines the macroscale lattice density distribution, which

enable the gripper to attain the target deformations by describing regions of void or lattice. Figure 8.6b shows the optimization convergence plot for the gripper. It demonstrates that the error functional is minimized until the target deformations are attained as shown in Fig. 8.5b. The macroscale topology of the two-prong gripper is similar to that attained by Zhu et al. [20], however via a lattice-based multiscale framework that freely optimizes material point properties in the space of the lattice micro-parameters. An investigation of the optimal solution domain consists of cubic and orthotropic lattice micro-architectures. Figure 8.7 shows the lattice reconstruction derived given radii distributions.

8.2 Case 5: Three-prong gripper

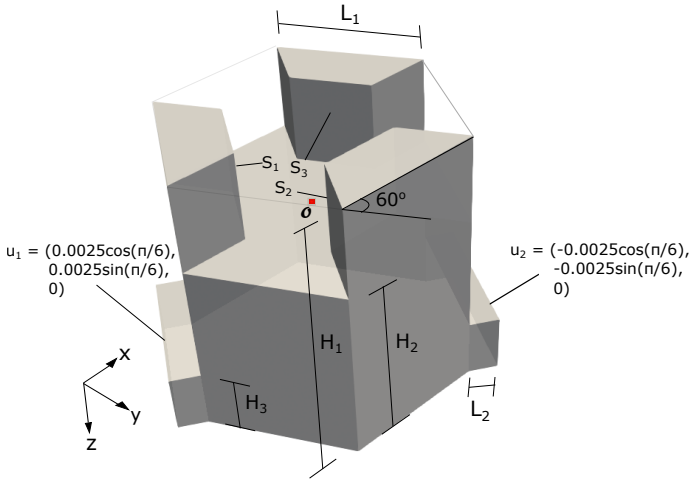


Figure 8.8: Three-prong gripper

Domain	
Design region	Full
L_1, L_2	0.025, 0.005 m
H_1, H_2, H_3	0.045, 0.030, 0.010 m
Design space volume, V	5.99×10^{-5} m^3
Base material, E_s, ν	209 GPa, 0.3
Mesh discretization	
Element type	Unstructured tetrahedral
No. of design nodes, N_n	126688 of 126688
No. of variables	$8 \times N_n$
Optimization settings	
Starting point, $r_{i\gamma}$, ρ_γ	0.113, 1
Bound constraints, r_{min}, r_{max}	0.07, 0.38
Bound constraints, ρ_{min}, ρ_{max}	0, 1
Filter radius, z	0.001
Step-size update strategy	Adaptive
Pseudo–lattice–density function penalization	$p = 3$
Volume constraint, V_D	–
Max. Iter.	450
Obj. Tol.	1×10^{-5}

Table 8.2: Three-prong gripper: Problem Definition

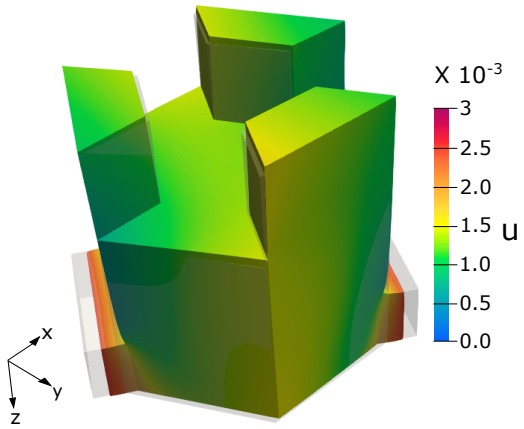


Figure 8.9: Three-prong gripper: Displacement, u (m) at Iteration 1

8.2.1 Problem Definition

Consider the three-prong gripper with material properties and Dirichlet boundary conditions specified in the problem definition of Fig. 8.8 and Table 8.2. The displacement profile attributed to the imposed conditions at the beginning of the optimization search is shown in Fig. 8.9. The goal of the optimization is to minimize the error functional between this displacement profile and predefined target displacements. For this multi-objective problem, three target displacements are defined, u_{D1}, u_{D2} and u_{D3}, defined mathematically within the design domain as

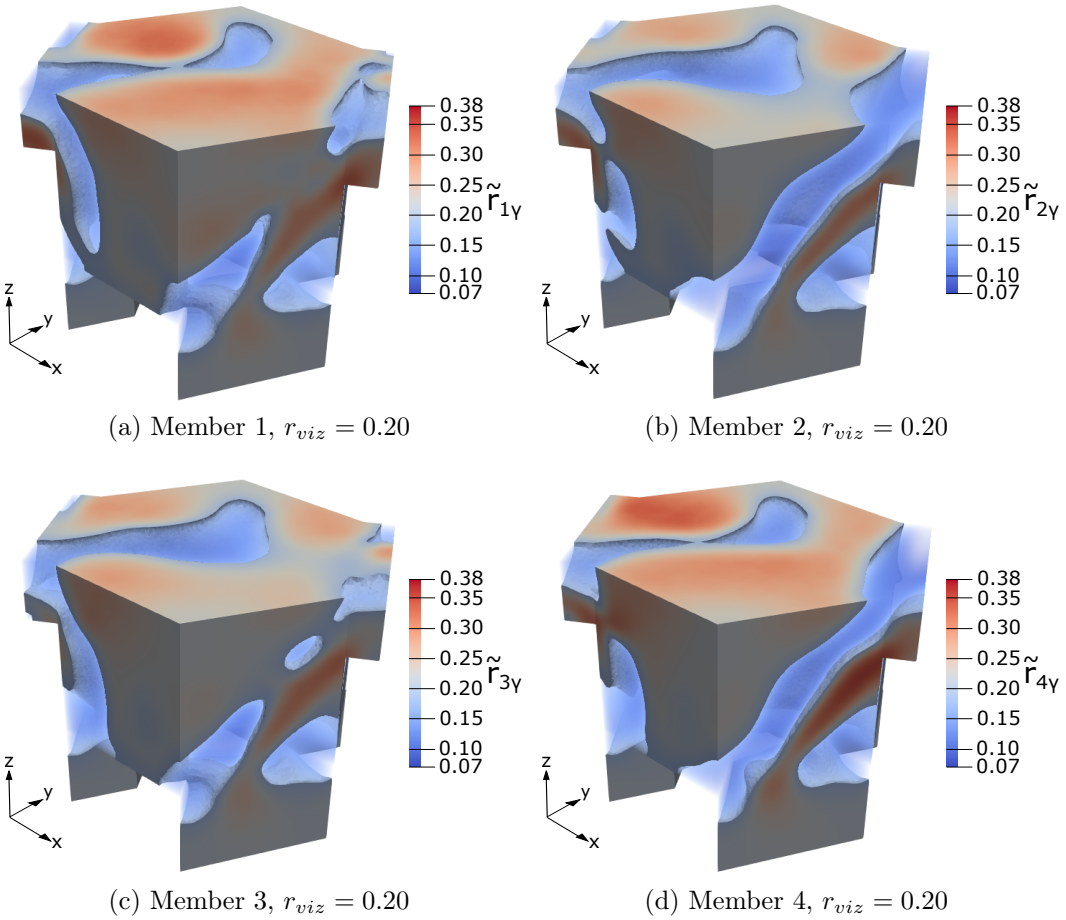
$$u_{D1}(x,y,z) = \begin{cases} (-0.17\cos(\frac{\pi}{6})z, -0.17\sin(\frac{\pi}{6})z, 0) & \text{if } x<0,\ \ y<0.001,\ \ z<0 \\ (0,0,0) & \text{everywhere else} \end{cases} \tag{8.3}$$

,

$$u_{D2}(x,y,z) = \begin{cases} (0, -0.17\cos(\frac{\pi}{6})z, 0) & \text{if } y>0,\ \ z<0 \\ (0,0,0) & \text{everywhere else} \end{cases} \tag{8.4}$$

and

$$u_{D3}(x,y,z) = \begin{cases} (0.17\cos(\frac{\pi}{6})z, -0.17\sin(\frac{\pi}{6})z, 0) & \text{if } x>0,\ \ y<0.001,\ \ z<0 \\ (0,0,0) & \text{everywhere else} \end{cases} \tag{8.5}$$



(a) Member 1, $r_{viz} = 0.20$

(b) Member 2, $r_{viz} = 0.20$

(c) Member 3, $r_{viz} = 0.20$

(d) Member 4, $r_{viz} = 0.20$

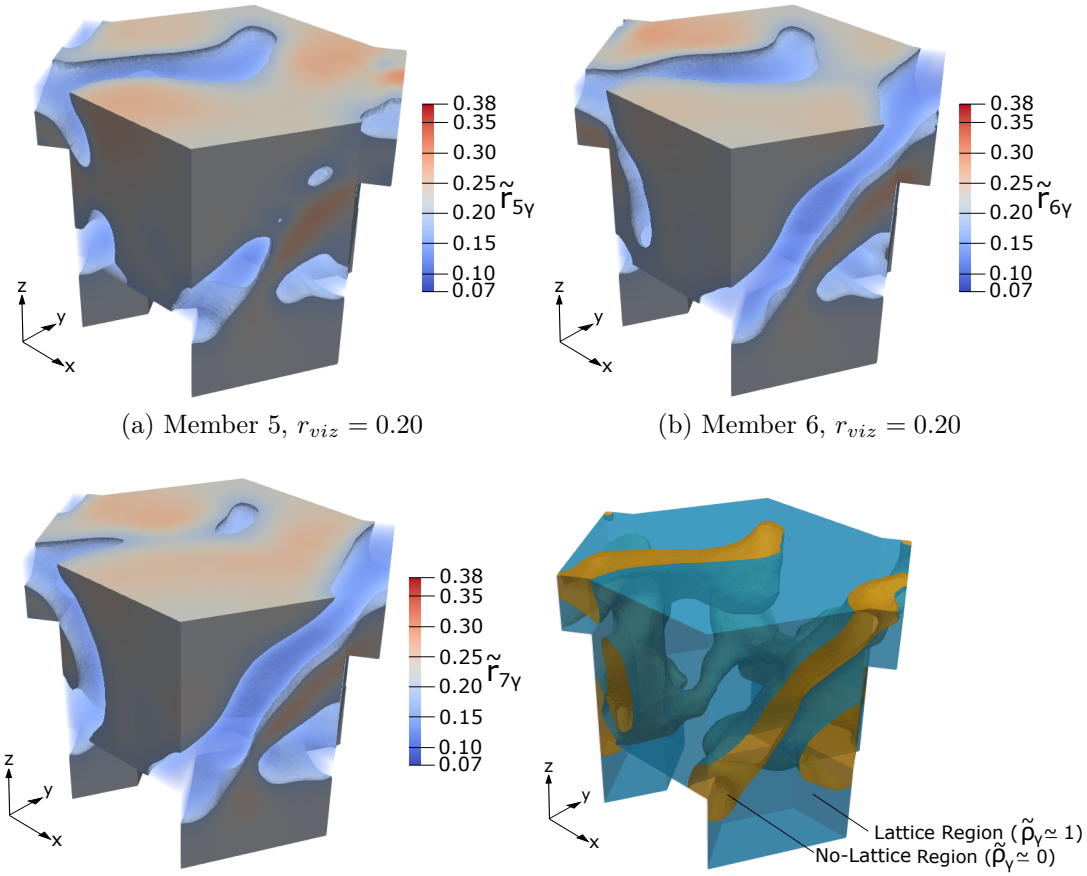
Figure 8.10: Three-prong gripper: Optimal radii distribution for diagonal members 1–4

respectively.

Three target surfaces, S_1, S_2 and S_3 can be identified in Fig. 8.8 which define the relevant nodes for error minimization. The target displacement distributions of Eqns. 8.3, 8.4 and 8.5 are shown in Fig. 8.12a.

As in the two-prong gripper test case, the error functional is evaluated as a weighted sum of the squared differences between the displacement of the target surfaces and their corresponding prescribed target displacements. Bound constraints have been imposed on the stacked vector of control variables to confine the search within the precomputed material space. Static equilibrium mechanics govern the linear elastic response. There is no prescribed design volume constraint. Where the displacements of the gripper jaws for the two-prong gripper were designed to lie in the plane of the prescribed Dirichlet

boundary conditions, this case features out-of-plane target displacements so that the three prongs move towards each other and out of the plane of the Dirichlet conditions.



(a) Member 5, $r_{viz} = 0.20$

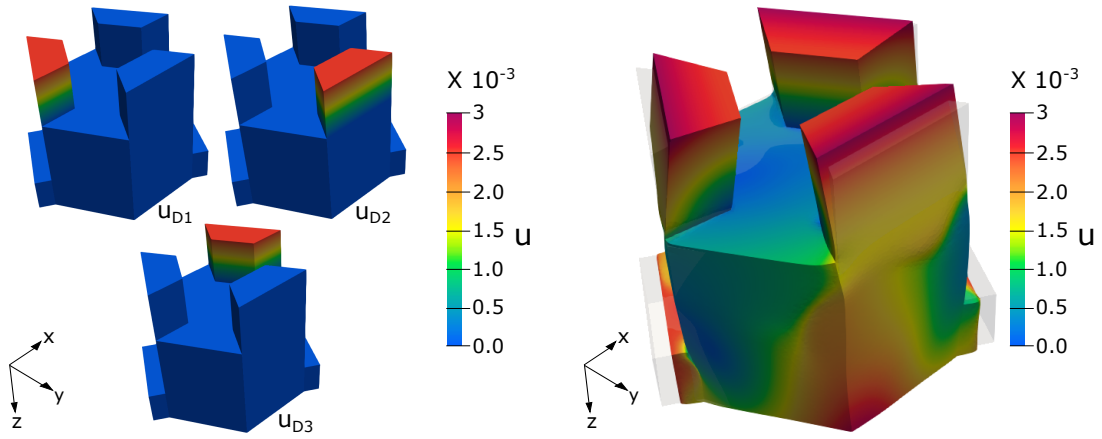
(b) Member 6, $r_{viz} = 0.20$

(c) Member 7, $r_{viz} = 0.20$

(d) Post-processed pseudo–lattice–density distribution

Figure 8.11: Three-prong gripper: Optimal radii distribution for face members 5–7

To exploit the capability of the framework for material point design, the three-prong gripper is positioned such that the orientation of its actuation shaft does not coincide with the axis of any of the micro-architecture lattice members. The optimal distribution of radii parameters at optimization convergence are shown in Figs. 8.10 and 8.11 for the diagonal and face members respectively. To facilitate visualization, a threshold has been set so that $r_{viz} = 0.20$. The solid regions in the solutions depict $r_{i\gamma} \geq 0.20$. The pale blue regions depict regions where $r_{min} \leq r_{i\gamma} < 0.20$.

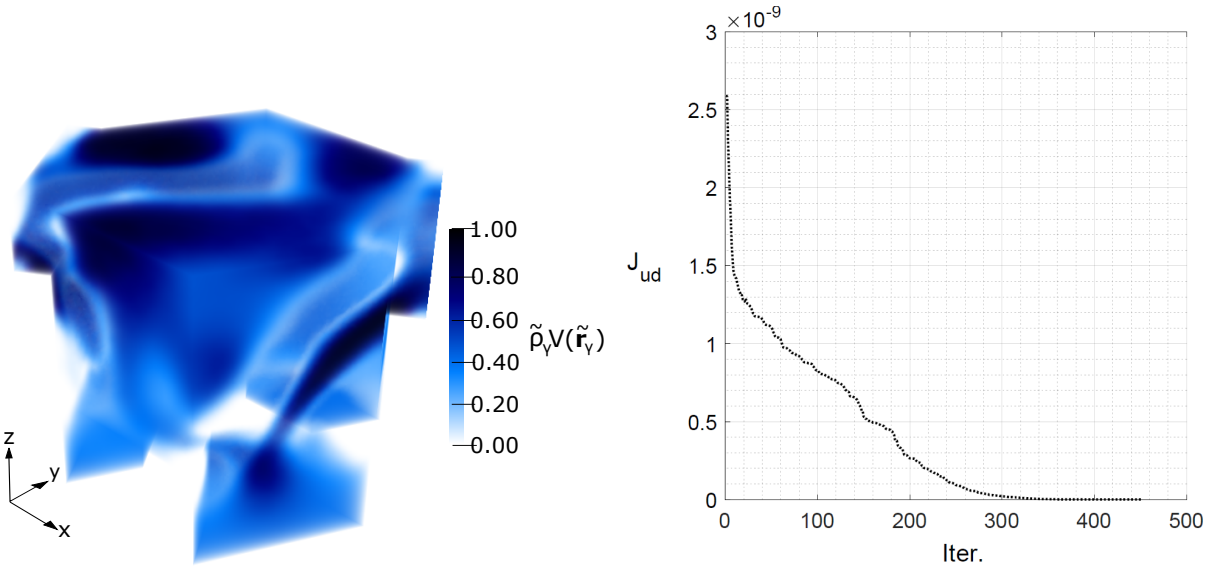


(a) Prescribed Target deformations (b) Deformed Three-prong gripper

Figure 8.12: Three-prong gripper: Displacement Target

8.2.2 Results and Discussion

Macroscopically, the radii distributions yield a volume fraction distribution that forms a mechanism that allows the target deformations to be attained as shown by Fig.8.13a.



(a) Volume fraction distribution (b) Lattice-based optimization convergence plot

Figure 8.13: Three-prong gripper: Lattice-based material distribution and optimization convergence plot

The diagonal members demonstrate regional symmetries in radii distribution by virtue of their orientation as shown by Fig. 8.10. All members demonstrate regions of dominance since their orientations present components in the necessary directions to facilitate the

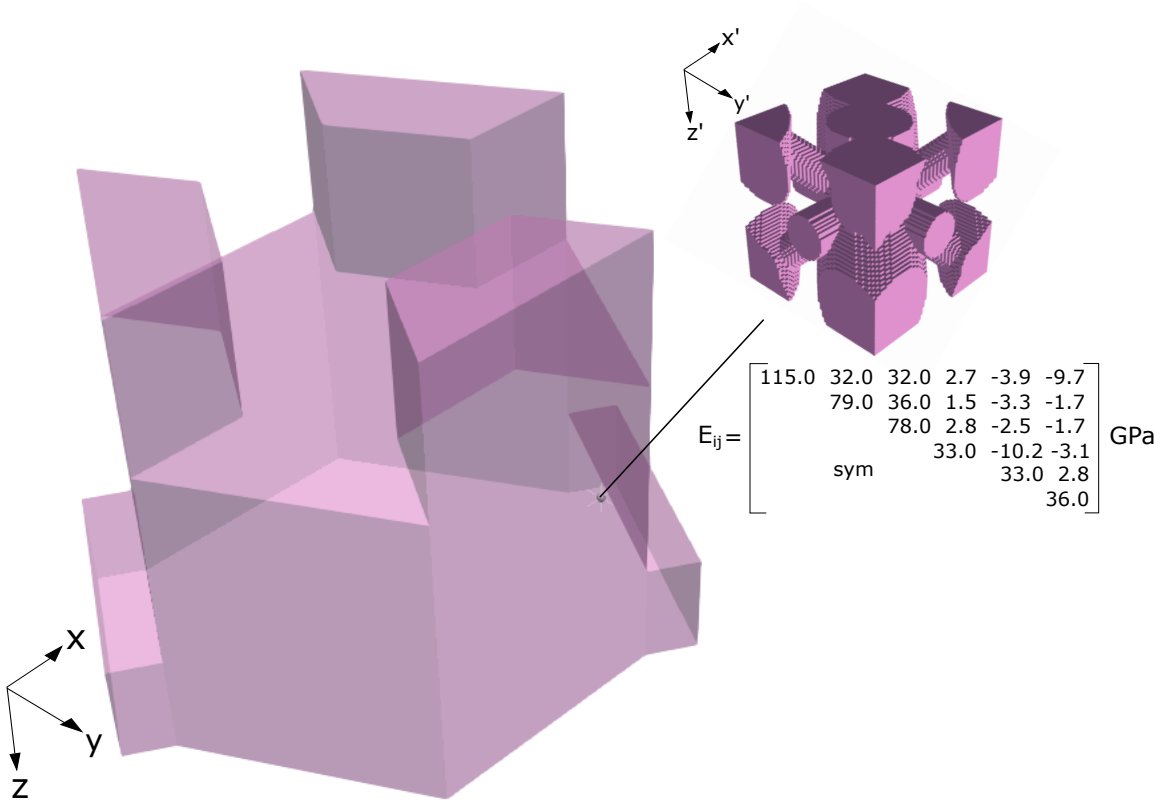


Figure 8.14: Local anisotropic micro-architecture

fulfillment of the objective. The diagonal members generally have higher radii values in the regions of dominance than the face members (8.11). The pseudo–lattice–density function defines the macroscale lattice density distribution, which enables the gripper to attain the target deformations. Figure 8.13b shows the optimization convergence plot for the gripper. It demonstrates that the error functional is minimized until the target deformations are attained on the relevant target surfaces as shown in Fig. 8.12b.

At the optimal solution, the lattice micro-architectures within design domain were investigated. It is observed that fully anisotropic micro-architectures exist within the design domain that facilitate the attainment of the macroscale multi-objective target displacements as shown at nodal location $\boldsymbol{x} = (0.020874, 0.008266, 0.023735)$ in Fig. 8.14. Infact, the solution features orthotropic, cubic and anisotropic micro-architecture as enabled by the micro-architecture parameterization. This is a significant result since a means is derived to achieve local anisotropic properties with a corresponding manufacturable micro-architecture. This test case demonstrates the derivation of an optimal solution

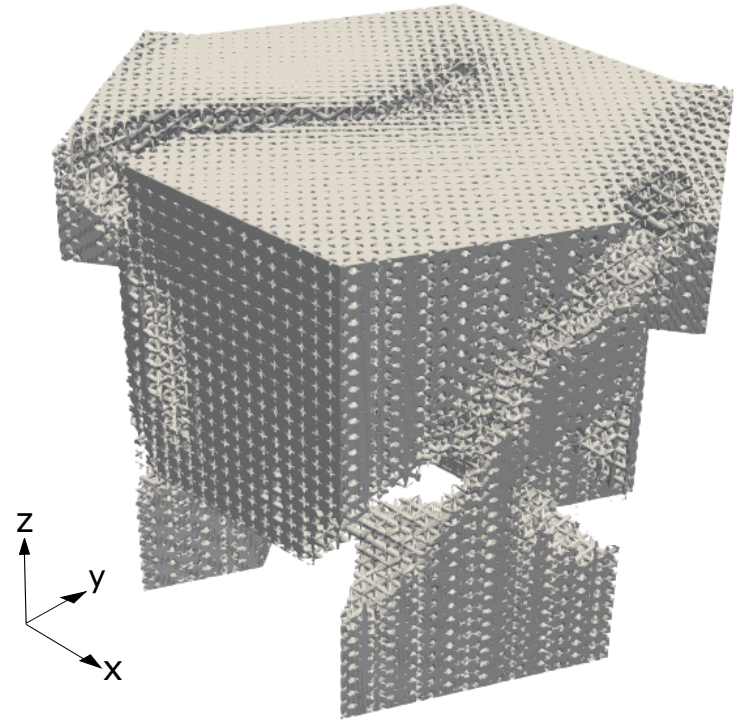


Figure 8.15: Three-prong gripper: Lattice reconstruction

with full control over all aspects of anisotropy afforded by the parameterization implemented. Figure 8.15 shows the lattice reconstruction derived given radii distributions.

8.3 Structural Optimization: Summary of results

In the last two chapters, the capacity of the derived multiscale framework is demonstrated for free material structural optimization in the space of lattice micro-parameters. The optimal solutions attained for the compliance minimization problems are consistently better than obtained by the SIMP methodology. The derived method is applicable to real-world problems. More difficult multi-objective optimization problems are solved and the capacity for full control of local anisotropy is demonstrated. This class of problems cannot be achieved by methodologies based on isotropic material law. The solutions can be physically realized by additive manufacturing.

Chapter 9

Thermal and Thermo-structural Optimization

Having conveyed the capability of the framework to structural optimization, this chapter demonstrates further extensions to the class of problems that can be solved by the derived framework. The following test case minimizes the average temperature (also referred to as thermal compliance) in a restricted heat-generating design domain given a constraint on the availability of heat-conducting material towards a heat sink.

9.1 Case 6: Cylindrical Heat Sink

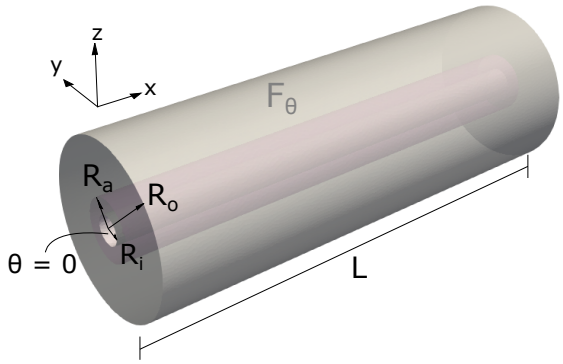


Figure 9.1: Cylindrical Heat Sink

Domain	
Design region	Restricted
R_i, R_a, R_o, L	0.12, 0.25, 0.70, 4 m
Design space volume, V	5.37 m^3
Heat Source, F_θ	1 Wm^{-3}
Base material, K_s	40 $Wm^{-1}K^{-1}$
Mesh discretization	
Element type	Unstructured tetrahedral
No. of design nodes, N_n	117773 of 128255
No. of variables	$8 \times N_n$
Optimization settings	
Starting point, $r_{i\gamma}$, ρ_γ	0.113, 1
Bound constraints, r_{min}, r_{max}	0.07, 0.38
Bound constraints, ρ_{min}, ρ_{max}	0, 1
Filter radius, z	0.02
Step-size update strategy	Adaptive
Pseudo–lattice–density function penalization	$p = 3$
Volume constraint, V_D	$0.37 \times V$
Max. Iter.	150
Obj. Tol.	1×10^{-5}

Table 9.1: Cylindrical Heat Sink: Problem Definition

9.1.1 Problem Definition

Consider the Cylindrical Heat Sink (CHS) with thermal and geometric properties specified in the problem definition of Fig. 9.1 and Table 9.1. The design region generates an internal heat source, F_θ and a heat sink is defined at the internal surface of the hollow cylinder. A non-design region is specified about the internal surface as shown in Fig. 9.2. The temperature profile of the CHS is shown for the thermal properties specified at the beginning of the optimization search in Fig. 9.3. The goal of the optimization formulation is to determine the optimal layout of material that minimizes the thermal compliance of the design region of the cylinder. This optimization problem is constrained by the PDE that governs steady-state pure conduction phenomenon given by Eqn. 6.10. It is also subject to a constraint on the volume fraction of the optimized design, $V_D = 0.37$. Bound constraints on the components of the stacked vector of control variables confine

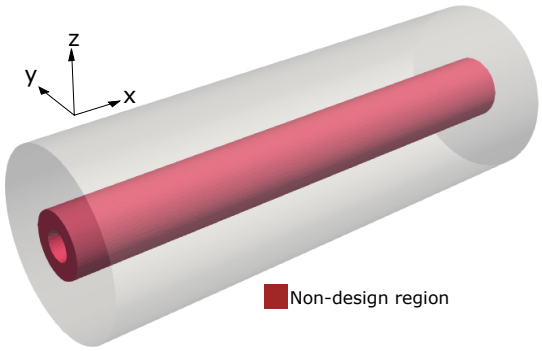


Figure 9.2: Cylindrical Heat Sink: Non-design region definition

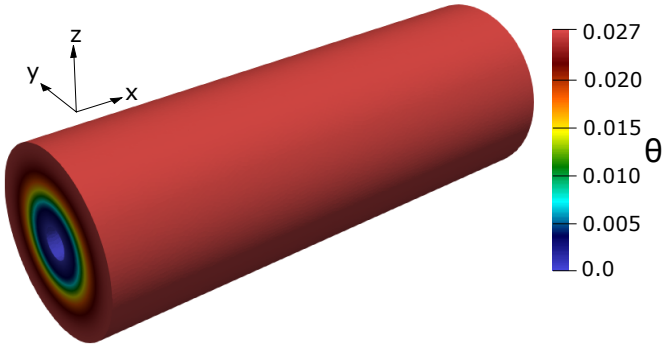


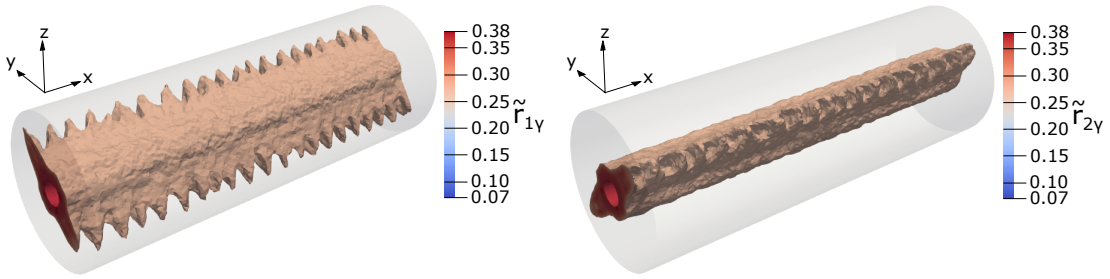
Figure 9.3: Cylindrical Heat Sink: Temperature, θ (K) at Iteration 1

the optimization search to the space of the precomputed thermal properties.

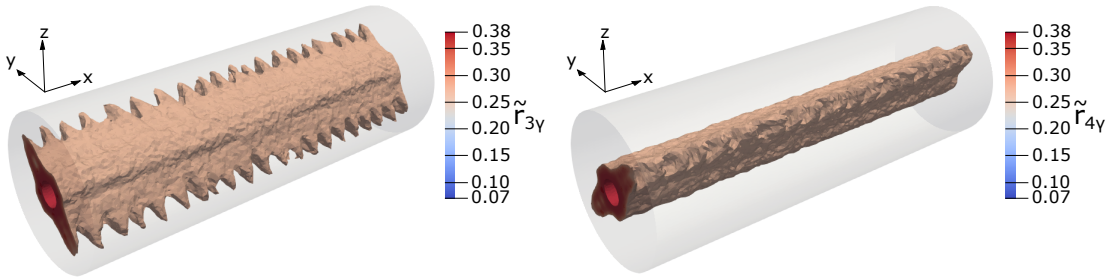
9.1.2 Results and Discussion

The optimal distribution of radii parameters at termination of the search are displayed in Figs. 9.4 and 9.5 for the diagonal and face members respectively. Visualization of the normalized radii distributions has been set such that, $r_{viz} = 0.25$. The solid regions in the solutions depict $r_{i\gamma} \geq 0.25$.

It can be observed that radii distributions of Member 1 and 3 are similar by virtue of their orientation. Similarly, Members 2 and 4 (Figs. 9.4b and 9.4d) share similar radii distributions. Member 5 (Fig. 9.5a) does not contribute significantly to the minimization of objective function since its orientation is co-linear with the centroidal axis. Members with orientations that facilitate the transfer of heat flux from the cylinder's design domain to the heat sink are those to which average temperature is most sensitive and hence the

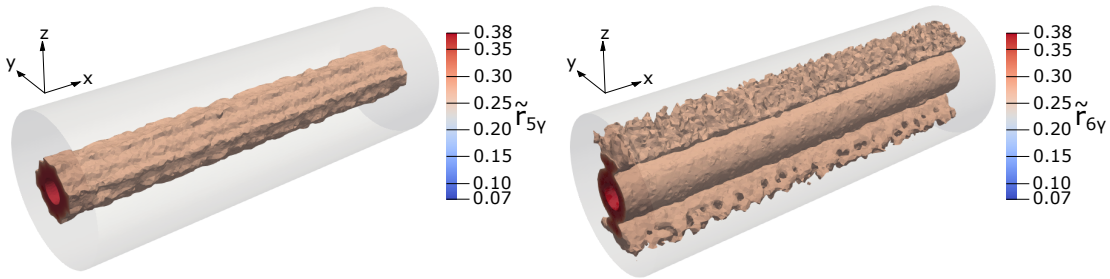


(a) Member 1, $r_{viz} = 0.25$ (b) Member 2, $r_{viz} = 0.25$

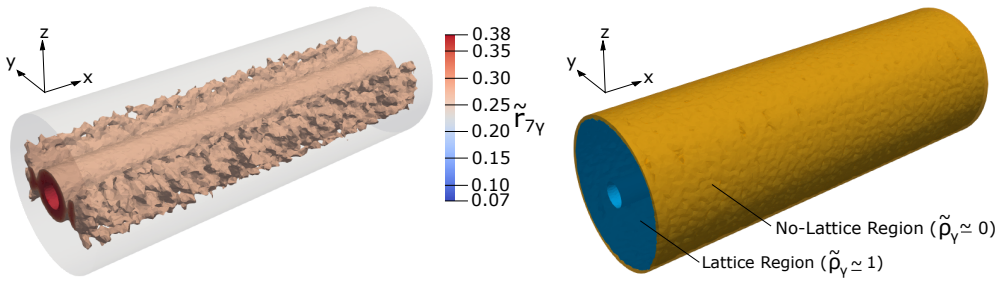


(c) Member 3, $r_{viz} = 0.25$ (d) Member 4, $r_{viz} = 0.25$

Figure 9.4: Cylindrical Heat Sink: Optimal radii distribution for diagonal members 1–4

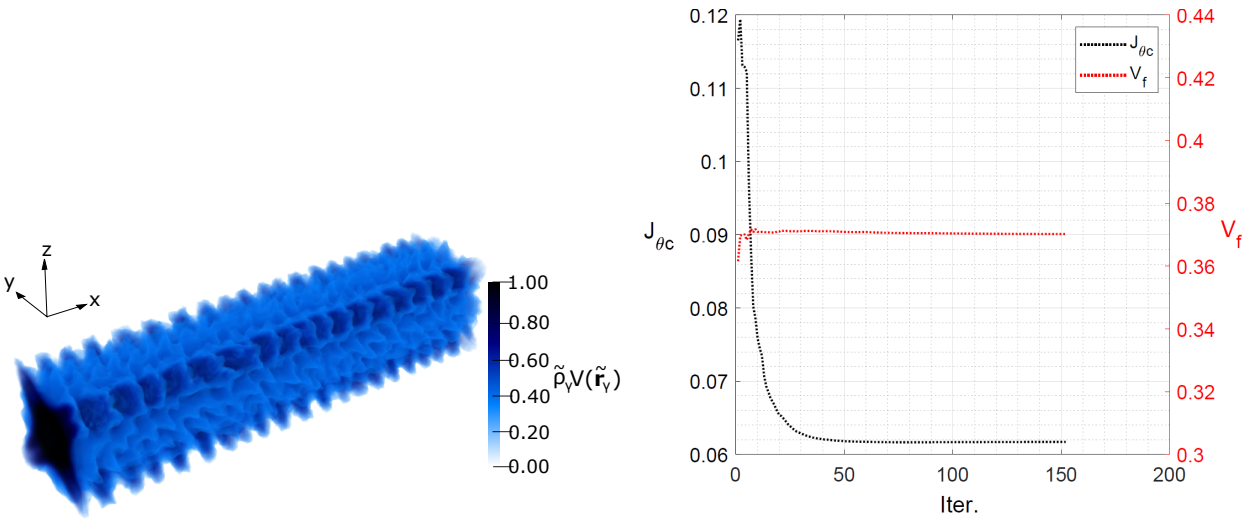


(a) Member 5, $r_{viz} = 0.25$ (b) Member 6, $r_{viz} = 0.25$



(c) Member 7, $r_{viz} = 0.25$ (d) Post-processed pseudo–lattice–density distribution, $r_{viz} = 0.7$

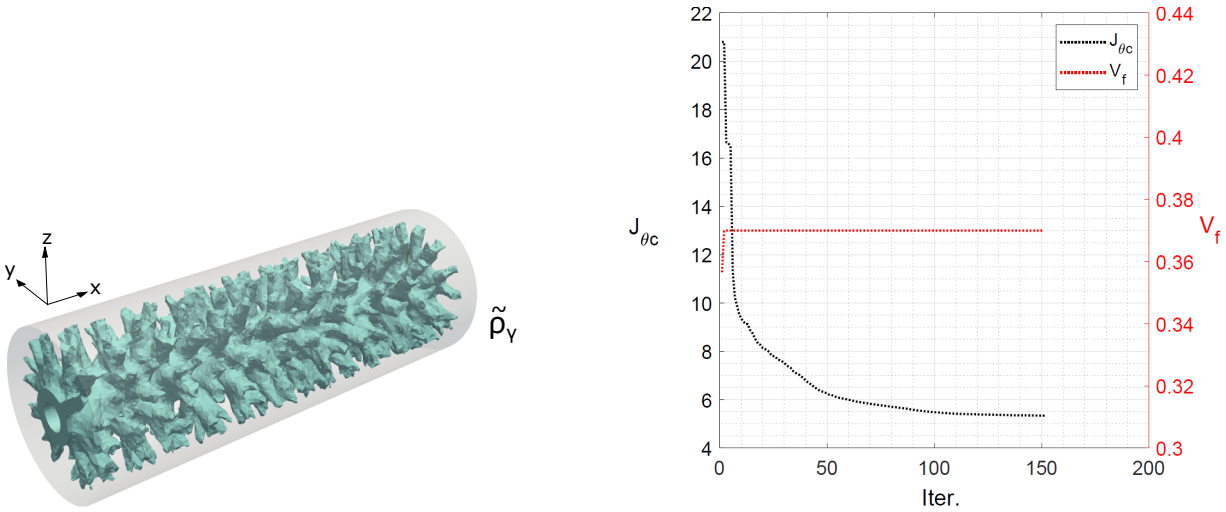
Figure 9.5: Cylindrical Heat Sink: Optimal radii distribution for face members 5–7



(a) Volume fraction distribution (b) Lattice-based optimization convergence plot

Figure 9.6: Cylindrical Heat Sink: Lattice-based material distribution and optimization convergence plot

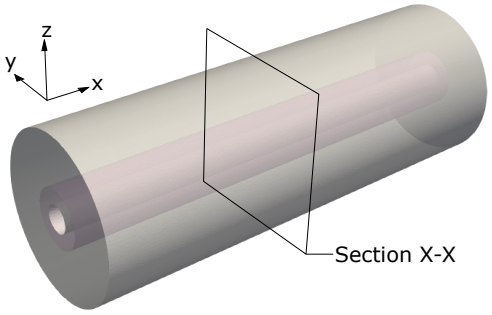
most dominant. Members 6 and 7 (Figs. 9.5b and 9.5c) have symmetric distributions differing only based on their respective orientations. The pseudo–lattice–density function (Fig. 9.5d), describing the macroscale lattice density distribution indicates that lattice is present in most of the design domain. The regions of no-lattice only exist at the radial extremities of the cylinder, where the magnitudes of the radii are mostly at the lower



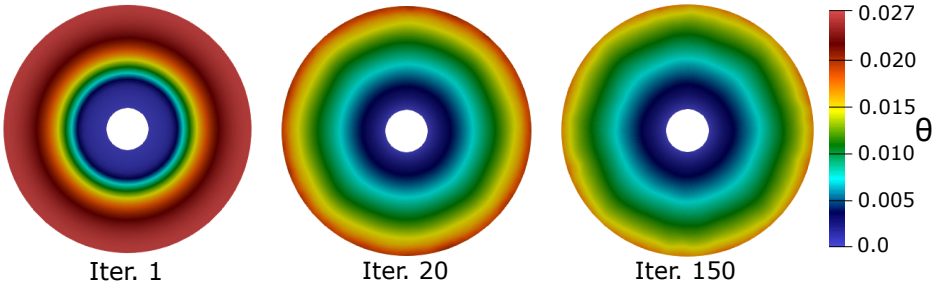
(a) Density distribution, $r_{viz} = 0.7$ (b) SIMP-based optimization convergence plot

Figure 9.7: Cylindrical Heat Sink: SIMP material distribution and optimization convergence plot

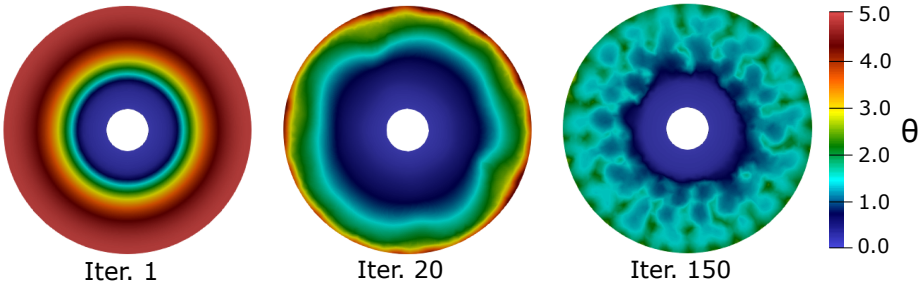
bound. The volume fraction distribution of Fig. 9.6a shows that, macroscopically, the layout of material corresponding to the radii distributions forms structured projections that link the design region to the sink, with increasing radii magnitude as the radial distance to the sink decreases. Lower member radii values at radial extremities increase the surface area of the members so as to increase the efficiency of heat conduction. The SIMP implementation for the same problem yields the material layout shown in Fig. 9.7a with finger-like projections branching out into the heat generating design domain. However, the projections are not structured as in the lattice-based implementation.



(a) Through-section X-X at plane (2, y, z)



(b) Lattice-based temperature evolution



(c) SIMP-based temperature evolution

Figure 9.8: Cylindrical Heat Sink: Section X-X showing temperature evolution through iterations

The SIMP framework also commences the search from a much higher objective value due to the penalization associated to the density function. More importantly, the thermal

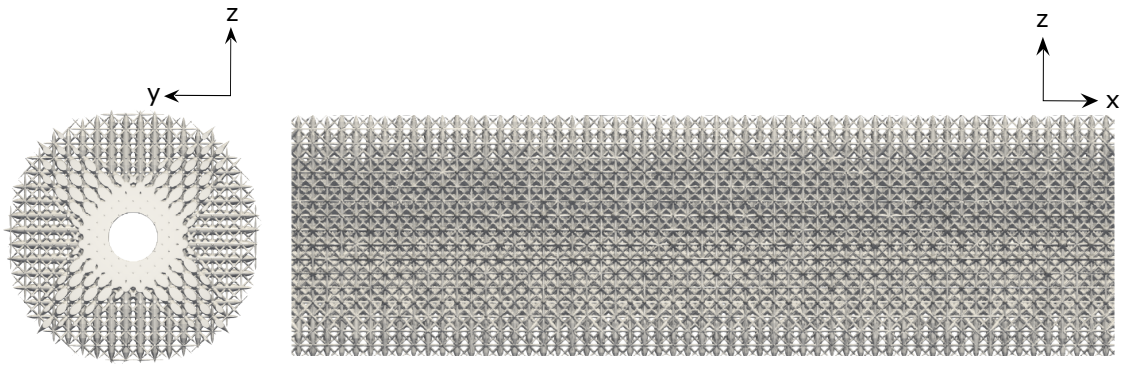


Figure 9.9: Cylindrical Heat Sink: Lattice Reconstruction

compliance, $J_{\theta c}$ attained at termination for the lattice-based approach is 0.062 WK. The SIMP methodology yields a thermal compliance of 5.34 WK at optimization convergence. The optimization convergence plots of the implementation are shown in Figs. 9.6b and 9.7b for the lattice-based and SIMP-based implementations respectively. It is of note to appreciate the significant improvement enabled by the lattice-based framework in the final objective function. The minimum thermal compliance attained by the lattice-based solution corresponds to a 98.8% reduction compared to the SIMP-based solution. Figure 9.8 shows the evolution of the temperature distribution against the optimization iterations at a through section X-X of the CHS for both approaches. Figure 9.9 shows the lattice reconstruction derived given radii distributions.

9.1.3 Thermal Optimization: Summary of results

By integrating the thermal property response surface models within the macroscale optimization framework, a means is derived to tailor macroscopic thermal properties in the space of lattice micro-parameters with significant improvement in the conductive efficiency of the layout. The solution is also manufacturable so that it demonstrates free material optimization in the space of producible structure.

9.2 Thermo-structural Optimization

In this section, the derived multiscale framework's capability is extended to the class of weakly-coupled thermo-structural optimization problems. The following test case minimizes the structural deformation of specific boundary surfaces of a restricted design domain as the structure expands under thermal load.

9.3 Case 7: Hollow-pipe section

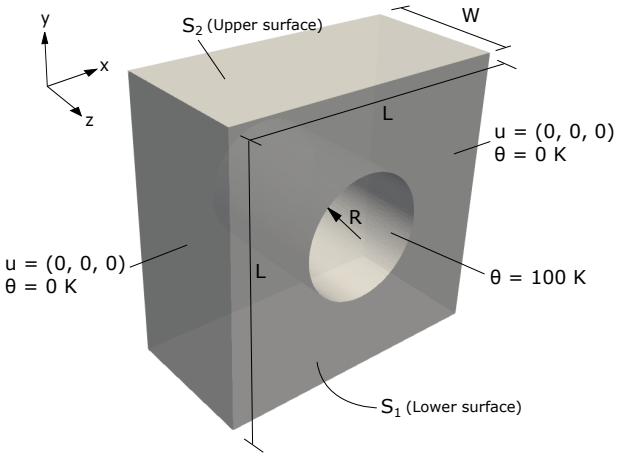


Figure 9.10: Hollow-pipe section

9.3.1 Problem Definition

Consider a 25 mm-section of a square hollow pipe (HPS) with material properties and Dirichlet boundary conditions specified in the problem definition of Fig. 9.10 and Table 9.2. Given the displacement and temperature boundary conditions as shown, the steady-state temperature profile is projected unto the deformed domain mesh according to the displacement distribution – a consequence of the thermo-structural coupling as introduced in Sec. 6.3.3 (see Fig. 9.12). Observe that due to the Dirichlet boundary conditions imposed on the near and far-side surfaces, the bottom and top surfaces, S_1 and S_2 bulge out of the x–z plane as the structure expands under thermal load. The goal of the

Domain	
Design region	Restricted
L, W, R	0.05, 0.025, 0.011 m
Design space volume, V	5.3×10^{-5} m^3
Base material, E_s, K_s, ν	209 GPa, 40 Wm^{-1}K^{-1}, 0.3
Mesh discretization	
Element type	Unstructured tetrahedral
No. of design nodes, N_n	62458 of 67265
No. of variables	$7 \times N_n$
Optimization settings	
Starting point, $r_{i\gamma}$	0.113
Bound constraints, r_{min}, r_{max}	0.07, 0.38
Filter radius, z	0.001
Step-size update strategy	Adaptive
Pseudo–lattice–density function penalization	–
Volume constraint, V_D	–
Max. Iter.	200
Obj. Tol.	1×10^{-5}

Table 9.2: Hollow-pipe section: Problem Definition

optimization is to minimize the deformation of the target surfaces, S_1 and S_2 along the y-axis. It is assumed that the non-displacement of these surfaces in the y-axis is critical to the optimal design of this section of the pipe and indeed the entire pipe length (not shown). A non-design region surrounds the hollow as shown in Fig. 9.11.

The error functional is evaluated as the squared difference between the y-component of the displacement distribution of the target surfaces, u_y and the y-component of a zero-displacement distribution within the domain of the pipe section. Bound constraints have been imposed on the stacked vector of control variables to confine the search within the precomputed mechanical and thermal property spaces. Static equilibrium mechanics as well as pure conduction steady-state phenomenon govern the thermo-structural response of the section.

There exists no penalized pseudo–lattice–density function for this problem so that lattice structure exists everywhere within the design domain between the bounds specified in

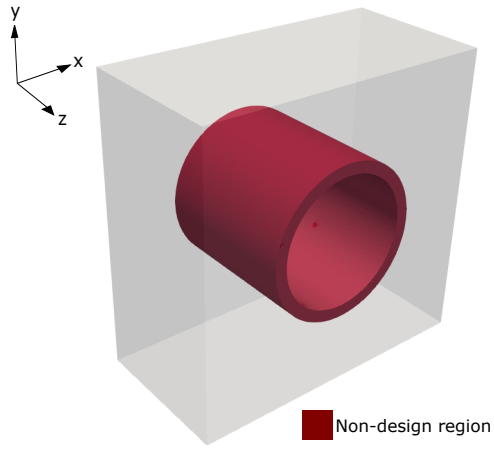


Figure 9.11: Hollow-pipe section: Non-design region definition

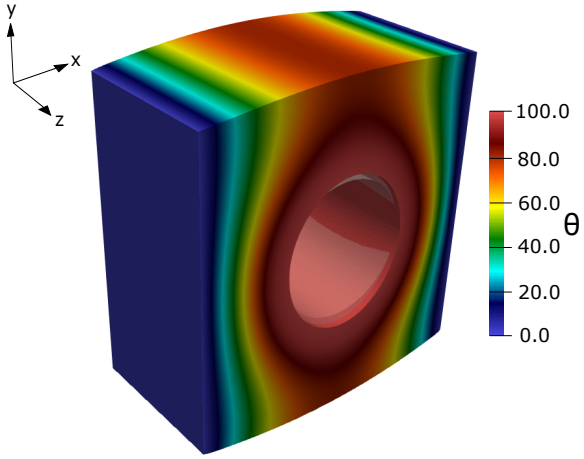


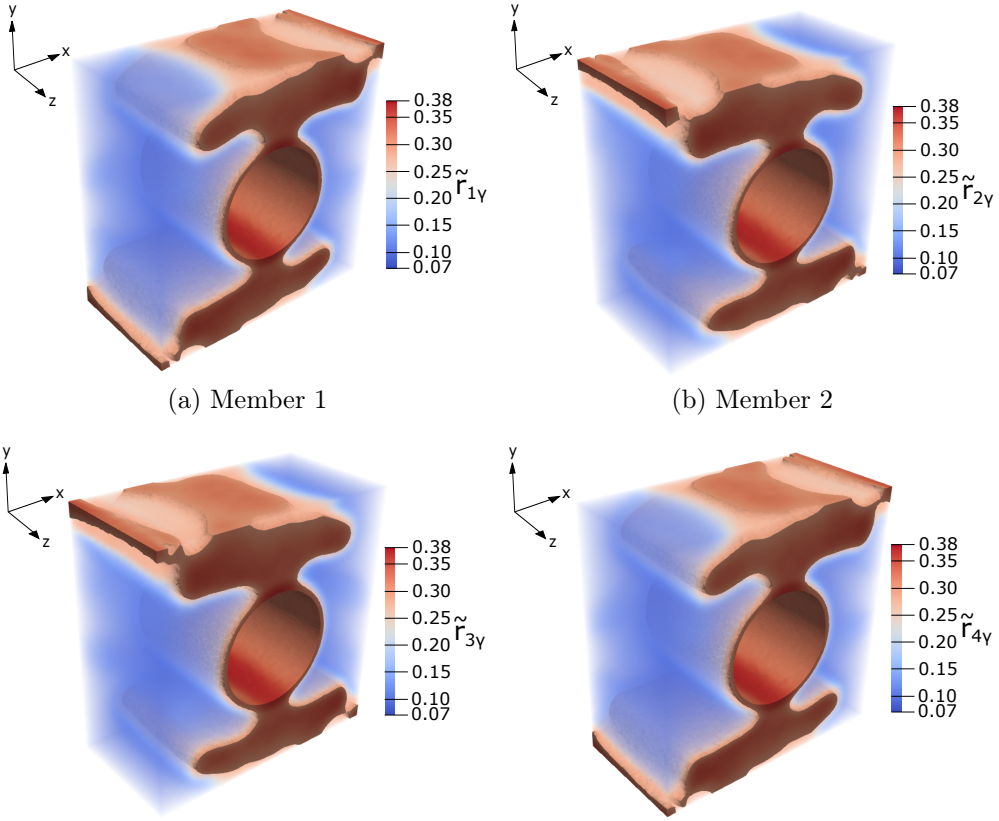
Figure 9.12: Hollow-pipe section: Temperature, θ (K) on deformed mesh at Iteration 1

Table 9.2. The emphasis is on the design of local structure within the macroscale towards satisfying the macroscale objective.

9.3.2 Results and Discussion

The optimal distribution of radii parameters at termination of the search are displayed in Figs. 9.13 and 9.14 for the diagonal and face members respectively. The solid regions in the solutions depict $r_{i\gamma} \geq 0.28$. The pale blue regions depict regions where $r_{min} \leq r_{i\gamma} < 0.28$.

The diagonal members demonstrate symmetries by virtue of their orientation as shown by Fig. 9.13. They also exhibit more dominance than the face members as they yield micro-architectures with properties suited to meeting the macroscale objective. Members 1 and



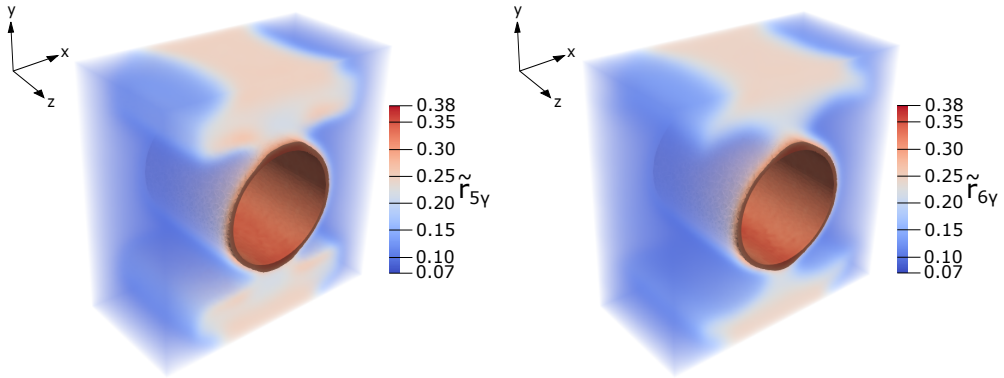
(a) Member 1 (b) Member 2

(c) Member 3 (d) Member 4

Figure 9.13: HPS: Optimal radii distribution for diagonal members 1–4

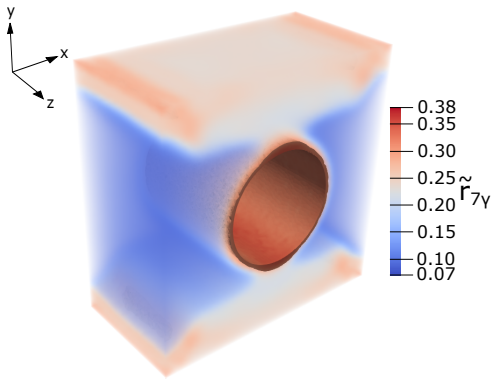
4 (Figs. 9.13a and 9.13d) conduct heat flux towards the bottom-half near-side heat sink as well as the top-half far-side heat sink. Members 2 and 3 (Figs. 9.13b and 9.13c) serve a similar purpose but are oriented to conduct heat flux towards the bottom-half far-side heat sink and top-half near-side heat sink. Recall that from the heat flux characterization of Sec. 4.7, diagonal members feature off-diagonal components in their conductivity matrices that essentially equips micro-architectures to transfer heat flux in orthonormal directions to temperature gradient. The consequence of this radii distributions can be appreciated in the steady-state temperature distributions of Fig. 9.15 where the steady-state temperature profile within the design domain is altered with the radii distributions such that the predefined non-displacement objective function is satisfied. The resulting orthotropic lattice micro-architectures offer increased macroscale conductivity towards the heat sink but also feature diagonals that can expand in non-critical directions.

The face members feature much lower radii values as shown in Fig. 9.14 within the design



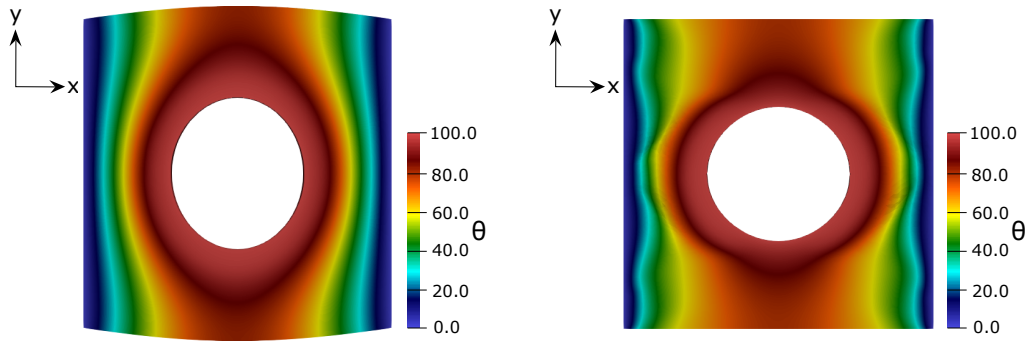
(a) Member 5

(b) Member 6



(c) Member 7

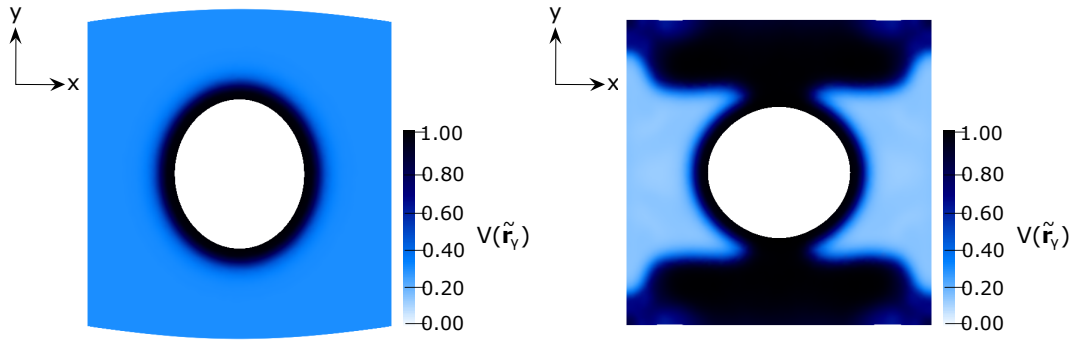
Figure 9.14: HPS: Optimal radii distribution for face members 5–7



(a) Starting temperature distribution on deformed mesh

(b) Final temperature distribution on deformed mesh

Figure 9.15: HPS: Temperature profile (Deformation Scale: 50:1)



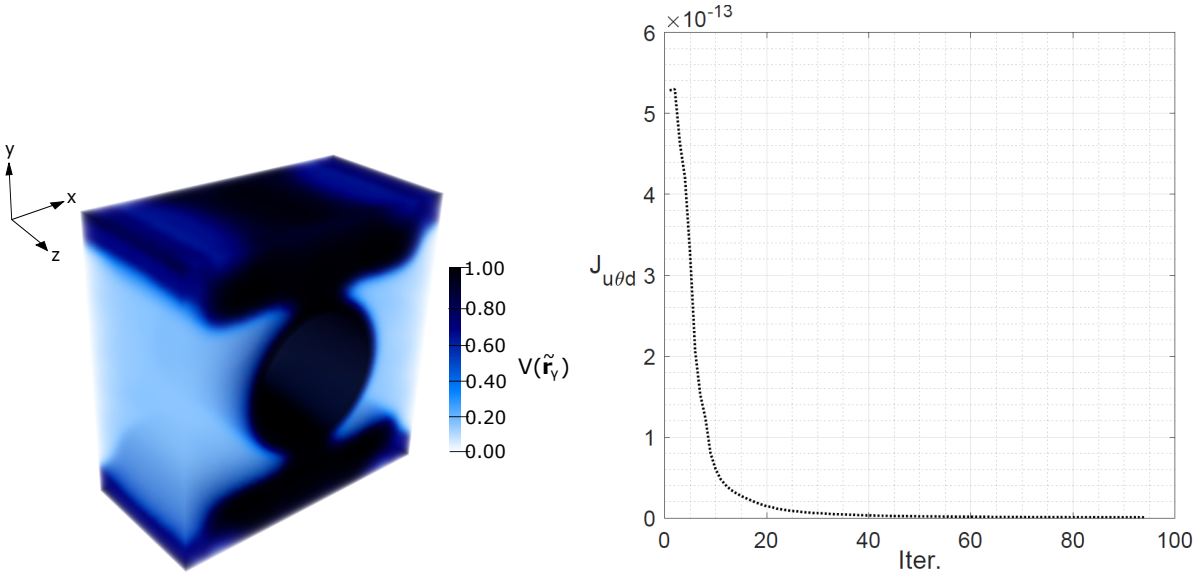
(a) Starting volume fraction on deformed mesh (b) Final volume fraction on deformed mesh

Figure 9.16: HPS: Volume fraction distribution (Deformation Scale: 50:1)

domain. Member 5 (Fig. 9.14a) is oriented to conduct heat towards the heat sink but cannot expand under thermal load due to the Dirichlet boundary conditions. Member 6 (Fig. 9.14b) works against the non-displacment objective, conducting heat flux towards the target surfaces and expanding in the y-directions. Member 7 (Fig. 9.14c) does not improve conductivity towards the heat sink. The displacement of the target surfaces is also insensitive to the thermal expansion of Member 7.

This capability exhibited by the orthotropic micro-architectures with diagonals to enhance macroscale conductivity in orthonormal directions to the temperature gradient is key to achieving the prescribed macroscale objective of this problem.

Figure 9.16 shows the volume fraction distribution at the starting point and the final iteration projected unto a deformed domain. An optimization convergence plot for the problem is shown in Fig. 9.17b. Figure 9.18 shows the lattice reconstruction derived given radii distributions.



(a) Volume fraction distribution (b) Lattice-based optimization convergence plot

Figure 9.17: HPS: Lattice-based material distribution and optimization convergence plot

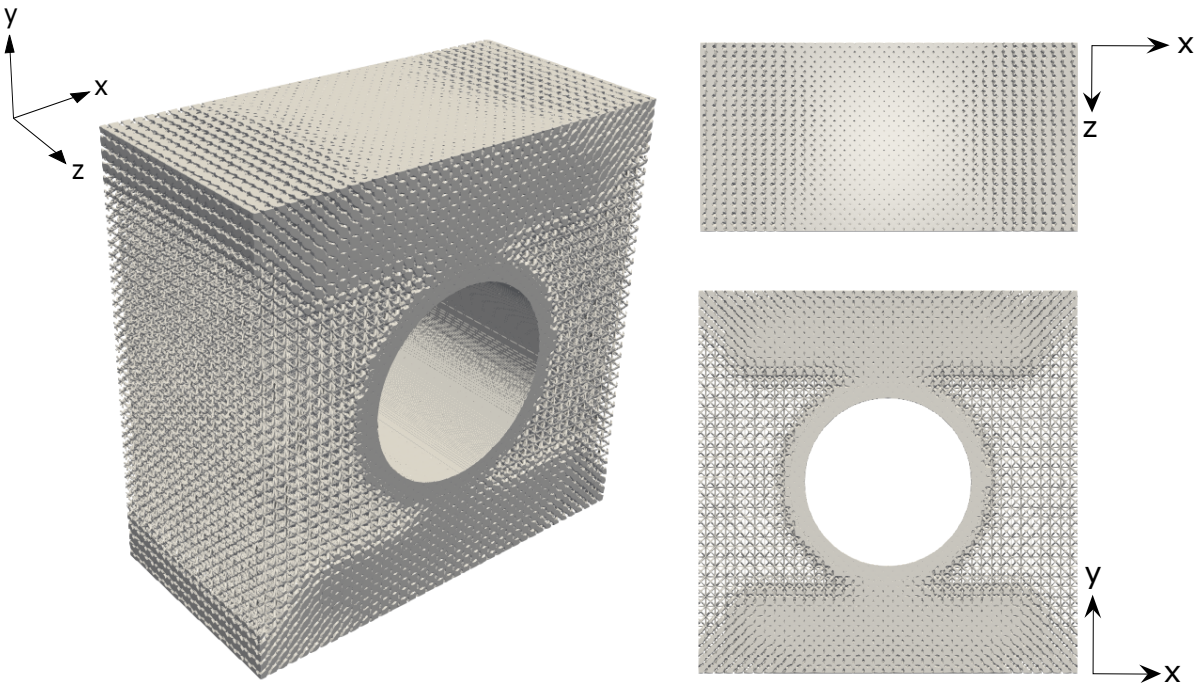


Figure 9.18: HPS: Lattice Reconstruction

9.3.3 Thermo-structural Optimization: Summary of results

In this chapter, the derived framework is demonstrated to be capable of solving thermo-structural optimization problems. The parameterization scheme implemented features diagonal members that support macroscale conductivity in orthonormal directions from temperature gradient directions so that macroscale properties can be tailored to meet predefined functional objectives. The potential for full control of anisotropic properties suggests that there exists a capability for solving multi-objective thermo-structural optimization problems.

Chapter 10

Conclusion

With recourse to the objectives for this work enumerated in Sec. 1.3, this Chapter summarizes the methods and results of this work. The key achievements of the work are clearly enumerated and the significance to the optimization community are highlighted. Limitations associated with the derived multiscale framework are described leading to inspiration for future works relevant to advancing the accuracy and efficiency of the framework.

10.1 Summary

A robust multiscale framework was derived for the structural, thermal and thermo-structural optimization of printable structures using lattice-based micro-architectures. Structured according to HMM, the framework was derived over two computational phases – a precomputation phase which featured the development of a lattice-based microscale model suited to additive manufacturing constraints and an optimization phase which executed structural and thermal tailoring of properties in the space of micro-architecture geometry parameters. By exploiting the homogenization theory, structural and thermal properties were derived given microscale lattice geometry parameters so that the properties represented material point properties within a large-scale design domain. The space

of material properties covered by the lattice parameterization was populated by a full-factorial design of experiments at only 5% of the computational cost of evaluating the entire full-factorial DoE - facilitated by micro-architecture symmetry considerations. Material property response surface models were generated so that microscale material properties were efficiently integrated into the macroscale optimization framework. By the method of adjoints, sensitivities of prescribed objectives to the lattice micro-architecture parameters were determined, facilitated by the readily differentiable explicit material response surfaces and the chain rule of differentiation. The outcome was the development of a variant of free material optimization executed in the space of physically realizable architected material properties. This work demonstrates the capacity of the framework for structural and thermal optimization as well as thermo-structural optimization through typical problem cases. In applicable cases, the lattice-based framework yielded better solutions than conventional SIMP strategies. Other cases demonstrate that the framework features full control over local anisotropy – a capability unachievable by optimization strategies based on isotropic material. The derived solutions are physically realizable through a process of lattice reconstruction given the optimal distribution of radii parameters. The precision and flexibility of additive manufacturing techniques have inspired the development of the framework and the realization of its optimal solutions.

10.2 Thesis Achievements and Significance

The following are key achievements of this work:

1. A lattice microscale model was developed. The model yields elastic and thermal properties given the lattice geometry parameters. The parameterization of the model supports smoothly changing material properties for slowly changing geometry micro-parameters so that there is no requirement for a computational investigation of connectivity of adjacent micro-architectures when it is integrated into the macroscale optimization framework. This is an advancement to works featuring discrete

mapping of micro-architectures in the domain of structures [10, 16, 20]. It is also suited to several additive manufacturing techniques since it features no enclosed volumes or suspended solids in void. This means that unsintered powder or uncured resin of SLS and SLA additive manufacturing techniques respectively are not trapped within the optimized geometry. Micro-architectures composed of struts and bending beams are known to cover a large material space and support the implementation of free material optimization in the space of physical geometry parameters where manufacturing constraints are imposed. Principal stress and heat flow characterization in this work demonstrates the suitability of the lattice parameterization to macroscale structural, thermal and thermo-structural optimization.

2. A library of elastic and thermal properties was generated for 823,543 lattice micro-architectures along with their volume fraction at the cost of only 5% of the full-factorial simulation cost. This was achieved by leveraging the existence of rotational and reflection symmetries associated with the implemented parameterization. The database of properties scales with Young's Modulus and thermal conductivity so that the framework remains valid for a different base material, provided the Poisson's Ratio for the new material is similar to the value implemented in this work. This database is available for analyses and for future optimization problems. Concurrent methods [56] have to re-evaluate point properties for new optimization endeavors – a waste of computational resources.

3. Response surface models were generated so that the material property evaluations within the macroscale optimization framework was efficient. The polynomial functions are readily differentiable explicit expressions convenient for the determination of sensitivities and ultimately gradient-based optimization. The result is a rapid evaluation of point material properties and efficient optimization schemes.

4. Macroscale optimization was executed in the space of microscale design parameters so that lattice micro-architecture were automatically generated as optimal radii distributions were determined. Single objective and multi-objective optimization prob-

lems were solved facilitated by the microscale model's capability for full control of locally anisotropic properties. The derived framework was applied to structural and thermal problems. Results obtained were consistently better than commonly implemented structural optimization strategies. Optimal solutions were manufacture-ready by 3-D printing techniques.

The results of this work demonstrate the capability for bespoke structural, thermal and thermo-structural optimization. The capacity for controlling local anisotropy is also a significant achievement of this work as structural and thermal properties can be tailored to satisfy multiple objectives such as morphing shape-change objectives and multi-objective compliance minimization problems. This access to anisotropic point properties is a significant advancement to the state-of-the-art where orthotropic material properties are used at best. The result is a more robust multiscale optimization scheme that is capable of solving difficult multi-objective problems. The optimal solutions attained also correspond directly to manufacturable lattice layout so that this work is a form of free material optimization in the space of physical lattice parameters. Classical FMO solutions [19, 13] are post-processed by a tape-layering technique which may introduce deviations in the physical structure from the optimized solution. Investigation of this possible loss of precision was not found in literature.

10.3 Limitations

The derived framework has its limitations. By definition, the theory of homogenization assumes an infinite scale separation so that the micro-architectures represent material point properties within the macroscale design domain. This work aims for an 'as-large-as-possible' separation of scales, however, computational and manufacturing constraints prevent the physical realization of an infinite scale separation. Computationally, there exists cost constraints that limit the fineness of the discretization of the macroscale domain where each node represents material point properties. Physically, there exists a constraint

on the minimum length scale for each base material for which the mechanical response of the material agrees with documented behavior, despite significant advancement in the precision of additive manufacturing techniques. As a consequence, this work admits that the realized physical optimized lattice structure is an approximation of the derived optimal solution.

This work makes reference to a penalized pseudo-lattice-density function that defines the lattice layout within the design domain of solutions. The optimal distribution of this function features small regions of intermediate values similar to that obtained for the pseudo-density function of the SIMP methodology. Post-processing of the data is required to obtain a clear description for the 'lattice or no-lattice' regions.

This work makes no considerations for stress constraints. Compliance minimization with volume constraints may yield optimal solutions with regions of impermissible stresses particularly for lattice structures which comprises of intersections of lattice members of different radii. In Sec. 4.3, Figs. 4.9 and 4.10 show that stress concentrations exist at lattice member intersections, constituting possible failure locations. Homogenized stresses on the macroscale do not capture the local stress concentrations. Local stress constraints suitable for optimization will have to be defined based on response surface models of local stress properties within the microscale model.

Thirdly, though the parameterization implemented in this work yields several advantages suited to additive manufacturing techniques, its performance against the Hashin-Shtrikman (HS) bounds presents room to improve the results obtained by the framework. Literature suggests that the requirements to satisfy additive manufacturing constraints yields three-dimensional micro-architectures with bulk and shear moduli off-set from the upper HS-bounds [122, 121].

This framework is based on linear elastic structural response and steady-state conduction phenomenon so that only small deformations are permissible. Also, for thermo-structural problems of this work, the temperature and displacement fields are only weakly coupled

so that the temperature field is not reliant on mechanical response. This is an approximation associated with thermo-mechanical analyses. Non-linear and transient considerations could expand the space of optimal solutions as interesting problems such as auxetic phenomenon may be attained by integrating the buckling of members.

10.4 Future Research Directions

Inspired by the limitations of this work and significant advancements in additive manufacturing, the derived framework has a promising future for the derivation of optimal lattice-based structures tailored to prescribed macroscale objectives.

The effective macroscale stress fields of this work do not capture the critical local stress evaluations required to monitor the integrity of the reconstructed lattice optimal solution. However, the necessary data was utilized in deriving the homogenized properties of the micro-architecture in the microscale model development. A merit function can be developed using the localized stress evaluations that yields critical stress values given the lattice parameters so that stress constraints can be integrated into the macroscale framework. This is the subject of current research. Full macroscale lattice simulations are also being investigated to validate the derived framework.

Advanced projection methods exist for the SIMP methodology that helps to eliminate the transition regions between solid and void [139]. These methods are equivalently suited to deriving a clear boundary for the macroscale lattice layout.

A systematic methodology can be developed to investigate optimal parameterization schemes that will generate three-dimensional micro-architecture geometries with properties that lie closer to the HS-bounds, bearing manufacturing constraints in mind. This will be a guaranteed approach to improve the results obtained in this work provided the parameterization satisfies the suitability requirements in this work such as micro-architecture connectivity and smoothly varying properties for smoothly varying geometry, e.t.c.

This work was aimed at the derivation of a thermal, structural and thermo-structural multiscale optimization strategy. However, the principles of HMM and the implementation of the homogenization theory used for this work can be applied to other fields such as acoustics, electro-magnetics, and the tailoring of structural properties to produce predefined resonant frequencies. Extending the methodology to non-linear elastic problems and fully coupled thermo-mechanical formulations has the potential to yield interesting capabilities. It also demonstrates promise for uncertainty quantification in the multiscale modelling of metamaterials.

Bibliography

[1] N. P. Van Dijk, K. Maute, M. Langelaar, and F. Van Keulen, "Level-set methods for structural topology optimization: A review," *Structural and Multidisciplinary Optimization*, vol. 48, no. 3, pp. 437–472, 2013.

[2] O. Sigmund and K. Maute, "Topology optimization approaches: A comparative review," *Structural and Multidisciplinary Optimization*, vol. 48, no. 6, pp. 1031–1055, 2013.

[3] T. Wu, K. Liu, and A. Tovar, "Multiphase topology optimization of lattice injection molds," *Computers and Structures*, vol. 192, no. November, pp. 71–82, 2017.

[4] L. Cheng, J. Bai, and A. C. To, "Functionally graded lattice structure topology optimization for the design of additive manufactured components with stress constraints," *Computer Methods in Applied Mechanics and Engineering*, vol. 344, pp. 334–359, 2019.

[5] D. Brackett, I. Ashcroft, and R. Hague, "Topology optimization for additive manufacturing," *Solid Freeform Fabrication Symposium*, pp. 348–362, 2011.

[6] S. H. Masood, "Advances in Fused Deposition Modeling," *Comprehensive Materials Processing*, vol. 10, pp. 69–91, 2014.

[7] R. F. Pereira and P. J. Bártolo, "Recent Advances in Additive Biomanufacturing," *Comprehensive Materials Processing*, vol. 10, pp. 265–284, 2014.

[8] T. Zegard and G. H. Paulino, "Bridging topology optimization and additive manufacturing," *Structural and Multidisciplinary Optimization*, vol. 53, no. 1, pp. 175–192, 2016.

[9] K. Salonitis, "Stereolithography," *Comprehensive Materials Processing*, vol. 10, pp. 19–67, 2014.

[10] J. Panetta, Q. Zhou, L. Malomo, N. Pietroni, P. Cignoni, and D. Zorin, "Elastic textures for additive fabrication," *ACM Transactions on Graphics*, vol. 34, no. 4, pp. 1–135, 2015.

[11] M. Bendsøe, J. M. Guedes, R. B. Haber, P. Pedersen, and J. E. Taylor, "An Analytical Model to Predict Optimal Material Properties in the Context of Optimal Structural Design," *Journal of Applied Mechanics*, vol. 61, no. 4, p. 930, 1994.

[12] J. Zowe, M. Kocvara, and M. Bendsoe, "Free material optimization via mathematical programming," *Mathematical Programming, Series B*, vol. 79, no. 1-3, pp. 445–466, 1997.

[13] M. Kočvara and M. Stingl, "Free material optimization for stress constraints," *Structural and Multidisciplinary Optimization*, vol. 33, no. 4-5, pp. 323–335, 2007.

[14] M. Kočvara, M. Stingl, and J. Zowe, "Free material optimization: recent progress," *Optimization*, vol. 57, no. 1, pp. 79–100, 2008.

[15] J. H. Lee, J. P. Singer, and E. L. Thomas, "Micro-/nanostructured mechanical metamaterials," *Advanced Materials*, vol. 24, no. 36, pp. 4782–4810, 2012.

[16] C. Schumacher, B. Bickel, J. Rys, S. Marschner, C. Daraio, and M. Gross, "Microstructures to control elasticity in 3D printing," *ACM Transactions on Graphics*, vol. 34, no. 4, pp. 1–136, 2015.

[17] Bendsøe M.P. and O. Sigmund, *Topology Optimization: Theory, Methods and Applications*. Berlin: Springer Berlin Heidelberg, 2003.

[18] T. P. Hughes, A. Marmier, and K. E. Evans, "Auxetic frameworks inspired by cubic crystals," *International Journal of Solids and Structures*, vol. 47, no. 11-12, pp. 1469–1476, 2010.

[19] H. R. Hörnlein, M. Kočvara, and R. Werner, "Material optimization: Bridging the gap between conceptual and preliminary design," *Aerospace Science and Technology*, vol. 5, no. 8, pp. 541–554, 2001.

[20] B. Zhu, M. Skouras, D. Chen, and W. Matusik, "Two-Scale Topology Optimization with Microstructures," *ACM Transactions on Graphics*, vol. 34, no. 4, pp. 1–17, 2017.

[21] H. A. Eschenauer and N. Olhoff, "Topology optimization of continuum structures: A review," *Applied Mechanics Reviews*, vol. 54, no. 4, p. 331, 2001.

[22] M. B. Dühring, J. S. Jensen, and O. Sigmund, "Acoustic design by topology optimization," *Journal of Sound and Vibration*, vol. 317, no. 3-5, pp. 557–575, 2008.

[23] Y. Deng and J. G. Korvink, "Topology optimization for three-dimensional electromagnetic waves using an edge element-based finite-element method," *Proceedings of the Royal Society A: Mathematical, Physical and Engineering Sciences*, vol. 472, no. 2189, 2016.

[24] P. Gomes and R. Palacios, "Aerodynamic-driven topology optimization of compliant airfoils," *Structural and Multidisciplinary Optimization*, 2020.

[25] M. Pietropaoli, F. Montomoli, and A. Gaymann, "Three-dimensional fluid topology optimization for heat transfer," *Structural and Multidisciplinary Optimization*, vol. 59, no. 3, pp. 801–812, 2019.

[26] Martin Philip Bendsoe and Noboru Kikuchi, "Generating optimal topologies in structural design using a homogenization method," *Computer Methods in Applied Mechanics and Engineering*, vol. 71, pp. 197–224, 1988.

[27] R. V. Kohn and G. Strang, "Optimal Design and Relaxation of Variational Problems, III," *Communications on pure and applied mathematics*, vol. XXXIX, pp. 113–137, 1986.

[28] M. Bendsøe, "Optimal shape design as a material distribution problem," *Structural Optimization*, vol. 4, no. 1, pp. 193–202, 1989.

[29] M. Zhou and G. Rozvany, "The COC algorithm, Part II: Topological, geometrical and generalized shape optimization.," *Computational Method in Applied Mechanical Engineering*, vol. 89, pp. 309–336, 1991.

[30] A. Takezawa, G. H. Yoon, S. H. Jeong, M. Kobashi, and M. Kitamura, "Structural topology optimization with strength and heat conduction constraints," *Computer Methods in Applied Mechanics and Engineering*, vol. 276, pp. 341–361, 2014.

[31] T. Gao, W. H. Zhang, J. H. Zhu, Y. J. Xu, and D. H. Bassir, "Topology optimization of heat conduction problem involving design-dependent heat load effect," *Finite Elements in Analysis and Design*, vol. 44, no. 14, pp. 805–813, 2008.

[32] T. Gao, P. Xu, and W. Zhang, "Topology optimization of thermo-elastic structures with multiple materials under mass constraint," *Computers and Structures*, vol. 173, pp. 150–160, 2016.

[33] K. R. Saviers, R. Ranjan, and R. Mahmoudi, "Design and validation of topology optimized heat exchangers," *AIAA Scitech 2019 Forum*, no. January, pp. 1–7, 2019.

[34] R. C. Amigo, D. S. Prado, J. L. Paiva, R. W. Hewson, and E. C. Silva, "Topology optimisation of biphasic adsorbent beds for gas storage," *Structural and Multidisciplinary Optimization*, vol. 58, no. 6, pp. 2431–2454, 2018.

[35] J. Petersson and O. Sigmund, "Slope constrained topology optimization," *International Journal for Numerical Methods in Engineering*, vol. 41, no. 8, pp. 1417–1434, 1998.

[36] B. S. Lazarov and O. Sigmund, "Filters in topology optimization based on Helmholtz-type differential equations," *International Journal for Numerical Methods in Engineering*, vol. 86, pp. 765–781, 2011.

[37] O. Sigmund, "On the design of compliant mechanisms using topology optimization," *Mechanics of Structures and Machines*, vol. 25, no. 4, pp. 493–524, 1997.

[38] O. Sigmund and J. Petersson, "Numerical instabilities in topology optimization: A survey on procedures dealing with checkerboards, mesh-dependencies and local minima," *Structural Optimization*, vol. 16, no. 1, pp. 68–75, 1998.

[39] L. Ambrosio and G. Buttazzo, "An optimal design problem with perimeter penalization," *Calculus of Variations and Partial Differential Equations*, vol. 1, no. 1, pp. 55–69, 1993.

[40] R. B. Haber, C. S. Jog, and M. P. Bendsøe, "A new approach to variable-topology shape design using a constraint on perimeter," *Structural Optimization*, vol. 11, no. 1, pp. 1–12, 1996.

[41] B. Bourdin, "Filters in topology optimization," *International Journal for Numerical Methods in Engineering*, vol. 50, no. 9, pp. 2143–2158, 2001.

[42] M. Stolpe and K. Svanberg, "On the trajectories of penalization methods for topology optimization," *Structural and Multidisciplinary Optimization*, vol. 21, no. 2, pp. 128–139, 2001.

[43] M. Stolpe and K. Svanberg, "An alternative interpolation scheme for minimum compliance topology optimization," *Structural and Multidisciplinary Optimization*, vol. 22, no. 2, pp. 116–124, 2001.

[44] A. Dadalau, A. Hafla, and A. Verl, "A new adaptive penalization scheme for topology optimization," *Production Engineering*, vol. 3, no. 4-5, pp. 427–434, 2009.

[45] V. Young, O. M. Querin, G. P. Steven, and Y. M. Xie, "3D and multiple load case bi-directional evolutionary optimization (BESO)," *Structural Optimization*, vol. 18, pp. 183–192, 1999.

[46] G. I. N. Rozvany, "A critical review of established methods of structural topology optimization," *Structural and Multidisciplinary Optimization*, vol. 37, no. 3, pp. 217–237, 2009.

[47] S. Osher and J. A. Sethian, "Fronts Propagating with Curvature-Dependent Speed: Algorithms Based on Hamilton-Jacobi Formulations," *Journal of Computational Physics*, vol. 79, pp. 12–49, 1988.

[48] G. Allaire, F. Jouve, and A.-M. Toader, "A level-set method for shape optimization," *C. R. Acad. Sci. Paris, Ser. I*, vol. 334, pp. 1125–1130, 2002.

[49] M. Wang, X. Wang, and D. Guo, "A level set method for structural topology optimization," *Computer methods in applied mechanics and . . .*, vol. 192, pp. 227–246, 2003.

[50] H. Rodrigues, J. M. Guedes, and M. P. Bendsoe, "Hierarchical optimization of material and structure," *Structural and Multidisciplinary Optimization*, vol. 24, no. 1, pp. 1–10, 2002.

[51] P. G. Coelho, P. R. Fernandes, J. M. Guedes, and H. C. Rodrigues, "A hierarchical model for concurrent material and topology optimisation of three-dimensional structures," *Structural and Multidisciplinary Optimization*, vol. 35, no. 2, pp. 107–115, 2008.

[52] P. G. Coelho, P. R. Fernandes, H. C. Rodrigues, J. B. Cardoso, and J. M. Guedes, "Numerical modeling of bone tissue adaptation-A hierarchical approach for bone apparent density and trabecular structure," *Journal of Biomechanics*, vol. 42, no. 7, pp. 830–837, 2009.

[53] X. Yan, X. Huang, Y. Zha, and Y. M. Xie, "Concurrent topology optimization of structures and their composite microstructures," *Computers and Structures*, vol. 133, pp. 103–110, 2014.

[54] X. Yan, X. Huang, G. Sun, and Y. M. Xie, "Two-scale optimal design of structures with thermal insulation materials," *Composite Structures*, vol. 120, pp. 358–365, 2015.

[55] K. Liu, "Multiscale Topology Optimization of Structures and Periodic Cellular Materials," in *Proceedings of the ASME 2013 International Design Engineering Technical Conferences and Computers and Information in Engineering Conferences*, pp. 1–14, ASME, 2013.

[56] L. Xia and P. Breitkopf, "Concurrent topology optimization design of material and structure within FE2 nonlinear multiscale analysis framework," *Computer Methods in Applied Mechanics and Engineering*, vol. 278, pp. 524–542, 2014.

[57] V. J. Challis, A. P. Roberts, and A. H. Wilkins, "Design of three dimensional isotropic microstructures for maximized stiffness and conductivity," *International Journal of Solids and Structures*, vol. 45, no. 14-15, pp. 4130–4146, 2008.

[58] J. Deng, J. Yan, and G. Cheng, "Multi-objective concurrent topology optimization of thermoelastic structures composed of homogeneous porous material," *Structural and Multidisciplinary Optimization*, vol. 47, no. 4, pp. 583–597, 2013.

[59] W. Chen, L. Tong, and S. Liu, "Concurrent topology design of structure and material using a two-scale topology optimization," *Computers and Structures*, vol. 178, pp. 119–128, 2017.

[60] D. Chen, M. Skouras, B. Zhu, and W. Matusik, "Computational Discovery of Extremal Microstructure Families | The Computational Fabrication Group," *Science Advances*, pp. 1–8, 2018.

[61] A. Ben-Tal, M. Kočvara, A. Nemirovski, and J. Zowe, "Free material design via semidefinite programming: the multiload case with contact conditions," *SIAM Review*, vol. 42, no. 4, pp. 695–715, 2000.

[62] J. Nordmann, M. Aßmus, and H. Altenbach, "Visualising elastic anisotropy: theoretical background and computational implementation," *Continuum Mechanics and Thermodynamics*, vol. 30, no. 4, pp. 689–708, 2018.

[63] M. Kočvara, M. Stingl, and J. Zowe, "Free material optimization: recent progress," *Optimization*, vol. 57, no. 1, pp. 79–100, 2008.

[64] X. Yu, J. Zhou, H. Liang, Z. Jiang, and L. Wu, "Mechanical metamaterials associated with stiffness, rigidity and compressibility: A brief review," 5 2018.

[65] C. Wenshan and V. Shalaev, *Optical Metamaterials: Fundamentals and Applications*. New York: Springer-Verlag New York, 2010.

[66] M. Wegener, "Metamaterials beyond optics," *Science*, vol. 342, no. 939, p. 940, 2013.

[67] M. Maldovan, "Sound and heat revolutions in phononics," *Nature*, vol. 503, no. 7475, pp. 209–217, 2013.

[68] Lakes Roderic, "Foam Structures with a Negative Poisson's Ratio," *Science*, vol. 235, pp. 1038–1040, 1987.

[69] S. Babaee, J. Shim, J. C. Weaver, E. R. Chen, N. Patel, and K. Bertoldi, "3D soft metamaterials with negative poisson's ratio," *Advanced Materials*, vol. 25, no. 36, pp. 5044–5049, 2013.

[70] X. Ren, J. Shen, P. Tran, T. D. Ngo, and Y. M. Xie, "Design and characterisation of a tuneable 3D buckling-induced auxetic metamaterial," *Materials and Design*, vol. 139, no. November, pp. 336–342, 2018.

[71] R. Gatt and J. N. Grima, "Negative compressibility," *Physica Status Solidi - Rapid Research Letters*, vol. 2, no. 5, pp. 236–238, 2008.

[72] J. Christensen, M. Kadic, O. Kraft, and M. Wegener, "Vibrant times for mechanical metamaterials," *MRS Communications*, vol. 5, no. 3, pp. 453–462, 2015.

[73] S. Kang, J. Cha, K. Seo, S. Kim, Y. Cha, H. Lee, J. Park, and W. Choi, "Temperature-responsive thermal metamaterials enabled by modular design of thermally tunable unit cells," *International Journal of Heat and Mass Transfer*, vol. 130, pp. 469–482, 2019.

[74] E. M. Dede, F. Zhou, P. Schmalenberg, and T. Nomura, "Thermal Metamaterials for Heat Flow Control in Electronics," *Journal of Electronic Packaging, Transactions of the ASME*, vol. 140, no. 1, pp. 1–10, 2018.

[75] Y. Li, Y. Chen, T. Li, S. Cao, and L. Wang, "Hoberman-sphere-inspired lattice metamaterials with tunable negative thermal expansion," *Composite Structures*, vol. 189, no. February, pp. 586–597, 2018.

[76] R. L. Lincoln, F. Scarpa, V. P. Ting, and R. S. Trask, "Multifunctional composites: a metamaterial perspective," *Multifunctional Materials*, vol. 2, p. 043001, 12 2019.

[77] G. Nolas, J. Sharp, and J. Goldsmid, *Thermo-electrics: Basic principles and new materials developments*. Berlin: Springer-Verlag Berlin Heidelberg, 2001.

[78] F. Wang, "Systematic design of 3D auxetic lattice materials with programmable Poisson's ratio for finite strains," *Journal of the Mechanics and Physics of Solids*, vol. 114, pp. 303–318, 2018.

[79] M. Mohsenizadeh, F. Gasbarri, M. Munther, A. Beheshti, and K. Davami, "Additively-manufactured lightweight Metamaterials for energy absorption," *Materials and Design*, vol. 139, pp. 521–530, 2018.

[80] B. Engquist, P. Lötstedt, and O. Runborg, *Multiscale Methods in Science and Engineering*, vol. 44. Stockholm: Springer Berlin Heidelberg, 2005.

[81] E. Weinan, B. Engquist, X. Li, and W. Ren, "The Heterogeneous Multiscale Method: A Review," *Communications in Computational Physics*, vol. 2, no. 3, pp. 367–450, 2007.

[82] A. Abdulle, E. Weinan, B. Engquist, and E. Vanden-Eijnden, "The heterogeneous multiscale method," *Acta Numerica*, vol. 21, no. 21, pp. 1–87, 2012.

[83] J. M. Guedes and N. Kikuchi, "Preprocessing and postprocessing for materials based on the homogenization method with adaptive finite element methods," *Computational Methods in Applied Mechancs and Engineering*, vol. 83, no. 1, pp. 143–198, 1990.

[84] B. Hassani and E. Hinton, "A review of homogenization and topology optimization I - Homogenization theory for media with periodic structure," *Computers and Structures*, vol. 69, no. 6, pp. 707–717, 1998.

[85] B. Hassani and E. Hinton, "A review of homogenization and topology opimization II - Analytical and numerical solution of homogenization equations," *Computers and Structures*, vol. 69, no. 6, pp. 719–738, 1998.

[86] B. Hassani, "A review of homogenization and topology optimization III - topology optimization using optimality criteria," *Computers & Structures*, vol. 69, no. 6, pp. 739–756, 1998.

[87] S. Arabnejad and D. Pasini, "Mechanical properties of lattice materials via asymptotic homogenization and comparison with alternative homogenization methods," *International Journal of Mechanical Sciences*, vol. 77, pp. 249–262, 2013.

[88] C. L. Farmer, "Upscaling : a review," *International Journal for Numerical Methods in Fluids*, vol. 78, no. October 2001, pp. 63–78, 2002.

[89] L. Kharevych, P. Mullen, H. Owhadi, and M. Desbrun, "Numerical coarsening of inhomogeneous elastic materials," *ACM Transactions on Graphics*, vol. 28, no. 3, pp. 1–8, 2009.

[90] E. Andreassen and C. S. Andreasen, "How to determine composite material properties using numerical homogenization," *Computational Materials Science*, vol. 83, pp. 488–495, 2014.

[91] M. G. D. Geers, V. G. Kouznetsova, and W. a. M. Brekelmans, "Multi-scale computational homogenization: Trends and challenges," *Journal of Computational and Applied Mathematics*, vol. 234, no. 7, pp. 2175–2182, 2010.

[92] A. I. J. Forrester, A. Sóbester, and A. J. Keane, *Engineering Design via Surrogate Modelling*. John Wiley & Sons, Ltd., 2008.

[93] A. Ryberg, R. D. Bäckryd, and N. Larsgunnar, "Metamodel-Based Multidisciplinary Design Optimization for Automotive Applications," Tech. Rep. September, Linkoping University, 2012.

[94] W. Lafayette, "A UAV Design / Sizing Study from a System of Systems Perspective," *Proceedings 51st AIAA Aerospace Sciences Meeting*, no. January, pp. 1–14, 2013.

[95] S. J. Bates, J. Sienz, V. V. Toropov, E. Latin, H. Doe, D. O. Experiments, L. H. Doe, O. Latin, S. Lecturer, P. Aerospace, P. Design, and O. Specialist, "Experiments Using a Permutation Genetic Algorithm," *Optimization*, no. April 2004, pp. 1–8, 2011.

[96] M. R. Kianifar, F. Campean, and A. Wood, "Application of permutation genetic algorithm for sequential model building - model validation design of experiments," *Soft Computing*, vol. 20, no. 8, pp. 3023–3044, 2016.

[97] D. R. Jones, M. Schonlau, and W. J. Welch, "Efficient Global Optimization of Expensive Black-Box Functions," *Journal of Global Optimization*, vol. 13, no. 4, pp. 455–492, 1998.

[98] A. Nealen, "An As-Short-as-possible introduction to the least squares, weighted least squares and moving least squares methods for scattered data approximation and interpolation," *URL: http://www. nealen. com/projects*, no. 1, pp. 0–2, 2004.

[99] J. P. Romano and M. Wolf, "Resurrecting weighted least squares," *Journal of Econometrics*, vol. 197, no. 1, pp. 1–19, 2017.

[100] H. Y. Wang, D. H. Xiang, and D. X. Zhou, "Moving least-square method in learning theory," *Journal of Approximation Theory*, vol. 162, no. 3, pp. 599–614, 2010.

[101] F. M. A. Acosta, "Radial basis function and related models: An overview," *Signal Processing*, vol. 45, no. 1, pp. 37–58, 1995.

[102] J. P. Christophersen and S. R. Shaw, "Using radial basis functions to approximate battery differential capacity and differential voltage," *Journal of Power Sources*, vol. 195, no. 4, pp. 1225–1234, 2010.

[103] D. A. Cervantes Cabrera, P. González-Casanova, C. Gout, L. H. Juárez, and L. R. Reséndiz, "Vector field approximation using radial basis functions," *Journal of Computational and Applied Mathematics*, vol. 240, pp. 163–173, 2013.

[104] Z. Majdisova and V. Skala, "Radial basis function approximations: comparison and applications," *Applied Mathematical Modelling*, vol. 51, pp. 728–743, 2017.

[105] J. P. Kleijnen, "Regression and Kriging metamodels with their experimental designs in simulation: A review," *European Journal of Operational Research*, vol. 256, no. 1, pp. 1–16, 2017.

[106] C. Durantin, J. Marzat, and M. Balesdent, "Analysis of multi-objective Kriging-based methods for constrained global optimization," *Computational Optimization and Applications*, vol. 63, no. 3, pp. 903–926, 2016.

[107] W. Sun, B. Minasny, and A. McBratney, "Analysis and prediction of soil properties using local regression-kriging," *Geoderma*, vol. 171-172, no. m, pp. 16–23, 2012.

[108] T. W. Simpson, T. M. Mauery, J. Korte, and F. Mistree, "Kriging models for global approximation in simulation-based multidisciplinary design optimization," *AIAA Journal*, vol. 39, no. 12, pp. 2233–2241, 2001.

[109] J. Zou, Y. Han, and S. S. So, *Overview of artificial neural networks*, vol. 458. Humana Press, 2008.

[110] B. Liu, *Application of artificial neural networks in computer-aided diagnosis*. Humana Press, 2014.

[111] N. R. Secco and B. S. De Mattos, "Artificial neural networks to predict aerodynamic coefficients of transport airplanes," *Aircraft Engineering and Aerospace Technology*, vol. 89, no. 2, pp. 211–230, 2017.

[112] P. Hao, S. Feng, K. Zhang, Z. Li, B. Wang, and G. Li, "Adaptive gradient-enhanced kriging model for variable-stiffness composite panels using Isogeometric analysis," *Structural and Multidisciplinary Optimization*, vol. 58, no. 1, pp. 1–16, 2018.

[113] M. A. Bouhlel and J. R. Martins, "Gradient-enhanced kriging for high-dimensional problems," *Engineering with Computers*, vol. 35, no. 1, pp. 157–173, 2019.

[114] N. Guenther and M. Schonlau, "Support-Vector Networks," *Machine learning*, vol. 20, no. 3, pp. 273–297, 1995.

[115] S. Deng and T. H. Yeh, "Using least squares support vector machines for the airframe structures manufacturing cost estimation," *International Journal of Production Economics*, vol. 131, no. 2, pp. 701–708, 2011.

[116] L. Xia and P. Breitkopf, "Multiscale structural topology optimization with an approximate constitutive model for local material microstructure," *Computer Methods in Applied Mechanics and Engineering*, vol. 286, pp. 147–167, 2015.

[117] L. Colabella, A. P. Cisilino, V. Fachinotti, and P. Kowalczyk, "Multiscale design of elastic solids with biomimetic cancellous bone cellular microstructures," *Structural and Multidisciplinary Optimization*, 2019.

[118] S. Hollister and K. N., "A comparison of homogenization and standard mechanics analyses for periodic porous composites," *Computational Mechanics*, vol. 10, no. 2, pp. 73–95, 1992.

[119] J. Pinho-da Cruz, J. Oliveira, and F. Teixeira-Dias, "Asymtotic homogenisation in linear elasticity. Part I: Mathematical formulation and finite element modeling," *Computational Materials Science*, vol. 45, pp. 1073–1080, 2009.

[120] J. A. Oliveira, J. Pinho-da Cruz, and F. Teixeira-Dias, "Asymptotic homogenisation in linear elasticity. Part II: Finite element procedures and multiscale applications," *Computational Materials Science*, vol. 45, no. 4, pp. 1081–1096, 2009.

[121] O. Sigmund, N. Aage, and E. Andreassen, "On the (non-)optimality of Michell structures," *Structural and Multidisciplinary Optimization*, vol. 54, no. 2, pp. 361–373, 2016.

[122] Z. Hashin and S. Shtrikman, "A variational approach to the elastic behavior of multiphase materials," *J. Mech. Phys. Solids J. Mech. Phys. Solids*, vol. 11, no. 42, pp. 127–140, 1963.

[123] R. Hill, "The Elastic Behaviour of a Crystalline Aggregate," in *Proceeding of the Physical Society*, (Bristol), pp. 349–354, University of Bristol, 1952.

[124] S. Tsai, "Mechanics of composite materials," tech. rep., Air Force Materials Laboratory Technical Report, AFML-TR-66-149, 1966.

[125] R. Jones, *Mechanics of Composite Materials*. New York: Taylor & Francis Inc., 2nd ed., 1999.

[126] R. Newnham, *Properties of Materials: Anisotropy, Symmetry, Structure*. Oxford University Press, 2004.

[127] J. Aboudi, S. Arnold, and B. Bednarcyk, *Micromechanics of Composite Materials*. Butterworth-Heinemann, 2013.

[128] G. Dvorak, *Micromechanics of Composite Materials*. New York: Springer Dordrecht Heidelberg, 2013.

[129] M. F. Doerner, D. S. Gardner, and W. D. Nix, "Plastic properties of thin films on substrates as measured by submicron indentation hardness and substrate curvature techniques," *Journal of Materials Research*, vol. 1, no. 6, pp. 845–851, 1986.

[130] M. F. Pantano, H. D. Espinosa, and L. Pagnotta, "Mechanical characterization of materials at small length scales," *Journal of Mechanical Science and Technology*, vol. 26, no. 2, pp. 545–561, 2012.

[131] P. E. Farrell, D. Ham, S. Funke, and Rognes M.E., "Automated derivation of the adjoint of high-level transient finite element programs," *SIAM Journal of Scientific Computing*, vol. 35, no. 4, pp. C369–C393, 2013.

[132] A. Logg, K. A. Mardal, and G. N. Wells, "Automated solution of differential equations by the finite element method," *Lecture Notes in Computational Science and Engineering*, vol. 84, pp. 1–73, 2012.

[133] M. S. Alnæs, J. Blechta, J. Hake, A. Johansson, B. Kehlet, A. Logg, C. Richardson, J. Ring, E. Rognes, and G. N. Wells, "The FEniCS Project Version 1 . 5," *Archive of Numerical Software*, vol. 3, no. 100, pp. 9–23, 2015.

[134] A. Wächter and L. T. Biegler, "On the implementation of an interior-point filter line-search algorithm for large-scale nonlinear programming," *Mathematical Programming*, vol. 106, no. 1, pp. 25–57, 2006.

[135] C. Imediegwu, R. Murphy, R. Hewson, and M. Santer, "Multiscale structural optimization towards three-dimensional printable structures," *Structural and Multidisciplinary Optimization*, 2019.

[136] T. Lewiner, H. Lopes, A. W. Vieira, and G. Tavares, "Efficient Implementation of Marching Cubes' Cases with Topological Guarantees," *Journal of Graphics Tools*, vol. 8, no. 2, pp. 1–15, 2003.

[137] R. D. Murphy, C. Imediegwu, R. Hewson, M. J. Santer, and M. Muir, *Multiscale Concurrent Multi-Objective Structural Optimization of a Goose Neck Hinge*. AIAA Scitech 2020 Forum, 2020.

[138] H. D. Morgan, H. U. Levatti, J. Sienz, A. J. Gil, and D. C. Bould, "GE Jet Engine Bracket Challenge: A Case Study in Sustainable Design," *The Journal of Innovation Impact*, vol. 7, no. 1, pp. 95–107, 2014.

[139] F. Wang, B. S. Lazarov, and O. Sigmund, "On projection methods, convergence and robust formulations in topology optimization," *Structural and Multidisciplinary Optimization*, vol. 43, no. 6, pp. 767–784, 2011.